

Measurements of Suprathermal Particles at 1 AU and in the inner Heliosphere

Dissertation zur Erlangung des Doktorgrades
der Mathematisch-Naturwissenschaftlichen-Fakultät
der Christian-Albrechts-Universität zu Kiel

vorgelegt von
Jia Yu

April 1, 2018

Erster Gutachter (Supervisor):
Prof. Dr. R. F. Wimmer-Schweingruber

Zweiter Gutachter (Advisor):
Prof. Dr. W. J. Duschl

Tag der mündlichen Prüfung:
28.05.2018
Zum Druck genehmigt:
01.06.2018

Zusammenfassung

In dieser Arbeit wird das Verhalten von suprathermalen interplanetaren Teilchen mit Hilfe von drei Flugzeitmassenspektrometern auf drei unterschiedlichen Raumsonden untersucht. Alle drei Raumsonden befinden sich eine astronomische Einheit (AU) von der Sonne entfernt. Wir untersuchen dabei die Variation und Evolution von suprathermalen Teilchen in Strominteraktionsregionen (stream interaction regions, SIRs), die entstehen, wenn ein schneller Sonnenwindstrom einen langsamen Sonnenwindstrom einholt. Dabei wird oft eine Anreicherung von suprathermalen Teilchen beobachtet, was seit bereits über zehn Jahren das Interesse von Wissenschaftlern weckt.

Als Vorbereitung für unsere physikalische Analyse wird der Hintergrund des Spektrometers STOF (Suprathermal Time-of-Flight) auf der Raumsonde SOHO (Solar and Heliospheric Observatory) untersucht. Wir identifizieren den Hintergrund von STOF als überwiegend von energetischen durchdringenden Teilchen hervorgerufen. Durch eine auftretende Verunreinigung mit Photonen am Eintrittssystem von STOF werden diese mit einer höheren als der ursprünglich erwarteten Rate beobachtet. Zusätzlich stellen wir eine Methode zur Beschreibung des Hintergrundes für den STEP Sensor (SupraThermal Electrons and Protons Sensor) vor, der bald seine Forschungsreise auf der vorraussichtlich im Februar 2020 startenden Raumsonde *Solar Orbiter* beginnen wird. Sowohl STOF als auch STEP decken den suprathermalen Energiebereich ab und die Hauptquelle ihres Hintergrundes sind energetische durchdringende Teilchen.

In der hier vorgestellten SIR-Studie beobachten wir, dass suprathermale Teilchen innerhalb der Region des komprimierten schnellen Sonnenwindes (F') nahe der hinteren Flanke der Kompressionsregion ein Maximum erreichen. Aus Sicht eines Beobachters, der sich von der F' Region durch die hintere Flanke in den ungestörten schnellen Sonnenwind (F) bewegt, verhärtet sich das Spektrum mit voranschreitender Zeit. Gleichzeitig steigt das Häufigkeitsverhältnis von $\text{He}^+/\text{He}^{++}$. Unsere Beobachtungen sind mit früheren Messungen konsistent, decken aber zusätzlich auch niedrigere suprathermale Energien ab, als dies bisher möglich war. Darüber hinaus haben wir in manchen SIRs Spektren mit Umkehrpunkten bei niedrigen suprathermalen Energien identifiziert. Wir haben dabei ausgeschlossen, dass diese von instrumentellen Effekten wie der Effizienz oder dem Hintergrund hervorgerufen worden sein können. Diese spektrale Form wurde von der klassischen Theorie in Fisk and Lee (1980) bereits vorhergesagt und ist hier zum ersten Mal experimentell nachgewiesen worden. Allerdings war es uns nicht möglich einen gemeinsamen Parametersatz zu finden, der unsere Beobachtungen in dem Fisk and Lee (1980) Modell darstellt. Dies legt nahe, dass weitere Effekte wie zum Beispiel Querfelddiffusion und magnetische Spiegelung im Bereich zwischen der Sonne und der Kompressionsregion berücksichtigt werden müssen.

Abstract

In this thesis, interplanetary suprathermal particles at 1 astronomical unit (AU) are studied with three time-of-flight mass spectrometers onboard three spacecraft. We study the variation and evolution of suprathermal particles during stream interaction regions (SIRs) which form when fast solar wind streams overtake slow solar wind streams. The flux enhancements of suprathermal particles are often observed in association with SIRs, which has strongly interested scientists over tens of years.

As preparation work, the background of the Suprathermal Time-of-Flight spectrometer (STOF) of the Solar and Heliospheric Observatory (SOHO) is analyzed. We identify that the STOF background is mainly caused by energetic penetrating particles. Due to a possible leakage of photons at the entrance system of STOF, these particles are more easily recorded by STOF than originally anticipated. In addition, we propose a method for the background estimation, referring to the approach of Hilchenbach et al. (1998). This part of work guides the event selection for the SIR analysis, i.e., only events with high signal-to-noise ratio are chosen. In addition, based on this work, we further estimate the background for the SupraThermal Electrons and Protons sensor (STEP) which will be carried by the Solar Orbiter spacecraft and start its journey of exploration in February 2020. Both STOF and STEP cover suprathermal energies and the main source of their background is energetic penetrating particles.

For the SIR study, we have observed that the time profile of the suprathermal particles peaks inside the compressed fast wind (F') region, close to the trailing edge. When observers travel from the F' region via the trailing edge into the undisturbed fast wind (F) region, spectra harden with time, together with an increase of the $\text{He}^+/\text{He}^{++}$ abundance ratio. These observations are consistent with previous ones, but cover lower suprathermal energies than before. Moreover, we have identified turnover spectra at low suprathermal energies during some SIR events, excluding the instrumental influence, e.g., efficiency and background. The turnover spectral shape is predicted by the classical Fisk and Lee (1980) theory and has not been reported in previous observations. However, we can not fit the Fisk and Lee (1980) model to the data with meaningful parameters, suggesting that other effects (e.g., cross-field diffusion, magnetic mirroring effect in the region between the compression and the Sun) need to be taken into account.

Contents

| | | |
|----------|-------------------------------------------|-----------|
| 1 | Introduction | 1 |
| 1.1 | Solar Wind | 1 |
| 1.2 | Suprathermal Tail | 4 |
| 1.3 | The Structure of Thesis | 5 |
| 2 | Corotating Interaction Regions | 7 |
| 2.1 | CIR Structure | 8 |
| 2.2 | Theoretical Model | 11 |
| 2.3 | Previous Work | 14 |
| 3 | Instrumentation | 19 |
| 3.1 | The SOHO Mission | 19 |
| 3.2 | CELIAS/STOF | 22 |
| 3.2.1 | Working Principle of STOF | 23 |
| 3.2.2 | Entrance System | 24 |
| 3.2.3 | Time-of-Flight System | 25 |
| 3.2.4 | Solid State Detector System | 25 |
| 3.2.5 | Working Principle of HSTOF | 27 |
| 3.2.6 | PHA Data Acquisition | 27 |
| 3.3 | Background Analysis for STOF | 30 |
| 3.3.1 | Unexpected Behavior of SSDs | 30 |
| 3.3.2 | Background Generation Mechanism | 36 |
| 3.3.3 | Background Estimation Model | 45 |
| 3.4 | Conclusions | 49 |
| 4 | Case Study | 51 |
| 4.1 | Introduction | 51 |
| 4.2 | Publication | 52 |
| 5 | Full Study | 57 |
| 5.1 | Introduction | 57 |
| 5.2 | Publication | 57 |
| 6 | Verification with PLASTIC | 69 |
| 6.1 | Introduction | 69 |
| 6.2 | Publication | 70 |
| 7 | Conclusions and Outlook | 81 |

| | |
|------------------------------------------------------|----------------|
| Appendix A The Solar Orbiter Mission | 85 |
| A.1 EPD/STEP | 88 |
| A.1.1 STEP as a Part of EPD | 90 |
| A.2 Background Analysis for STEP | 90 |
| A.2.1 Flux Spectrum Investigation | 92 |
| A.2.2 Shielding Design | 94 |
| A.2.3 Signal to Noise Ratio | 100 |
| A.2.4 Background Generation Mechanism | 103 |
| A.2.5 Background Estimation Pixel | 106 |
| A.3 Conclusions | 109 |
| Appendix B STOF Sweep Voltage Description | 115 |

List of Figures

| | | |
|------|-----------------------------------------------------------------------------------------------------------------------|----|
| 1.1 | Parker spiral | 3 |
| 1.2 | Solar wind speed at different heliographic latitudes | 4 |
| 2.1 | Schematic view of CIR | 8 |
| 2.2 | Time profiles of the CIR during DOY 206 to 211, 2003 | 9 |
| 2.3 | Velocity distribution of suprathermal particles described by the Fisk and Lee (1980) model | 13 |
| 2.4 | Energy spectra of suprathermal particles reported by Mason et al. (1997) | 14 |
| 2.5 | Energy spectra of suprathermal alpha particles reported by Reames et al. (1997) | 15 |
| 2.6 | Cast study of two CIR events done by Chotoo et al. (2000) | 16 |
| 3.1 | Schematic view of the SOHO spacecraft | 20 |
| 3.2 | Photograph of pre-flight model (PFM) of (H)STOF | 22 |
| 3.3 | Schematic drawing of (H)STOF | 23 |
| 3.4 | Sequence diagram of (H)STOF | 24 |
| 3.5 | SSD pixel array of (H)STOF | 26 |
| 3.6 | Ion species measured by STOF | 29 |
| 3.7 | Data output of (H)STOF over the same time period as in Figure 3.6 . . . | 31 |
| 3.8 | Measurements of STOF in the left and right two hybrids | 32 |
| 3.9 | Normalized count distribution in the SSD system of (H)STOF during solar events from the year 1998 to 2005 | 33 |
| 3.10 | Same as Figure 3.9, but during the solar quiet times of each year | 34 |
| 3.11 | Energy measurements for the oversensitive pixel 31 of HSTOF | 35 |
| 3.12 | (H)STOF measurements during solar quiet times in 1998 after rejecting data in the lowest E_{SSD} channels | 36 |
| 3.13 | STOF measurements on Hybrids 0 and 2 during solar quiet times of 1998 | 37 |
| 3.14 | Count distribution over the TOF, E_{SSD} , and E/q channels with the same data as in Figure 3.13 | 38 |
| 3.15 | HSTOF measurements during solar quiet times in 1998 | 39 |
| 3.16 | Schematic view of SEM | 40 |
| 3.17 | Comparison between the UV flux and the count rates of MCP triggers . . | 41 |
| 3.18 | Schematic view of EPHIN | 43 |
| 3.19 | Mechanism of the STOF background generation | 44 |
| 3.20 | Method of the background estimation for HSTOF given by Hilchenbach et al. (1998) | 46 |
| 3.21 | Method of the background estimation for STOF used in this thesis | 47 |
| 3.22 | An application example of the STOF background estimation method . . . | 48 |
| 4.1 | Schematic view of SWICS | 51 |

| | | |
|------|----------------------------------------------------------------------------------------------------------------------|-----|
| 6.1 | Cutaway view of PLASTIC's entrance system | 69 |
| 7.1 | Anisotropy measurements for 12 SIR events in the third publication with STEREO/SEPT data | 83 |
| A.1 | Artist's illustration of ESA's Solar Orbiter observing the Sun | 85 |
| A.2 | Payload accommodation onboard the Solar Orbiter spacecraft | 86 |
| A.3 | Functional diagram of EPD's instruments | 88 |
| A.4 | Energy coverage of EPD's instruments | 89 |
| A.5 | Profile of STEP's two sensor units | 91 |
| A.6 | Energy spectra of proton and electron during solar quiet times | 92 |
| A.7 | Energy spectra of proton and electron during a SEP event reported by Mewaldt et al. (2005) | 93 |
| A.8 | Photon flux during solar quiet times studied by Hannah et al. (2010) | 94 |
| A.9 | Energy spectra of gamma-rays during the solar flare event on Dec. 6th, 2006 | 95 |
| A.10 | Geant4 simulation model for STEP | 96 |
| A.11 | Distribution of proton deposited energy versus primary energy obtained from the Geant4 simulation for STEP | 98 |
| A.12 | Same as Figure A.11 but with electrons as incident particles | 98 |
| A.13 | Differential count rates of the STEP background during solar quiet times | 99 |
| A.14 | SNR during solar quiet times at 1 AU for a single SSD | 101 |
| A.15 | SNR during the event on 28/10/2013 at 1 AU | 102 |
| A.16 | Geant4 simulation of solar protons at 1 AU | 103 |
| A.17 | Photon background derived with the spectrum in Figure A.9 | 103 |
| A.18 | Distribution among energy deposit of primary and secondary particles | 104 |
| A.19 | Count distribution of primary and secondary particles on the single SSD | 105 |
| A.20 | Four cases of particle hits on the single SSD | 106 |
| A.21 | The SSD board of STEP | 106 |
| A.22 | Comparison of background generated on the single SSD and pixel array | 107 |
| A.23 | Count distribution in 16 big SSD pixels of STEP | 108 |

List of Tables

| | | |
|-----|------------------------------------------------------------------------------------------------------------------------------------------------------|-----|
| A.1 | Simulation parameters for the STEP Geant4 model | 95 |
| A.2 | STEP response function | 97 |
| A.3 | Product of the probability array and the geometrical factor of the simulation source for all 16 big pixels of STEP for the case of protons | 112 |
| A.4 | Same as Table A.3, but shoot STEP with electrons. | 114 |

Chapter 1

Introduction

The Sun, as the nearest star to Earth, has attracted continuous attention in human history. No other stars can offer us more detailed studies than the Sun. Its structure can be divided into a core, radiative zone, tachocline, convective zone, photosphere and atmosphere. The core of the Sun is the hottest part, where nuclear fusion continually produces an appreciable amount of thermal energy through a series of steps called the p-p (proton-proton) chain (Broggini, 2003). From the core out to about 0.7 solar radii is the radiative zone, where the temperature starts to drop down from seven million to two million Kelvin with increasing distance from the core. The way of energy transmission is, as its name implies, by radiation. The tachocline is the transition layer between the radiative zone and outer convective zone. It was hypothesized that the Sun's magnetic field is generated within this place by a magnetic dynamo (Roberts, 1972). From the tachocline to the solar surface, the temperature continuously decreases and heavier atoms are not fully ionized. In this case, radiative heat transport is less effective and convective energy transmission becomes dominant. The photosphere is the visible surface of the Sun, above which visible sunlight is free to propagate into space, and its energy escapes from the Sun entirely. Now the temperature reaches the minimum in the solar atmosphere at about 500 km above the photosphere with a temperature of about 4100 Kelvin and then surprisingly rises up. The reason is still not well known, but evidence suggests that waves may have enough energy to heat the solar atmosphere. In the solar corona which is the outer layer of the solar atmosphere, the temperature can reach a few million Kelvin and atoms become highly ionized. The ionized atoms which are released from the corona are the so-called solar wind which flows outward at supersonic speed to great distances, filling a region known as the heliosphere, an enormous bubble-like region of space.

1.1 Solar Wind

As introduced above, the solar wind is a stream of charged particles emitted radially away from the Sun. Viewed in the historic light, this idea can date back to the 19th century when Carrington and Richard Hodgson independently found a sudden outburst of energy (likely an intensive solar flare) from the Sun's atmosphere in 1859. On the second day, a geomagnetic storm was observed and Carrington suspected a connection between two observations (Odenwald and Green, 2008). Both Fitzgerald in 1892 and 1900, and Lodge in 1900, suggested that the geomagnetic storms were caused by a flying cloud of charged particles (Dessler, 1967). But Birkeland in 1896 suggested a continuous solar wind rather than a transient one (Dessler, 1967) based on the effects of a beam

of charged particles on a terrella in his laboratory. Later, Biermann (1951, 1952, 1957) pointed out that a continuous solar wind has the virtue to explain cometary tails which are typically observed to be deflected from the flight path towards the radial direction away from the Sun. Based on these earlier observational suggestions of the existence of the solar wind, E. N. Parker in 1958 gave a theoretical model which predicts that the wind is supersonic. Similar flow profiles which show acceleration from subsonic to supersonic speeds are known from Laval nozzles. In the early 1960s, these ideas were confirmed by the first in-situ observations from a series of Russian (Luna 2, Luna 3, and Venus 3) (Gringauz et al., 1960; Gringauz et al., 1961; Gringauz et al., 1967) and American (Explorer 10, Mariner 2, and Imp 1) (Bonetti et al., 1963; Ness et al., 1964; Snyder and Neugebauer, 1965; Neugebauer and Snyder, 1966, 1967) space probes and satellites. Moreover, the solar wind composition was well measured. $^1\text{H}^+$ and $^4\text{He}^{++}$ were observed to be the most abundant solar wind ions by Mariner 2 (Snyder and Neugebauer, 1964). The number ratios $^4\text{He}^{++}/^1\text{H}^+$ extend from < 0.005 to > 0.15 . Using solar wind measurements with electrostatic analyzers on the earth-orbiting Vela 3A and 3B satellites, Bame et al. (1968) reported the presence of ions of $^3\text{He}^{++}$, $^4\text{He}^+$, and various ion species of ^{16}O . Bame et al. (1970) further identified $^{56}\text{Fe}^{+8}$ to $^{56}\text{Fe}^{+12}$, $^{28}\text{Si}^{+7}$, $^{28}\text{Si}^{+8}$, $^{28}\text{Si}^{+9}$, and $^{16}\text{O}^{+6}$ in the solar wind with Vela 5A measurements. Compared with $^1\text{H}^+$ and $^4\text{He}^{++}$, the abundance of heavy ions in the solar wind is rather small. Bame et al. (1975) found the average ratios of Iron, Silicon, and Oxygen to Hydrogen during the period in 1969-1971 are 5.3×10^{-5} , 7.6×10^{-5} , 5.2×10^{-4} , respectively.

Parker (1958) also considered the relation between the solar wind and the configuration of the Sun's magnetic field. As the wind is a plasma of high electrical conductivity, the magnetic field is frozen-in. The magnetic field is then transported away from the rotating Sun into the interplanetary space by the solar wind. Its shape is determined by the wind speed together with the rotation of the Sun. As shown in Figure 1.1, the wind is purely radial, whilst the streamlines of flow are curved with a form of an Archimedean spiral due to the rotation, also known as the Parker spiral. In short, the geometrical figure of the magnetic field lines corotates, while the fluid of solar wind does not corotate but instead travels radially outwards. Depending on the location in the hemisphere and the phase of the solar cycle, the magnetic field points inward or outward. The direction of the magnetic field is opposite in the northern and southern parts of the heliosphere. The polarity reversal of magnetic field, which is found within the low-speed wind and which maps back to the solar magnetic equator, is commonly called the Heliospheric Current Sheet (HCS) (Schatten, 1972). Near solar minimum, the HCS tends coincide approximately with the solar equatorial plane. If the dipole global field of the Sun is inclined, e.g., during the approach to solar minimum, the rotation of the Sun leads to the HCS having a configuration similar to a twirled "ballerina's skirt" (Alfvén, 1957). This configuration changes in shape through the solar cycle as the Sun's magnetic field reverses about every 11 years.

Sources of the Solar Wind

In-situ observations have established that there are two components of the quiescent solar wind, respectively termed the slow solar wind and the fast solar wind. The fast solar wind is known to originate in solar coronal holes (Krieger et al., 1973; Nolte et al., 1976), where the Sun's corona is easily visible as dark regions in white-light, X-ray, and extreme ultraviolet images. The magnetic fields in coronal holes can be considered as open, then plasma is relatively unconstrained to escape away from here, producing a low density and low temperature in this area. Based on data from three recurrences of the same

coronal hole, Krieger et al. (1973) found that the size of the coronal hole is well correlated with the speed of the solar wind emanating from the coronal hole. Recently, Wang and Sheeley (2006) invoked the superradial expansion to explain the fast solar wind speed. These authors compared solar wind speed with superradial expansion factors derived from the potential field source surface model and found them to be well explained by a conservation of mass and energy along a flux tube. By contrast, the origin of slow solar wind is controversial. Wang et al. (1998) found that the edges of coronal holes are a source of the slow solar wind. Later Neugebauer et al. (1998) and Burton et al. (1999) found that the slow wind also maps back to streamers themselves. Until today, the origin of the slow solar wind is one of the major open questions in solar physics. Therefore, it is listed as a highest-priority scientific objective for the Solar Orbiter mission (see “How and where do the solar wind plasma and magnetic field originate in the corona?” in Appendix A).

Figure 1.2 shows solar wind speed as a function of the solar latitude as measured by Ulysses which is an out-of-ecliptic spacecraft, providing detailed information on the latitudinal structure of the solar wind. The data was obtained during Ulysses’ first polar orbit around the Sun extending from February 1992 through December 1997 on the declining phase to the minimum of the 22nd solar cycle (Gosling and Pizzo, 1999). The solar wind variability is confined to a narrow latitude band centered on the heliographic equator. Both low- and high-speed solar wind were observed within this band, the width of which ranges from about $\pm 20^\circ$ to $\pm 35^\circ$ in latitude (Gosling and Pizzo, 1999). At high latitudes, where coronal holes are located, the wind speed is nearly constant

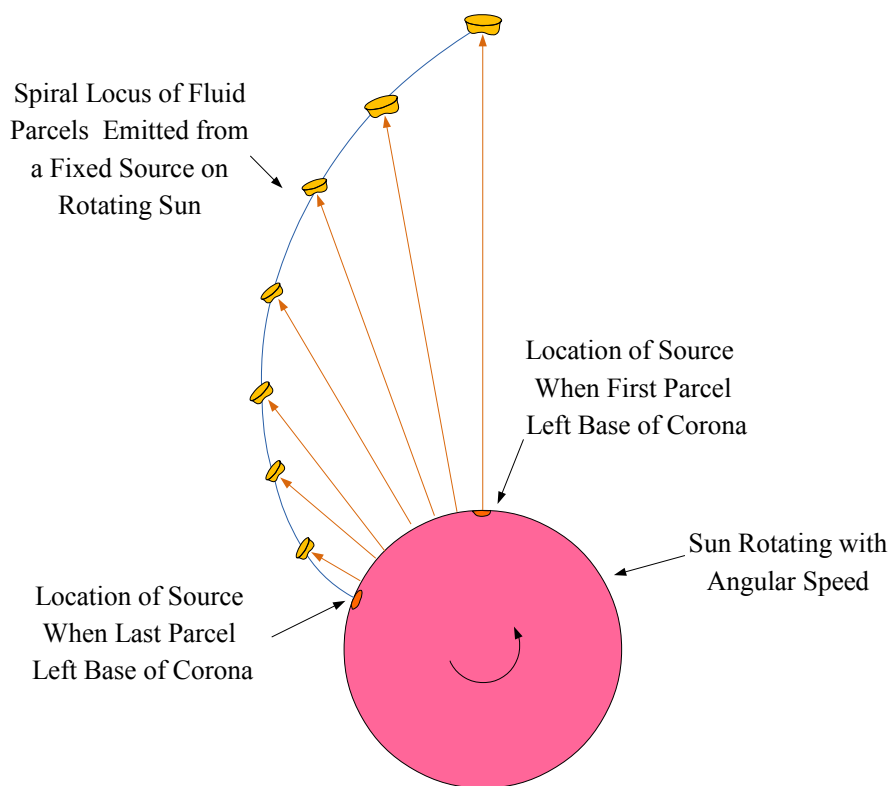


Figure 1.1: The drawing out of plasma carrying magnetic field outward with it. Frozen-in transport of magnetic field away from the rotating Sun creates a spiral field structure - Parker Spiral

about 750 km/s. These observations are consistent with the earlier opinion on the solar wind properties from Zhao and Hundhausen (1981); Burton et al. (1996). These authors found that the wind properties vary strongly with distance from the HCS, i.e., with flow speed increasing and density decreasing away from the HCS. Due to the warped and tilted HCS with respect to the heliographic equator, both slow and fast solar wind are expected to be observed at low heliographic latitudes as the Sun rotates.

1.2 Suprathermal Tail

In-situ measurements have identified two distinct distributions of particles in the heliosphere. (1) Low-energy particles with a speed around the solar wind bulk speed. These particles are not very mobile and simply alternatively expanded and compressed, normally referred to as core particles. Their velocity distribution is a form of Maxwell-Boltzmann function, carrying most of the wind mass. (2) At some higher energies, suprathermal tails on the distribution functions of solar wind ions are always observed. The origin of these tails is still under debate. Schwadron et al. (1996) suggest that transit-time damping the IMF magnitude variations can statistically accelerate particles within corotating interaction regions (CIRs). A recent series of publications of Fisk and Gloeckler (2006, 2007, 2008) suggest that particles are accelerated by stochastic acceleration due to turbulent compressions and rarefactions in the solar wind plasma, exhibiting a remarkably common spectral shape in many different circumstances. In the

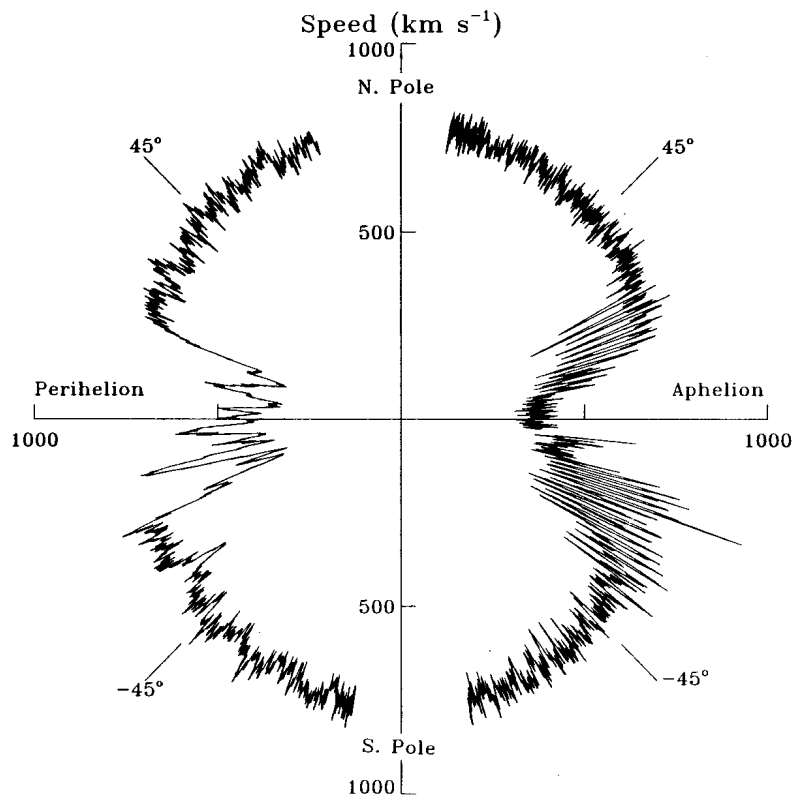


Figure 1.2: Solar wind speed as a function of the heliographic latitude measured by Ulysses. The figure is taken from Gosling and Pizzo (1999).

frame of the solar wind, the suprathermal tail extends from several keV/nuc to a few MeV/nuc, and is typically characterized by an omni-directional distribution function of the form $f(v) \propto v^{-5}$ (Mewaldt et al., 2000; Gloeckler, 2003). This common spectral shape occurs in the quiet solar wind, in disturbed conditions downstream from shocks, and particularly in the heliosheath (Decker et al., 2005). Jokipii and Lee (2010) have found that the Fisk & Gloeckler equation does not conserve particles, and that stochastic acceleration driven by a spectrum of Alfvén waves and transit-time damping of oblique magnetosonic waves can not produce power-law spectra with indices less than -3. These authors believed that the -5 spectrum in solar quiet times is the remnant contribution from solar events, e.g., Solar Energetic Particle (SEP) events and corotating ion events. However, Fisk et al. (2010) re-derived the basic equations of their theory and insisted that both particles and energy are conserved.

Due to their elevated energies, suprathermal particles were identified as a prime seed population for further acceleration in solar gradual events (Bamert et al., 2002). Chottoo et al. (2000) have identified that the source of suprathermal ions during two Corotating Interaction Region (CIR) events is at or near 1 Astronomical Unit (AU) using properties of particle peak intensities, magnetic field connection, and spectral shape. These authors concluded the ion populations contain the seed population. Recent anisotropy measurements during three CIRs support this conclusion (Ebert et al., 2012). The study of suprathermal particles can help us understand the 'injection' process of the Diffusive Shock Acceleration (DSA) which dates back to Fermi in the 1940s (Fermi, 1949) and is regarded as a classic theory for the origin of the galactic cosmic rays (Drury, 1983). In the DSA mechanism, particles scatter back and forth across a shock and gain energy by drifts in the electric field at the shock. To inject in the DSA, the initial speed of particles needs to be in the suprathermal range to cross the shock front (Zank et al., 1996). Based on DSA, Fisk and Lee (1980) developed a theoretical model to explain the spectral variations associated with CIRs, considering the adiabatic deceleration. Detailed introduction and discussion of the Fisk & Lee model is given in Chapter 2.

1.3 The Structure of Thesis

In this chapter, the background knowledge about the solar wind origin and suprathermal tails has been given (see Sections 1.1, and 1.2 respectively). The main topic of this thesis is suprathermal tail particles in CIRs, including the scientific data extraction and calibration, and investigation of spectral shape.

Chapter 2 introduces the Fisk and Lee (1980) model which describes spectral properties and evolution associated with CIRs. Meanwhile, previous work based on this theory is also listed.

In Chapter 3, an overview of the SOHO mission and the (H)STOF sensor is presented. Particularly, the source of the background of STOF has been identified with data from another two instruments (SEM and EPHIN) onboard SOHO spacecraft. The corresponding background estimation method is then described.

Chapter 4 shows a case study for a CIR event occurring in 2003, with data from SOHO/STOF and ACE/SWICS. The time profile of suprathermal He^{++} flux is consistent with previous observations. The flux peaks inside the CIR compression region, close to the reverse shock. The suprathermal $\text{He}^+/\text{He}^{++}$ abundance ratio increases with time, the same trend as seen before. However, the spectral shape outside the CIR is not a power law as suspected based on previous observations, but consists lack of particles just above the bulk solar wind speed up to ~ 40 keV/nuc, exhibiting a bump shape. This

spectral characteristic is observed for the first time and predicted by Fisk and Lee (1980). However, the Fisk and Lee (1980) model is not valid at low suprathermal energies, e.g. 40 keV/nuc. We cannot explain our observations quantitatively.

In Chapter 5, we include more CIR events (16 in total) into our spectral investigation. Of the sixteen CIRs, ten CIRs showed continuous power law spectra in the fast solar wind regions, i.e., the same behavior as reported in previous observations. Six CIRs showed possible signs of a turnover between ~ 10 -40 keV/nuc in the fast solar wind trailing the compression regions. Two of them even showed this behavior inside the compressed fast wind. However, the turnover spectra can not be well fitted with the Fisk and Lee (1980) model, implying that some other effects can modify the spectral shape, e.g., cross-field transport of suprathermal particles and particle reflection in the inner heliosphere.

The work shown in Chapter 6 is to verify the observations reported in Chapters 4 and 5 with STEREO/PLASTIC data, especially the turnover spectra at low suprathermal energies. Compared with combined observations from SOHO/STOF and ACE/SWICS, STEREO/PLASTIC can uniquely measure both the solar wind bulk and its suprathermal tails, together with much better counting statistics. Of twelve surveyed SIR events, we observed turnover spectra directly and clearly in six events when the ion speed is smaller than ~ 2500 km/s (~ 32 keV/nuc). The remaining six SIRs exhibit continuous power laws in both downstream and upstream of the SIR-driven reverse shocks. In addition, the suprathermal tails at high ion velocities (>2500 km/s) are observed to overall harden from the compressed fast wind regions to the fast wind regions, consistent with previous observations (Reames et al., 1997; Ebert et al., 2012).

At the beginning of Chapters 4, 5, and 6, we present a brief introduction and overview then a publication. Chapter 7 contains the conclusions and outlook of the work of this thesis. In Chapter 3, we understand how the STOF background is generated. This knowledge is then applied to STEP, a suprathermal particle detector onboard the coming space mission Solar Orbiter, see Appendix A. Appendix B is part of a technical document describes the sweep voltage of (H)STOF.

Chapter 2

Corotating Interaction Regions

Dating back to the early 1960s, intensity enhancements of MeV ions near the Earth were detected by spacecraft instruments. This phenomenon was considered to be related with the appearance of active regions on the Sun and often appeared during several successive rotations of the Sun (Bryant et al., 1965; Fan et al., 1968). Later, one found out that these energetic particles are mainly accelerated in CIRs as described by Gosling and Pizzo (1999). CIRs can be produced when fast solar wind emerging from solar coronal holes runs into slower solar wind ahead. Typically, coronal holes can remain stable for many months (Krieger et al., 1973), leading to a pattern of corotating fast and slow solar wind flows in the heliosphere. The interaction of these two streams of solar wind forms a compression region of high magnetic and plasma pressure surrounding the stream interface. Due to the roughly time-stationary coronal holes, these compression regions form spirals in the solar equatorial plane that corotate with the Sun, hence the name corotating interaction regions (Gosling and Pizzo, 1999).

As we introduced in the Chapter 1, the magnetic field in each solar wind stream is drawn out into an Archimedean spiral pattern from the Sun by the radially-flowing plasma. As the Sun rotates, flows of different velocity become radially aligned within the low-latitude band of solar wind variability (Gosling and Pizzo, 1999). The plasma can not interpenetrate due to its high conductivity, thus the interface between two streams is approximately parallel to the mean magnetic field, in other words, the interface forms a rough spiral intermediate between those of the two streams. Near the Sun, two adjacent solar wind streams slide by each other with little interaction. However, when they propagate outward from the solar corona, the slower stream can be pushed on by its following faster stream. As a result, a compression will form on the rising-speed portion of the high-speed solar wind and a rarefaction will form on the trailing edge (Parker, 1963). The continuous interaction between the streams causes increased compression in the region surrounding the interface which becomes more and more perpendicular to a radial line from the Sun (Lazarus et al., 1999). In short, the interaction therefore strengthens with heliocentric distance. If the velocity difference across the interface becomes large enough relative to the local magnetosonic wave speeds in the streams, shocks can form at the boundaries of the interaction region. A forward shock is expected to form first at the downstream edge of the interaction regions due to the smaller wave velocity in the slow wind stream (Lazarus et al., 1999). By contrast, a reverse shock would eventually form at the upstream edge of the interaction region in the fast wind stream. But typically it is later than the formation of the forward shock, since the wave speed is larger in the hotter and faster wind stream than that in the cooler and slower wind stream. Beyond about 2-3 AU, forward-reverse shock pairs are a common

feature of CIRs (Lazarus et al., 1999). For the case at 1 AU and 0.72 AU, the shock-association rate of CIR events (with a forward shock, or a reverse shock, or a forward-reverse shock pair) is approximately 31% and 3%, respectively (Jian et al., 2008). Based on in-situ observations from the Wind and ACE spacecraft, Jian et al. (2006) have conducted a comprehensive investigation of the Stream Interaction Region (SIR) events at 1 AU, including a separate assessment of recurrent CIRs. These authors found that the occurrence rate of shocks at SIRs at 1 AU is about 24%. In these events with shocks, 70% of them have only forward shocks, while 24% of them have only reverse shocks. The remaining about 6% events were bounded with a pair of forward-reverse shocks.

The origin of the fast or high-speed solar wind associated with CIRs has been clearly identified as the coronal holes with open magnetic field structures (see details in the Chapter 1). The origin of the slow solar wind is less clear and may originate from a range of coronal configurations adjacent to, or above magnetically closed structures (Balogh et al., 1999). Recent observations by Tian et al. (2014) show that intermittent small-scale jets from the networks of the solar transition region and chromosphere can produce plasma with speeds of 80-250 km/s. These jets can be clearly detected at any location on the solar disk outside active regions. In the coming future, the Solar Orbiter mission will help us to answer the question of the origin of the slow wind (Müller et al., 2013).

2.1 CIR Structure

A sketch of the overall CIR geometry is illustrated in Figure 2.1. Following Richardson et al. (1993) and Chottoo et al. (2000), we mark four regions: the slow wind region (S),

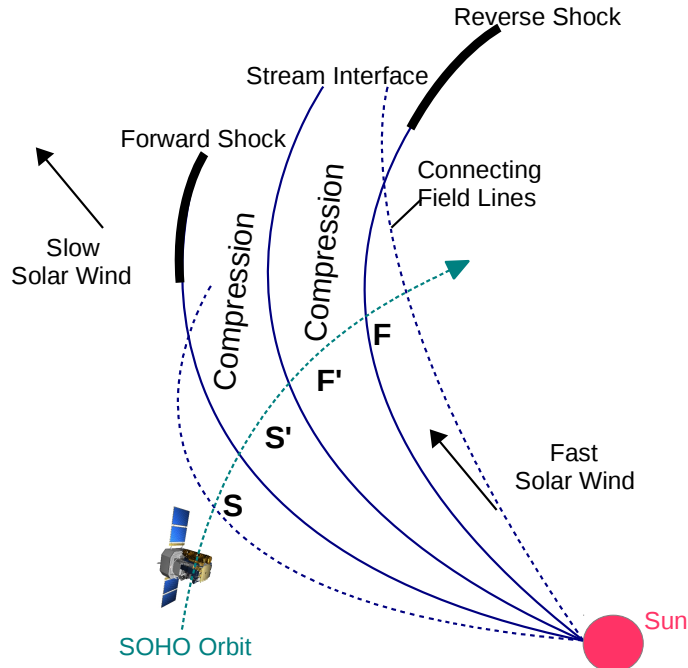


Figure 2.1: Schematic view of a CIR event adapted from Richardson et al. (1993). The green dashed line with arrow indicates the SOHO spacecraft path. The symbols S, S', F' and F represent slow wind, compressed slow wind, compressed fast wind and fast wind regions respectively.

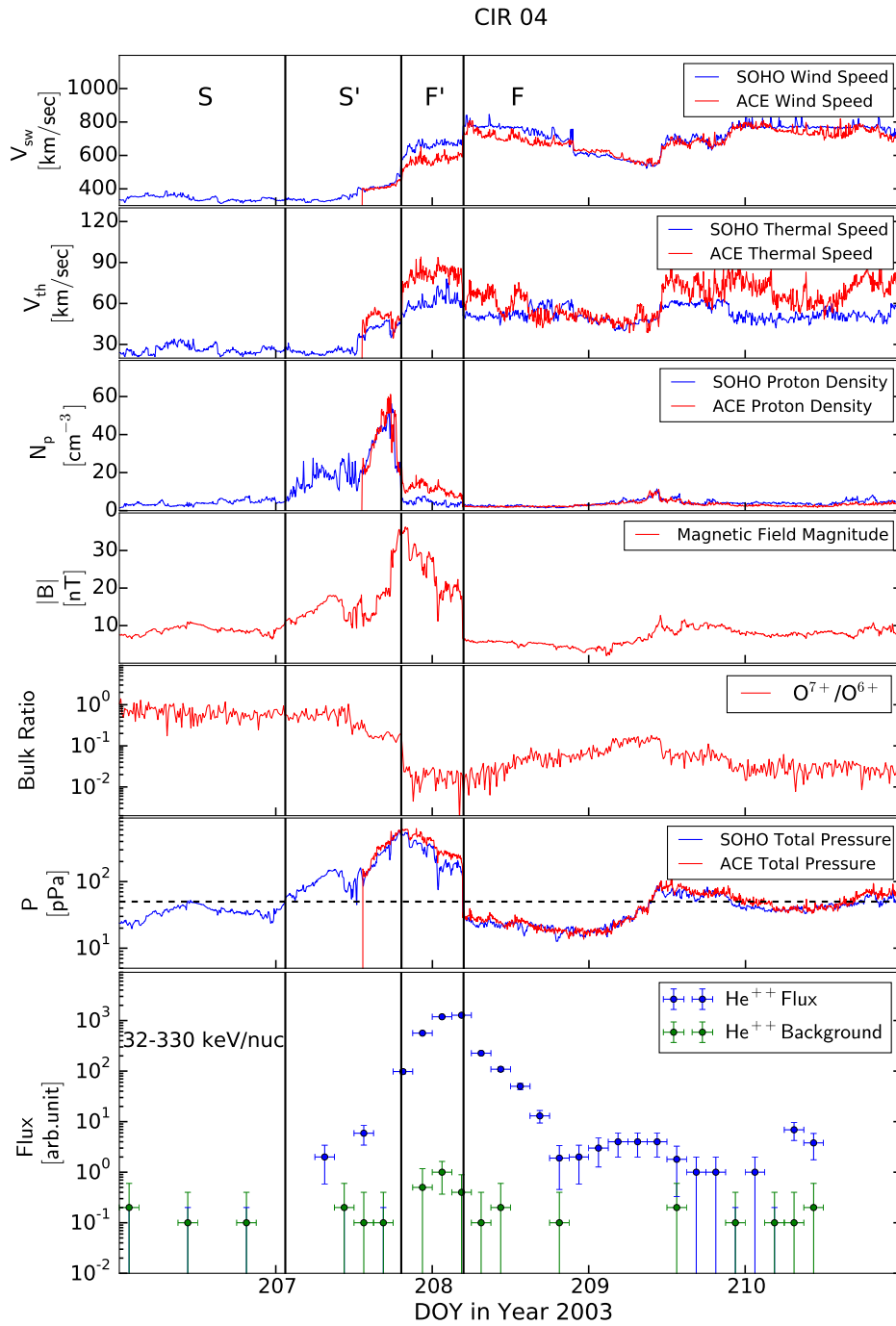


Figure 2.2: The time profiles of CIR-associated suprathermal helium identified by STOF during the period from Day of Year (DOY) 206 to 211, 2003. (The figure is reproduced from Yu et al. (2016), with the permission of AIP Publishing.)

the compressed slow wind region (S'), the compressed fast wind region (F'), and the fast wind itself (F), divided by the leading edge, the stream interface and the trailing edge. The Solar and Heliospheric Observatory (SOHO) spacecraft at Lagrangian Point 1 (L1) traverses four regions (S, S', F' and F) of the CIR successively along the green dashed circular path. The leading and trailing edges of the CIR (i.e., the S-S' and F'-F interfaces) can finally evolve into forward and reverse shocks, typically beyond Earth orbit (1 AU), as shown with the thickening of the S-S' and F'-F interface lines in Figure 2.1. The stream interface (S'-F') is where the slow and fast solar wind plasma meet. The magnetic connection between the CIR and the SOHO spacecraft is shown by the dotted lines. In the S region, it is beyond 1 AU and moves inward with time until at the leading edge (i.e. the magnetic connection becomes 1 AU at the S-S' interface). While inside the CIR itself, the connection actually moves inside 1 AU, referring to Chotoo et al. (2000). At the trailing edge (F'-F interface), the connection is at 1 AU, and then moves outward at later times.

Figure 2.2 illustrates solar wind plasma and magnetic field measurements for the CIR occurring between July 26 and 27, 2003 (days of year 207-208). The leading and trailing edge and the stream interface are indicated with vertical solid lines in this figure. Shown from top to bottom are 5-min averaged solar wind proton speed (v_{sw}), thermal speed (v_{th}) and proton number density (n_p) measured by SOHO/CELIAS/PM (the Solar and Heliospheric Observatory/the Charge, Element, and Isotope Analysis System/the Proton Monitor (Hovestadt et al., 1995)) and ACE/SWEPAM (the Advanced Composition Explorer spacecraft (also at L1)/the Solar Wind Electron, Proton, and Alpha Monitor (McComas et al., 1998)), 4-min averaged interplanetary magnetic field strength ($|B|$) measured by ACE/MAG (the Magnetometer (Smith et al., 1998)), 12-min averaged O^{7+}/O^{6+} abundance ratio measured by ACE/SWICS (the Solar Wind Ion Composition Spectrometer (Gloeckler et al., 1998)), total pressure ($P = n_p v_{th}^2 m + B^2/2\mu_0$, where m is mass and μ_0 is the permeability constant), and 3-hour averaged He^{++} fluxes measured by SOHO/CELIAS/STOF (the Suprathermal Time-of-Flight Spectrometer (Hovestadt et al., 1995)) and corresponding background estimation in the energies ~ 32 to 330 keV/nuc. This CIR event is bounded by a reverse shock but no forward shock. We define the CIR boundaries (the leading and trailing edge) with the total pressure using a 50pPa threshold which is suggested by Bučík et al. (2009). In Figure 2.2 this criteria also works at the reverse shock location. The stream interface, which separates the slow wind from the fast wind, is typically characterized by a sharp drop in density, a sharp increase in thermal speed (or temperature) and a small increase in bulk speed, while the original increase in wind speed is washed out by two stream interactions (Burlaga, 1974; Gosling and Pizzo, 1999). Herein, the stream interface is indicated by a sharp decrease of O^{7+}/O^{6+} abundance ratio in the bulk solar wind, based on the work of Wimmer-Schweingruber et al. (1997, 1999). Considering different origins of two solar wind streams, we think the freezing-in temperature changes obtained from ratios of different charge states of an element (e.g., O^{7+}/O^{6+}) is a more robust indicator of the stream interface. For the CIR event shown in Figure 2.2, these two methods are equivalent to identify the stream interface. Because SOHO has no magnetometer onboard, we use magnetic field data from ACE/MAG which is also located at around L1. Comparing plasma parameters measured by SOHO/PM and ACE/SWEPAM, we found that the physical conditions at SOHO and ACE spacecraft were almost the same, and that the time difference between passages of the CIR boundaries is less than ten minutes.

Associated with CIRs, enhancements of suprathermal and energetic particles are often observed at 1 AU. These corotating ion events were originally believed to originate

at the Sun because flux enhancements are well related with appearance of solar active regions (Bryant et al., 1965; Fan et al., 1968). However, later it was discovered that the intensities of these ions increased with increasing heliocentric distance from the Sun, with the data from the Pioneer 10 and 11 deep space probes (McDonald et al., 1976). Subsequently the Helios 1 and 2 and Mariner 10 probes to the inner heliosphere showed that the intensities of suprathermal and energetic ions dropped inside the orbit of the Earth (Van Hollebeke et al., 1978). Observations of sunward energetic ions following CIRs are further evidence for a source outside the orbit of the Earth (Marshall and Stone, 1978). Additional evidence for a source at several AUs came from the observation that proton fluxes at these distances peaked in association with the leading and trailing edges of CIRs (Barnes and Simpson, 1976). That means that the accelerated energetic particles originate from these two locations. A broad increase in the intensity of ~ 1 MeV/nuc particles occurs in the F region of CIRs. This enhancement extends from the reverse shock back to the orbit of the Earth, and is seen as far inward toward the Sun as ~ 0.4 AU, from Helios or Mariner 10 (Van Hollebeke et al., 1978). An increase of energetic particles is also seen in front of the forward shock. However, this increase generally involves fewer particles than those behind the reverse shock, and exhibits a softer spectrum. And the associated energetic particles at the forward shock do not appear to extend back to the Earth. For the CIR shown in Figure 2.2, we find that in the S region, no suprathermal alpha particles are observed. In other words, we did not detect accelerated particles extending back to 1 AU, which is consistent with previous observations (Chottoo et al., 2000). The flux rises abruptly in the F' region and peaks around the reverse shock, which indicates that the reverse shock is the dominant acceleration source. After the passage of the reverse shock, suprathermal He^{++} continuously shows up for more than one day, which is normally believed to be due to the sunward particles accelerated beyond Earth orbit. In summary, the temporal flux variations over this CIR event observed by us are consistent with previous observations (Chottoo et al., 2000; Bućík et al., 2009; Ebert et al., 2012).

2.2 Theoretical Model

The evolution of suprathermal ion populations associated with CIRs can be described with the diffusion-convection transport equation (Roelof, 1969) for the isotropic part of the phase space density $f(r, p, t)$ (e.g., Jokipii, 1966), based on the Fokker-Planck equation.

$$\frac{\partial f}{\partial t} = \nabla \cdot (\kappa \cdot \nabla f) - (V + V_D) \cdot \nabla f + \nabla \cdot V \frac{p}{3} \frac{\partial f}{\partial p} + \frac{1}{p^2} \frac{\partial}{\partial p} \left[p^2 \langle D_{pp} \rangle \frac{\partial f}{\partial p} \right] + I - S \quad (2.1)$$

where f is the phase space density, κ is the symmetric part of the spatial diffusion tensor, V is the bulk flow velocity of the background solar wind, V_D is the drift velocity of particles in the magnetic field, $\langle D_{pp} \rangle$ is the diffusion coefficient in momentum space, p , I and S are the source term and the sink term, respectively. The left hand side denotes the explicit time dependence of phase space density. The first term on the right hand side describes the spatial diffusion of particles. The second term describes the effect of spatial convection and drift of suprathermal ions. The third and fourth terms are so-called the adiabatic deceleration term and the momentum diffusion term (Scholer, 1999).

Fisk and Lee (1980) presented a theoretical model based on the diffusive shock acceleration (first order Fermi acceleration) for corotating shocks in the expanding solar

wind. They simplify Equation 2.1 by neglecting the drift, momentum diffusion, source and sink terms. They assume that in the frame of reference corotating with the Sun, the distribution function f , in a given magnetic flux tube or equivalently along a given streamline, is the steady-state, one-dimensional, radially-dependent convection-diffusion equation (Scholer, 1999), and can be written as:

$$-\frac{1}{3r^2} \frac{\partial}{\partial r} (r^2 V) v \frac{\partial f}{\partial v} = \frac{1}{r^2} \frac{\partial}{\partial r} \left(r^2 \kappa \frac{\partial f}{\partial r} \right) - V \frac{\partial f}{\partial r} \quad (2.2)$$

where r is the heliocentric radial distance, v is the particle velocity (instead of momentum p), V is the solar wind speed and κ is the diffusion coefficient. In the Fisk and Lee (1980) model, κ is assumed to be proportional to r and v and is written as $\kappa = \kappa_0 v r$ where κ_0 is constant. In order to solve Equation 2.2, the appropriate boundary condition is assumed that for a given magnetic flux tube the product of particle differential streaming and the cross-sectional area of a flux tube should be conserved through the shock front, i.e., particles crossing the shock are conserved. Additionally the magnetic flux should also be conserved across the shock front, then the boundary condition for f at a shock located at $r = r_s$ is (Fisk and Lee, 1980):

$$-\frac{Vv}{3} \frac{\partial f}{\partial v} - \kappa \frac{\partial f}{\partial r} = -\beta \frac{Vv}{3} \frac{\partial f}{\partial v} \quad \text{at } r = r_s \quad (2.3)$$

where $\beta = \frac{1}{H}$ is the inverse of compression ratio, H , at the CIR-driven shock, and

$$\beta = \frac{(V'^2 + \Omega_\odot^2 r_s^2)^{1/2} B}{(V^2 + \Omega_\odot^2 r_s^2)^{1/2} B'} \quad (2.4)$$

Here B , and Ω_\odot are respectively the magnetic field strength upstream from the shock and the angular velocity of the Sun. V' and B' refer to conditions downstream of the shock. If the corotating speed, $\Omega_\odot r$, is small compared to the particle speed, v , then f is the same in both the corotating frame and the spacecraft frame, to order $(\Omega_\odot r/v)^2$ (Fisk and Lee, 1980).

With the assumptions that particles travel downstream from the shock primarily by convection, and that f is continuous across the shock front, the solution for f in the downstream region (inside CIR) is given as (Fisk and Lee, 1980):

$$f = \left(\frac{r}{r_s} \right)^{-2/(1-\beta)} v^{-3/(1-\beta)} \exp \left[-\frac{6\kappa_0 \beta v}{V(1-\beta)^2} \left(\frac{r}{r_s} \right)^{2/3} \right] \quad (2.5)$$

The solution for f in the upstream region from the shock (outside CIR), which satisfies Equation 2.3 and is finite as r goes to zero, is (Fisk and Lee, 1980):

$$f = \left(\frac{r}{r_s} \right)^{2\beta/(1-\beta) + V/(\kappa_0 v)} v^{-3/(1-\beta)} \exp \left[-\frac{6\kappa_0 \beta v}{V(1-\beta)^2} \right] \quad (2.6)$$

For the case of a shock-bounded CIR, e.g., the CIR event shown in Figure 2.2, $r \approx r_s$ inside the compression region. Then Equation 2.5 can be simplified as:

$$f = v^{-3/(1-\beta)} \exp \left[-\frac{6\kappa_0 \beta v}{V(1-\beta)^2} \right] \quad (2.7)$$

What do we expect to measure?

No matter Equation 2.5 or its simplified Equation 2.7, the spectra inside CIR have a form of power law with exponential rollover i.e., $j_0 v^{-n} \exp(-v/v_0)$, where j_0 is the normalizing constant, and n and v_0 are the low-energy slope and rollover speed, respectively (Desai et al., 1999). The spectral index n is a function of the compression ratio (Fisk and Lee, 1980), H , of the shock:

$$n = \frac{(H + 2)}{(H - 1)}$$

By comparison, the spectral shape outside CIR given in Equation 2.6 contains an additional factor:

$$\left(\frac{r}{r_s}\right)^{V/(\kappa_0 v)}$$

This factor describes the suppression of particles streaming inward from the shock region to the observer (e.g., at 1 AU) (Chottoo et al., 2000), which can also affect the spectral index, particularly in the low suprathermal energy range.

In Figure 2.3, the blue dashed curves show the theoretical spectral evolution from inside to outside the CIR, with the same parameters as used by Fisk and Lee (1980). Inside CIR, the spectrum is a power law in energy per mass (E/m) with an exponential rollover. The spectra outside CIRs show an additional turnover, shaped like a bump in the low suprathermal energy range. Our observations are actually the superposition

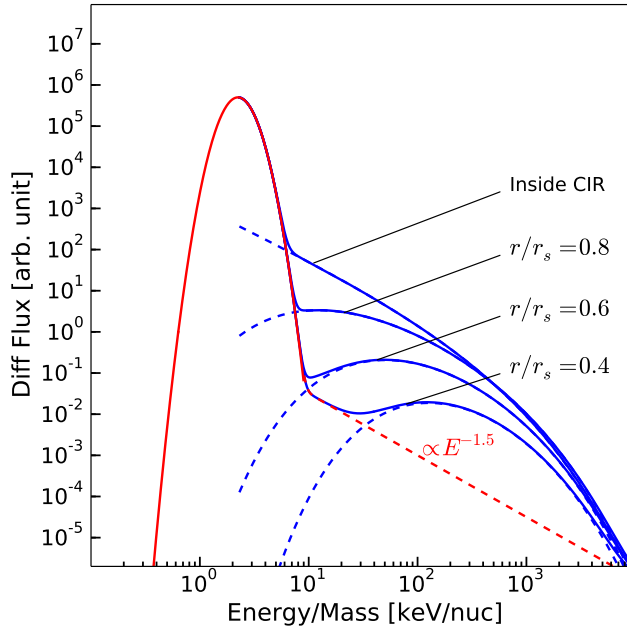


Figure 2.3: The local distribution consists of the solar bulk Maxwellian distribution shown with a red full line and a suprathermal tail (red dashed line with index -1.5) based on the work of Fisk and Gloeckler (2007). Blue solid curves are the superposition of the Fisk & Lee model and the local distribution. Blue dashed curves, standing for the remote acceleration, are derived from the Fisk & Lee model, using $\beta = \frac{1}{3}$ and $\frac{V}{\kappa_0} = 2$ (MeV/nuc) $^{1/2}$, the values used in the Fisk and Lee (1980) paper.

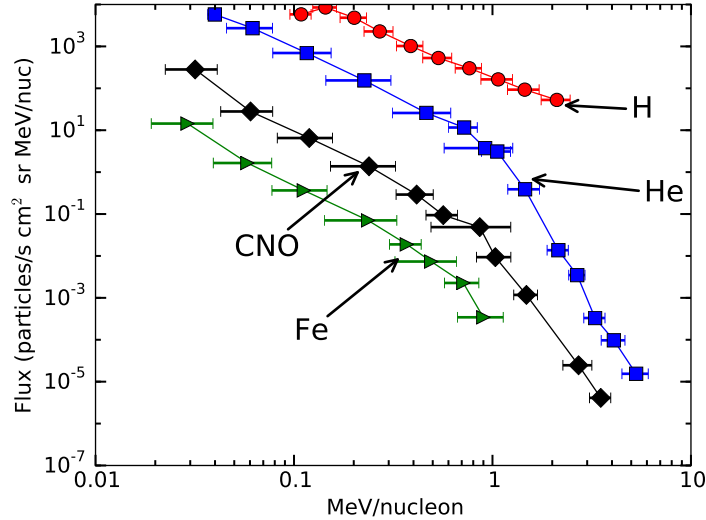


Figure 2.4: Energy spectra for the 24-hour period starting from 1994 December 6, 18:00 UT. Note power-law spectra at low energies, rolling over above about 1 MeV nucleon⁻¹. The figure is replotted from Mason et al. (1997) at higher resolution.

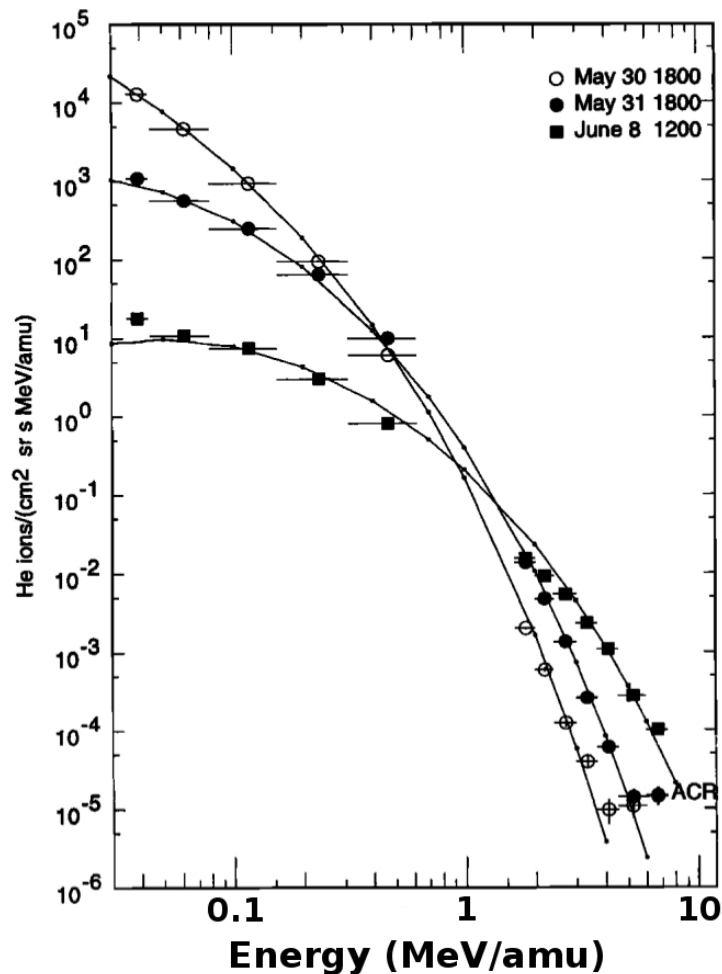
(blue solid curve) of locally (red solid and dashed curve) and remotely accelerated particles (blue dashed curve). For our observations in this thesis at around 1 AU, r is the heliocentric location of the observer and can be considered fixed. r_s is the heliocentric location of reverse shock which is connected to the observer. Different r/r_s ratios (0.8, 0.7 and 0.6) in Figure 2.3 mean different connection distances $r_s - r$ (0.25 AU, 0.43 AU and 0.67 AU) from the spacecraft to the reverse shock. Thus, the smaller the r/r_s ratio, the larger the connection distance. The flux of sunward particles decreases with connection distance, and is accompanied by a shift of the turnover towards higher energies. When the connection distance is small, e.g., the cases where $r/r_s = 0.8$ and 0.6, accelerated particles from the remote shocks dominate the spectral shape. If the flux of these sunward streaming suprathermal particles is low, particles accelerated locally by the Fisk and Gloeckler (2007) mechanism may become visible in the spectra (see the case when $r/r_s = 0.4$).

However, we should point out that the spectral turnover may be problematic at low suprathermal energies in Figure 2.3 due to the assumption $v \gg \Omega_{\odot} r$ of the Fisk and Lee (1980) theory. The corotating speed $\Omega_{\odot} r$ at 1 AU is around 429 km/s which is calculated with the sidereal period (25.38 days) of solar rotation (Beck, 2000). By contrast, the spectral turnover shown in Figure 2.3 is in the range of tens of keV/nuc up to around 100 keV/nuc (~ 4400 km/s), where the assumption is not well satisfied. Therefore, we think it is difficult to quantitatively explain the observed spectra at 1 AU at low suprathermal energies with the Fisk and Lee (1980) model.

2.3 Previous Work

Mason et al. (1997) have surveyed the composition and energy spectra of heavy ions accelerated in 17 CIRs from 1992 December to 1995 July. Scientific data were obtained from the Low-energy Ion Composition Analyzer (LICA) instrument on the Solar Anomalous and Magnetospheric Particle Explorer (SAMPEX) spacecraft, and the Energetic Particle

Figure 2.5: Energy spectra of alpha particles are shown from 3 time periods (May 30 12:00-24:00 UT, May 31 12:00-24:00 UT and June 8 00:00-24:00 UT). Fitted curves based on the Fisk and Lee (1980) model are shown through the observed points. From top to bottom, the fitted parameter r_s (the shock heliocentric distance) of these three spectra are equal to 1.2, 2, and 4 AU, while β (the inverse of the shock compression ratio) are equal to 0.4, 0.36 and 0.2 respectively. The figure is taken from Reames et al. (1997).



Acceleration, Composition, and Transport (EPACT), Supra-Thermal Energetic Particle (STEP) and Low Energy Matrix Telescope (LEMT) telescopes on the Wind spacecraft. Figure 2.4 shows energy spectra for a 24-hour period starting from 1994 December 6, 18:00 UT. The spectra are typical in the events of the survey. Below about 1 MeV/nuc, the measured species are H, He, CNO group, and Fe. Above 2 MeV/nuc, He, CNO are shown (Mason et al., 1997). Note that the low-energy spectra continue to decline as power laws from the instrumental threshold of roughly 30 keV/nuc up to about 1 MeV/nuc. Above 1 MeV/nuc, the spectra steepen significantly, as predicted by the Fisk and Lee (1980) model. Although the spectral rollover at 1-2 MeV/nuc is consistent with the Fisk and Lee (1980) theory, the continued power-law shape at low energies is not consistent with this model which predicts that spectra also turn over toward low energies (see Figure 2.3). Mason et al. (1997) considered that this could be an effect related to the hardening of spectra seen in these events, which suggests that at 1 AU the low-energy particles may come from portions of the CIR close to the Earth.

Another CIR event, occurring on May 30, 1995, was studied by Reames et al. (1997). These authors found that the flux of low-energy helium peaks inside the compressed fast wind and declines after the passage of the trailing edge of the CIR. But high-energy helium at ~ 5 MeV/nuc peaks later in the fast wind region, and is named as “late-phase MeV ions” in Reames et al. (1997). These energetic ions are believed to be accelerated in the distant heliosphere as the reverse shock of the CIR propagates completely across the rarefaction region produced by the declining solar wind with growing acceleration

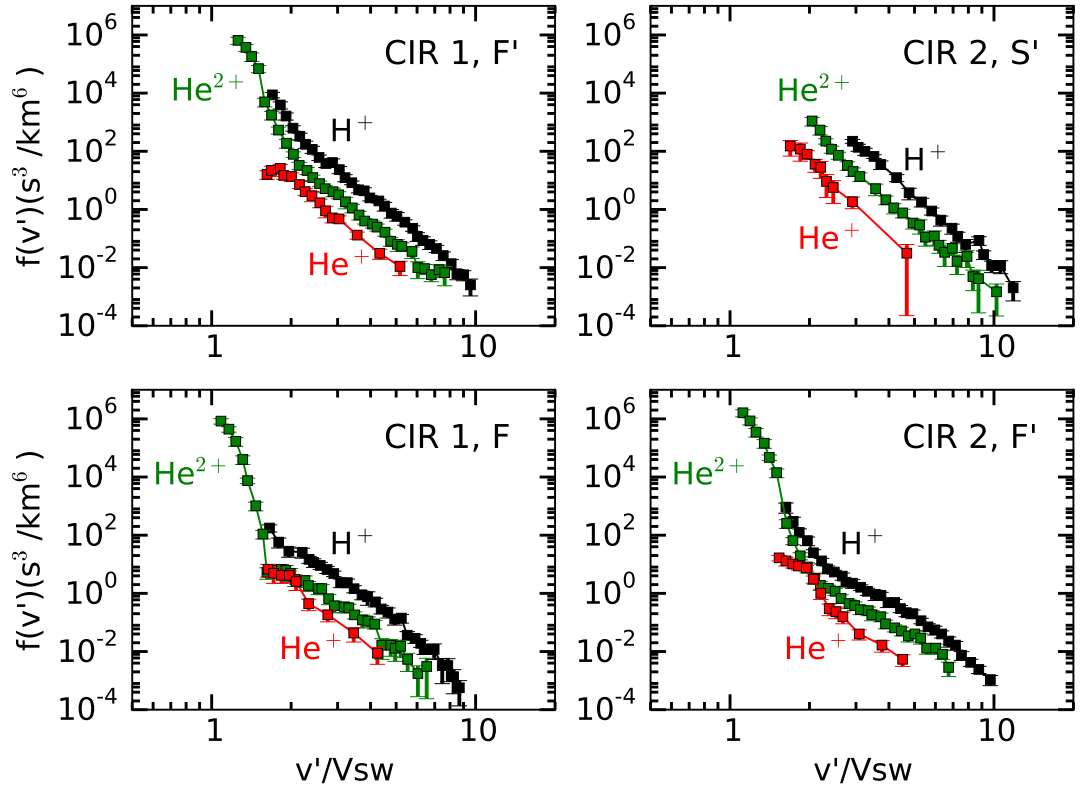


Figure 2.6: Left two panels show distribution functions for H^+ , He^{++} , and He^+ of CIR 1 in the F' and F regions. Right panels illustrate distribution functions for these ions of CIR 2 in the S' and F' regions respectively. The figure is replotted from Chotoo et al. (2000) at higher resolution.

efficiency. The scientific data that they used are also obtained from EPACT, STEP and LEMT onboard the Wind spacecraft. Fitting curves in spectra shown in Figure 2.5 are calculated from the asymptotic expansion in particle velocity given by Equation 2.6. We can see that all three spectra show an exponential rollover around 1 MeV/nuc, and a power law shape below 1 MeV/nuc continuing down to the instrumental threshold near 40 keV/nuc. No low-energy turnover has been found. To fit spectra, Reames et al. (1997) used the observed solar wind speed for V of Equation 2.6, treated β and r_s of the Fisk and Lee (1980) model as adjustable parameters and normalized each spectrum to the observations. The parameters r_s and β , determined from fitting the theory of Fisk and Lee (1980), are equal to 1.2 AU, 2 AU, 4 AU and 0.4, 0.36, 0.2 respectively. The lowest spectrum with $\beta = 0.2$ indicates a compression ratio of 5, larger than the Rankine-Hugoniot limiting value of 4. With the asymptotic Fisk-Lee formula, Reames et al. (1997) were unable to fit the observations with a smaller value of the compression ratio. Therefore, they pointed out, the above values of r_s and β should not be taken too literally.

Chotoo et al. (2000) investigated H^+ , He^{++} , and He^+ distribution functions from solar wind energies through the suprathermal energy range during two CIR events occurring in April and May 1995. These events were observed by the Suprathermal Ion Composition Spectrometer (STICS), High MASS Resolution Spectrometer (MASS), and STEP instruments of the Wind spacecraft. Figure 2.6 illustrates measurements of veloc-

ity distribution functions which are averaged over all directions in the spacecraft frame. Note that in CIR 1 the transition between solar wind bulk and the accelerated tail is more gradual in the compressed fast solar wind region (F') than in the uncompressed fast solar wind (F). Spectra of H^+ and He^{++} (of solar origin) change smoothly from the core at solar wind speeds to a power law (F region) or a power law multiplied by an exponential component at higher energies (F' region). No turnover was observed at intermediate energies. The spectrum in the F' region of CIR 2 is similar to that of CIR 1. But no spectra in the F region are shown. So we do not know whether turnover spectra predicted by Fisk and Lee (1980) exist or not in this event. In addition, Chotoo et al. (2000) pointed out that the Fisk and Lee (1980) model may be violated at the low suprathermal energies, because this model requires that the particle speed should be much larger than the solar wind speed and because the velocity distribution is assumed to be isotropic. From Figure 2.6, we know that suprathermal power-law tail can extend as low as around two times the bulk speed in the velocity space. The speed of particles in the low-energy tail is not much larger than wind speed, therefore, it is not appropriate to apply the Fisk and Lee (1980) model at low suprathermal energies. Hence, as Chotoo et al. (2000) claimed, their spectral fitting is only for the purpose of illustration. Moreover, the assumption of an isotropic distribution was proved to be invalid in the energy range considered here, based on the recent observations by Ebert et al. (2012). These authors found a large anisotropy in the CIR of Figure 2.2.

Compared with the observations in Chotoo et al. (2000), the observations in Mason et al. (1997); Reames et al. (1997) have no information about the charge state. For example, both helium spectra shown in Figure 2.4 and Figure 2.5 are the superposition of He^{++} and He^+ . The former is mainly of the solar origin while the latter is mainly of the interplanetary origin (typically named as pickup ions). As Hill et al. (2009) observed, the ratio of He^+/He^{++} in the interplanetary is a function of energy and heliocentric distance. Therefore, it is not appropriate to apply the Fisk and Lee (1980) model to the observations of Mason et al. (1997); Reames et al. (1997) and the observations of Chotoo et al. (2000) have more advantage to compare with the Fisk and Lee (1980) theory. But still, none of Mason et al. (1997); Reames et al. (1997); Chotoo et al. (2000) observe a spectral turnover at low suprathermal energies as the Fisk and Lee (1980) theory predicts.

Chapter 3

Instrumentation

3.1 The SOHO Mission

The SOHO mission is an international cooperation between European Space Agency (ESA) and National Aeronautics and Space Administration (NASA). It was designed to answer the three following fundamental scientific questions about the Sun (Fleck, 1995):

- What is the structure and dynamics of the solar interior?
- Why does the solar corona exist and how can it be heated to the extremely high temperature of about roughly one million degree centigrade?
- Where is the solar wind produced and how is it accelerated?

Together with ESA's Cluster mission (<http://sci.esa.int/cluster/>), SOHO can also help to understand the Sun-Earth interaction. The SOHO spacecraft was launched by NASA on December 2nd, 1995. It is in orbit between the Earth and the Sun, which is around a mathematical point between the Earth and the Sun known as the Lagrange point or the L1 point.

SOHO is a three-axis stabilized spacecraft and points at the Sun with an accuracy of 10 arc seconds and has a pointing stability of 1 arc second per 15-minute interval. The total mass is about 1850 kg and 1150 W power is provided by its solar panels. In a modular concept, SOHO consists of two main parts: the payload module accommodating 12 instrument packages shown in Figure 3.1, and the service module carrying the spacecraft subsystems and the solar panels.

Here, we briefly summarize the 12 scientific instruments referring to Fleck (1995):

- **Global Oscillations at Low Frequencies (GOLF)** aims to study the internal structure of the Sun by measuring the spectrum of global oscillations over the entire solar disc in the frequency range 10^{-7} to 10^{-2} Hz (Gabriel et al., 1995).
- **Michelson Doppler Imager/Solar Oscillations Investigation (MDI/SOI)** probes the interior of the Sun by measuring the acoustic waves in the interior of the Sun as they perturb the photosphere (Scherrer et al., 1995). MDI also measures the longitudinal component of the Sun's magnetic field.
- **Variability of Solar Irradiance and Gravity Oscillations (VIRGO)** characterizes the pressure and internal gravity oscillations by measuring the total solar irradiance (known as the solar constant) to quantify its variability over periods of days to the duration of the mission (Fröhlich et al., 1995).

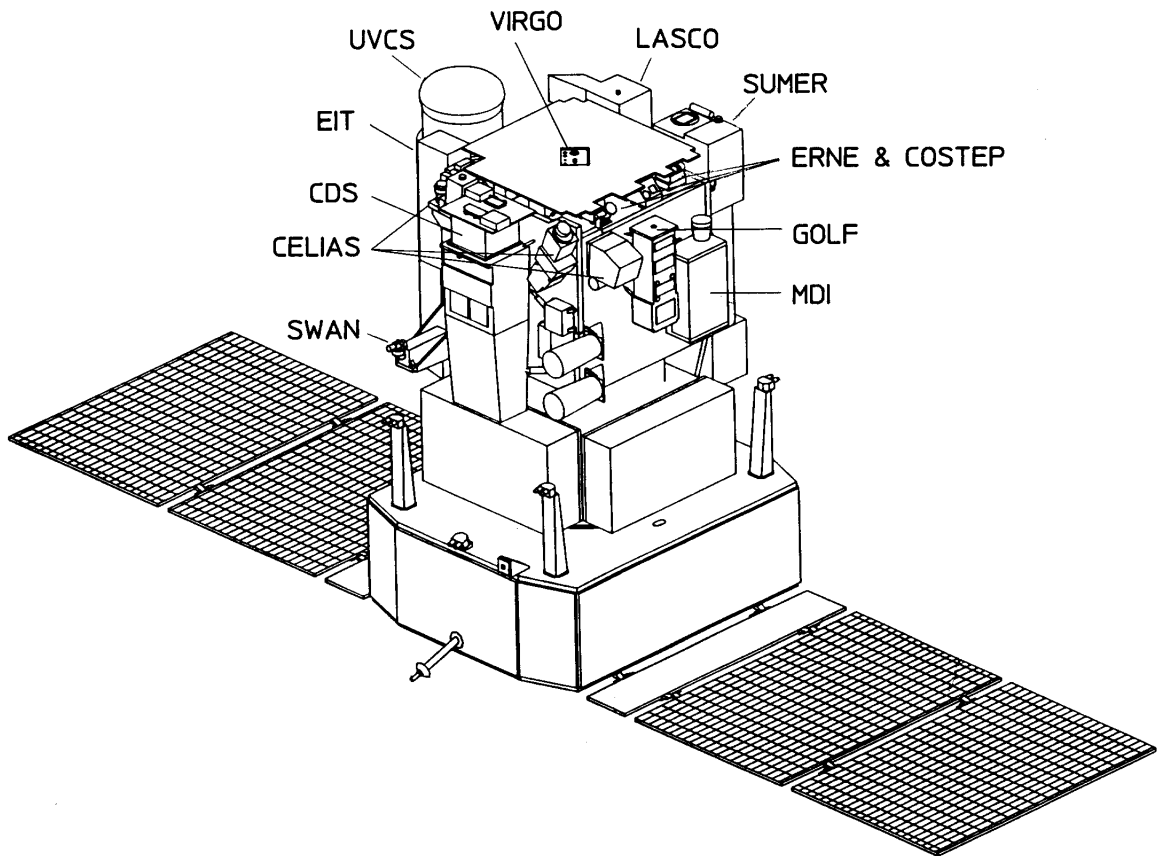


Figure 3.1: SOHO spacecraft schematic view from Fleck (1995). According to the research subject, the payload onboard SOHO can be divided into three groups: helioseismology (e.g., GOLF, MDI/SOI and VIRGO), solar atmospheric remote sensing (e.g., CDS, EIT, LASCO SUMER, SWAN, and UVCS), and in-situ particle measurements (e.g., CELIAS, COSTEP and ERNE)

- **Coronal Diagnostic Spectrometer (CDS)** detects emission lines in the extreme ultraviolet from ions and atoms of the solar corona and transition region, providing diagnostic information especially of the hottest plasma in the (non-flare) solar atmosphere (Harrison et al., 1995).
- **Extreme Ultraviolet Imaging Telescope (EIT)** provides wide-field images on the solar disc at four selected wavelengths in the extreme ultraviolet, from the corona and transition region up to $1.5 R_{\odot}$ above the solar limb (Delaboudiniere et al., 1995).
- **Large Angle and Spectrometric Coronagraph (LASCO)** is comprised of three coronagraphs: C1, C2 and C3, that together sample the solar corona from 1.1 to $30 R_{\odot}$. LASCO blocks direct Sun light with an occulter, artificially creating an eclipse. It can be also used as SOHO's principal comet finder (Brueckner et al., 1995).
- **Solar Ultraviolet Measurements of Emitted Radiation (SUMER)** performs detailed spectroscopic plasma diagnostics, which aims to study the structure and dynamic processes of the solar atmosphere, from the chromosphere through the transition region to the inner corona, over a temperature range from 10^4 to 2×10^6 K and above (Wilhelm et al., 1995).
- **Solar Wind Anisotropies (SWAN)** is the only remote sensing instrument on SOHO that looks not at the Sun but at the rest of the sky. It is devoted to measuring the distribution of the solar wind mass flux with the heliographic latitude through an intensity map of the sky Lyman α emission (Bertaux et al., 1995).
- **UltraViolet Coronagraph Spectrometer (UVCS)** performs ultraviolet (UV) spectroscopy and visible polarimetry combined with plasma diagnostic analysis techniques, sampling the extended solar corona from the coronal base to a heliocentric height of 12 solar radii (Kohl et al., 1995). Similar to LASCO, UVCS blocks the bright light from the solar disc.
- **Charge, Element, and Isotope Analysis System (CELIAS)** measures the mass, ionic charge and energy of the low and high speed solar wind, of suprathermal ions and of low-energy flare particles, as these particles sweep past SOHO. The energy range of CELIAS is from 0.1 keV/nuc to 80 MeV (Hovestadt et al., 1995; Bamert et al., 2002). Moreover, the persistent stream of CELIAS data also allows the forecast of space weather (Hovestadt et al., 1995).
- **Comprehensive Suprathermal and Energetic Particle Analyzer (COSTEP)** studies the suprathermal and energetic particle populations of solar, interplanetary and galactic origin. It is a complementary instrument to ERNE (Müller-Mellin et al., 1995).
- **Energetic and Relativistic Nuclei and Electron (ERNE)** is at the upper end in energy among the SOHO particle instruments, covering the energy range from a few MeV/nuc up to a few hundred MeV/nuc for ions and 2 to 50 MeV for electrons. ERNE and COSTEP jointly form the COSTEP-ERNE Particle Analyzer Collaboration (CEPAC) (Valtonen et al., 1997).

3.2 CELIAS/STOF

In this thesis work, we use the CELIAS instrumentation which contains three mass-discriminating sensors based on the time-of-flight (TOF) technique: the Charge Time-of-Flight (CTOF), the Mass Time-of-Flight (MTOF) and the Suprathermal Time-of-Flight (STOF) spectrometers as well as the Solar Extreme Ultraviolet Monitor (SEM). As part of MTOF, the Proton Monitor (PM) provides measurements of solar wind speed, temperature as well as density for the work reported in Chapter 4 and 5. STOF in this thesis is referred to as (H)STOF (following Bamert et al. (2002)), because it employs two sections of electrostatic analyzers: one with curved plates (STOF main) and the other with flat deflection plates called HSTOF (Highly Suprathermal Time-of-Flight Spectrometer). In this thesis, we refer to STOF and HSTOF separately to avoid confusion. STOF can measure the elemental and ionic composition in the energy-per-charge (E/q) range from 35 to 660 keV/e. HSTOF can only measure the elemental composition of particles but covers a higher and larger energy range above 80 keV/e to 80 MeV. (H)STOF bridges the gap between solar wind experiments (e.g. CTOF, MTOF) and solar energetic particle instruments (e.g. COSTEP/ERNE). The (H)STOF instrument is divided into three parts. The entrance system of STOF contains a stack of curved deflection plates and serves as an electrostatic analyzer with a Field of View (FOV) $3^\circ \times 17^\circ$ pointing 7° west off the Sun-SOHO line. By contrast, HSTOF utilizes a stack of flat plates at the entrance, directing 37° west of the Sun-SOHO line with a FOV of $4^\circ \times 34^\circ$ (Hovestadt et al., 1995). Both STOF and HSTOF share the two remaining components, the TOF system and the Solid State Detector (SSD) system. A photograph of (H)STOF can be seen in Figure 3.2.

In the following, we introduce the working principle of STOF. The functional description for three components of this instrument is given in more details in Section

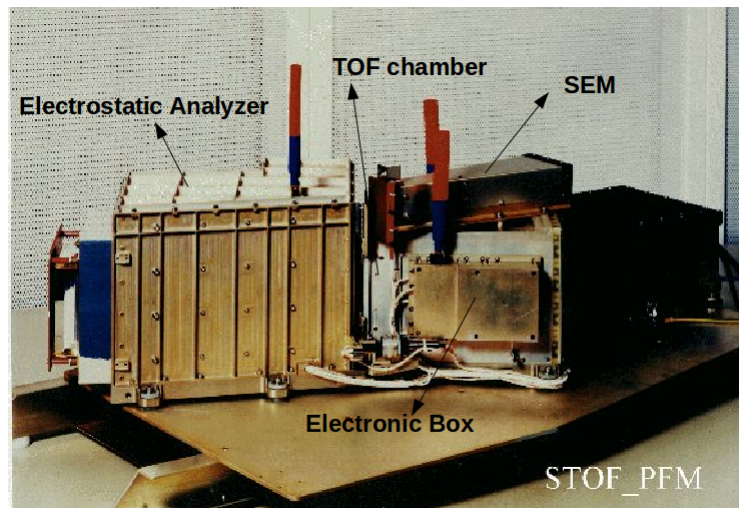


Figure 3.2: Photograph of pre-flight model (PFM) of (H)STOF, taken from <http://www.ieap.uni-kiel.de/et/soho/celias/gallery.html#STOF>. The left gold-colored box is the housing of the electrostatic analyzer. On the right part of this photo, the front unit (the small golden box) is the electronic box (E-Box), comprising high voltage supplies and various electronics. Behind the E-Box is the silver-colored TOF chamber. The brown long box, mounted piggyback on the TOF chamber is SEM which is also part of the CELIAS instrumentation.

3.2.1, where we explain how to determine an ion's mass, mass-per-charge, and velocity from three measurements (the E/q , TOF and residual energy).

3.2.1 Working Principle of STOF

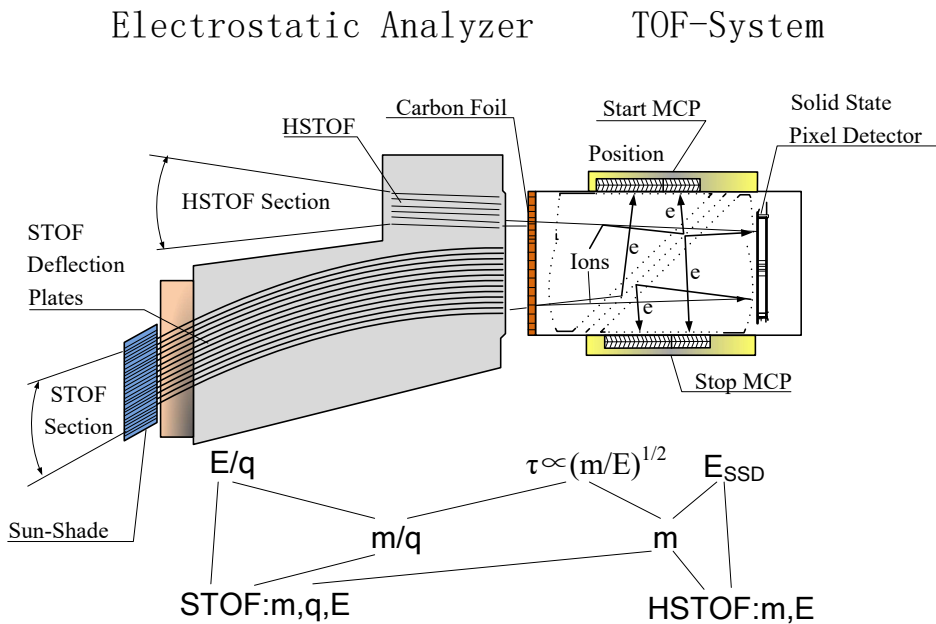


Figure 3.3: Schematic drawing of (H)STOF. Incident particles within a certain energy-per-charge (E/q) range are selected by the electrostatic analyzer. The velocities of incident particles are measured by the TOF system with secondary electrons which are generated at the carbon foil and the surface of SSDs. These electrons are accelerated to ~ 1 keV by a thin wire mesh and are then deflected by an electrostatic mirror (see inclined dashed lines) to the MCPs (Bamert et al., 2002). The incident particles finally deposit in the SSD system and the energy deposit E_{SSD} is then measured.

As illustrated in Figure 3.3, the measurement of an ion detected by STOF can be described as follows: firstly, an incident ion within a particular E/q range is selected by the corresponding E/q channel of the electrostatic analyzer. Secondly, this ion penetrates the carbon foil in front of the TOF unit and generates enough secondary electrons at the rear side of foil to trigger the microchannel plates (MCPs) for a START signal. Thirdly, this ion goes through the TOF chamber until it hits an SSD pixel. Here it not only triggers sufficient secondary electrons at the surface of the SSD pixel for a detectable STOP signal in the MCPs, but also deposits its remaining energy in the SSD pixel. The whole procedure is a triple coincidence event which can remarkably suppress the noise caused by accidental coincidences. For example, the energetic particles from Galactic Cosmic Rays (GCRs) can easily penetrate STOF's housing and trigger MCPs or SSDs, however, the possibility for a penetrating particle to trigger the START, STOP and SSD within a valid TOF range is very small. Even if all three triggers are generated by GCRs, the resulting TOF is very small due to the high energy of penetrating particles. When the TOF is smaller than ~ 2.2 ns, the event is rejected by STOF.

From the combination of the energy-per-charge E/q , TOF τ , and residual energy measured in the SSD E_{SSD} , the ion's mass m , mass-per-charge m/q , and the ion's initial energy E , can be determined unambiguously based on the in-flight calibration performed by Bamert et al. (2002):

$$\frac{m}{q} = 2 \cdot \left(\frac{\tau}{d}\right)^2 \cdot \left(\frac{E}{q} - \frac{\Delta E_{foil}}{q}\right) \quad (3.1)$$

$$m = \frac{2}{d^2} \cdot \tau^2 \cdot E_{SSD} \cdot \left(1 - 2.2 \cdot \left(\frac{d^2}{2\tau^2}\right)^{-0.45}\right)^{-1} \quad (3.2)$$

$$E = \frac{E}{q} \cdot \left(\frac{m}{q}\right)^{-1} \cdot m \quad (3.3)$$

Here, d denotes length of the flight path in the TOF chamber, and $d^2/2 = 207285 \text{ ns}^2 \cdot \text{keV}/\text{amu}$. ΔE_{foil} is the energy loss in the carbon foil which can be approximated by 5% of the initial energy for heavy ions (Bamert et al., 2002). The other three parameters (E/q , τ , and E_{SSD}) can be calculated with Equations 3.4, 3.5, 3.6, 3.7, and 3.8, given in the following sections. With measurements of mass, mass-per-charge, and initial energy we can further determine the ion species and derive the energy spectra which are required for the suprathreshold particles study in Chapters 4 and 5.

3.2.2 Entrance System

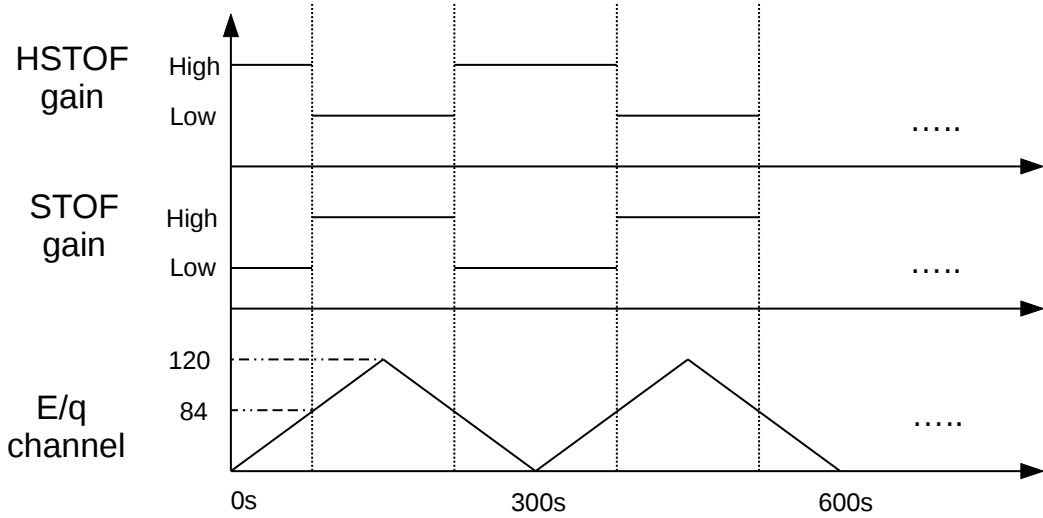


Figure 3.4: Sequence diagram of (H)STOF. The electrostatic analyzer is operated by periodically incrementing and decrementing the E/q channel. Associated with this behavior, the energy gain of (H)STOF's SSDs switches between high and low.

The STOF entrance system includes a stacked assembly of 18 cylindrical high-voltage plates which serves as an electrostatic analyzer with an E/q resolution of $\Delta E/q = 10\%$ (full width at half maximum (FWHM)). 120 logarithmically spaced voltages can be applied to the gaps between neighboring plates. Thus, the entrance system acts as an E/q filter for incident ions. The E/q range is stepped through twice during one cycle (120 steps up, 120 steps down), see Figure 3.4. Each step takes 1.25 second, and hence

a cycle takes five minutes to complete. The nominal energy-per-charge response of an E/q step is given by

$$E/q[\text{keV}] = 35 \cdot 1.024962^{E/q_{\#}}, 0 \leq E/q_{\#} < 120 \quad (3.4)$$

$$E/q[\text{keV}] = 35 \cdot 1.024962^{239-E/q_{\#}}, 120 \leq E/q_{\#} < 240 \quad (3.5)$$

where $E/q_{\#}$ denotes the concurrent high-voltage (HV) step of a sweep cycle. The STOF entrance system has a geometric factor of about $0.1 \text{ cm}^2\text{sr}$. A black copper sulfide coated collimator (called 'sunshade') is mounted in front of the STOF deflection plates to suppress the solar UV light by 10^7 and the visible light by up to 2×10^6 .

3.2.3 Time-of-Flight System

After passing through the electrostatic analyzer, incoming ions enter the TOF chamber through a grid-supported carbon foil with a thickness of $4 \mu\text{g}/\text{cm}^2$ and reach the SSD pixels at the end of the TOF system. The process of traversing the foil has two consequences. Firstly, a shower of secondary electrons are emitted and are accelerated to about 1 keV by a thin wire mesh and then deflected by an electrostatic mirror on to the START MCPs to generate a START signal. Secondly, ions lose a portion of their primary energy when they interact with the foil which results in a net-deceleration of ions. This energy loss in foils ΔE_{foil} is considered in the derivation of m/q of incident particles in Equation 3.1. When incident ions hit the SSD, a shower of secondary electrons can also be generated at the SSD surface, then steered onto the STOP MCP to trigger the STOP signal and complete the TOF, τ , measurement. The START and STOP signals are processed linearly in a 10-bit time-to-amplitude converter. Here we present the conversion from the TOF channel, $\tau_{\#}$, to τ [ns] as follows:

$$\tau[\text{ns}] = 0.72 \cdot (\tau_{\#} - 18) \quad (3.6)$$

The bias voltage applied to each MCP is roughly 1400 V. It can be adjusted in flight via ground command by up to 20% above the nominal level in order to compensate for the degradation of the MCP with time. Actually, when we analyze the housekeeping data of STOF, we find that the MCPs have degraded much faster than expected because of a large unanticipated UV background. The UV-induced electrons lead to a much higher trigger rate on MCPs. More details will be introduced in Section 3.3.2.

3.2.4 Solid State Detector System

To measure the energy of incident ions, 192 SSD pixels (Figure 3.5) are placed at the end of the TOF chamber. STOF has 128 pixels on the right four hybrids, i.e., Hybrids 0, 1, 2 and 3. The signal in each pixel can be pulse-height analyzed. The position information of each pixel can be used for the correction of the flight-path length, which is one purpose of separating the large area of the detector system. The other purpose of this design is to reduce the effective capacitive noise of the full detector area (Hovestadt et al., 1995). The total pixels have an area of 105 cm^2 and a thickness of $300 \mu\text{m}$ with an equivalent 200 nm dead layer. Similar to the entrance foils, the dead layer not only generates secondary electrons but also absorbs a fraction of the ion's energy. Hence, we have to also consider the energy loss in the dead layer when we derive the initial ion energy. The signal read-out circuits of the SSDs are implemented by a CAMEX32 multiple amplifier chip. This chip has outstanding linearity and large dynamic range of about 4000 (from 20 keV up to 85 MeV) (Hovestadt et al., 1995). In this chip, the feedback capacitors of

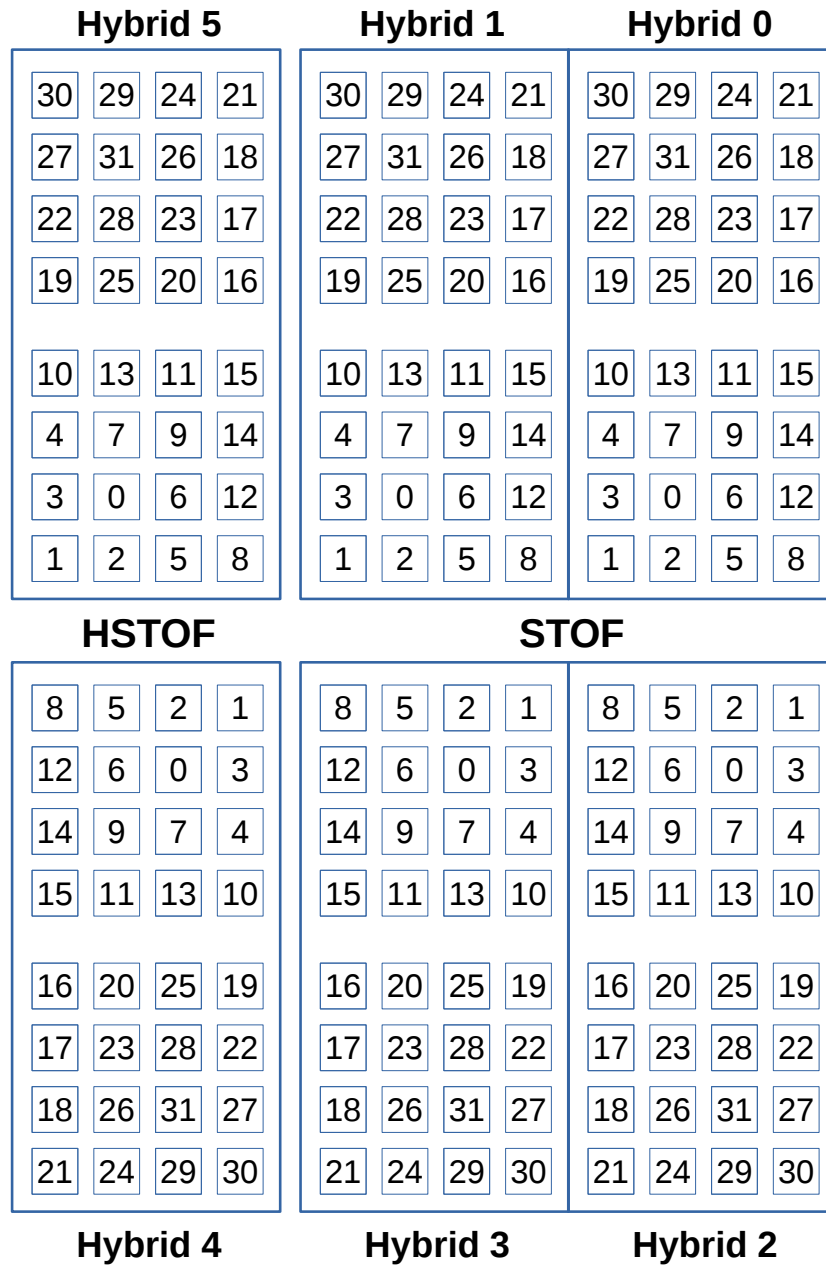


Figure 3.5: The pixel array of (H)STOF contains 12 detector chips mounted on six ceramic hybrids. Each hybrid contains two detectors and a CAMEX32 multiple amplifier chip together with relevant analog and digital electronics for the signal processing. The left two hybrids (Hybrids 4 and 5, in total of 64 pixels.) belong to HSTOF while the right four hybrids (Hybrids 0, 1, 2 and 3, in total of 128 pixels.) belong to STOF.

the first amplification stage are switched in two gain steps synchronously with the E/q stepping as shown in Figure 3.4. The conversion from SSD's energy channel, $E_{SSD\#}$, to $E_{SSD}[keV]$ for STOF in the two gains (high (H) and low (L)) is described by the following equations:

STOF:

$$E_{SSD}[keV] = 40 \cdot (E_{SSD\#} - 30), \text{ if gain is high.} \quad (3.7)$$

$$E_{SSD}[keV] = 7 \cdot (E_{SSD\#} - 36), \text{ if gain is low.} \quad (3.8)$$

Additionally, three correction mechanisms are applied to the SSD system (Hovestadt et al., 1995): (1) There is a digital offset applied to each input of the pixel amplifier so that the threshold of every SSD pixel can be adjusted in flight. (2) The SSD system implements a masking scheme to suppress pulse height output from pixels getting noisy. During the late phase of the SOHO mission, this scheme seems to be invalid on some noisy pixels, as discussed in more details in the Section 3.3. (3) The gain factor of each channel (varying up to 3 %) can be corrected digitally for the purpose of in-flight calibration via ground command.

3.2.5 Working Principle of HSTOF

The main difference between STOF and HSTOF is the entrance system. The HSTOF's entrance system consists of a stack of parallel plates which allow only ions with E/q above 80 keV/e to enter the TOF section (Bamert et al., 2002). No E/q information is available for the charge-state determination, as the potential of incident particles across the plates is fixed. At the entrance of HSTOF, Lyman-alpha UV and visible stray light (zodiacal light) are suppressed by the start detection foil with a special compound coating, for details see Hovestadt et al. (1995). Another difference lies at the entrance foil of the TOF system. The HSTOF foil is made of a three-layer composite Silicon-Lexan-Carbon (roughly 28/30.5/5 nm, much thicker than STOF's carbon foil) which suppresses scattered Lyman alpha and generates the START signals. The SSD system of HSTOF has 64 pixels on the left 2 hybrids, i.e., Hybrids 4 and 5 in Figure 3.5. Similarly to STOF, each SSD pixel of HSTOF also can be operated with two different energy gains. The gain switches of STOF and of HSTOF are inversely phased, as illustrated in Figure 3.4. The energy conversion in two gains is defined as follows:

HSTOF:

$$E_{SSD}[keV] = 120 \cdot (E_{SSD\#} - 30), \text{ if gain is high.} \quad (3.9)$$

$$E_{SSD}[keV] = 7 \cdot (E_{SSD\#} - 36), \text{ if gain is low.} \quad (3.10)$$

As shown in Figure 3.3, the ion's mass and initial energy can be determined with two measurements (τ and E_{SSD}) of HSTOF. The calculation of the mass in Equation 3.2 can be applied to the HSTOF measurements. The determination of initial energy E needs to rely on simulations with the software Transport of Ions in Matter (TRIM) (Ziegler and Chu, 1974; Ziegler, 2013).

3.2.6 PHA Data Acquisition

STOF can provide two different forms of data products: the matrix rate and the pulse height analysis (PHA) data. The former is produced by fast particle identification with onboard look-up tables and counting ions in mass versus mass-per-charge bins. The parameters in the look-up tables are derived from pre-launch calibration data. The matrix rates consist of the number of detected events of a given ion or mixture of ions

within a certain time interval and energy range. Hence, the matrix rates exhibit good statistics, as only accumulated measurements are transferred. However, matrix rates do not provide any information on the E/q , τ , and E_{SSD} . By contrast, the PHA words contain more information about a single event. Each incoming ion that satisfies the event selection algorithm is characterized by the follow 16 keywords:

- LOBT - International Atomic Time (TAI) seconds since 1970-01-01 00:00:00
- ID - Number of bits: 1. Range: 0-1. Instrumental identification: 0 denotes STOF and 1 means HSTOF
- Step - Number of bits: 3. Range: 0-3. The PHA step. The PHA electronics have three parameters, offset, gain and threshold, which are switched every three steps of the E/q sweep voltage. Therefore, these triplets of voltage steps are called PHA steps. Referring to the 120 voltage steps between the minimum and the maximum value, there are 40 PHA steps, which also means a total of 80 PHA steps for one cycle. More details are given in Appendix B.
- SubSt - Number of bits: 2. Range: 0-2. The substep of one PHA step. The substep numbers and step numbers must be combined (PHA step \times 3+substep) to obtain the number (0-11) in the Experiment Data Block (EDB) which is the basic data package transferred by SOHO.
- Range - Number of bits: 3. Range: 0-5. The priority class, described in Hovestadt et al. (1995) in detail.
- Prior - Number of bits: 1. Range: 0-1. The sensor priority. 1 denotes a proton event and 0 represents a heavy ion event.
- Res - Number of bits: 2. Reserved bits.
- Stop - Number of bits: 1. Range: 0-1. The rear positions on MCPs.
- PFx - Number of bits: 4. Range: 0-15. The front positions on MCPs.
- PChan - Number of bits: 2. Range: 0-3. The hybrid number of the SSD system, referring to Figure 3.5. For STOF, the 'PChan' values 0, 1, 2, 3 stand for Hybrids 0, 1, 2, 3. For HSTOF, 0, 1 denote Hybrids 5 and 6.
- PPos - Number of bits: 5. Range: 0-31. The pixel number on a certain hybrid. By using the position information on MCPs ('Stop' and 'PFx' values) and the position determination on the SSD pixel array ('Pchan' and 'PPos' values), the distinction between STOF and HSTOF events can be made, and events in high-background SSD pixels can be rejected (Bamert et al., 2002).
- Gain - Number of bits: 2. Range: 0-3. The energy gain of the SSD system. The 'Gain' values 1 and 3 identify the high gain of STOF and HSTOF, respectively. The values 2 and 0 denote STOF's and HSTOF's low gain.
- Esum - Number of bits: 9. Range: 0-511. 'Esum', short for Energy Sum, is used for the event selection logic, shown in the STOF/HSTOF sensor event analysis (Hovestadt et al., 1995).

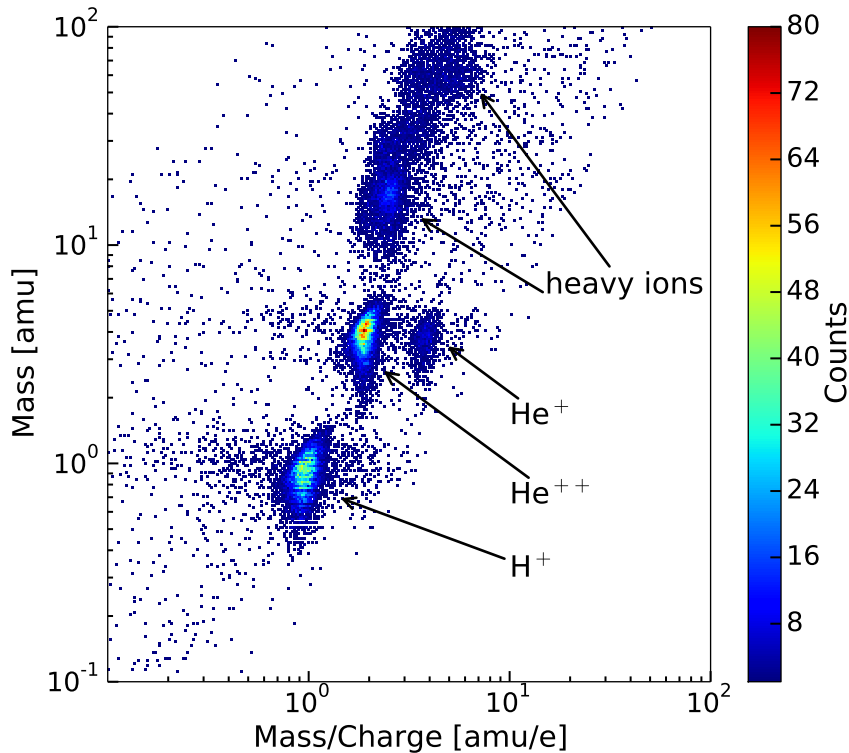


Figure 3.6: Ion species measured by STOF. The investigated time interval is from DOY 120 to 126, 1998 (from April 30th to May 6th), when a sequence of Solar Energetic Particle (SEP) events and Coronal Mass Ejections (CMEs) occurred, also named as 'May 1998 Events' by Bamert et al. (2002). Only measurements from the SSD pixels of Hybrids 0 and 2 are chosen for this plot, as STOF's data from Hybrids 1 and 3 are contaminated by HSTOF, see Section 3.3.1.

- Energy - Number of bits: 10. Range: 0-1023. Energy deposit in the SSD. The linearly spaced energy channel $E_{SSD\#}$ is linked to the deposit energy E_{SSD} with Equations 3.7, 3.8, 3.9, and 3.10.
- TOF - Number of bits: 10. Range: 0-1023. The TOF channel of (H)STOF. The linearly spaced TOF channel $\tau_{\#}$ is used to determine TOF τ of an incident ion with Equation 3.6.
- EoqSt - Range: 0-240. E/q step from 0 to 239 in a sweep cycle. 120 logarithmically spaced E/q steps $E/q_{\#}$ are corresponding to the E/q information of an incident ion by Equations 3.4 and 3.5.

The PHA data are generated with a program called 'spsc' (splitter for celiac science data). With the PHA data we can evaluate the instrument performance which helps us to update some in-flight settings if necessary, e.g., the MCP bias voltage (see Section 3.3.2). Moreover, the PHA data are very useful for the in-flight calibration of (H)STOF. Fortunately, the calibration work has been successfully achieved by Bamert et al. (2002), and we do not need to analyze all the 16-keyword data but only concentrate on the scientific constituents: LOBT, ID, PChan, Ppos, Gain, Energy, TOF and EoqSt. Figure 3.6 shows the STOF data acquired during days 120-126 of year 1998, when a series of

intensive solar particle events occurred which were analyzed by Bamert et al. (2002). STOF measurements during this time period exhibit large signal to noise ratio (SNR). Four types of ions can be distinguished in this figure. From bottom to top these are H^+ , He^{++} , He^+ , and heavy ions such as a CNO group, Mg, Si and iron ions. On one hand, the count distribution of some ions (e.g., H^+ , He^{++} and He^+) is well separated, so that we can simply use box rates to extract the data. On the other hand, the instrumental background is not as well suppressed as expected. A noise pattern is present in adjacent areas of the real-ion tracks, see Figure 3.6.

3.3 Background Analysis for STOF

In this section, we concentrate on the PHA data set of STOF, with which we can further understand the in-flight performance of STOF. Four defects of this instrument have been identified, i.e., contamination from HSTOF on Hybrids 1 and 3, overtriggered pixels, pile-up background and accidental-coincidence background. The corresponding approaches to overcome these four problems are also presented and discussed as follow.

3.3.1 Unexpected Behavior of SSDs

Using all the calibrated parameters and equations introduced in Section 3.2, we first investigate the performance of HSTOF and STOF separately. Figure 3.7 shows the derived mass/mass-per-charge results of STOF and HSTOF with data from all hybrids in the same time period as in Figure 3.6. At a first glance, both subplots display five clear tracks of ions with different mass, indicating both HSTOF and STOF have achieved the desired functionality of ion-mass measurement. According to Equation 3.2, the ion mass is calculated based on TOF and the energy deposit in SSDs, which indicates that the TOF unit and SSDs work as expected. Although the PHA words of HSTOF have different values of E/q , these data are useless and meaningless because the section of E/q of HSTOF is fixed. Therefore, the ion trace measured by HSTOF extends along the mass-per-charge horizontally according to Equation 3.1. The proton measurements in the left panel of Figure 3.7 exhibit two distinct distributions due to the energy-gain switch on the SSDs. But this characteristic does not show in the heavy-ion measurements, which is not understood. For STOF, its E/q analyzer can provide E/q information, allowing us to determine the charge state of incident ions. However, the right panel of Figure 3.7 does not show convincing charge-state measurement as expected. We can see clear intensity enhancements at the positions of protons and alpha particles on Figure 3.7, and vague ones at the heavy ions' positions, e.g., the CNO group of high charge states. But similarly to the left panel, all these ions show expanding tracks along their mass-per-charge, which is abnormal. We infer that STOF events may be mingled with HSTOF events.

HSTOF Contamination

As introduced in Section 3.2, keywords 'PChan' and 'PPos' of PHA data can be used to extract measurements from any SSD pixel of (H)STOF. In order to verify our speculation of the HSTOF contamination in STOF's data set, we analyzed the mass and mass-per-charge measurements for all pixels of STOF. We found that data obtained from the left two hybrids of STOF (Hybrids 1 and 3), adjacent to the two hybrids of HSTOF (Hybrids 4 and 5), exhibit a trace behavior very similar to that of HSTOF (see the left panel of Figure 3.8). By contrast, the right two hybrids of STOF (Hybrids 0 and 2) show only

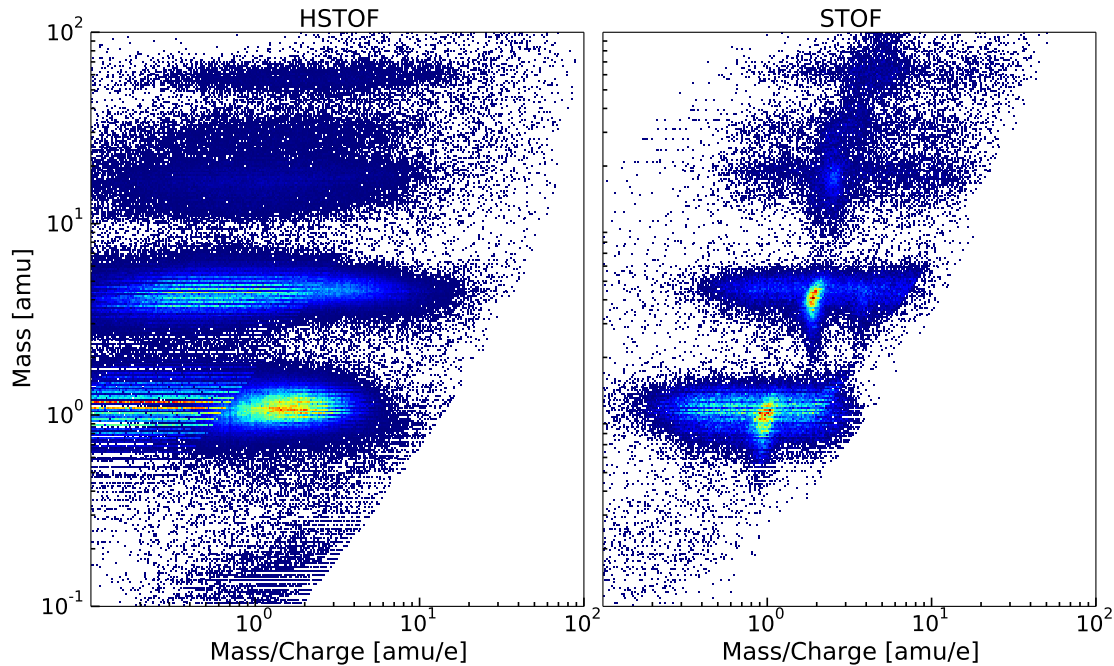


Figure 3.7: Data output of (H)STOF over the same time period as in Figure 3.6. Both HSTOF (the left panel) and STOF (the right panel) show plausible mass measurements. But the charge state measurements of STOF are not satisfactory. Proton data measured by HSTOF seem to have two distributions, which is caused by the energy-gain switch on the SSD system. To answer why other ion species measured by HSTOF do not exhibit this characteristic is beyond the scope of this thesis.

the anticipated measurements, e.g., H^+ , He^{++} and He^+ show clear traces in the right panel of Figure 3.8. Therefore, in this work, we only use the STOF data recorded on Hybrids 1 and 3 for the CIR study in the following chapters. The reduced geometric factor of STOF is $0.05 \text{ cm}^2\text{sr}$, half of the original value ($0.1 \text{ cm}^2\text{sr}$ in Section 3.2.2). The reason why Hybrids 1 and 3 mainly collect particles incident from the HSTOF entrance is unknown. Maybe this is due to the larger geometric factor of HSTOF compared to STOF, together with the fixed E/q selection of HSTOF compared with multiple E/q selection of STOF. This could lead to more incident particles entering the TOF unit via the HSTOF entrance. After penetrating the front foil, these particles scatter as estimated by TRIM simulations and many of them can reach Hybrids 1 and 3 of STOF.

Oversensitive Pixels

To understand the long-term performance of SSDs, we investigate in this section the count distribution in the pixel array of (H)STOF (see Figure 3.5) from the year 1998 to 2005. Figure 3.9 illustrates the count distribution during solar events, e.g., CIRs, Coronal Mass Ejections (CMEs), Solar Energetic Particle events (SEPs) and solar flares, while Figure 3.10 shows only the measurements during solar quiet times of each year. More specifically, counts obtained by every pixel are normalized by the pixel's geometric factor which we assume to be constant. According to the calibration work done by Bamert et al. (2002), the geometric factors of HSTOF and STOF are $0.22 \text{ cm}^2\text{sr}$ and $0.1 \text{ cm}^2\text{sr}$, respectively. In addition, we find that pixels 13, 24 and 30 of all (H)STOF's hybrids are disabled. So the geometric factor of a HSTOF pixel is $0.22/58=0.003793 \text{ cm}^2\text{sr}$, where 58

is the total number of the enabled HSTOF pixels. The geometric factor of a STOF pixel is $0.1/116=0.0008620$ cm^2sr , where 116 is the total number of the enabled STOF pixels. After we obtain normalized counts (with the corresponding geometric factors) for all pixels of (H)STOF, we show the count distribution in the pixel array of Figure 3.5 for every year from 1998 to 2005. For each subplot in Figures 3.9 and 3.10, the pixel array is further normalized to the maximum number of its counts.

As shown in Figure 3.9, the count distribution in the pixel array during solar-event times does not change much over eight years. We can see that Hybrids 4 and 5 of HSTOF always detect more particles than four hybrids of STOF. This is because the applied voltage of the HSTOF entrance is fixed so that all the particles above 80 keV/e are free to go through. By contrast, the entrance of STOF sweeps with different E/q , so only a certain and narrow E/q range of incident particles can enter STOF. In four hybrids of STOF, Hybrids 1 and 3 observed more particles than Hybrids 0 and 2. This feature is clearly visible in the first three years, and continues in the following five years from 2001 to 2005 although it cannot be easily identified in Figure 3.9. Not only the count number on different hybrids are different, we can also see that the count distribution over pixels of each hybrid is not uniform. For example for the HSTOF measurements, more particles are recorded by the pixels in the second and third columns than in the first and fourth columns. Moreover, we notice that this pattern of count distribution in the HSTOF's hybrids also shows up on Hybrids 1 and 3 of STOF but not on the other STOF's hybrids, which indicates an effect, i.e., contamination, from HSTOF on Hybrids 1 and 3 of STOF.

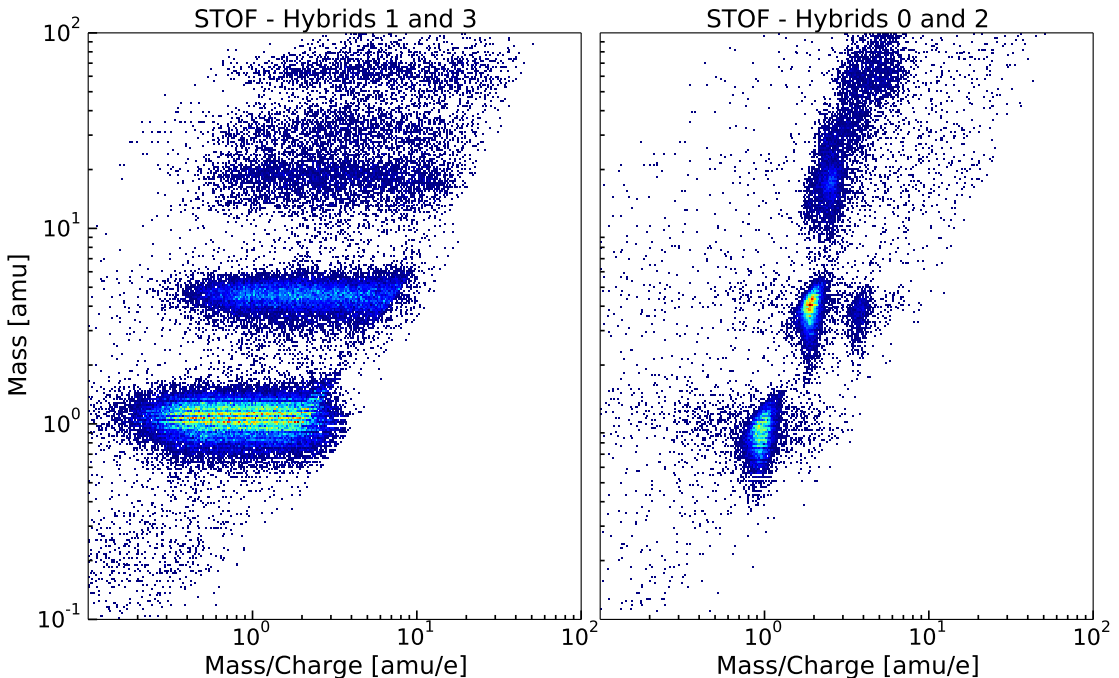


Figure 3.8: Measurements of STOF in the left and right two hybrids. The left two hybrids which are close to HSTOF's two hybrids exhibit the same pattern as HSTOF's measurements, which indicates a contamination from HSTOF on these two STOF's hybrids.

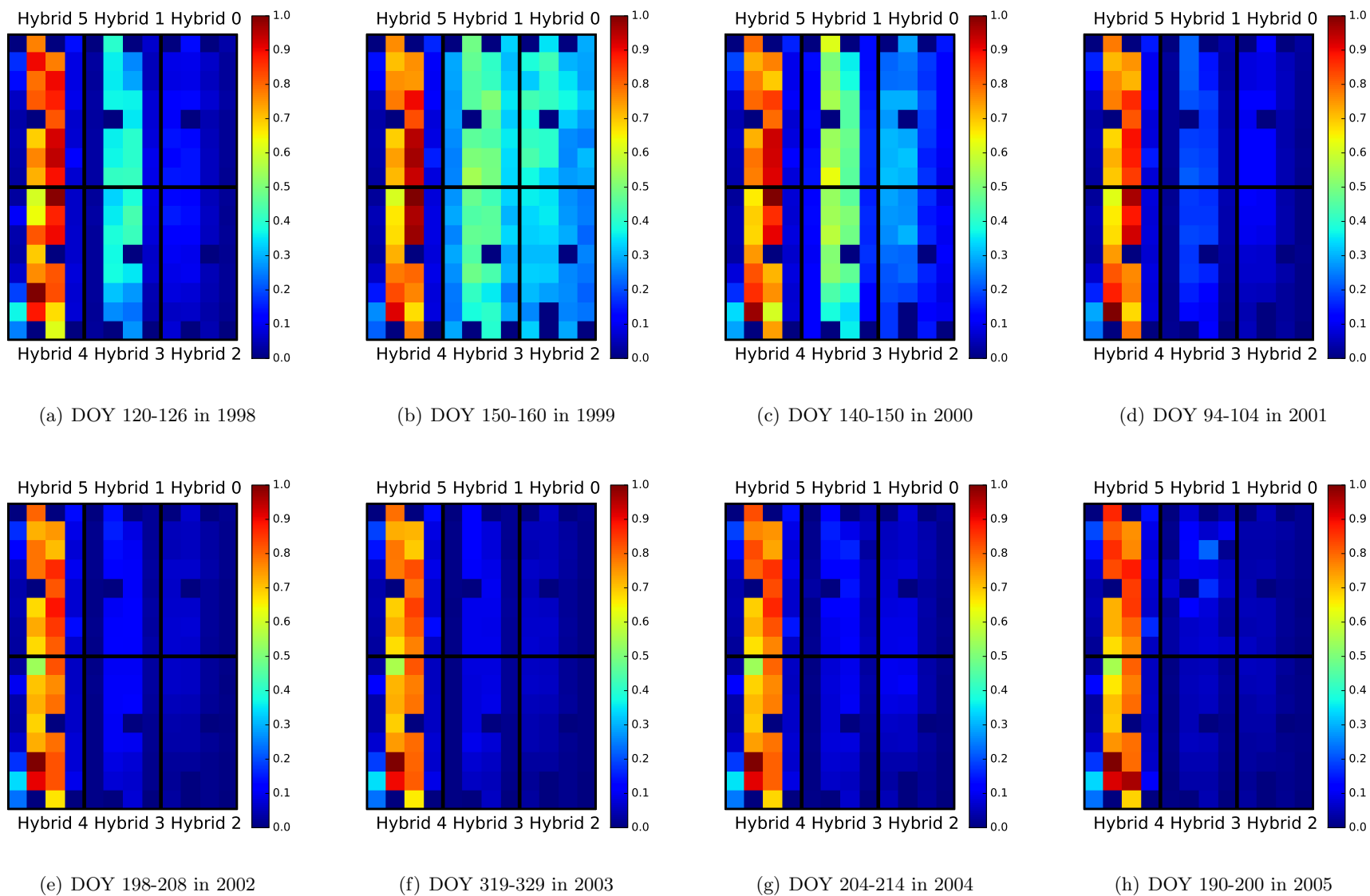
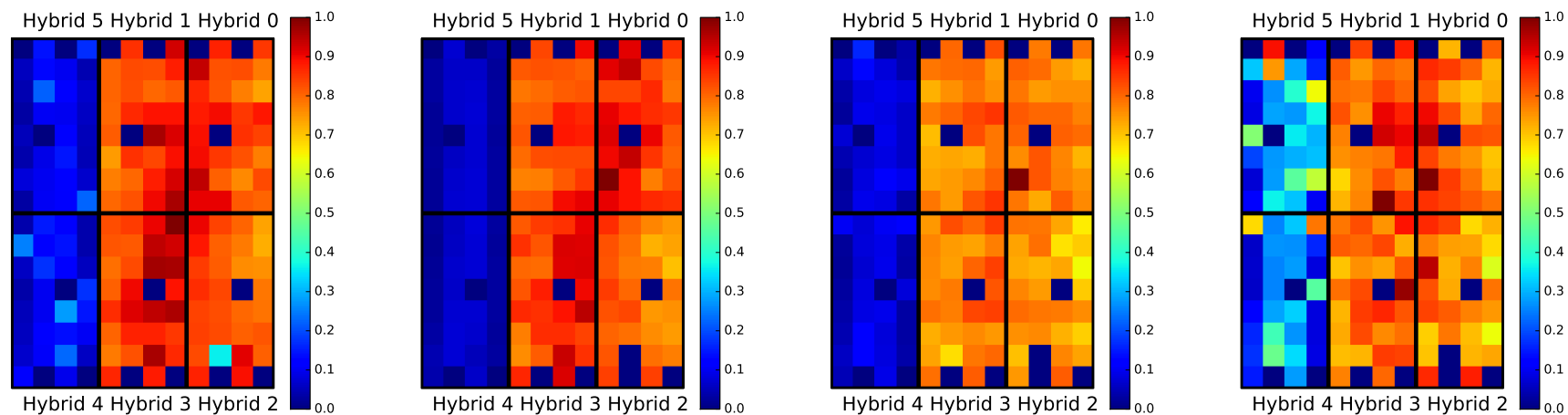


Figure 3.9: Normalized count distribution in the SSD system of (H)STOF during solar events from the year 1998 to the year 2005.

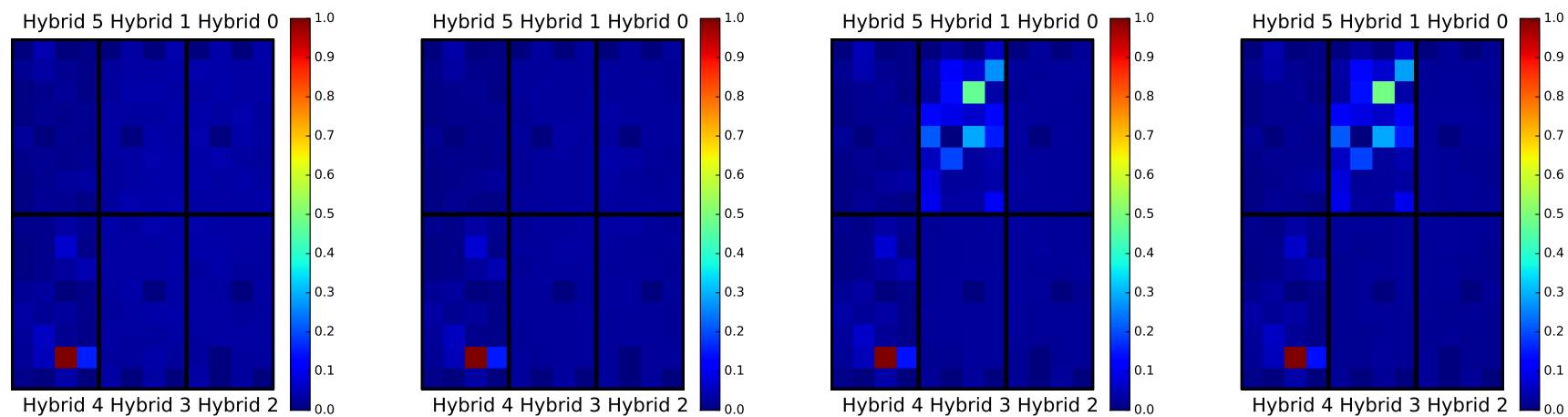


(a) 73 days in 1998

(b) 111 days in 1999

(c) 76 days in 2000

(d) 58 days in 2001



(e) 64 days in 2002

(f) 114 days in 2003

(g) 162 days in 2004

(h) 101 days in 2005

Figure 3.10: Same as Figure 3.9, but during the solar quiet times of each year.

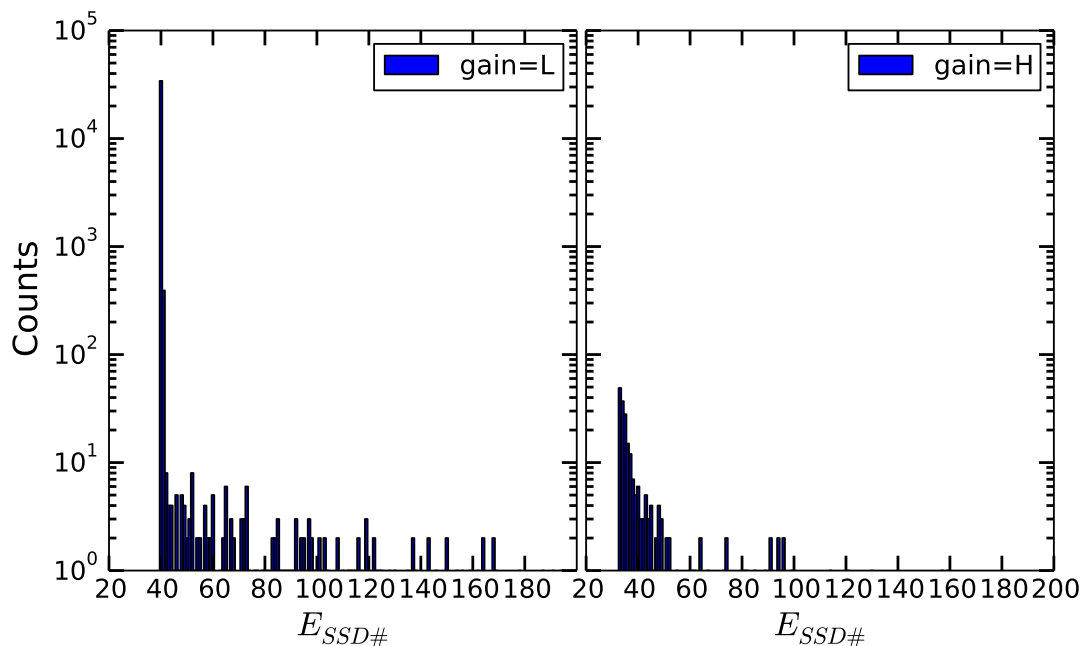


Figure 3.11: Energy measurements for the oversensitive pixel 31 of HSTOF's Hybrid 4 in both high and low energy gains.

During solar quiet times, Figure 3.10 exhibits a more variable count distribution. In the years 1998, 1999, 2000, and 2001 STOF detected more particles than HSTOF, which is unexpected and inverse to the case during solar events. HSTOF measurements exhibit a similar count distribution in its hybrids like that in Figure 3.9, i.e., the two middle columns of pixels detected more particles than the two side columns of pixels. However, unlike in the case of Figure 3.9, Hybrids 1 and 3 of STOF did not show this pattern, but their measured counts look uniformly distributed in the same way as Hybrids 0 and 2. Since the year 2002 the pixel 31 of Hybrid 4 of HSTOF recorded considerably more particle hits than any other pixels of (H)STOF. Starting from the year 2004, several STOF pixels on Hybrid 1 also become oversensitive - like the pixel 31 of HSTOF's Hybrid 4. To identify the problem of the overtriggered SSD pixels, we surveyed their energy measurements, see one example in Figure 3.11. When the gain of pixel 31 of Hybrid 4 is low (the left panel), in the lowest two energy channels (40 and 41) this pixel recorded considerably more particle hits than those in the other energy channels. This behavior of pixel 31 never occurred in the first five years of the SOHO mission. By contrast, this behavior disappears if the gain is high. As shown in the right panel of Figure 3.11, the counts slightly decrease with the energy channels. Similar to the pixel 31 of HSTOF's Hybrid 4, some pixels of STOF also become oversensitive in their lowest energy channel ($E_{SSD\#} = 42$) since 2004 if their energy gain is low. At the same time, we notice that as soon as a pixel becomes overtriggered in the lowest energy channel, it does not return to normal. We infer that this is due to an instrumental defect. According to Hovestadt et al. (1995), each pixel of (H)STOF has an energy threshold, and only particles with energy higher than this threshold can be recorded by (H)STOF. We believe that the threshold of these oversensitive pixels might become invalid for some unknown reason, so that these pixels start to record all particle-hit events.

In Figure 3.12 we eliminate the effect of oversensitive pixels over the years 2002 to

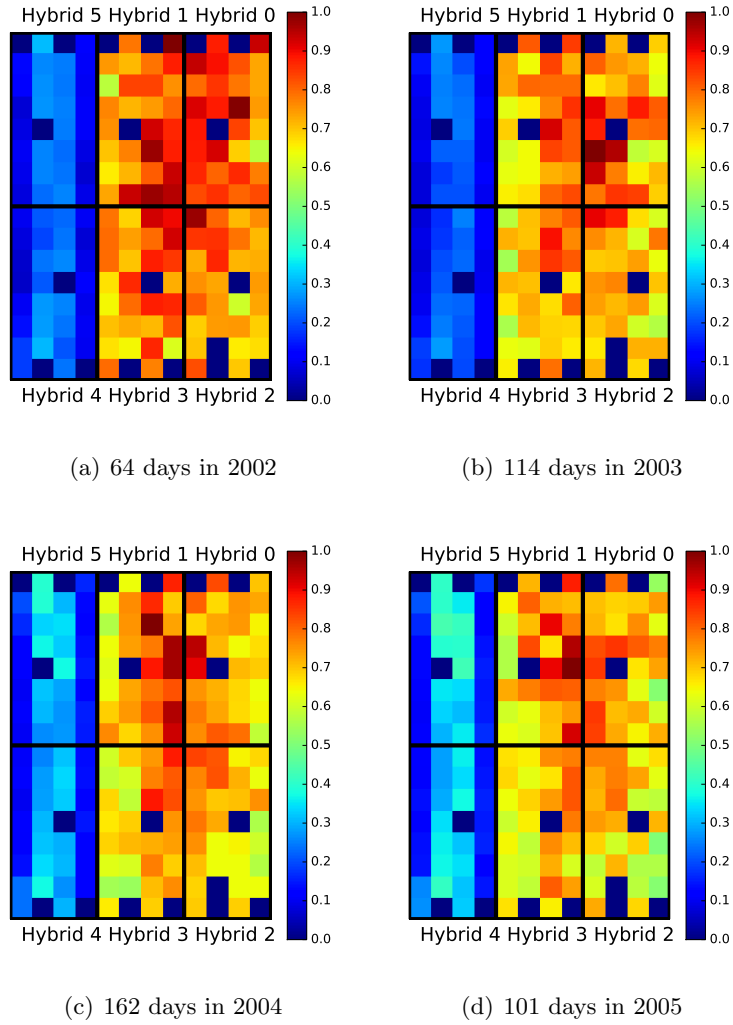


Figure 3.12: (H)STOF measurements during solar quiet times in 1998 after rejecting data in the lowest E_{SSD} channels.

2005 by rejecting the data obtained by these pixels in the lowest energy channels if the energy gain is low, i.e., 40 and 41 of HSTOF and 42 of STOF. Then we find that the count distribution during these four years looks similar to that during the earlier four years. However, we still need to answer the following questions: why is the count distribution during solar events and quiet times nearly inverse? and why can STOF unexpectedly detect more particles than HSTOF in solar quiet times? As we know, the main difference during solar events and quiet times is the flux of solar particles which can increase several orders of magnitude when solar events occur. It seems that STOF is capable to measure another unknown source of particles, the flux of which is higher than that of solar particles in quiet times but lower than that of solar particles during solar events.

3.3.2 Background Generation Mechanism

To answer the questions presented in the end of the previous section, we concentrate our analysis on measurements of (H)STOF in solar quiet times. The unknown source

of particles seen by STOF is identified as the accidental coincidence. With data from two other instruments (SEM and Electron Proton Helium Instrument (EPHIN)) onboard SOHO and the housekeeping data of (H)STOF, we additionally clarify why the accidental coincidence is more easily recorded by STOF rather than by HSTOF.

Background characteristics

Figure 3.13 shows STOF measurements during the solar quiet times of 1998. We present the joint distribution of each two of three parameters, i.e., E/q , TOF, and energy deposit in SSDs, as well as the mass versus mass-per-charge distribution derived with these parameters. Figure 3.14 shows the count distribution over channels for these three parameters separately. At a first glance, all subplots of Figure 3.13 look noisy. No clear traces of ion species show up at the expected positions of the $E/q_{\#}$ vs. $\tau_{\#}$ graphic (see the upper left panel), which indicates most of the particle hits recorded by STOF during solar quiet times are background. We can clearly see that the density of the background is higher in $E/q_{\#} \leq 84$ (the gain of SSDs is low) than that in $E/q_{\#} > 84$ (the gain of SSDs is high). If $\tau_{\#} > 50$, the background looks uniform in the TOF channels, which is a characteristic of accidental coincidence (Hilchenbach et al., 1998). In addition, we find the background piles up around the 24th and 40th TOF channels (see two apparent peaks in the upper left panel of Figure 3.14) which is not understood. In the upper right panel of Figure 3.13, we can see that the background uniformly distributes among channels $E/q_{\#} \leq 84$ and $E/q_{\#} > 84$, respectively. This pattern is clearer in the lower left panel of Figure 3.14 except for the fourth and fifth E/q channels where the count number decreases by nearly 50%. The count number of the background

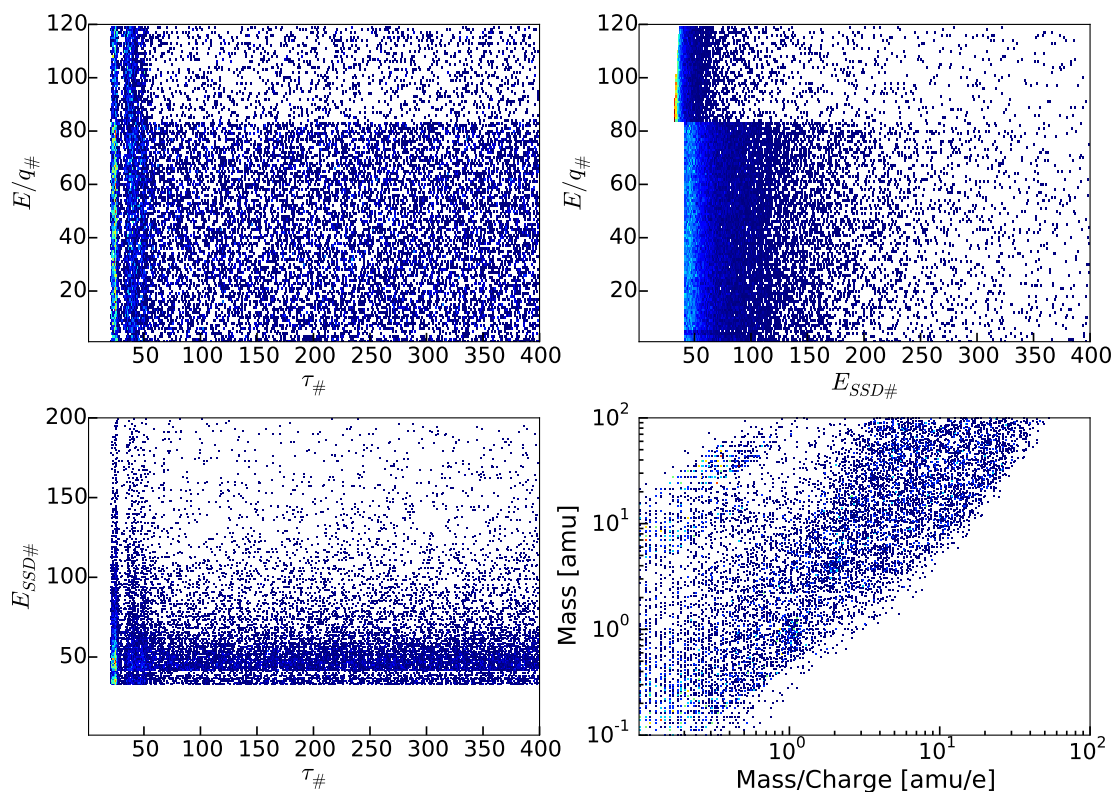


Figure 3.13: STOF measurements on Hybrids 0 and 2 during solar quiet times of 1998.

drops considerably with $E_{SSD\#}$. As shown in the upper right panel of Figure 3.14, this decrease exhibits double power laws in both low and high gains. We further find that the indices of the corresponding power laws during the other seven years are similar, which implies that the source of the background is stable. In the graphic of $\tau_{\#}$ vs. $E_{SSD\#}$ (lower left panel of Figure 3.13), the density of the pile-up background at low TOF channels decreases with $E_{SSD\#}$. In the lower right panel of Figure 3.13, we can identify a slight enhancement at the positions of proton and alpha particles. However, at the positions of the heavy ions we cannot see any hint of valid measurements in this panel.

By comparison, Figure 3.15 shows the corresponding measurements of HSTOF during the same quiet times of 1998. What we can easily distinguish in the left panel are four tracks of real ions which are protons and alpha particles, i.e., two upper tracks are obtained in the low gain while the two lower ones are measured in the high gain. As same as the STOF measurements, the pile-up background also appears in the low TOF channels of HSTOF. In the right panel, the track extending from the lower left to the upper right corner is the contribution of this kind of background, which tells us that the pile-up background can only affect the measurements at the highest energies. Moreover, the accidental-coincidence background exists too, but its density is lower than that of STOF. According to the approach of background estimation of Hilchenbach et al. (1998), the count rate of real ions is roughly one order higher than that of accidental coincidence events.

Here, we identify that both STOF and HSTOF suffer from the two types of background: the pile-up background and the accidental-coincidence background. The former can only affect the energy measurements of (H)STOF at the highest channels. Its generation mechanism is unknown. However, the effect of the accidental-coincidence

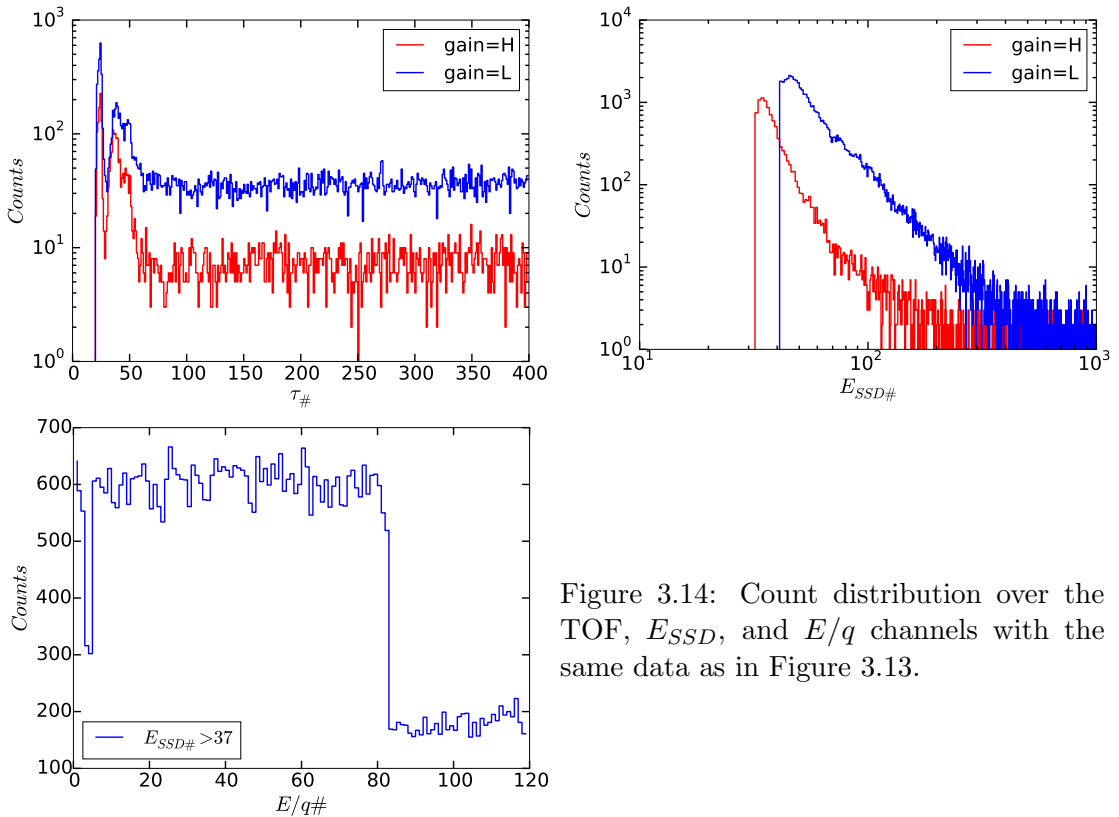


Figure 3.14: Count distribution over the TOF, E_{SSD} , and E/q channels with the same data as in Figure 3.13.

background goes through the total energy coverage of (H)STOF. In the following, we summarize the characteristics of this kind of background:

- More background is recorded by the SSDs of (H)STOF in the low gain than in the high gain. This indicates that the background may originate from interplanetary particles that show a flux decrease with energy.
- The background is distributed uniformly over the TOF channels. This feature might be the influence of the UV light considered by Hilchenbach et al. (1998); Bamert et al. (2002), although these authors did not explain it in detail. We can imagine that if the UV light is not well suppressed at the instrument entrance, photoelectrons can continuously and randomly generate at the foil of the TOF chamber and trigger both Start MCP and Stop MCP. As STOF is directed 7° west of the SOHO-Sun axis while HSTOF points 37° west of this axis, the UV light can enter the entrance system of STOF more easily than HSTOF. This could explain why STOF records a higher accidental-coincidence background than HSTOF.
- For STOF, more background counts are recorded in the low E/q channels ($E/q_{\#} \leq 84$) than in the high E/q channels ($E/q_{\#} > 84$). This can be explained by the gain switch behavior of Figure 3.4 and the first background characteristic mentioned above. The counts in the two groups of E/q channels is uniformly distributed, which means the background is independent from the E/q selection of the electrostatic analyzer. So the background particles do not enter STOF from the entrance. One possibility could be energetic penetrating particles which have enough energy to penetrate the housing of (H)STOF and trigger SSDs.
- The count number of the STOF background drops dramatically with the E_{SSD} channels, exhibiting a double power-law shape. The indices of power laws vary little over the surveyed eight years, indicating a stable source of the background. Regarding the third background characteristic and the uniform count distribution in Figure 3.10 and 3.12, we think the GCRs may play an important role in the generation of the background during solar quiet times.

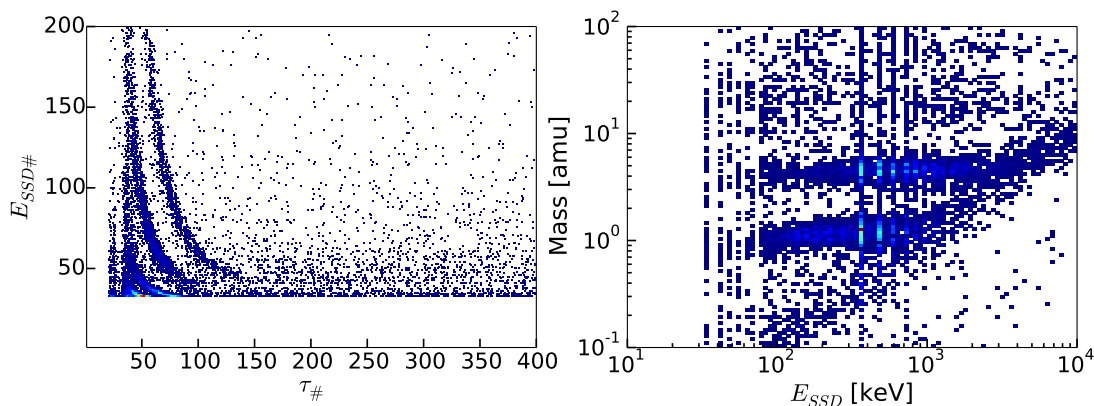


Figure 3.15: HSTOF measurements during solar quiet times in 1998. Compared with the lower left panel of Figure 3.13, the tracks of ions are clearly seen in the left panel of this figure. Compared with the lower right panel of Figure 3.13, the tracks of proton and helium are visible in the right panel of this figure.

To verify our above hypotheses, we further analyze the flux of the UV light and interplanetary energetic particles measured by another two instruments onboard the SOHO spacecraft, see details in the following sections.

Comparison with SEM

The Solar EUV Monitor (SEM) is a highly stable photodiode spectrometer, mounted piggyback on the TOF section of the STOF sensor. It can measure the full disk absolute solar flux at the He II 30.4 nm line, as well as the absolute integral flux between 17 and 70 nm (Hovestadt et al., 1995). As shown in Figure 3.16, in front of the entrance aperture, SEM has solar wind deflector plates which deflect away solar wind particles in order to protect the aluminum filter behind the entrance. The filtered incident radiation is dispersed by a high-density (5000 lines/mm) free standing gold transmission grating (Hovestadt et al., 1995). The 0th order image is measured by a photodiode to obtain the integrated solar EUV in the aluminum bandpass (17 and 70 nm). At the same time, the solar He II 30.4 nm line is measured in the \pm first order by similar diodes.

As suspected in the last section, MCPs of STOF can be overtriggered by photoelectrons, which is verified here with the housekeeping data of STOF, i.e., MCP signals Start Front (SF) and Stop Front-Rear (SFR or double coincidence). We compare the count rates of SF and SFR signals with the UV flux measured by SEM in Figure 3.17. The top panel shows temporal variations of the photon flux measured in the 0th order (bandwidth: 0.1-50 nm, blue curve) and the \pm 1st order (bandwidth: 26-34 nm, green curve). The UV flux fluctuates with time and peaks during solar events, e.g. CMEs and SEPs. Sometimes the flux bottoms out, which indicates data gaps. From the second panel, we find that the count rates of the SF signal decrease roughly exponentially with time, more rapidly than expected. On the DOY \sim 56 and \sim 258, there are two jumps, indicating the bias voltage of MCPs has been increased to raise their efficiency. Addi-

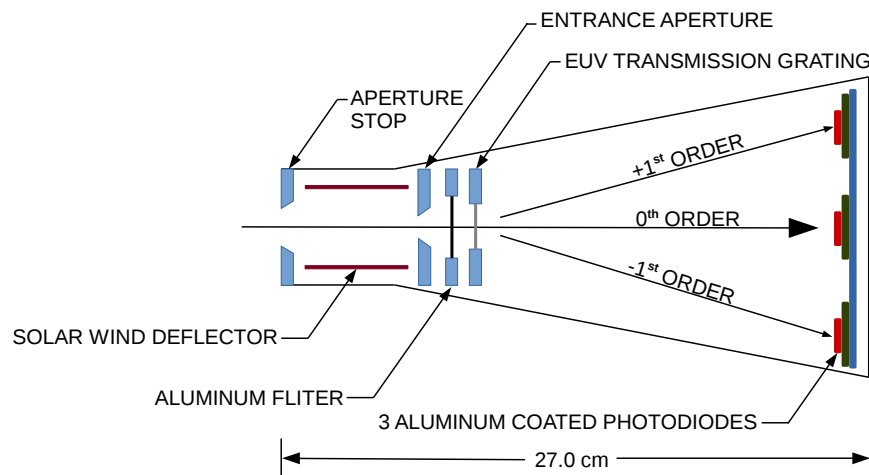


Figure 3.16: Schematic view of SEM. The entrance system consists of a 5000 line/mm transmission grating, placed behind a free standing Al filter (total 150 nm thick). The filter limits the radiation to the Al bandpass (17-70 nm). Any potential degradation of the filter due to solar wind is eliminated by the “solar wind deflector”. The prominent He II 30.4 nm line will be measured by the two side photodiodes (the \pm 1st order), while the center photodiode responds to the direct light (the 0th order) (Hovestadt et al., 1995).

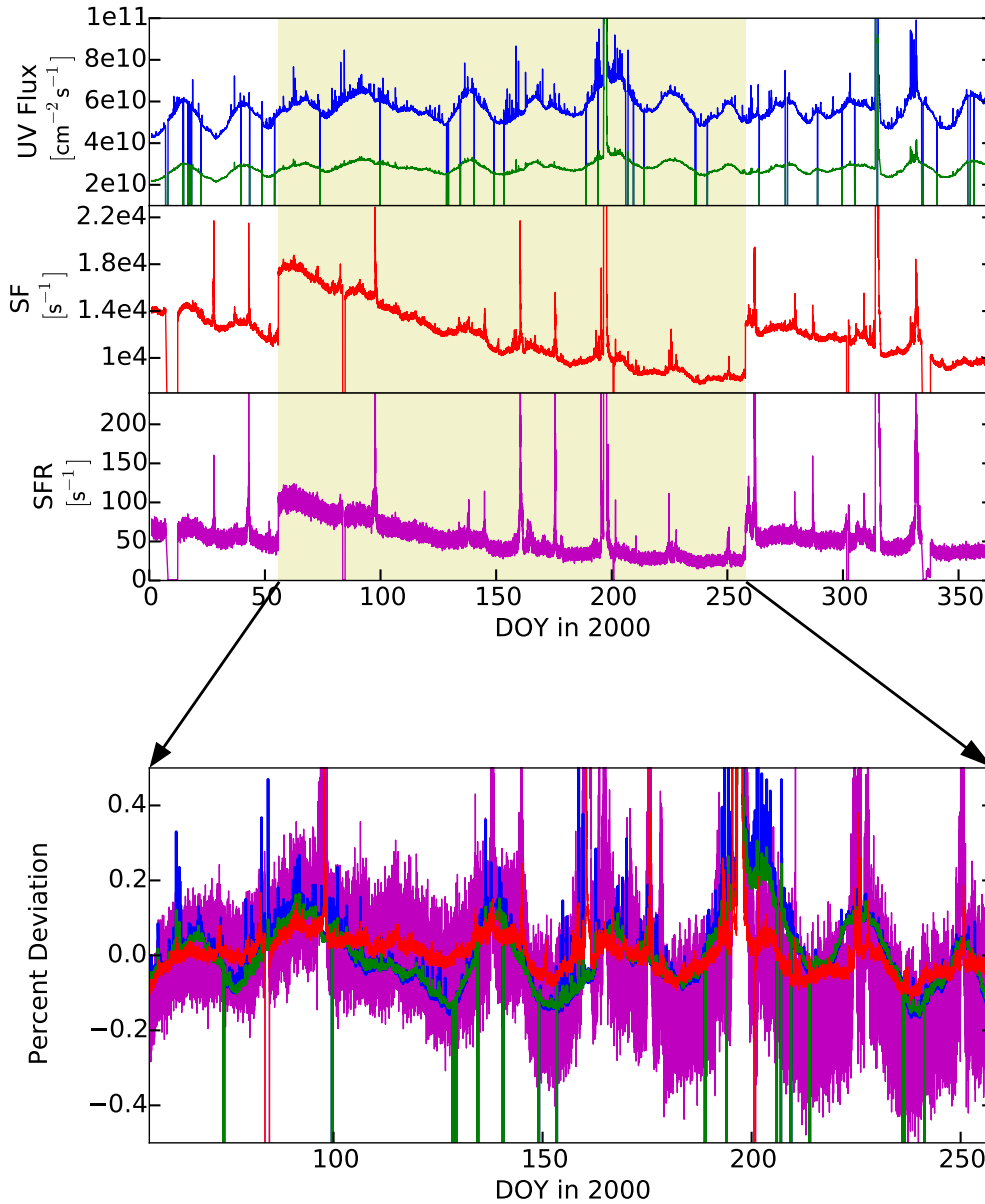


Figure 3.17: Comparison between the UV flux (blue curve for the 0th order; green curve for the 1st order) and count rates of MCP triggers (red curve for the SF count rates; magenta curve for the SFR count rates).

tionally, we notice that a similar fluctuation to that of the UV flux piggyback on the decreasing count rates, implying that there can be some correlation between the UV light and the SF signal. The third panel shows the SFR temporal count rates. Their absolute values are about two orders smaller than those of SF, but exhibit a similar temporal decrease and fluctuation. In this work, we define a percent deviation (hereafter PD) as $(data - expectation)/expectation$, where *data* denotes time series of a certain measurement, e.g., flux, and *expectation* is expected time series of this measurement. The PDs of these four measurements are shown in the bottom panel, zooming in the time period of DOY 56 to 258. More specifically, for the SEM measurements *data* is the temporal UV flux in the 0th and 1th orders and *expectation* is the flux average in this time period. As for the SF and SFR count rates, the clear degradation with time

indicates that the *expectation* is not constant. Here, we assume the *expectation* as a power-law function of time, and fit the count rates of the SF and SFR with $A \cdot \text{DOY}^{-\gamma}$, where A is normalizing constant and γ is the power-law index. As the lower panel shows, the PDs of the UV light in the two wavelength bands are almost the same in the surveyed time period. Flux in the wide band exhibits more peaks than that in the narrow band. The PD of the SF count rates shows similar variations to that of the UV flux. But its amplitude is roughly half of that of the UV flux. Although the deviation of the SFR count rates is relatively large, we can still recognize similar fluctuations to those of the SF count rates and the UV flux.

The above observations tell us that UV photons were not well suppressed by the entrance system of STOF. The secondary electrons generated by these photons over-triggered MCPs, resulting in a relatively more rapid efficiency decrease of MCPs than anticipated. In fact, with the housekeeping data of STOF, we find the bias voltage applied on MCPs had been switched at least two times per year in order to overcome the degradation of the MCPs. A direct consequence is that the instrumental efficiency of STOF becomes uncertain. In other words, the absolute flux of particles cannot be determined by STOF, which was also pointed out by Bamert et al. (2002). Although Hilchenbach et al. (1998) reported higher background of STOF from accidental coincidence rates than expected, due to the effect of scattered UV light. But their work has not clarified the process how the UV light contributes to the accidental coincidence rates, i.e., which kinds of particles trigger SSDs of STOF, UV photons themselves or some other sources of particles. Referring to the Geant 4 simulation in Appendix A, most photons penetrate the SSD without energy loss, while energetic electrons and ions always deposit energy as long as they hit the SSD. Therefore, we believe that penetrating particles are the main source for the additional triggers on the SSDs of STOF. To validate this idea, we analyzed the flux variations of interstellar energetic particles measured at 1 AU, see details in the following paragraph.

Comparison with EPHIN

As shown in Figure 3.18, the EPHIN sensor consists of a multi-element array of SSDs surrounded by an anticoincidence shield of plastic scintillator to measure energy spectra of electrons in the range 250 keV to >8.7 MeV, and of hydrogen and helium isotopes in the range 4 MeV/nuc to >53 MeV/nuc (Müller-Mellin et al., 1995). The front A and B detectors define a 83° full width conical FOV with a geometric factor of $5.1 \text{ cm}^2\text{sr}$, pointing 45° west of the SOHO-Sun line, the direction of the nominal IMF at 1 AU. Both of them have six segments (0 to 5) which allow sufficient correction for path length variations to resolve isotopes of hydrogen and helium. Another benefit of the detector segmentation is the capability to implement a commandable geometric factor by disabling some segments. The lithium-drifted silicon detectors C, D, and E stop electrons up to 10 MeV and hydrogen and helium nuclei up to 53 MeV/nuc. The detector F allows particles stopping in the telescope to be distinguishable from penetrating particles. Detector G is a fast plastic scintillator viewed by a 1 inch photomultiplier. This detector is used in anticoincidence and helps to reduce background Müller-Mellin et al. (1995). The detector F of EPHIN provides measurements for energetic particles. All the incident particles recorded by this detector have to penetrate a stack of five silicon detectors in front. We believe that measurements of detector F can give us a good estimate for the energetic penetrating particles of STOF.

In Figure 3.19 we compare three kinds of count rates: energetic particles measured by the EPHIN/F detector, the SFR signal and the accidental triple coincidence (ATC)

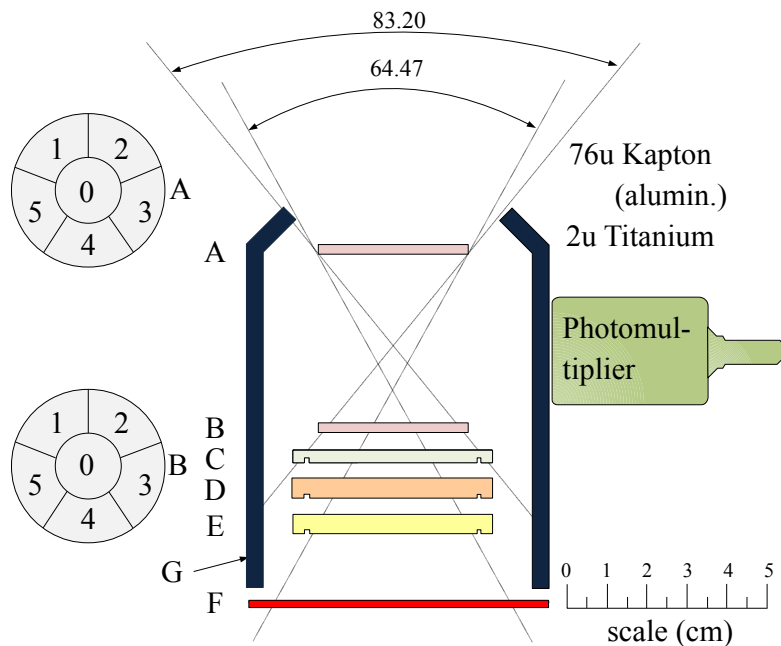


Figure 3.18: Schematic view of EPHIN. The sensor head of EPHIN consists of a stack of five silicon detectors (A, B, C, D, E) which measure electrons, hydrogen and helium isotopes. The detector stack is surrounded by an anticoincidence shield of plastic scintillator (G) and another silicon detector (F) to distinguish between absorption and penetration mode (Müller-Mellin et al., 1995).

(Hilchenbach et al., 1998) of STOF. The top three panels show their long-term variations from the year 1998 to 2000, while the zoomed-in three panels in the bottom are an example of short-term variations during DOY 100 to 200 of 1999. In the long run, both measurements of EPHIN and STOF are not continuous, but have a large data gap in 1998 and several data gaps in 1999. The peaks of count rates indicate solar events, e.g., SEPs, CMEs. The number of solar events increases in 2000 as the solar activity enters the maximum of the solar cycle 23. Apart from these peaks, i.e., in solar quiet times, we can see that the flux of energetic particles measured by EPHIN/F (the first panel) decreases by more than 50% from 1998 to 2000. Because GCRs are normally considered as the main source of energetic particles in solar quiet times, and are anticorrelated with the solar activity (Barouch and Burlaga, 1975). Both the SFR (the second panel) and background count rates of STOF (the red curve in the third panel) exhibit a sawtooth shape, which is due to the multiple efficiency switches on MCPs and the rapid decrease of their efficiency. In the zoomed-in short term, seven peaks of EPHIN's measurements indicate energetic particle events, while the SFR signal only shows two peaks, one of which is simultaneous with the second particle event observed by EPHIN/F. This behavior indicates the flux of UV photons and energetic penetrating particles is independent from each other. The most remarkable finding comes from the comparison of the STOF background and the product of count rates of SFR and energetic particles (the black curve in the third panel). Their long-term consistency can be clearly seen in the top third panel of Figure 3.19, after scaling the product with a constant of 3300. This consistency is strikingly apparent in the bottom panel, e.g., during the three time periods marked with yellow color. In the first time period, both SFR and energetic particles show a peak, which means their product definitely exhibits a corresponding peak. At the same time, the

STOF background also appears a peak. In the second case, only energetic particles display two clear peaks, while the SFR signal is nearly constant during this time period. The two peaks again show up in their product. Simultaneously the STOF background represents two peaks but with smaller amplitudes. Synchronous peaks of the scaled product and the background also occur in the third time period, where the SFR signal shows a peak and the flux of energetic particles is relatively stable.

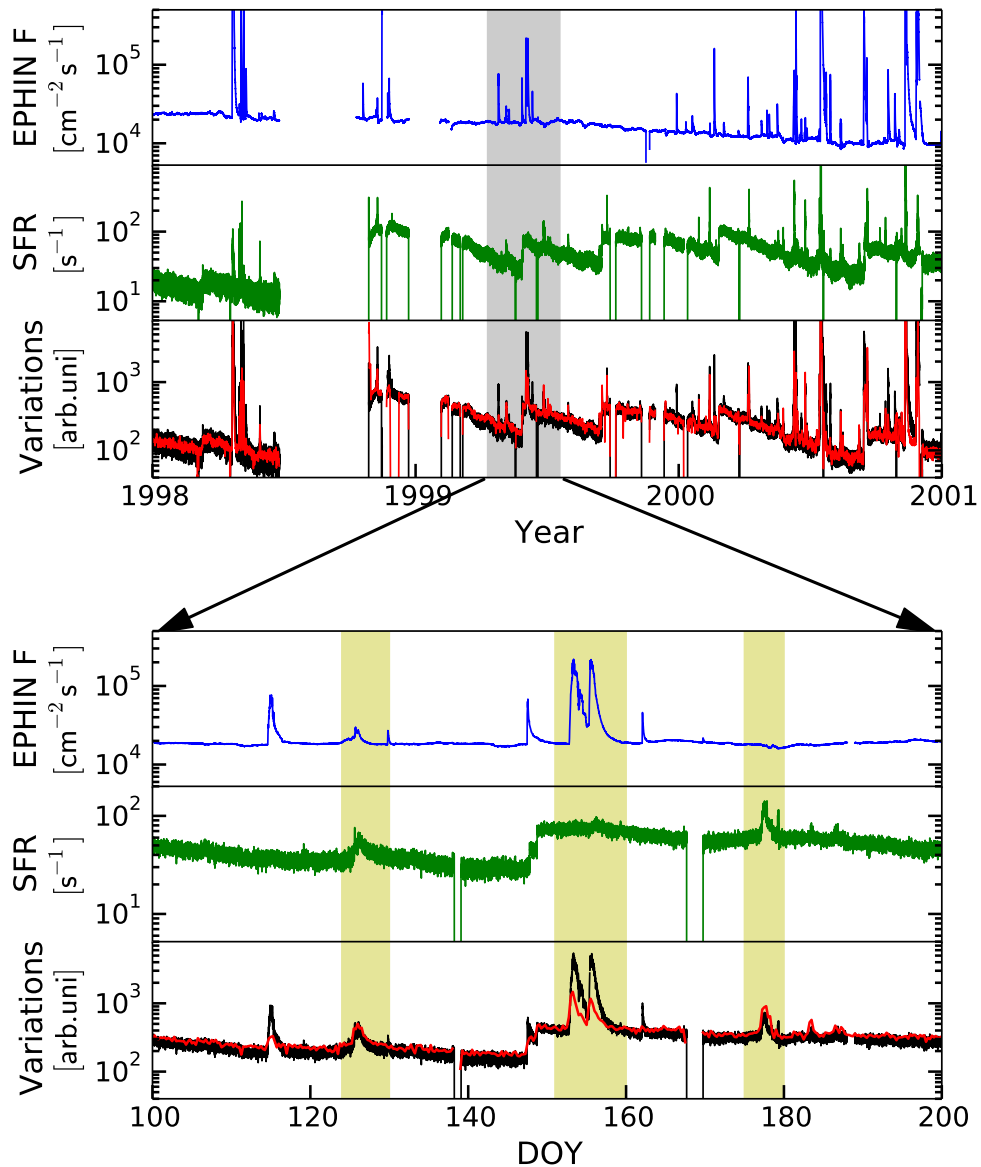


Figure 3.19: Comparison of the STOF background, the SFR signals, and the penetrating particles in the short and the long terms. The blue and green curves are the count rates of the penetrating particles (EPHIN/F measurements) and SFR signals (STOF housekeeping data) respectively. The red curve shows the count rate of the STOF background. For the purpose of comparison, we scale the product of STOF's SFR count rate and penetrating-particle count rate by a factor of 3300. The scaled product is shown with the black curve.

These observations can be explained with the occurrence probabilities of the ATC (P_{atc}), the SFR (P_{SFR}) signal, and the penetrating particles (P_{pt}) that can be approximated with the measurements of EPHIN/F. Given the independent behavior of the SFR signal and EPHIN/F measurements, we can have:

$$P_{atc} = P_{SFR} \cdot P_{pt} \quad (3.11)$$

In other words, we believe that energetic penetrating particles contribute to the triggers on the SSDs of STOF, while the START and STOP MCP triggers are mainly influenced by the UV photons (see the previous section). If we assume that the probability of occurrence is proportional to the count rates (CR), then Equation 3.11 can be expressed as:

$$\begin{aligned} CR_{bg} &\propto CR_{SFR} \cdot CR_{pt} \\ &= A \cdot CR_{SFR} \cdot CR_{pt} \end{aligned} \quad (3.12)$$

Equation 3.12 well describes the consistency between the STOF background and the product of count rates of SFR and energetic particles in solar quiet times. In the case of solar events, the normalizing term A of this equation might not be a constant any more according to the difference of the peak magnitude in Figure 3.19, but a function of CR_{SFR} and CR_{pt} .

The above work helps us to understand how the STOF background is generated. The main cause of the background is that the collimator of STOF does not suppress the UV light as well as anticipated. Thus, photoelectrons are generated in the process of the interaction between the UV photons and the TOF unit of STOF, so that MCPs of the TOF unit are overtriggered by these photoelectrons. This process has two consequences: (1) The MCP efficiency decreases more rapidly than expected. To compensate the degradation of MCPs, their bias voltage needs to be increased at least twice per year. For the flux measurements, it becomes difficult to know the absolute value of flux, therefore both Bamert et al. (2002) and Bamert et al. (2004) used arbitrary unit for their spectral analysis. (2) Penetrating particles originating from solar events or GCRs can easily be registered as valid particle hits, as long as they trigger one SSD pixel together with the START and STOP MCP triggers provided by the UV light. Therefore, in this work we identify the source of the STOF background as the ‘‘coincidence’’ of the UV light with penetrating particles.

3.3.3 Background Estimation Model

Hilchenbach et al. (1998) have successfully identified energetic hydrogen atoms (EHAs) between 55 and 80 keV using HSTOF data. To eliminate the effect of background caused by accidental coincidence events, they present a background estimation approach shown in Figure 3.20. Similar to what we show in Figure 3.15, events due to real particles in Figure 3.20a fall along well-defined tracks in the plane of residual energy channels versus TOF channels. Background events are uniformly distributed throughout the entire TOF region, and mingle with the real events. To estimate the background among the proton events (particle tracks in Figure 3.20b), Hilchenbach et al. (1998) displace the $M = 1$ track, with its track width, by a block of TOF channels (e.g., 500 channels, in Figure 3.20c) in the TOF- E_{SSD} plane, where no real particle tracks are expected. Since the background is observed to be uniformly distributed over TOF channels, all events on this displaced track provide a valid background measurement in the same energy channel intervals on the real $M = 1$ track. The background rate obtained by Hilchenbach et al.

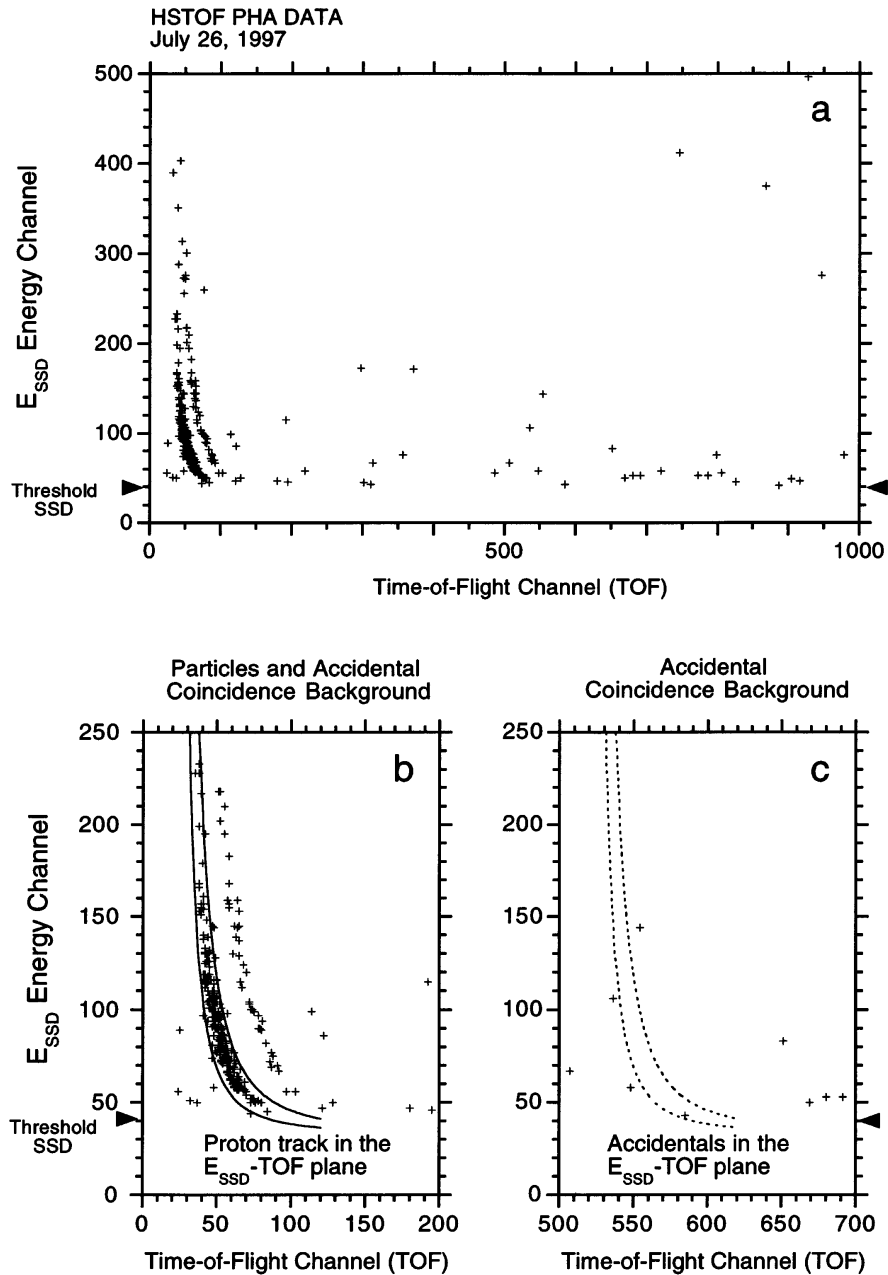


Figure 3.20: (a) An example of PHA data is plotted in the TOF- E_{SSD} plane. H and He events and the accidental coincidence events are clearly distinguishable. (b) Proton events congregate along well-defined tracks in the TOF- E_{SSD} plane. Real particles can only be detected in the first half-section of the TOF range. (c) The accidental coincidence events scatter uniformly throughout the entire TOF region and fall uniformly within the tracks (Hilchenbach et al., 1998).

(1998) is about three times that obtained by the Monte Carlo simulation of Bamert et al. (2002), who consider an isotropic source of energetic cosmic-ray protons and electrons. This disagreement between the simulation and the observation could be due to the UV photons overtriggering MCPs, which is discussed in previous sections.

Due to the fixed E/q of the HSTOF's entrance, measurements of different ion species exhibit their corresponding tracks at their fixed positions on the graphic of E_{SSD} vs.

TOF. However, for the case of STOF, incident particles are selected by different E/q . So ions measured in one E/q step by STOF are expected to show several peaks (not tracks as in the case of HSTOF), each corresponding to a charge state of the element. These peaks are not fixed in their positions but are E/q dependent and shift from low to high position in the TOF- E_{SSD} plane with E/q . Therefore, the method of Hilchenbach et al. (1998) cannot be directly applied to the background estimate for STOF.

Here, we present our approach to estimate the STOF background in Figure 3.21. It is very similar to the method of Hilchenbach et al. (1998), but considers a peak area moving with E/q . The acquired STOF data during DOY 206-211 of 2003 in Figure 3.21 show measured energy, E_{SSD} , vs. TOF, with an inset showing the corresponding STOF data mapped to the mass/mass-per-charge space. Several types of ions can readily be distinguished in the inset. From bottom to top they are protons, alpha particles (surrounded by a red rectangle), He^+ , a CNO group, and heavy ions such as Mg, Si and Fe ions. The corresponding E_{SSD} vs. TOF is shown in the surrounding plot. The track of alpha particles in integrated 60-84 E/q channels can be identified by close inspection of

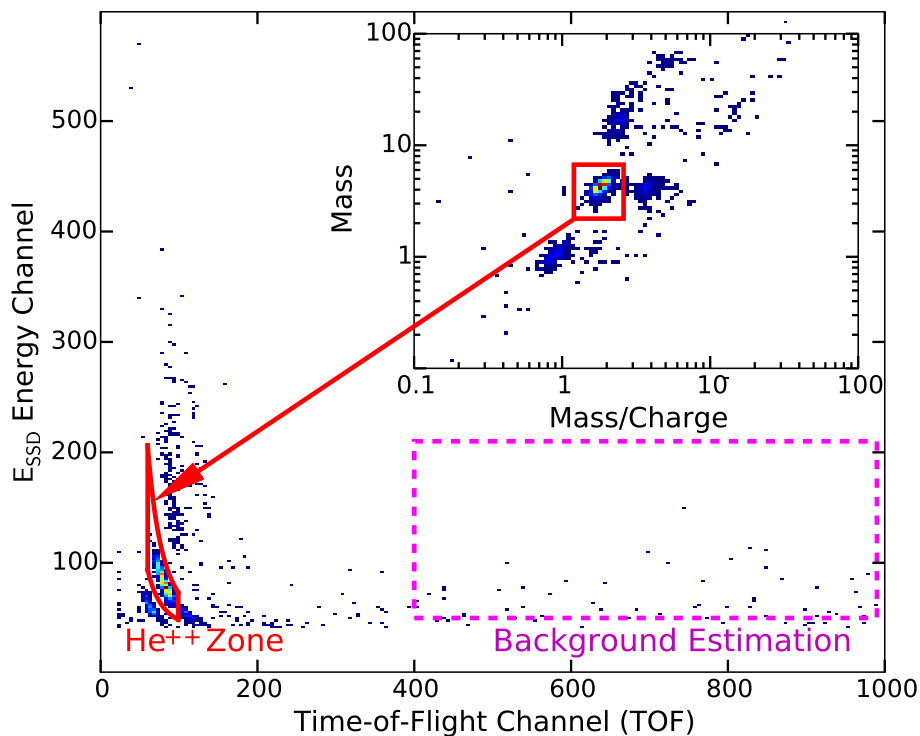


Figure 3.21: Example of the background estimation for STOF. STOF data are acquired for the range of 60-84 E/q steps during DOY 206-211 of year 2003. The panel shows measured energy E_{SSD} vs. TOF, while its inset shows the same data mapped to the $m-m/q$ space. Alpha particles are surrounded by a red square in the inset. The corresponding TOF- E_{SSD} measurements are surrounded by a mapped closed red curve which corresponds to the red rectangle in the $m-m/q$ space. The accidental coincidence events (or instrumental background) are uniformly distributed throughout the entire TOF region and fall uniformly within the real ion region, e.g., the He^{++} region. The large dashed magenta rectangle in the high TOF region is used to derive the background density in every E_{SSD} channel and further estimate the background level in the red ion region.

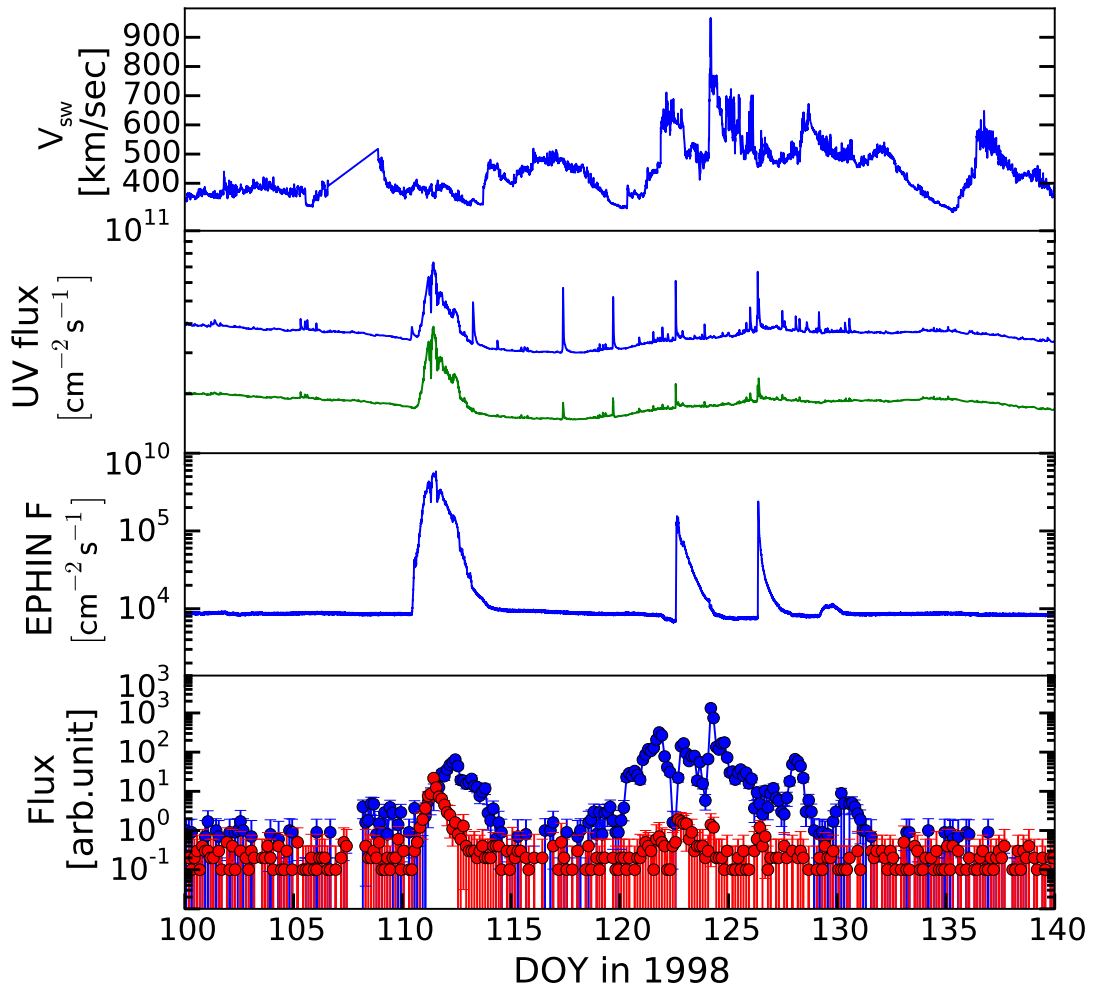


Figure 3.22: An application example of the STOF background estimation method during DOY 100-140 of year 1998. The solar wind speed in the top panel is obtained from SOHO/PM. The flux of UV light in the integrated (blue) and first-order (green) channels measured by SOHO/SEM is given in the second panel. The third panel shows the count rate of penetrating particles measured by SOHO/EPHIN. The bottom panel shows the differential flux of alpha particles measured by STOF (blue dots) and the background estimation (red dots) with the method introduced in Figure 3.21.

the data and is surrounded by a red shape corresponding to the mapped rectangle in the mass/mass-per-charge space. As indicated by the dashed magenta rectangle in Figure 3.21, we sample the background in a high TOF region and calculate the linear density of the background along the TOF axis in every energy channel. Then the background located in the closed red curve can be estimated by summing up the background in all energy channels inside this curve, which is the product of the linear density of background and the number of TOF channels in this area. With this method, we achieve a robust estimate for the expected background around the alpha particles.

Figure 3.22 illustrates an application example of our STOF background estimation model during DOY 100-140 of 1998. During DOY 100-106, the solar wind speed (top panel) is steadily around 400 km/s, while both SEM (second panel) and EPHIN/F (third panel) measurements are also relatively stable, indicating a time period of solar quiet

times. The He^{++} flux (blue dots) measured by STOF in the bottom panel is slightly above the estimated background (red dots) with large error bars. Additionally, we notice that the counting statistics of alpha particles are worse than that of the background. It is because the area of background estimation in the TOF- E_{SSD} plane of Figure 3.21 (the dashed magenta rectangle) is much larger than the area of the He^{++} track (closed red curve). More accidental coincidence events can be included in the background estimation. Over the time period of DOY 110-115, both SEM and EPHIN/F have detected a significant simultaneous flux enhancement, while the solar wind is stable around 400 km/s. Based on the generation mechanism of the STOF background identified in previous section, the STOF background is also expected to rise considerably during this time period. This expectation is well consistent with the background measurement in the bottom panel. In the starting phase of this time period, the SNR is approximately 1, and increases after the background peak (on around DOY 111). In the beginning of May 1998 (from DOY 120 to 130), a sequence of very intense SEP events and CMEs were observed by an impressive number of instruments, both remote-sensing optical and in-situ particle instruments (Bamert et al., 2002). The solar wind speed shows large variations and several discontinuities (indicating interplanetary shocks). The SEM data exhibit several impulsive short-duration peaks of UV light. EPHIN measurements show only two peaks around DOY 123 and 127, associated with a background enhancement during these two days. Apart from these two days, the SNR on the other days of this time period is larger than ~ 100 , providing high reliability of the STOF data studied by Bamert et al. (2002) in this time period.

3.4 Conclusions

In this chapter, we have introduced the working principle of CELIAS/(H)STOF as part of the SOHO mission and show how we use the PHA data obtained by this instrument. By analyzing the (H)STOF data, we have identified several instrumental defects, e.g., the contamination of two hybrids of STOF by HSTOF, oversensitive SSD pixels, and two kinds of background: the pile-up background and the accidental-coincidence background. For the second background, we determine its generation mechanism with assistance of data from SEM and EPHIN and the housekeeping data of (H)STOF. We explain that this kind of background results from the interaction of the instrument, the UV light, and penetrating particles. Based on the background-estimation method from Hilchenbach et al. (1998) for HSTOF, we present our own approach to estimate the STOF background. With our method, we survey the SNR of the STOF measurements in the year 1998 and find that the SNR is ~ 1 in solar quiet times and normally more than 10 during solar events.

Chapter 4

Case Study

4.1 Introduction

As we introduce in Chapter 2, we expect to observe a spectral turnover shifting from low to high suprathermal energies during CIR events, which can be done with an instrument like SOHO/STOF. Based on the work of Chapter 3, we know that during solar events, e.g., CIRs, the SNR of STOF measurements is usually satisfactory. Regarding STOF does not cover the whole suprathermal energies, we add measurements from SWICS onboard ACE to extend our energy coverage to lower solar wind energies. Then we expect to observe spectra with both solar wind bulk and its suprathermal tail as shown in Figure 2.3 of Chapter 2. Similar to STOF, SWICS is also a TOF mass spectrometer, providing a nominal E/q coverage from 0.6 to 86 keV/e (see Figure 4.1). Different from STOF, SWICS has equipped with additional post acceleration for the incident particles after they are selected by the electrostatic analyzer. Then these particles can gain enough energy to penetrate the carbon foil and deposit in SSDs. More details can be found in Gloeckler et al. (1998); Berger (2008).

This chapter contains our first publication “Suprathermal helium associated with corotating interaction regions: A case study” (Reproduced from Yu et al. (2016), with the permission of AIP Publishing.), which is published in AIP Conference Proceedings,

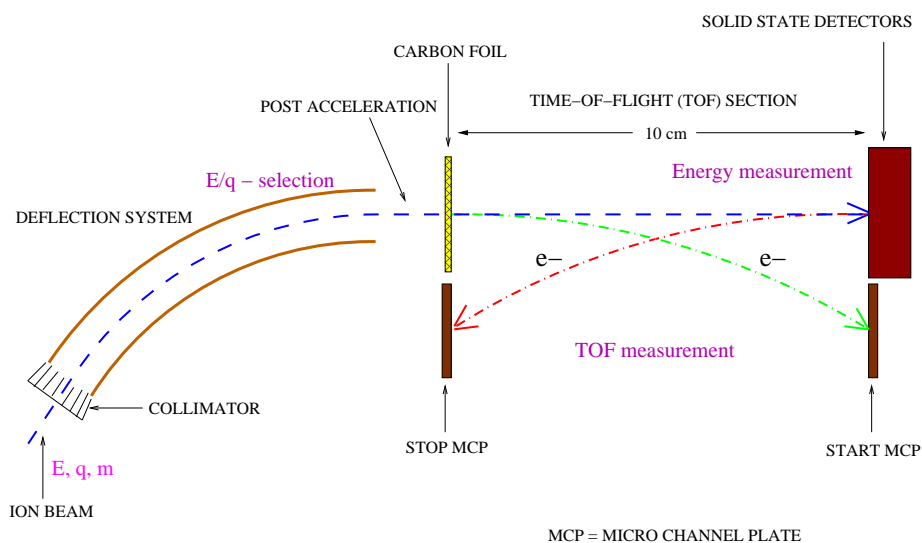


Figure 4.1: Schematic view of SWICS, taken from Berger (2008).

Vol 1720. This publication mainly introduces the time profile and the spectral evolution of suprathermal He^{++} as well as the variability of $\text{He}^+/\text{He}^{++}$ during the CIR event between July 26 and 27 of 2003 which has been widely studied by Jian et al. (2006); Mason et al. (2008); Ebert et al. (2012) as a typical CIR event. The spectra of this event exhibit an evolution as described by the Fisk and Lee (1980) model (see Figure 2.3).

4.2 Publication

Contributions to this paper are listed below and my contribution is around 80%.

| Contributions | Authors |
|-----------------------------|-------------------------------------------------------------|
| Study conception and design | J. Yu, L. Berger, and R.F. Wimmer-Schweingruber |
| Data acquisition | J. Yu, L. Berger |
| Data analysis | J. Yu |
| Data interpretation | J. Yu |
| Drafting of manuscript | J. Yu |
| Critical revision | J. Yu, L. Berger, R.F. Wimmer-Schweingruber, and B. Klecker |

Suprathermal Helium Associated with Corotating Interaction Regions: A Case Study

J. Yu^{1,a)}, L. Berger¹, R. F. Wimmer-Schweingruber¹, M. Hilchenbach², R. Kallenbach², B. Klecker³ and J. Guo¹

¹*Institut für Experimentelle und Angewandte Physik (IEAP), Christian Albrechts-Universität zu Kiel, Leibnizstrasse 11, 24118 Kiel*

²*Max-Planck-Institut für Sonnensystemforschung, Göttingen, Germany*

³*Max-Planck-Institut für extraterrestrische Physik, Garching, Germany*

^{a)}yu@physik.uni-kiel.de

Abstract. Enhancements of suprathermal particles observed at 1 AU often can be related to Corotating Interaction Regions (CIRs). The compression regions associated with CIRs and their driven shocks which typically form at a few AU distance to the Sun can efficiently accelerate particles. If accelerated at the trailing edge of a CIR these particles can travel sunward along the ambient magnetic field and thus enhanced fluxes can be observed even if the acceleration region has passed over the spacecraft. We have analysed a CIR that has been observed at L1 by ACE/SWICS and SOHO/CELIAS/STOF on days 207 and 208 in 2003. The combination of SWICS and STOF data allowed us to study suprathermal Helium ranging from its onset at solar wind bulk energies up to 330 keV/nuc. Here we present our results for the temporal evolution of the flux, energy spectra and the He⁺/He⁺⁺ ratio. In particular we present observational evidence for a turnover of the energy spectra at lower energies after the CIR passage which has been theoretically predicted but never been observed so far.

INTRODUCTION

CIRs are caused by the interaction of fast solar wind with slower solar wind ahead resulting in a compression region. The interaction strengthens with the heliocentric distance. Consequently forward and reverse shocks normally form around 2 AU from the Sun or even further away. Enhanced suprathermal or energetic particles were detected during CIRs with a series of spacecraft, e.g., Helios 1 and 2, Ulysses, Wind, SOHO, and ACE, as the compressed plasma and shocks are effective acceleration regions. Chotoo et al.[1] found that in the suprathermal energy range (~10-500 keV/nuc) particle intensities peak inside the CIR itself, i.e., in the compressed and decelerated fast solar wind, consistent with previous observation by Hilchenbach et al.[2].

Fisk and Lee[3] proposed a model based on diffusive shock acceleration to explain the energy spectra in the vicinity of CIRs. The predicted power-law spectral shape with an exponential component for higher energies inside CIRs is typically observed. For regions outside CIRs, this model implies that suprathermal particle enhancements at 1 AU associated with CIRs arise from sunward propagating particles accelerated by CIR-driven shocks beyond 1 AU. These particles are subject to scattering when they propagate in the expanding solar wind, which results in a turnover in the energy spectrum much below ~0.5 MeV/nuc, depending on scattering conditions. However, this turnover has not been observed in previous studies[1][4].

Additional evidence for the suprathermal particle source outside of the Earth orbit in CIR's fast wind regions is the increasing He⁺/He⁺⁺ ratio. Chotoo et al.[1] showed that the He⁺/He⁺⁺ ratio in the 10-35 keV/nuc energy range remained relatively constant near the reverse shock, which can be interpreted as evidence for local acceleration of solar wind He⁺⁺ and interplanetary He⁺. However, in the higher energy range covered by ACE/SEPICA (0.25-0.8 MeV/nuc), Kucharek et al.[5] found that the He⁺/He⁺⁺ ratio increased linearly extending from compressed fast wind to fast wind regions, which can be explained by the increasing distance between the spacecraft and the reverse shock along the connecting flux tube and by the increase of pickup He⁺ relative to solar wind He⁺⁺ with radial distance[6].

OBSERVATIONS

The Solar and Heliospheric Observatory/Charge, Element, and Isotope Analysis System/Suprathermal Time-of-Flight (SOHO/CELIAS/STOF) mass spectrometer was designed to measure suprathermal ions in the energy range of $\sim 35\text{-}660$ keV/Q. The geometric factor of STOF is 0.05 cm²sr, with the field of view pointing 7° west off the SOHO-Sun line[7]. The Solar Wind Ion Composition Spectrometer (SWICS) onboard the Advanced Composition Explorer (ACE) can measure the composition of solar wind and pickup ions from ~ 0.6 to ~ 86 keV/Q[8]. With these two instruments, our measurements can fully cover the energy of the solar wind up to its suprathermal tail, thus helping us to better understand the origin of suprathermal particles and their injection and acceleration processes. Since there is no magnetometer onboard of the SOHO spacecraft, we used magnetic field data from ACE/MAG, as both spacecraft are located around Lagrangian Point 1 (L1). Solar wind bulk speed, thermal speed and proton density were provided by SOHO/PM and ACE/SWEPAM, respectively.

Temporal Variation of Flux

Figure 1 shows plasma and magnetic field measurements for the CIR which occurred during July 26th and 27th (days 207 - 208), 2003. Following Chotoo et al.[1], we defined four regions: the slow wind region (S), the compressed slow wind region (S'), the compressed fast wind region (F') and the fast wind itself (F), divided by the leading edge, stream interface and trailing edge (vertical solid lines in the plot). The trailing edge here has already evolved into a reverse shock. The total pressure P was derived from the sum of plasma and magnetic field pressure, i.e., $P = n_p v_{th}^2 m + B^2/2\mu_0$, where n_p and v_{th} are the proton density and thermal speed respectively and B is the magnitude of magnetic field. Here we used 50 pPa total pressure as a threshold (see the dashed line in Figure 1) to determine CIR boundaries[9], and used O^{7+}/O^{6+} abundance ratio in the bulk solar wind to determine the stream interface[10][11]. Comparing plasma parameter measurements with PM and SWEPAM, we know that the ambient wind properties of SOHO and ACE are almost the same, and especially the time difference at CIR boundaries is less than 10 minutes. The data in Figure 1 show the following behaviour: in the S region no suprathermal He^{++} was found during DOY 206; in the S' region the flux tended to increase with time, however, the absolute values were still very small; the flux rose abruptly in the F' region and peaked around the reverse shock; in the F region the flux started to decline, but the absolute values were still comparable with those in F' after half a day. Based on the work by Ebert

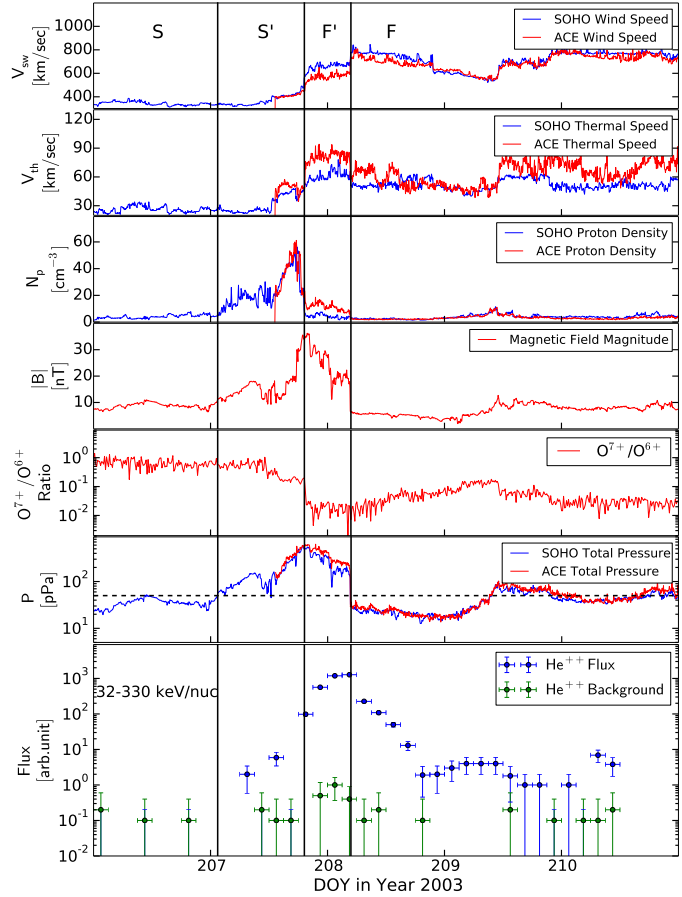


FIGURE 1. The time profiles of CIR-associated suprathermal He^{++} enhancement identified by STOF. Shown from top to bottom are 5-min averaged solar wind proton bulk speed, thermal speed and proton density measured by SOHO/PM and ACE/SWEPAM, 4-min averaged interplanetary magnetic field strength measured by ACE/MAG, 12-min averaged O^{7+}/O^{6+} abundance ratio measured by ACE/SWICS, total pressure ($n_p v_{th}^2 m + B^2/2\mu_0$), and 3-hour averaged He^{++} fluxes and the corresponding background estimation.

et al.[12], the distribution of suprathermal particles in the F' region of this event can be considered as anti-sunward while it becomes dominantly sunward in the F region. These sunward particles are normally believed to be accelerated beyond the Earth orbit. Additionally, we could find that the signal to noise ratio (SNR) in both F and F' regions was better than 100, providing high reliability of the data.

Turnover Spectra

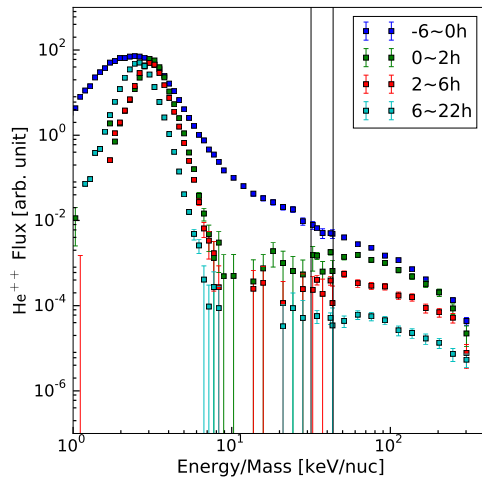


FIGURE 2. The figure shows the spectral evolution from inside to outside of the CIR on DOY 207-208, 2003. Two full vertical lines marks the overlapping energy range of SWICS and STOF. Four colored bars correspond to different time intervals (blue: 6 hours before encountering the shock, green: 0-2 hours, red: 2-6 hours, cyan: 6-22 hours after traversing the shock).

complementary capability to measure the intermediate energy range (33-165 keV/nuc). In Figure 3, we show the temporal variation of the $\text{He}^+/\text{He}^{++}$ ratio for the above CIR. The horizontal error bars reflect the time interval over which the ratio has been averaged, the vertical error bars indicate the statistical errors of the ratio. The statistical errors increase with time because of the flux decrease. The vertical dashed line marks the time when the spacecraft crossed the boundary between the fast compressed and the fast solar wind, separating regions F' and F respectively[5]. From Figure 3, we found that this CIR shows a pronounced increase in the $\text{He}^+/\text{He}^{++}$ ratio with time ranging from roughly 0.06 inside the CIR to around 0.4 well outside the CIR.

DISCUSSION

We have found that suprathermal ions mainly appear inside the compressed and decelerated fast wind region of this CIR event and that the intensity peaks close to the trailing edge. This indicates that suprathermal particles are more likely to undergo acceleration in the fast wind than in the slow wind. Particles are believed to be pre-accelerated by stochastic acceleration in the compressed plasma, and then injected into more effective shock acceleration[13].

In the fast wind region of this CIR event, we found that the suprathermal particle spectra exhibit the turnover spectral feature predicted by Fisk & Lee (1980). However, this is not always the case, many CIRs show a simple power

The spectral evolution during the above CIR event is shown in Figure 2. When the spacecraft is inside the CIR, we observe the approximately Maxwellian distribution of the bulk solar wind. Above the bulk solar wind, the suprathermal tail appears as a power law, and the spectrum rolls over and becomes steeper above ~ 200 keV/nuc. This spectral shape is consistent with the Fisk & Lee model and previous observations[1, 4]. When the spacecraft crosses the CIR's reverse shock, the distance of the magnetic connection between spacecraft and shock increases with time. From the three spectra in the F region we can conclude that: (a) inside the CIR the suprathermal particles contribute substantially to the total pressure. (b) The flux above ~ 70 keV/nuc decreases with increasing distance to the reverse shock. (c) There appears to be a lack of particles between the bulk solar wind and the suprathermal tails (i.e., between ~ 8 keV/nuc and ~ 70 keV/nuc). This gap is not due to an instrumental deficiency, as is demonstrated by the clean spectrum observed inside the CIR. It appears that there is a true dearth of suprathermal particles in this energy range. In other words, we have observed the turnover predicted by Fisk & Lee [3]. As the suprathermal particles have to "fight their way" against the solar wind and turbulence, their flux is decreased because of their small mean free scattering length compared to more energetic particles.

$\text{He}^+/\text{He}^{++}$ Abundance Ratio

Comparing with the previous investigations of $\text{He}^+/\text{He}^{++}$ ratio by Chotoo et al. over the energy range of 10-35 keV/nuc and Kucharek et al. over 250-800 keV/nuc, SOHO/STOF has the

law decrease from the bulk solar wind to higher energies. This suggests that the scattering of these sunward particles differs from CIR to CIR.

With SOHO/STOF, we have observed a substantial increase in the $\text{He}^+/\text{He}^{++}$ ratio with time from the beginning of the CIR, which can explain some of the large $\text{He}^+/\text{He}^{++}$ “fluctuations” of long-term investigations observed by Hilchenbach et al. earlier[2]. Moreover, this work extends the work by Kucharek et al.[5] with ACE/SEPICA to a lower energy range. We observe the ~ 33 to 165 keV/nuc ions after they propagated from the acceleration region to inside 1 AU and then were convected outward, i.e. they probably have started at much higher energies, if adiabatic energy losses are important.

ACKNOWLEDGEMENTS

We are grateful to the many individuals who contributed to SOHO/CELIAS over the many, many years. JY thanks DAAD for financial support. RFWS acknowledges helpful comments from the ISSI Team “Exploration of the inner Heliosphere - what we have learned from Helios and what we want to study with Solar Orbiter”. This work was also supported by the German space agency, DLR, by grant 50 OT 1202 and 50 OC 1501.

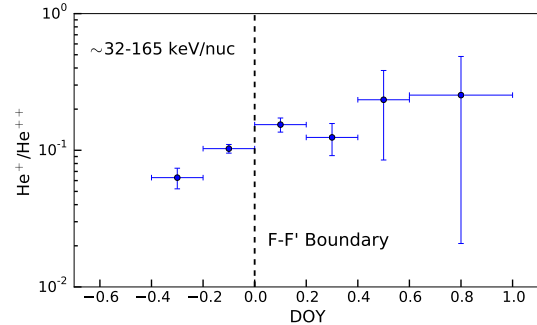


FIGURE 3. Variation of the $\text{He}^+/\text{He}^{++}$ ratio over the course of the CIR

REFERENCES

- [1] K. Chotoo, N. A. Schwadron, G. M. Mason, T. H. Zurbuchen, G. Gloeckler, A. Posner, L. A. Fisk, A. B. Galvin, D. C. Hamilton, and M. R. Collier, *J. Geophys. Res.* **105**, 23107–23122 (2000).
- [2] M. Hilchenbach, H. Grünwaldt, R. Kallenbach, B. Klecker, H. Kucharek, F. Ipavich, and A. Galvin, “Observation of suprathermal helium at 1 au: Charge states in cir,” in *The solar wind nine conference*, Vol. 471 (AIP Publishing, 1999), pp. 605–608.
- [3] L. A. Fisk and M. A. Lee, *ApJ* **237**, 620–626 (1980).
- [4] G. M. Mason, J. E. Mazur, J. R. Dwyer, D. V. Reames, and T. T. von Rosenvinge, *ApJ* **486**, L149–L152 (1997).
- [5] H. Kucharek, E. Möbius, W. Li, C. J. Farrugia, M. A. Popecki, A. B. Galvin, B. Klecker, M. Hichenbach, and P. A. Bochsler, *Journal of Geophysical Research (Space Physics)* **108**, p. 8040 (2003).
- [6] D. Morris, E. Möbius, M. A. Lee, M. A. Popecki, B. Klecker, L. M. Kistler, and A. B. Galvin, “Implications for source populations of energetic ions in co-rotating interaction regions from ionic charge states,” in *Joint SOHO/ACE workshop “Solar and Galactic Composition”*, American Institute of Physics Conference Series, Vol. 598, edited by R. F. Wimmer-Schweingruber (2001), pp. 201–204.
- [7] K. Bamert, R. F. Wimmer-Schweingruber, R. Kallenbach, M. Hilchenbach, B. Klecker, A. Bogdanov, and P. Wurz, *Journal of Geophysical Research (Space Physics)* **107**, p. 1130 (2002).
- [8] L. Berger, “Velocity Distribution Functions of Heavy Ions in the Solar Wind at 1 AU,” Ph.D. thesis, Christian-Albrechts-Universität zu Kiel 2008.
- [9] R. Bucik, U. Mall, A. Korth, and G. Mason, *Ann. Geophys* **27**, 3677–3690 (2009).
- [10] R. F. Wimmer-Schweingruber, R. von Steiger, and R. Paerli, *J. Geophys. Res.* **102**, 17407 – 17417 (1997).
- [11] R. F. Wimmer-Schweingruber, R. v. Steiger, and R. Paerli, *J. Geophys. Res.* **104**, 9933 – 9945 (1999).
- [12] R. W. Ebert, M. A. Dayeh, M. I. Desai, and G. M. Mason, *ApJ* **749**, p. 73 (2012).
- [13] N. A. Schwadron, L. A. Fisk, and G. Gloeckler, *Geophys. Res. Lett.* **23**, 2871–2874 (1996).

Chapter 5

Full Study

5.1 Introduction

Based on the work of Chapter 4, we further make a statistic study for the CIR spectra from February 1999 to October 2005. Sixteen CIR events are involved in this work, including seven contaminated events by upstream ion events and SEPs. We find that six of nine clean CIRs show possible signs of a turnover between $\sim 10\text{-}40$ keV/nuc in the F regions. Three of them even show this behavior inside the F' regions. The rest clean CIRs exhibit continuous power-law spectra in both the F' and the F regions. In contrast, we observe more variable spectra during seven contaminated events, i.e., power-law, turnover and superposition of these two shapes. Moreover, we fit spectra of the CIR event which is also reported in Chapter 4, with the Fisk and Lee (1980) theoretical model. We identify disagreements between the theory and observations. The reasons for that are given in the following paper which has been published on *Astronomy & Astrophysics*, Volume 599.

5.2 Publication

Contributions to this paper are shown as follow and my contribution is around 80%.

| Contributions | Authors |
|-----------------------------|--------------------------------------------------------------------------|
| Study conception and design | J. Yu, L. Berger, and R.F. Wimmer-Schweingruber |
| Data acquisition | J. Yu, L. Berger |
| Data analysis | J. Yu |
| Data interpretation | J. Yu |
| Drafting of manuscript | J. Yu |
| Critical revision | J. Yu, L. Berger, R.F. Wimmer-Schweingruber, P. Bochsler, and B. Klecker |

Suprathermal helium in corotating interaction regions: combined observations from SOHO/CELIAS/STOF and ACE/SWICS

J. Yu¹, L. Berger¹, R. Wimmer-Schweingruber¹, P. Bochsler², B. Klecker³, M. Hilchenbach⁴, and R. Kallenbach⁴

¹ Institut für Experimentelle und Angewandte Physik (IEAP), Christian-Albrechts-Universität zu Kiel, Leibnizstrasse 11, 24118 Kiel, Germany

e-mail: yu@physik.uni-kiel.de

² University of Bern, 3012 Bern, Switzerland

³ Max-Planck-Institut für extraterrestrische Physik, Garching, Germany

⁴ Max-Planck-Institut für Sonnensystemforschung, 37077 Göttingen, Germany

Received 5 April 2016 / Accepted 1 November 2016

ABSTRACT

Context. Energetic particle enhancements that are associated with corotating interaction regions (CIRs) are typically believed to arise from the sunward propagation of particles that are accelerated by CIR-driven shocks beyond 1 AU. It is expected that these sunward-travelling particles will lose energy and scatter, resulting in a turnover of the energy spectra below ~ 0.5 MeV/nuc. However, the turnover has not been observed so far, suggesting that the CIR-associated low-energy suprathermal ions are accelerated locally close to the observer.

Aims. We investigate the variability of suprathermal particle spectra from CIR to CIR as well as their evolution and variation as the observer moves away from the rear shock or wave.

Methods. Helium data in the suprathermal energy range from the Solar and Heliospheric Observatory/Charge, Element, and Isotope Analysis System/Suprathermal Time-of-Flight (SOHO/CELIAS/STOF) were used for the spectral analysis and were combined with data from the Advanced Composition Explorer/ Solar Wind Ion Composition Spectrometer (ACE/SWICS) in the solar wind energies.

Results. We investigated sixteen events: nine clean CIR events, three CIR events with possible contamination from upstream ion events or solar energetic particles (SEPs), and four events that occurred during CIR periods that were dominated by SEPs. Six of the nine clean CIR events showed possible signs of a turnover between ~ 10 – 40 keV/nuc in the fast solar wind that trails the compression regions. Three of them even showed this behaviour inside the compressed fast wind. The turnover part of the spectra became flatter and shifted from lower to higher energies with increasing connection distance to the reverse shock. The remaining three clean events showed continuous power-law spectra in both the compressed fast wind and fast wind regions, that is, the same behaviour as reported from previous observations. The spectra of the seven remaining events are more variable, that is, they show power law, turnover, and a superposition of these two shapes.

Key words. acceleration of particles – shock waves – solar wind – Sun: heliosphere – Sun: rotation

1. Introduction

Corotating interaction regions (CIRs) commonly form when high-speed solar wind streams that emerge from solar coronal holes overtake low-speed solar wind streams that have been emitted earlier (Gosling et al. 1978). The interaction between these two stream plasmas creates a compression region that corotates with the Sun and bounds with the leading and trailing edge. Forward and reverse shocks can form at the leading and trailing edge, respectively, when the interaction strengthens enough, normally at heliocentric distances greater than 2 AU (Balogh et al. 2000). It is widely known that suprathermal particles observed in association with CIRs have been interpreted to be accelerated in the compressed plasmas and shocks (Fisk & Lee 1980; Schwadron et al. 1996). During solar minimum, when the coronal mass ejections (CMEs) and solar flares are rare, CIRs are the dominant source of suprathermal particles in the interplanetary medium at 1 AU (Fisk & Jokipii 1999). Investigations of the origin of CIR-associated suprathermal particles have shown that these particles appear not only inside CIRs, but also often persist within the leading parts of fast-wind regions (Reames et al. 1997; Mason et al. 1997; Simnett et al. 1998; Hilchenbach et al. 1999; Chotoo et al. 2000). Commonly there

are believed to be two origins: (1) local acceleration by adiabatic compression in compressive turbulence (Fisk & Gloeckler 2006, 2007; Fisk et al. 2010), from transit-time damping of magnitude variations in the magnetic field (Schwadron et al. 1996); and (2) sunward-directed particles accelerated at remote reverse shocks as described by the model of Fisk & Lee (1980) (in this paper, we call this “remote acceleration”). Local acceleration is ubiquitous in the solar wind, and in quiet-time conditions, suprathermal tails show a common energy-spectrum shape: a power law with a constant index of -1.5 (Fisk & Gloeckler 2006). For particles accelerated remotely (origin 2), velocity distribution functions have been theoretically discussed by Fisk & Lee (1980), who considered a model of diffusive acceleration at CIR shocks several AU away followed by propagation into the inner heliosphere along magnetic field lines, including adiabatic cooling. The spectral shape of these sunward-streaming particles should be a power law multiplied with an exponential rollover, when the particle velocity is much higher than the speed of the corotating frame. Fisk & Lee (1980) pointed out that these accelerated sunward particles should have a low-energy threshold well above solar wind energies, as they have had multiple interactions with the shock and must have had sufficient speed after their first interactions to propagate upstream

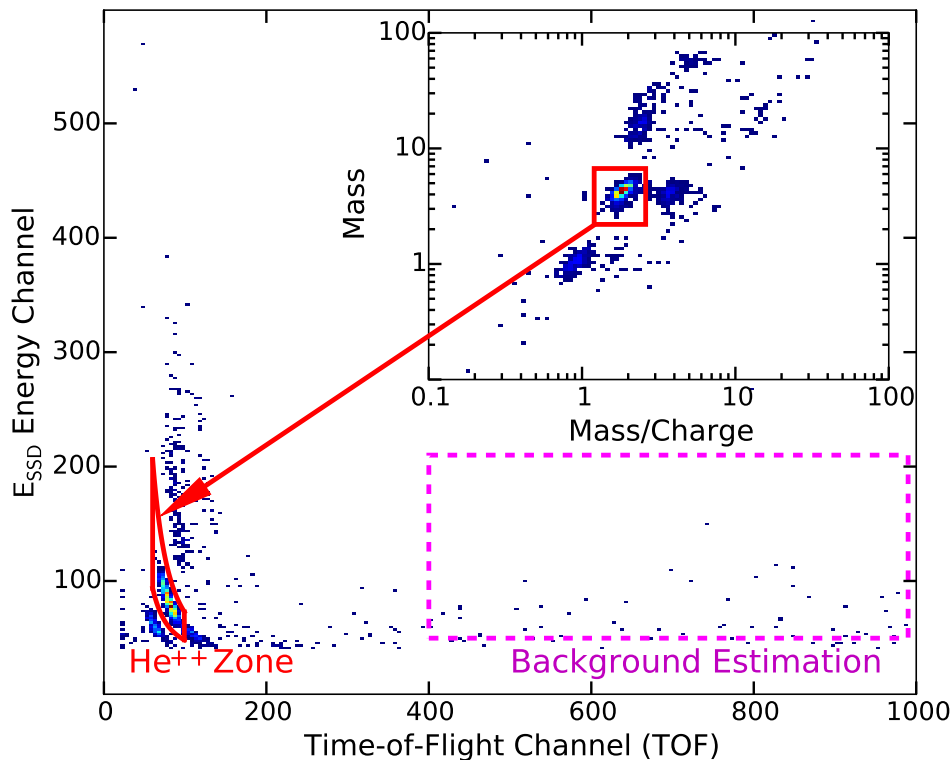


Fig. 1. STOF data acquired for the range of 60–84 E/q steps during days 206–211 in 2003. The panel shows the measured energy, E_{SSD} vs. TOF, while its *inset* shows the same data mapped to $m-m/q$ space. Alpha particles are surrounded by a red square in the *inset*. The corresponding E_{SSD} -TOF measurements are surrounded by a mapped closed red curve that corresponds to the red rectangle in $m-m/q$ space. The accidental coincidence events (or instrumental background) are uniformly distributed throughout the entire TOF region and fall randomly within the real ion zone, e.g., He^{++} . The large dashed magenta rectangle in the high-TOF region is used to estimate the background level of our measurements.

in the solar wind. In other words, the energy spectra may exhibit a turnover above solar wind energies. However, Chotoo et al. (2000), Mason et al. (1997), Reames et al. (1997) did not observe this turnover. CIR events studied by them showed power-law spectra above solar wind energies in both compressed fast-wind region and fast-wind region.

We used data from Solar Wind Ion Composition Spectrometer (SWICS) and Suprathermal Time-of-Flight (STOF) to study the temporal evolution of the alpha-particle spectra from the solar wind through the suprathermal energy range in the 16 events given in Table 1. We found that 6 of 9 clean CIR events are likely to show a turnover in their spectra between ~ 10 and 40 keV/nuc.

2. Instrumentation

The STOF mass spectrometer, which is part of the Charge, Element, and Isotope Analysis System (CELIAS) on board the Solar and Heliospheric Observatory (SOHO), measures suprathermal ions (Hovestadt et al. 1995). An electrostatic deflection system covers 35–660 keV/Q in 120 logarithmically spaced voltage steps. The geometrical factor of STOF is $0.05 \text{ cm}^2 \text{ sr}$ (Bamert et al. 2002) with the field of view ($3^\circ \times 17^\circ$), pointing 7° west off the SOHO-Sun line (Hilchenbach et al. 2001). The Proton Monitor (PM) of CELIAS consists of a Wide Angle, Variable Energy/charge (WAVE) passband deflection system to measure the solar wind proton bulk speed, density, thermal speed, and north/south flow direction (Ipavich et al. 1998). A detailed description of the CELIAS instruments has been given by Hovestadt et al. (1995). The SWICS on board the Advanced Composition Explorer (ACE) was designed to measure the composition of the solar wind and pickup ions from

~ 0.6 to ~ 86 keV/Q (see details in Gloeckler et al. 1998; Berger 2008). The Solar Wind Electron, Proton, and Alpha Monitor (SWEPAM) of ACE measures the solar wind plasma, electron, and ion fluxes as functions of their direction and energy. These data provide detailed knowledge of the physical parameters of the solar wind in every minute (see details in McComas et al. 1998), which were used to compare with the measurement of PM in this paper. The Magnetometer (MAG) on ACE measures the local interplanetary magnetic field (IMF) direction and magnitude to establish the large-scale structure and fluctuation characteristics of the IMF (see details in Smith et al. 1998).

STOF uses a triple-coincidence technique to identify particles; a start and stop trigger are generated in the time-of-flight (TOF) unit, the third comes from silicon solid-state detectors (SSDs). The measured TOF and energy, together with the known energy per charge of the particles (as determined by the electrostatic entrance system), allows us to measure the energy, mass, and mass per charge of a suprathermal ion (see e.g. Bamert et al. 2002). The triple coincidence suppresses accidental coincidences of penetrating energetic particles. However, using instrumental house-keeping data, we found that the count rate of the start and stop triggers of the micro channel plates (MCPs) on the TOF unit is correlated with the flux of solar ultraviolet light (UV). A possible leakage of photons may occur at the entrance of STOF, as the instrument faces the Sun almost directly. Then MCPs are triggered by a high flux of photoelectrons, resulting in much higher background than originally anticipated (Hilchenbach et al. 1998).

Figure 1 shows data acquired with STOF. The graphic shows the measured energy, E_{SSD} , vs. TOF, with an inset showing the corresponding STOF data mapped to mass/mass per charge

space. Five types of ions can readily be distinguished in the inset. From bottom to top they are protons, alpha particles (surrounded by a red rectangle), He^+ , a CNO group, and heavy ions such as Mg, Si, and iron ions. The corresponding E_{SSD} vs. TOF is shown in the surrounding plot, and the alpha-particle track is the region enclosed in the red line. To estimate the effect of the background on the He^{++} measurements, we used a method very similar to the one used by Hilchenbach et al. (1998) for HSTOF. We have verified that the background to the right of the He^{++} particles is evenly distributed in TOF. Since the background is caused by UV-triggered accidental coincidence events, these events should scatter uniformly throughout the entire TOF region, mingled with the real events. Thus, we can sample the background at higher TOF (where there are no heavy ions) to obtain a robust estimate of the expected background around the alpha particles. This is indicated by the dashed magenta rectangle. All events falling within any energy channel in this rectangle provide a true measure of the background in the same energy channel intervals in the real ion track. Then we can well estimate the background level in all the energy channels covered by the red He^{++} zone.

A further instrumental effect that needs to be accounted for is the gradual and unknown degradation of the MCPs, which means that we do not know the absolute fluxes measured with this instrument. Following Bamert et al. (2002), we therefore used arbitrary units for the differential fluxes described in this paper. Fortunately, the MCP degradation during CIR epochs is slow, so that we assume constant MCP efficiency during each CIR event in this paper.

3. Observations

Figure 2 shows solar wind plasma and magnetic field measurements for a CIR that occurred between July 26 and 27, 2003 (days of year 207–208). Following Chottoo et al. (2000), Richardson et al. (1993), we marked four regions in the plot: the slow wind region (S), the compressed slow wind region (S'), the compressed fast wind region (F'), and the fast wind itself (F). Throughout four regions, the mean charge states of iron measured by ACE/SWICS lies around 11^+ , consistent with typical values in the solar wind (Lepri et al. 2001). The stream interface (S'-F') is indicated by the vertical line in Fig. 2 and is characterized by a drop of the $\text{O}^{7+}/\text{O}^{6+}$ abundance ratio measured with SWICS in the bulk solar wind (Wimmer-Schweingruber et al. 1997, 1999). The leading (S-S') and trailing edge (F'-F) of the CIR were determined by the total pressure (Jian et al. 2006). Bućk et al. (2009) found that CIR boundaries can be well defined when the total pressure exceeds 50 pPa (indicated by the horizontal dashed line in Fig. 2), which is slightly higher than that in the background solar wind, which typically is 20–30 pPa, according to Jian et al. (2006). The total pressure P was obtained from the sum of plasma and magnetic field pressure, that is, $P = n_p v_{\text{th}}^2 m + B^2/2\mu_0$, where n_p and v_{th} are the proton density and thermal speed, respectively, and B is the magnitude of the magnetic field. Because SOHO has no magnetometer, we used magnetic field data from ACE/MAG (which is also around L1). Comparing plasma parameters (bulk speed, thermal speed, and proton density) measured by PM with those of SWEAPAM, we see that the physical conditions at SOHO and ACE were almost the same, and that the time difference between passages of the CIR boundaries is less than ten minutes. The CIR shown in Fig. 2 was bounded by a reverse shock (vertical line separating F' from F). We clearly see that the suprathermal He^{++} intensity peaks inside the decelerated and compressed fast-wind region (F'), close to the reverse shock. In contrast,

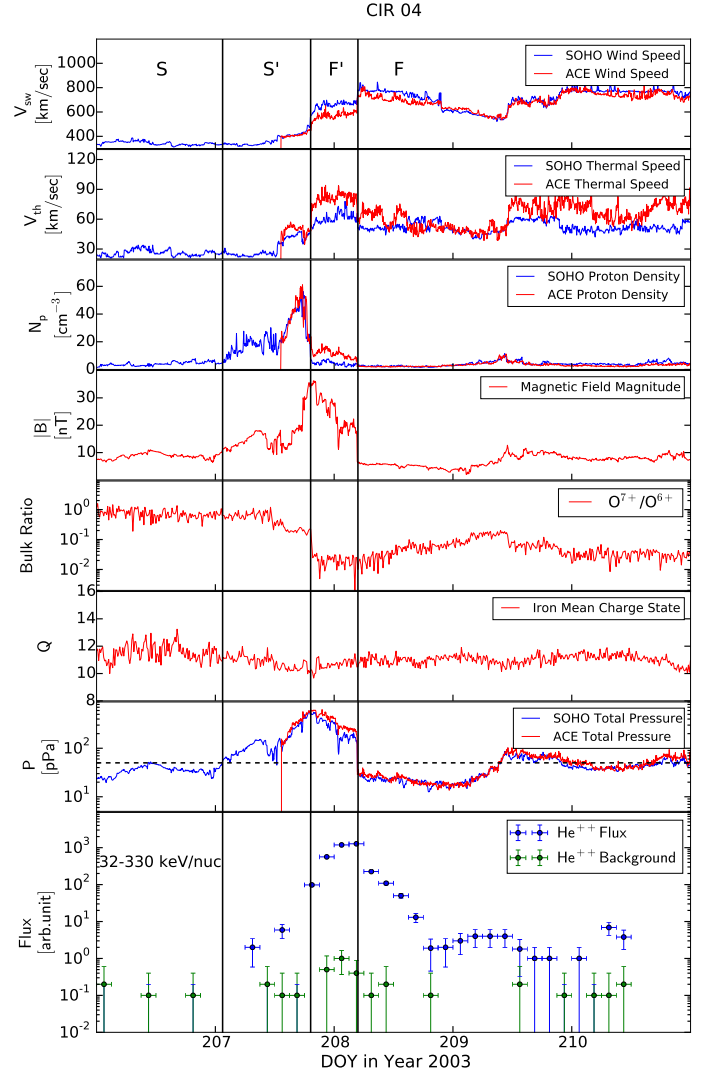


Fig. 2. Time profiles of CIR-associated suprathermal helium enhancement identified by STOF during the period from DOY 206 to DOY 211, 2003. Shown from top to bottom are the 5-min averaged solar wind proton speed, the thermal speed, and the proton density measured by PM and SWEAPAM, the 4-min averaged interplanetary magnetic field strength measured by ACE/MAG, the 12-min averaged $\text{O}^{7+}/\text{O}^{6+}$ abundance ratio measured by ACE/SWICS, the 12-min mean charge state of iron measured by ACE/SWICS, the total pressure ($n_p v_{\text{th}}^2 m + B^2/2\mu_0$), and three-hour-averaged helium fluxes and the corresponding background estimate from ~ 32 to 330 keV/nuc.

suprathermal particles are very rare in the S and S' regions. After passage of the reverse shock, suprathermal particles continue to be observable for more than one day. They are commonly believed to be the sunward particles accelerated by the reverse shock far beyond the Earth orbit. In other words, the observer saw the duration of the CIR particle event, which was longer than that of the CIR compression region itself. The background level shown in green was estimated using the method described above. The signal-to-noise ratio (S/N) in the F and F' regions is higher than 100, confirming that our observations are due to real He^{++} particles.

3.1. Event selection

Table 1 lists the sixteen CIR events investigated in this paper. We limited our investigation to the time interval from February 1999

Table 1. CIR events with suprathermal ions at STOF.

| Event | Year | Start time DOY, hh:mm | Stop time DOY, hh:mm | Spectra in F' | | | Spectra in F | | | Notes |
|------------------------|------|--------------------------|-------------------------|---------------|----|----|--------------|----|----|----------------|
| | | | | To | Mx | PI | To | Mx | PI | |
| With reverse shocks | | | | | | | | | | |
| 1 [◊] | 1999 | 137, 23:47 | 138, 19:17 | | | | ● | | | |
| 2 | 1999 | 227, 09:40 | 229, 01:23 | | | ● | | | ● | |
| 3 | 2000 | 054, 08:02 | 055, 13:59 | | | • | | • | | <i>h</i> |
| 4 * | 2003 | 207, 01:20 | 208, 04:42 | | | ● | ● | | | |
| 5 * | 2004 | 324, 14:16 | 326, 00:38 | | | ● | | | ● | |
| 6 * | 2005 | 236, 04:50 | 236, 20:23 | | | ○ | | ○ | | <i>a,b,c,f</i> |
| 7 * | 2005 | 280, 10:13 | 281, 06:14 | | | ● | ● | | | |
| Without reverse shocks | | | | | | | | | | |
| 8 | 1999 | 059, 12:38 | 061, 03:36 | | | ● | | | ● | |
| 9 | 2000 | 028, 05:16 | 029, 08:54 | | | • | • | | | <i>h</i> |
| 10 | 2000 | 036, 16:26 | 037, 23:02 | ● | | | ● | | | |
| 11 [◊] | 2000 | 082, 00:34 | 083, 01:40 | | ○ | | | | ○ | <i>c</i> |
| 12 * | 2000 | 143, 09:27 | 144, 13:45 | | | ○ | | | ○ | <i>a,b,c,d</i> |
| 13 * | 2001 | 284, 16:03 | 285, 12:14 | | | ○ | | | ○ | <i>a,b,c,g</i> |
| 14 * | 2002 | 010, 01:14 | 011, 07:19 | | | ○ | | | ○ | <i>e</i> |
| 15 * | 2002 | 324, 10:00 | 326, 00:15 | ● | | | ● | | | |
| 16 * | 2003 | 259, 23:15 | 260, 12:43 | ● | | | ● | | | |

Notes. Start and stop time of the compression region based on the physical properties of the solar wind are shown with day of year and coordinated universal time (DOY, hh:mm in the table). “To”, “Mx” and “PI” columns list different spectral shapes: turnover spectra, the superposition of turnover and power-law spectra, and power-law spectra, respectively. ^(◊) Events 1 and 11 have a data gap in STOF measurements and do not cover the full time period. ^(*) Events 4–7 and 12–16 include SWICS measurements. ^(●) Means “clean” CIR events, listed in [Jian et al. \(2006\)](#) and [Mason et al. \(2008\)](#). ^(○) Indicates ICMEs or SEPs. ^(*) Marks CIR events that are possibly contaminated by upstream ion events. ^(a) Interacted with ICMEs, suggested by [Jian et al. \(2006\)](#). ^(b) In the ICME list surveyed by [Richardson & Cane \(2010\)](#). ^(c) In the SEP list studied by [Cane et al. \(2010\)](#). ^(d) Analysed by [Mason et al. \(2004\)](#) as ³He-rich SEP events. ^(e) Included in the list of large SEP events, given by [Desai et al. \(2006\)](#). ^(f) Can be found in the SEP list of [Cliver et al. \(2012\)](#). ^(g) In the interplanetary shock event list of [Desai et al. \(2003\)](#). ^(h) Marks CIR events that are possibly contaminated by upstream ion events. There are strong indications of upstream events associated with CIR 09. For the case of CIR 03, however, upstream events are not clear (suggested by A. Klassen, pers. comm.).

to October 2005, when STOF (and especially its MCPs) performed well and the surveyed CIR events had good ion counting statistics. Based on the CIR list from [Jian et al. \(2006\)](#), we selected sixteen particle events for our study, the S/Ns of which are all better than 10. Twelve events are CIR-associated events ([Mason et al. 2008](#)), and 4 are solar energetic particle (SEP) events ([Mason et al. 2004](#); [Desai et al. 2006](#); [Cane et al. 2010](#)). As shown in Table 1, we divided our study into two groups: seven events bounded with reverse shocks, and nine events with a gradual change at the trailing edge. We added ACE/SWICS data for events occurring after May 2000 (indicated with * in Table 1), thus extending the coverage to lower energies. This resulted in energy spectra ranging from the solar wind bulk distribution to suprathermal tails. STOF data for events 1 and 11 (marked with ◊) do not cover the full time period. Out of the 12 CIR events, the 9 without notes are considered as clean events, all of which have the classic CIR structures similar to Fig. 2 (see event numbers with bold font in Table 1). For CIR 3 and 9 (see normal-font event numbers in Table 1), we found hints of upstream ion events following these 2 events (A. Klassen, pers. comm.). Although event 11 was included in the CIR event list of [Mason et al. \(2008\)](#), it was considered as an SEP event by [Cane et al. \(2010\)](#). Here, we treat it as a contaminated event. We have identified complex CIR structures during 4 SEP events in this work, see one example in Fig. 3. We can only determine the boundaries of the compression region but not the stream interface for this event. The variations in the O⁷⁺/O⁶⁺ ratio are not consistent with a stream interface being

present in this “CIR” ([Wimmer-Schweingruber et al. 1997, 1999](#)). Moreover, the mean charge state of iron abruptly jumps from ~10⁺ to ~15⁺ between 16:21 on day 284 and 12:36 on day 285, which indicates an ICME event according to [Lepri et al. \(2001\)](#), [Lepri & Zurbuchen \(2004\)](#), consistent with previous observations ([Jian et al. 2006](#); [Richardson & Cane 2010](#)). Spectral shapes of all events marked with a filled and empty large circle, and a filled small circle in F and F' regions are discussed in detail in the following sections.

3.2. Clean events with reverse shocks

Based on [Fisk & Lee \(1980\)](#), the velocity distribution function or differential flux of suprathermal particles is a function of heliocentric distance between the observer and the shock. We here computed the radial distance from the spacecraft at 1 AU to the location of the reverse shock, according to [Morris et al. \(2001\)](#). The equation for the connection distance is $l = v_f \cdot v_0 \cdot \Delta t / (v_f - v_0)$, where v_f is the local solar wind speed in the F region, v_0 is the solar wind speed just ahead of the reverse shock, and Δt is the time after passing the reverse shock. Figure 4 shows the energy spectrum of the first CIR event in Table 1 in the undisturbed fast-wind region. Because of a data gap, we have no He⁺⁺ data inside this CIR and for the time corresponding to a connection distance out to 4 AU. Following [Bamert et al. \(2002\)](#), we plot fluxes in 12 energy channels (from 32 to 330 keV/nuc), each of which sums over 8 E/q channels of STOF. We show the estimated

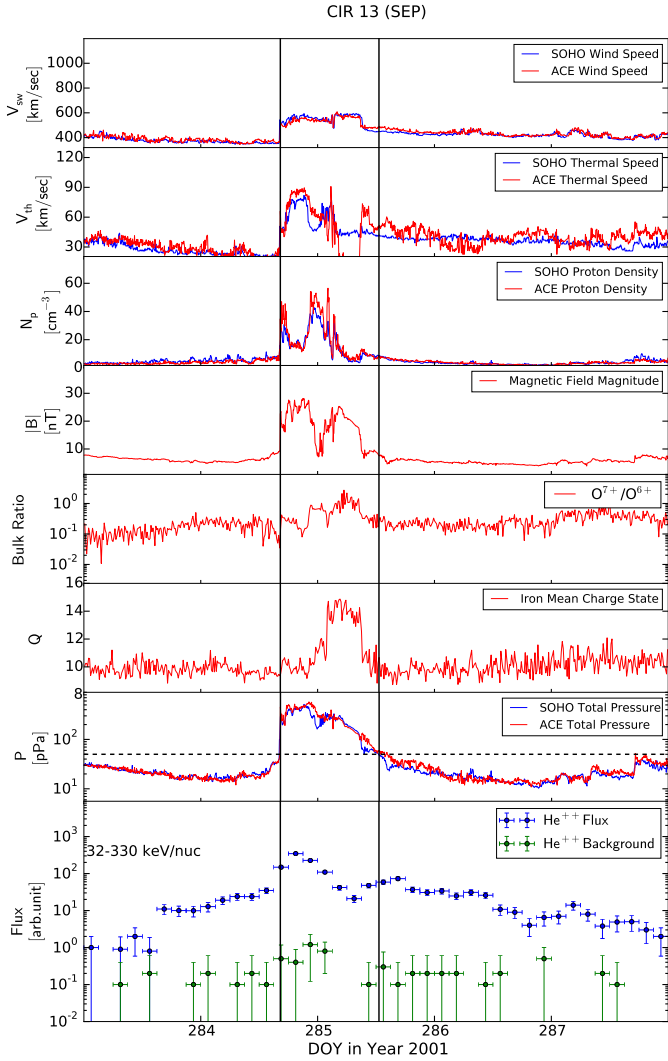


Fig. 3. Same format as Fig. 2, but the event contaminated with an ICME.

one-count level in the plot to evaluate the statistical significance of our measurement. The larger the difference between flux and the one-count level, the more reliable the statistics. Clearly, the spectrum in Fig. 4 is not a power law at low energies, but shows a turnover around ~ 50 keV/nuc.

Figure 5 shows the alpha-particle spectra for the other six shock-bounded events in four subplots each. From left to right, the subplots illustrate the spectral evolution from the F' region to the F region. Considering that the He^{++} flux peaks in the F' region and close to the reverse shock, we defined the data from six hours before the reverse shock as a sample of the F' region. As the compression region moves away, the flux of suprathermal particles decreases with time, and different events have different durations, during which the suprathermal particles satisfy our selection criterion ($S/N > 10$). Because of this decrease, we used progressively longer time intervals to obtain a comparable counting statistics in three plots of the F region. Each event has its own one-count level, which was determined using the relation of the differential flux dJ/dE to count rates,

$$dJ/dE = \frac{c}{g \cdot \Delta E \cdot \Delta t \cdot \eta}, \quad (1)$$

where g is the geometric factor, $\Delta E = q \cdot \Delta E/q$, where $\Delta E/q$ is the E/q passband of the electrostatic analyser, Δt the accumulation time, and η is an unknown efficiency for STOF (it is known

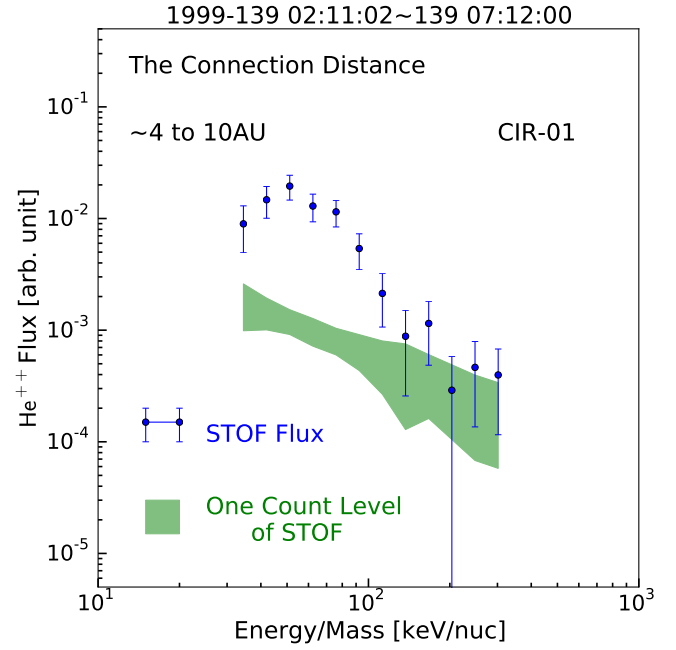


Fig. 4. Energy spectrum after CIR 01 during 02:11 to 07:12 in DOY 139, 1999. One count level is calculated using the flux with an error divided with the raw count in the corresponding energy bin. The connection distance is from the spacecraft to the reverse shock.

for SWICS, however). The one-count level is now determined by the ratio of dJ/dE to the number of measured counts, c . This is unambiguous for SWICS, and requires normalization for STOF to account for the unknown η_{STOF} . This normalization is discussed below. We used the same one-count level, but corrected for differing accumulation times across the full compression region and trailing parts. This assumes that the unknown η_{STOF} does not change appreciably during the event. Referring to the house-keeping data of STOF, the efficiency decrease in MCPs over a few days is negligible, therefore we assumed a constant instrumental efficiency for each individual event. For events 04 to 07, we added the spectra from SWICS shown in red in Fig. 5. A quantitative comparison of the STOF and SWICS fluxes is probably impossible and certainly beyond the scope of this paper, especially because of the unknown absolute efficiencies of the MCPs. In addition, SWICS has a much larger field of view than STOF (partially to accommodate the changing ACE pointing and spin). STOF, being on the three-axis-stabilized SOHO, covers a much smaller solid angle. We lined up the SWICS and STOF data by applying a calibration factor for each event. This calibration factor was determined for the spectra in the F' region (left-hand panels) using the counts in the four overlapping energy bins (between the two vertical lines at 32–44 keV/nuc) and by assuming that the suprathermal particles are isotropic. The same calibration factor was used for the three right-hand panels.

Here, we analyse five clean CIR events of the first event group (top half of Table 1). The spectra shown in the leftmost column of Fig. 5 were all accumulated in the F' region and exhibit $E^{-\gamma}$ or $E^{-\gamma} \cdot \exp(E/E_0)$ suprathermal tails above the solar bulk distribution. This spectral shape can be explained by diffusive shock acceleration, consistent with previous research (Fisk & Lee 1980; Savopulos et al. 1995; Chotoo et al. 2000; Mason et al. 1997). The three right-hand panels show the behaviour in the F region at successively larger distances from the F'-F interface. They are marked by their inferred connection distance to the reverse shock in the upper right corner. CIR 02

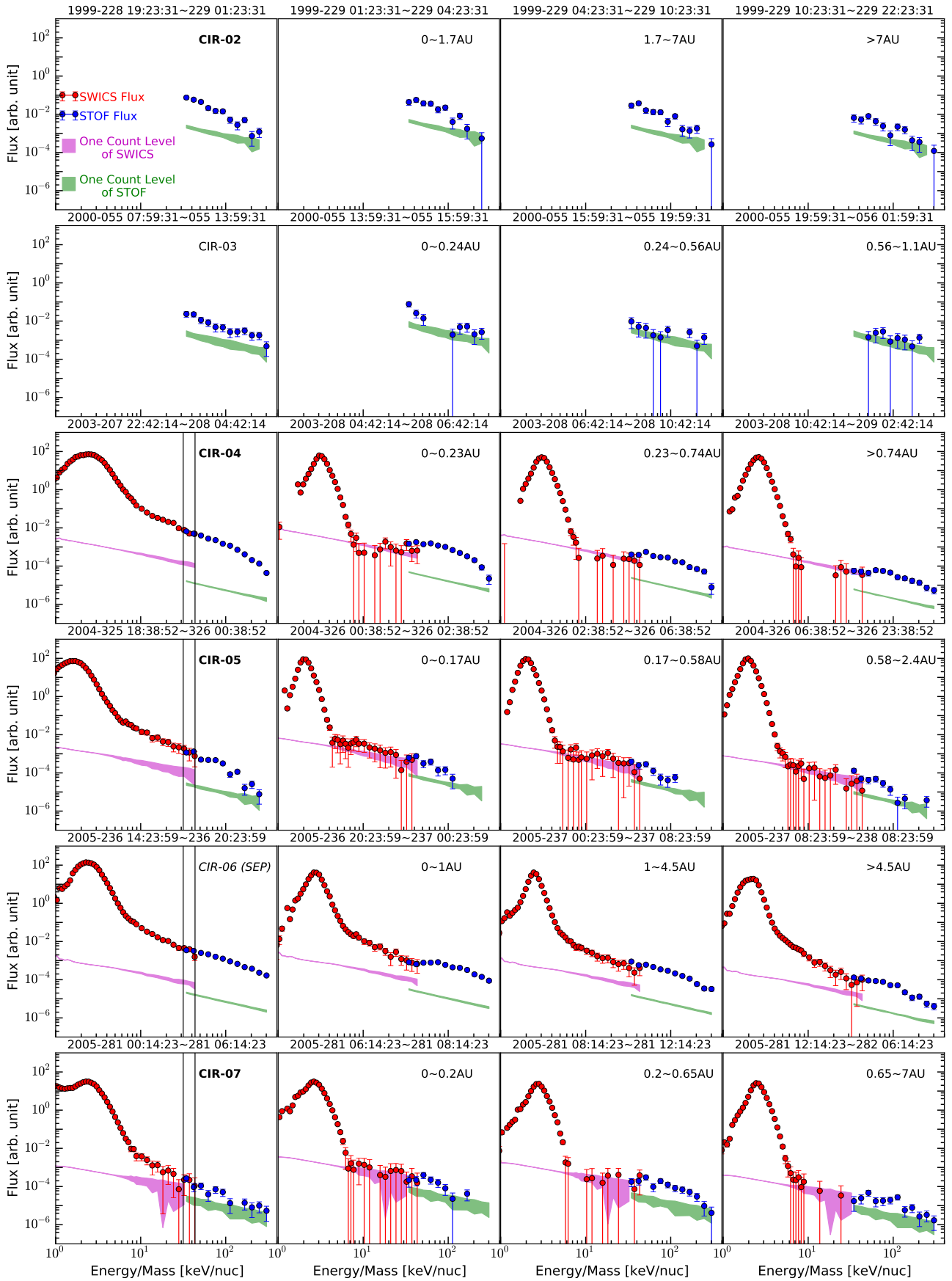


Fig. 5. Two vertical black lines in some plots mark the overlapping energy range between STOF and SWICS. Values within the two lines are used to intercalibrate SWICS and STOF. The *first column of the plots* displays the spectra inside the compression regions with the event number in the upper right corner. The remaining *three columns of the plots* show the spectra in the F regions with the connection distance in the upper right corner.

shows similar spectral shapes in the F region as in F'. Three spectra exhibit power-law tails below around 100 keV/nuc, and bend over above this energy. However, the signature is not very clear in the rightmost plot, possibly because of the statistical fluctuations. In CIR 05, fluxes of suprathermal particles measured by SWICS are only slightly above or at the one-count level. They clearly illustrate continuous power-law spectra from ~5 to ~100 keV/nuc. Below ~100 keV/nuc, STOF measurements of this event are above the one-count level, while beyond ~100 keV/nuc they indicate a possible exponential decay. CIRs 04 and 07 clearly show a turnover. In three plots in the F region of CIR 07, all the STOF spectra show a possible turnover at around 32–44 keV. Although SWICS spectra show some suprathermal particles in the second plot, the fluxes are at the one-count level and the errors of these measurement are large. Between 0.2 and 0.65 AU, only the one SWICS data point at the highest E/q channel is not an upper limit and fits in well with the STOF data. The rightmost panel shows clearer evidence of the turnover. The only two data points from SWICS are only upper limits, indicating a spectral gap in the flux of SWICS and of STOF, which is consistent with the turnover spectral shape from STOF. More apparent turnover spectra were observed in CIR 04, which was reported by Yu et al. (2016). In the second plot (0–0.23 AU), the flux measured by SWICS between solar wind bulk and ~18 keV/nuc is only an upper limit (below the one-count level), and data that are not upper limits only appear in the higher (SWICS) energy range. STOF data show good counting statistics, and therefore the spectrum probably turns over between ~18 and 44 keV/nuc. The turnover behaviour continues in the following two plots. In detail, all the suprathermal particles from SWICS stay in or below the one-count level with large errors in the third plot, which might mean that the turnover shifts to the higher energy range covered by STOF. In the fourth plot we observe a spectral gap in the suprathermal flux from SWICS extending from just above the solar wind bulk out to ~20 keV/nuc; this lasted sixteen hours. On the other hand, the STOF spectrum is nearly flat below ~60 keV/nuc and evolves into a power law at higher energies. In summary, in this first group of five clean CIR events with reverse shocks, we found three CIR events (01, 04, and 07) that indicate turnover spectra in the F regions above solar wind energies to ~40 keV/nuc. Two remaining CIR events (02 and 05) have continuous power-law spectra.

As we show in Fig. 6, we fitted the spectra of CIR 04 with the following theoretical expressions (2) (downstream of the shock) and (3) (upstream of the shock) given by Fisk & Lee (1980), as this event is associated with clear turnover spectra in the fast-wind region,

$$f = \left(\frac{r}{r_s}\right)^{-2/(1-\beta)} v^{-3/(1-\beta)} \exp\left[-\frac{6\kappa_0\beta v}{V(1-\beta)^2} \left(\frac{r}{r_s}\right)^{2/3}\right] \quad (2)$$

$$f = \left(\frac{r}{r_s}\right)^{2\beta/(1-\beta)+V/(\kappa_0 v)} v^{-3/(1-\beta)} \exp\left[-\frac{6\kappa_0\beta v}{V(1-\beta)^2}\right], \quad (3)$$

where f is the velocity distribution function, v is the ion speed, r is the heliocentric distance of the observer, r_s is the heliocentric distance of the reverse shock, V is the solar wind speed, κ_0 is a constant ($\kappa_0 = \kappa/vr$, where κ is the diffusion coefficient), and β is the inverse of compression ratio at the CIR-driven shock.

First, we fit the spectrum (blue dots) in the F' regions with Eq. (2), assuming $r_s = r$. Referring to the approach of Chotoo et al. (2000), we determined the parameters $\beta = 0.251$ and $V = 787 \text{ km s}^{-1}$ directly from measurements of ACE/MAG

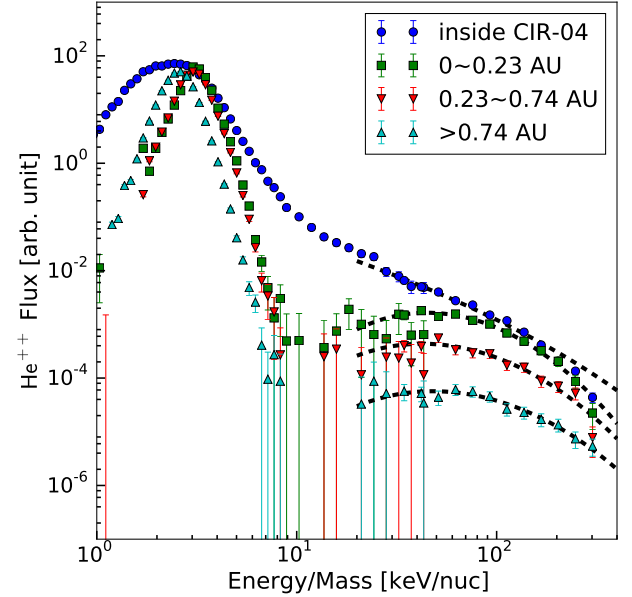


Fig. 6. Energy spectrum of He^{++} in the F' region of CIR 04 is shown with blue dots. The temporal evolution of three spectra in the F region are illustrated with green rectangles and red and cyan triangles. The fitted dashed curves through the observed points are based on the theory of Fisk & Lee (1980). The turnover shape of the spectra is clearly visible in the fast-wind region of CIR 04.

and SOHO/PM. Then we varied κ_0 to fit the observed spectrum and obtained $\kappa_0 = 0.077$. For the CIR event studied by Chotoo et al. (2000), they obtained $\kappa_0 = 0.014$, which is smaller than our result, but in a similar order of magnitude. For the three spectra in the F region, we followed the method of Reames et al. (1997) to fit spectra with Eq. (3). β and r_s were treated as adjustable parameters, and we normalized each spectrum to the observations assuming a fixed κ_0 , as κ_0 is considered as a constant in the theory of Fisk & Lee (1980). For the case of $\kappa_0 = 0.077$, the shock distances r_s are derived to be 10, 6.7, and 7.8 AU, and the parameters β are 0.40, 0.36, and 0.32, respectively, corresponding to observed green rectangles and red and cyan triangles. Apparently, the values of r_s are much higher than those determined with wind speed data. Although β decreases with the connection distance, consistent with the hardening spectra observed by Reames et al. (1997), its values are all lower than those derived at 1 AU, indicating a weaker reverse shock beyond 1 AU. If we increase the value of κ_0 , the above high values of r_s can be accommodated, but the derived β values will also increase, implying a lower compression ratio beyond 1 AU, which is in disagreement with our expectation. Therefore, we suggest that Eq. (3) does not perfectly explain the turnover spectra, and the fitted values of the parameters here should not be taken too literally. Possible reasons for this disagreement are discussed in the next section.

3.3. Clean events without reverse shocks

As mentioned by Jian et al. (2006), only about one third of all CIRs at 1 AU have a reverse shock. Nine of the 16 CIR events in our survey have a weak compression region with a gradual pressure decline at the trailing edges. Because we cannot know where reverse shocks form in these events, we cannot list the connection distances of the CIR events shown in Fig. 7.

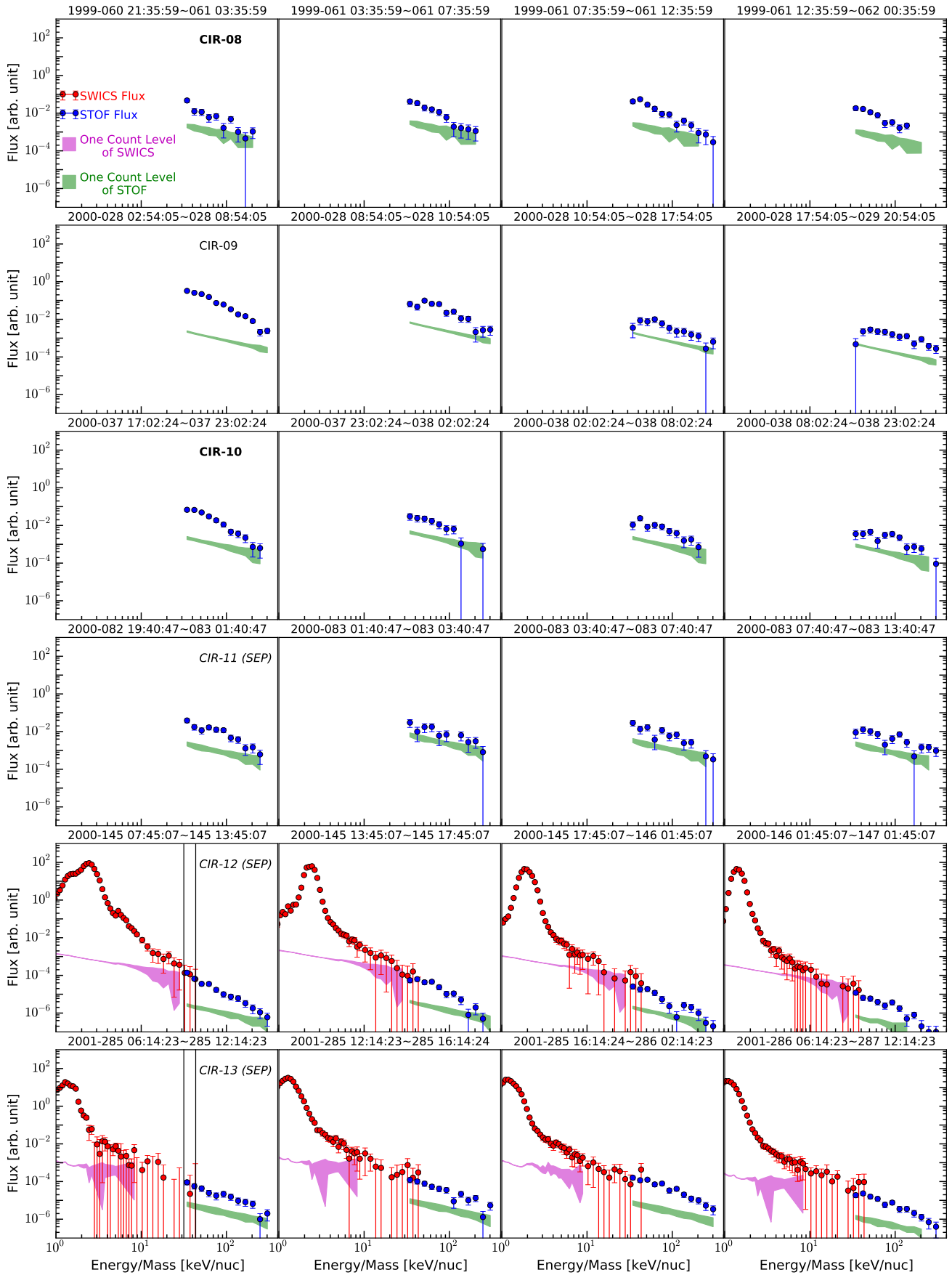


Fig. 7. Same as Fig. 5, but bounded without reverse shocks.

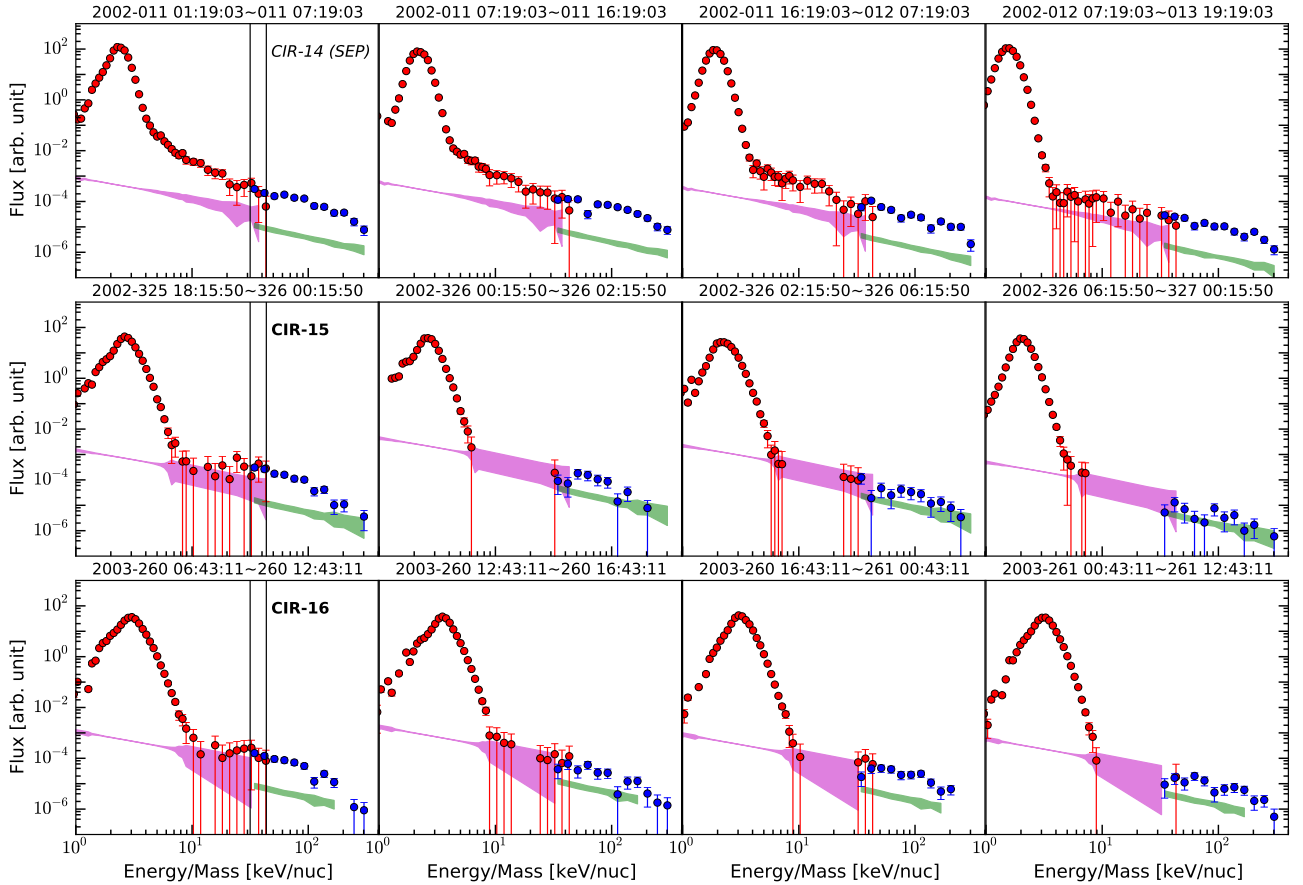


Fig. 7. continued.

Here, we analyse four clean CIR events of the second event group (bottom half of Table 1). In both F' and F regions, CIR 08 exhibits the usual (power-law) spectral behaviour, which is very similar to the events with shocks (CIRs 02 and 05). Although CIR 10 has only STOF measurements, the statistics in the F' region are good enough to show a turnover shape at the range where SWICS and STOF overlap. Similarly, during CIRs 15 and 16, turnover parts appear in the energy range (10–43 keV/nuc) covered by SWICS. In the F region, for the clean CIR 10 event without SWICS data, we note possible turnover spectra. Although unlikely given the shown errors, this may be caused by statistical fluctuations. The cleanest turnover spectrum in this group is shown in the fourth plot of CIR 16 with a flux peak at ~ 50 keV/nuc. Additionally, we note that in the energy range between the bulk solar wind and STOF measurements in CIR 15, only the very high SWICS E/q channels registered counts in the second and third plots. The same phenomenon also occurs in the third and fourth plots of CIR 16. Although these counts were all registered at the one-count level with large error bars, they are only seen at high energies, and no particles were registered at lower energies by SWICS. It appears reasonable to interpret this observation as a manifestation of a turnover spectrum in the higher energy range. As summarized in Table 1, three of four clean CIR events exhibit possible turnover spectra in both F' and F regions, while the remaining one event shows continuous power-law spectra.

3.4. Contaminated events

As observed routinely upstream of the Earth's bow shock, upstream ion events are characterized by a spiky pattern of the

intensity time profile of suprathermal particles (Klassen et al. 2008; Klassen et al. 2009), steep power-law spectra ($J \propto E^{-4}$) (Desai et al. 2008), and large field-aligned sunward anisotropies (Müller-Mellin et al. 2008). They were mainly found to occur after a CIR passed the Earth's magnetosphere (Kronberg et al. 2011). The duration time for each individual event is mostly less than 10 min (Klassen et al. 2008). The intensity time profile of CIRs 03 and 09 hint at upstream ion events, and the spectra exhibit power-law suprathermal tails in F' regions. However, we observed a possible superposition of turnover and power-law spectra in the F region of CIR 03. More specifically, CIR 03 shows a spectral gap in the energy range ~ 70 – 100 keV/nuc in the second plot from the left (see Fig. 5). This may be an indication of a turnover around 100 keV/nuc. Below ~ 70 keV/nuc, three STOF data points might indicate a power-law tail, which could be the contribution of upstream ion events. Not a single count was observed in the lowest energy bins (32–44 keV/nuc) in the last six hours (rightmost panel). In comparison with CIR 03, spectra of CIR 09 are more like a turnover shape. In the lowest eight energy channels the averaged flux is suppressed more and more heavily as we proceed from the second to the fourth plot, so that it finally falls into the one-count level with the ensuing large (upper limit) error bars, which clearly indicates that the spectrum starts to turn over below ~ 40 keV/nuc. Hence, the effect from upstream ion events can probably be neglected during CIR 09.

The spectra of four SEP events (06, 12, 13, and 14) in Figs. 5 and 7 show better counting statistics than the other CIR events. All the spectra of these four events exhibit power-law tails in F' regions, while three of them (events 12–14) remain power-law

spectra in F regions. The suprathermal spectrum in the F region of CIR 06 shows a clear power-law spectrum above solar wind energies up to 40 keV/nuc, together with a slight hump just below ~ 100 keV. As we move away from the CIR, this hump persists. However, the signature is not very clear. Event 11 was closely preceded by an impulsive or ^3He -rich SEP event, and the lowest energy ^3He population might still have been present inside this event. On the other hand, this event itself was considered to be an SEP event (Gopalswamy et al. 2002; Cane et al. 2010). The spectrum in the F' region of Fig. 7 behaves like a power law with a turnover component, similar to the second plots of events 03 and 06. However, there is no hint of spectral turnover in three spectra in the F region, but only continuous power-law tails.

4. Discussion

In our investigation, 6 of 9 clean CIR events show possible signs of a turnover between ~ 10 – 40 keV/nuc, which could be explained by the low-energy threshold of Fisk & Lee (1980). Mason et al. (1997) investigated as many as 17 CIR events, the energy coverage of their observations is from ~ 40 keV/nuc to ~ 6 MeV/nuc, just above the turnover energy range. In the survey by Mason et al. (2008), where 41 CIR events were analysed from 1998 to 2007, the lowest energy of the helium spectra is about 90 keV/nuc, which is also higher than the turnover energy range in this work. Hence, they did not observe turnover spectra.

However, if the Fisk & Lee (1980) mechanism works, why do not all CIR events show turnover spectra? This is probably due to two reasons: (a) low flux resulting in insufficient counting statistics; and (b) this is the consequence of the admixtures of suprathermal particles from different sources, for example, the v^{-5} tail of the Fisk & Gloeckler model (Fisk & Gloeckler 2006, 2007; Fisk et al. 2010), cross-field transport (Baring et al. 1997; Dwyer et al. 1997), upstream ion events, and solar particle events (see in Table 1). As shown in Fig. 2, the flux of suprathermal ions decreases with increasing connection distance, therefore it is difficult to measure the turnover directly because the flux is low, for instance, CIRs 04, 07, 15, and 16. We interpreted the spectral gap as due to the turnover. Additionally, when the flux of remote accelerated particles is low, particles from other sources can become visible in our observations. One of them, the ubiquitous v^{-5} or $E^{-1.5}$ suprathermal tails (Fisk & Gloeckler 2006, 2007; Fisk et al. 2010), may mask the remotely accelerated suprathermal particles and thus also the turnover. This effect is expected to be more pronounced at CIR reverse shocks than at other shocks because the higher bulk and thermal speed of the fast wind leads to a more efficient injection into the acceleration process (Giacalone & Jokipii 1997). An additional source of suprathermal particles may be due to enhanced perpendicular (or cross-field) transport associated with CIRs (Baring et al. 1997; Dwyer et al. 1997). In this case we would not necessarily be sampling particles from the reverse shock connected along an ideal Parker spiral, and thus at the inferred connection distance, but from a much closer reverse shock to which we are only connected by some kind of perpendicular diffusion process that is not understood. Another source of suprathermal particles may come from upstream events and solar particle events. For example, events 03, 06, and 11 exhibit a mixture of turnover and power-law spectra in regions F and F', respectively, while the power-law part might not be of CIR origin.

Although we found several turnover spectra in our investigation, they cannot be well fitted with reliable and physically

meaningful parameters based on the theory of Fisk & Lee (1980). The reason for this disagreement may be the underlying assumption of an isotropic distribution function in the model. In the energy range considered here, this assumption has been shown to be invalid by Ebert et al. (2012). These authors found a large anisotropy in CIR 04. Another possible explanation is that the diffusion coefficient does not necessarily depend linearly on r and v , as commonly assumed. For instance, Savopulos et al. (1995) showed that the expression $\kappa = \kappa_0 v^\alpha r^\epsilon$ results in a better fit to the spectrum. Furthermore, CIRs are three-dimensional structures, and their magnetic structure is much more complex than theoretical assumptions. Another possible effect of the CIR 3D structure is that ACE and SOHO may not be located in the same flux tube, therefore the combination of data from these two spacecraft shows variable spectra. Despite these shortcomings, we have observed the signature expected for the Fisk & Lee model in several CIR events, but a different theoretical or numerical approach may be needed to describe the turnover spectra in detail. Ebert et al. (2012) found that the He ion flows in one CIR, which occurred in 2008 and has only a weak compression region, were predominantly sunward streaming in both regions, downstream and upstream of the CIR trailing edge. This agrees with our observation for those CIR events (10, 15, and 16) with turnover spectra in F' regions, as turnover spectra already indicate that the remote acceleration or sunward particles are dominant. Suprathermal particles observed in the F regions may be attributed to stochastic acceleration in the F' regions beyond 1 AU before the reverse shocks could form. In this case, the Fisk & Lee model becomes invalid, and the model by Giacalone et al. (2002) may be more appropriate. This model considers the non-diffusive magnetic mirroring effect in the region between the compression and the Sun, where trapped ions can be effectively accelerated by scattering between converging scattering centers. Finally, we also point out that neither SWICS nor STOF directly view the sunward-propagating particles, but only those that are again reflected inside 1 AU and return out to ACE or SOHO. This requires sufficient mirroring inside 1 AU and may add to the obscuration of the Fisk & Lee (1980) turnover.

5. Conclusions

We examined energy spectra of alpha particles from the bulk solar wind (~ 1 keV/nuc) to 330 keV/nuc in 16 events observed between 1999 and 2005. A common feature is that the flux of these low-energy suprathermal particles peaks inside the compressed and decelerated fast-wind region, close to the trailing edges. After the spacecraft crosses the trailing boundary of the CIR, suprathermal particles continue to be observed for typically at least half a day. Away from this boundary, the flux of particles accelerated locally at the reverse shock or pressure wave decreases as they would have to diffuse perpendicularly to the local magnetic field to reach the observer. On the other hand, particles that are remotely accelerated at the reverse shock can travel inward more easily along the magnetic field lines. Our analysis of the suprathermal alpha particles shows that CIRs bounded with a reverse shock at 1 AU have power-law spectra (possibly with an exponential rollover) in the compressed fast solar wind (F') region. In the undisturbed fast wind (F), 3 of the 5 clean CIR events bounded by reverse shocks at 1 AU exhibited a possible sign of a turnover in the low suprathermal range, below approximately 40 keV/nuc, which is overall consistent with the basic idea underlying the model of Fisk & Lee (1980). Nevertheless, it was not possible to fit their model to the data with

meaningful parameters, suggesting that other effects need to be taken into account. Three of 4 clean CIR events that were not bounded by reverse shocks at 1 AU showed signs of a turnover in both the compressed fast solar wind (F') region and fast-wind region (F), indicating that the source of these suprathermal particles lies beyond 1 AU.

Acknowledgements. The authors thank all individuals and institutions who made CELIAS and SOHO possible. We thank the anonymous referee for the helpful and constructive comments, which greatly improved the final version of the paper. We also thank A. Klassen for evaluating the effect of upstream ion events for our measurements. This work and L.B. were supported by grants 50 OC 1103 and 50 OC 1501 from the German Space Agency, DLR. J.Y. thanks the DAAD for financial support, R.F.W.S. acknowledges helpful discussions during the ISSI Team meeting “Exploration of the Inner Heliosphere – what we have learned from Helios and what we want to study with Solar Orbiter”.

References

- Balogh, A., Gosling, J., Jokipii, J., Kallenbach, R., & Kunow, H. 2000, in *Corotating interaction regions* (Springer Science & Business Media), 7
- Bamert, K., Wimmer-Schweingruber, R. F., Kallenbach, R., et al. 2002, *J. Geophys. Res.*, **107**, 1130
- Baring, M. G., Ogilvie, W., Ellison, C., & Forsyth, R. J. 1997, *ApJ*, **476**, 889
- Berger, L. 2008, Ph.D. Thesis, Christian-Albrechts-Universität zu Kiel, Germany
- Bučík, R., Mall, U., Korth, A., & Mason, G. M. 2009, *Annales Geophysicae*, **27**, 3677
- Cane, H. V., Richardson, I. G., & von Roseninge, T. T. 2010, *J. Geophys. Res.*, **115**, A08101
- Chotoo, K., Schwadron, N. A., Mason, G. M., et al. 2000, *J. Geophys. Res.*, **105**, 23107
- Cliver, E. W., Ling, A. G., Belov, A., & Yashiro, S. 2012, *ApJ*, **756**, L29
- Desai, M. I., Mason, G. M., Dwyer, J. R., et al. 2003, *ApJ*, **588**, 1149
- Desai, M. I., Mason, G. M., Gold, R. E., et al. 2006, *ApJ*, **649**, 470
- Desai, M. I., Mason, G. M., Müller-Mellin, R., et al. 2008, *J. Geophys. Res.*, **113**, A08103
- Dwyer, J. R., Mason, G. M., Mazur, J. E., et al. 1997, *ApJ*, **490**, L115
- Ebert, R. W., Dayeh, M. A., Desai, M. I., & Mason, G. M. 2012, *ApJ*, **749**, 73
- Fisk, L. A., & Gloeckler, G. 2006, *ApJ*, **640**, L79
- Fisk, L. A., & Gloeckler, G. 2007, *Space Sci. Rev.*, **130**, 153
- Fisk, L. A., & Jokipii, J. R. 1999, *Space Sci. Rev.*, **89**, 115
- Fisk, L. A., & Lee, M. A. 1980, *ApJ*, **237**, 620
- Fisk, L. A., Gloeckler, G., & Schwadron, N. A. 2010, *ApJ*, **720**, 533
- Giactalone, J., & Jokipii, J. R. 1997, *Geophys. Res. Lett.*, **24**, 1723
- Giactalone, J., Jokipii, J. R., & Kóta, J. 2002, *ApJ*, **573**, 845
- Gloeckler, G., Cain, J., Ipavich, F. M., et al. 1998, *Space Sci. Rev.*, **86**, 497
- Gopalswamy, N., Yashiro, S., Michalek, G., et al. 2002, *ApJ*, **572**, L103
- Gosling, J. T., Asbridge, J. R., Bame, S. J., & Feldman, W. C. 1978, *J. Geophys. Res.*, **83**, 1401
- Hilchenbach, M., Hsieh, K. C., Hovestadt, D., et al. 1998, *ApJ*, **503**, 916
- Hilchenbach, M., Grünwaldt, H., Kallenbach, R., et al. 1999, in *AIP Conf. Ser.* 471, eds. S. R. Habbal, R. Esser, J. V. Hollweg, & P. A. Isenberg, 605
- Hilchenbach, M., Sierks, H., Klecker, B., Bamert, K., & Kallenbach, R. 2001, *International Cosmic Ray Conference*, **8**, 3144
- Hovestadt, D., Hilchenbach, M., Bürgi, A., et al. 1995, *Sol. Phys.*, **162**, 441
- Ipavich, F. M., Galvin, A. B., Lasley, S. E., et al. 1998, *J. Geophys. Res.*, **103**, 17205
- Jian, L., Russell, C. T., Luhmann, J. G., & Skoug, R. M. 2006, *Sol. Phys.*, **239**, 337
- Klassen, A., Gómez-Herrero, R., Böhm, E., et al. 2008, *Annales Geophysicae*, **26**, 905
- Klassen, A., Gómez-Herrero, R., Müller-Mellin, R., et al. 2009, *Annales Geophysicae*, **27**, 2077
- Kronberg, E. A., Bučík, R., Haaland, S., et al. 2011, *J. Geophys. Res.*, **116**, A02210
- Lepri, S. T., & Zurbuchen, T. H. 2004, *J. Geophys. Res.*, **109**, A01112
- Lepri, S. T., Zurbuchen, T. H., Fisk, L. A., et al. 2001, *J. Geophys. Res.*, **106**, 29231
- Mason, G. M., Mazur, J. E., Dwyer, J. R., Reames, D. V., & von Roseninge, T. T. 1997, *ApJ*, **486**, L149
- Mason, G. M., Mazur, J. E., Dwyer, J. R., et al. 2004, *ApJ*, **606**, 555
- Mason, G. M., Leske, R. A., Desai, M. I., et al. 2008, *ApJ*, **678**, 1458
- McComas, D. J., Bame, S. J., Barker, P., et al. 1998, *Space Sci. Rev.*, **86**, 563
- Morris, D., Möbius, E., Lee, M. A., et al. 2001, in *Joint SOHO/ACE workshop “Solar and Galactic Composition”*, ed. R. F. Wimmer-Schweingruber, *AIP Conf. Ser.*, **598**, 201
- Müller-Mellin, R., Gomez-Herrero, R., Böttcher, S., et al. 2008, *Int. Cosmic Ray Conf.*, **1**, 371
- Reames, D. V., Ng, C. K., Mason, G. M., et al. 1997, *Geophys. Res. Lett.*, **24**, 2917
- Richardson, I. G., & Cane, H. V. 2010, *Sol. Phys.*, **264**, 189
- Richardson, I. G., Barbier, L. M., Reames, D. V., & von Roseninge, T. T. 1993, *J. Geophys. Res.*, **98**, 13
- Savopulos, M., Quenby, J. J., & Bell, A. R. 1995, *Sol. Phys.*, **157**, 349
- Schwadron, N. A., Fisk, L. A., & Gloeckler, G. 1996, *Geophys. Res. Lett.*, **23**, 2871
- Simnett, G., Kunow, H., Flückiger, E., et al. 1998, *Space Sci. Rev.*, **83**, 215
- Smith, C. W., L’Heureux, J., Ness, N. F., et al. 1998, *Space Sci. Rev.*, **86**, 613
- Wimmer-Schweingruber, R. F., von Steiger, R., & Paerli, R. 1997, *J. Geophys. Res.*, **102**, 17407
- Wimmer-Schweingruber, R. F., von Steiger, R., & Paerli, R. 1999, *J. Geophys. Res.*, **104**, 9933
- Yu, J., Berger, L., Wimmer-Schweingruber, R. F., et al. 2016, *AIP Conf. Proc.*, **1720**

Chapter 6

Verification with PLASTIC

6.1 Introduction

In above two chapters, we report possible turnover spectra associated with CIRs, with combined data from SOHO/STOF and ACE/SWICS. However, these observations have three aspects of limitations:

- Different locations of observers. Although both SOHO and ACE are located at around L1, according to their own orbits the distance between them is large, varying from ~ 40 to $\sim 120 R_{\oplus}$ (R_{\oplus} is the earth radius, around 6371 km). There is no magnetometer (MAG) onboard the SOHO spacecraft, so that we have to extrapolate magnetic field from ACE to SOHO with MAG data of ACE. But the combined measurements of STOF and SWICS may come from different flux tubes. Moreover, SWICS and STOF point at different directions with different FOVs, as introduced in Chapter 5.
- Influence of upstream ion events. Regarding that SOHO and ACE always stay

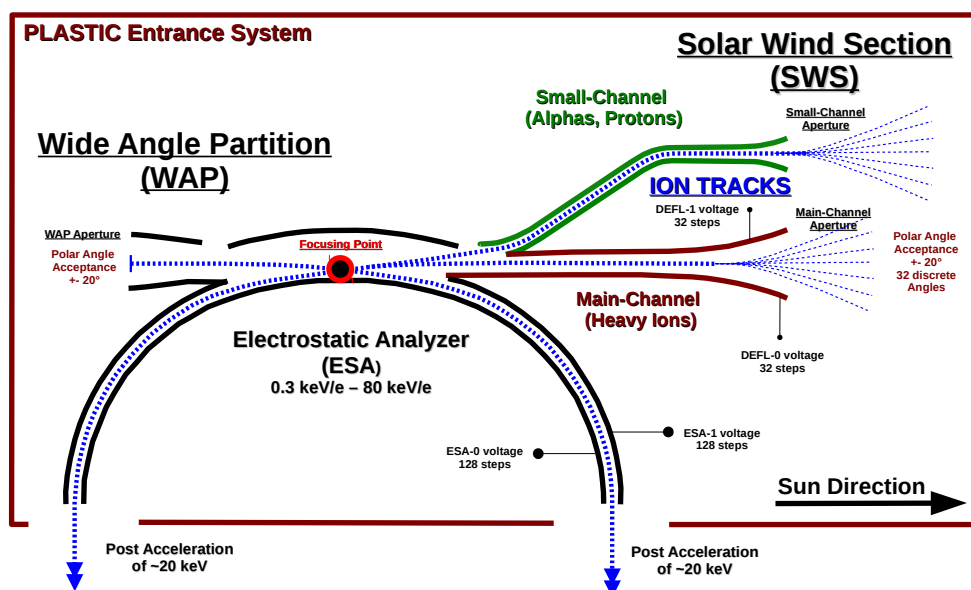


Figure 6.1: Cutaway view of PLASTIC's Entrance System / Electrostatic Analyzer (ESEA), taken from Drews (2013).

at around L1, their CIR measurements can be affected by upstream ion events (Klassen et al., 2008; Desai et al., 2008). When the spacecraft and the Earth's bow shock have a good magnetic connection, accelerated particles by the bow shock can travel along the magnetic field lines and reach the spacecraft. Regarding different locations of SOHO and ACE, the effect of upstream ion events on two observers can be different, depending on the configuration of IMF.

- Counting statistics. The turnover spectra we observed in Chapters 4 and 5 are inferred by spectral gaps between the solar wind bulk and the suprathermal tails. Their counting statistics are not good enough, which increases the uncertainties of our spectral measurements.

Fortunately, we have another option: the Plasma and Suprathermal Ion Composition Instrument (PLASTIC) on the Solar Terrestrial Relations Observatory (STEREO). First of all, PLASTIC is also a TOF mass spectrometer, providing a nominal E/q coverage from 0.3 keV/e to 80 keV/e. For the proton measurements of the follow publication, PLASTIC can cover the solar wind as well as low suprathermal energies. In addition, STEREO is equipped with a magnetometer. Then we do not need to do any extrapolation for the IMF as that in two above publications. STEREO can uniquely determine the boundaries of SIRs and measure spectra in the energy range from the solar wind bulk to the suprathermal tail. Moreover, two STEREO spacecraft, A and B, travel in orbits around the Sun, pulling farther ahead of and falling gradually behind the Earth, respectively. So most of the time, they are far away from the Earth's bow shock, so that the effect of upstream ion events does not need to be taken into account. Finally, with the two-channel design at the Solar Wind Section (SWS) of the entrance system, PLASTIC can provide satisfactory counting statistics for both the solar wind bulk and the suprathermal tail, see Figure 6.1. During operation, PLASTIC can alternate between these two channels (Main-Channel and Small-Channel) autonomously by monitoring the count rate.

6.2 Publication

The attached publication in this chapter has been accepted by the journal *Astronomy & Astrophysics*. Contributions to this paper are given below and my contribution is around 80%.

| Contributions | Authors |
|-----------------------------|-------------------------------------------------------------------|
| Study conception and design | J. Yu, L. Berger, and R.F. Wimmer-Schweingruber |
| Data acquisition | J. Yu, C. Drews |
| Data analysis | J. Yu |
| Data interpretation | J. Yu |
| Drafting of manuscript | J. Yu |
| Critical revision | J. Yu, L. Berger, C. Drew, R.F. Wimmer-Schweingruber, and A. Taut |

Spectral variation of suprathermal protons associated with stream interaction regions: STEREO A/PLASTIC observations

J. Yu, L. Berger, C. Drews, R. Wimmer-Schweingruber, and A. Taut

Institut für Experimentelle und Angewandte Physik (IEAP), Christian-Albrechts-Universität zu Kiel, Leibnizstrasse 11, 24118 Kiel, Germany
e-mail: yu@physik.uni-kiel.de

Received 10 December 2017 / Accepted 23 March 2018

ABSTRACT

Context. The observation of power-law spectra of suprathermal particles is typically associated with the occurrence of stream interaction regions (SIRs), indicating that these particles are accelerated close to the observer. However, recent observations have identified the existence of sunwards streaming particles at low suprathermal energies following SIRs. In addition, the observational evidence for turnover spectra in the low suprathermal energies has also been presented, suggesting that these particles might be accelerated at remote shocks and travel back to the Sun along the interplanetary magnetic field lines.

Aims. We investigate the spectral evolution and variation of suprathermal protons from SIR to SIR as the observer moves from inside the compression regions of SIRs to the outside undisturbed solar wind regions away from the reverse shocks.

Methods. The spectral analysis in the range from solar wind to suprathermal energies was based on proton data, which are obtained by the Plasma and Suprathermal Ion Composition instrument (PLASTIC) on the Solar Terrestrial Relations Observatory mission (STEREO).

Results. All spectra in the compressed fast wind regions (F' regions) of twelve SIRs exhibit power-law suprathermal tails. Six of them show clear turnover spectra at velocities below 2500 km s^{-1} in the undisturbed fast solar wind regions (F regions) following the compression regions, while the remaining six events exhibit continuous power-law spectra. Overall, the spectra at velocities higher than 2500 km s^{-1} harden in the F regions, consistent with previous observations.

Key words. acceleration of particles – shock waves – Sun: heliosphere – Sun: rotation – solar wind

1. Introduction

A stream interaction region (SIR) commonly forms when a stream of fast solar wind runs into a stream of slow solar wind. Due to the high conductivity, the two streams of plasma can not interpenetrate but instead form a compression region around their interface (Gosling et al. 1978). During solar minimum, the fast solar wind originates from solar coronal holes, which are relatively stable. Then SIRs can evolve into a spiral pattern which corotates with the Sun, called corotating interaction regions (CIRs). As two interacting streams of solar wind propagate outwards, the magnetic and plasma pressure continuously increases. The forwards and reverse waves at the leading and trailing edges of the compression region will eventually steepen into forwards and reverse shocks at heliocentric distances greater than about two astronomical units (AU) (Hundhausen & Gosling 1976; Smith & Wolfe 1976; Gosling & Pizzo 1999).

The flux enhancements of tens of keV to several MeV nuc^{-1} energetic particles are often observed to be associated with SIRs (McDonald et al. 1976; Van Hollebeke et al. 1978; Mason et al. 1997; Reames et al. 1997; Chottoo et al. 2000; Mason et al. 2008; Ebert et al. 2012). The long-standing theoretical interpretation for these enhancements is given by Fisk & Lee (1980), who suggest that these energetic particles are accelerated via the diffusive shock acceleration mechanism at the forwards or reverse shock, and then propagate back to the inner heliosphere along the interplanetary magnetic field (IMF). The spectral shape described by the Fisk & Lee (1980) model, a power law multiplied by

an exponential component, has been widely observed (Reames et al. 1997; Chottoo et al. 2000; Mason et al. 1997; Desai et al. 1999; Mason et al. 2008). However, the turnover of spectra at low suprathermal energies also predicted by this model has not been observed, until recently, Yu et al. (2016, 2017) and Zhao et al. (2016) reported turnover spectra of helium in the undisturbed fast wind regions following CIRs at around 40 and 100 keV nuc^{-1} respectively. The observations of Zhao et al. (2016) fit well with their own theoretical model, which is based on the transport equation and calculates the particle differential intensities using a Monte Carlo simulation. Both the Fisk & Lee (1980) model and the Zhao et al. (2016) model assume that particles move only along the IMF and experience no cross-field diffusion. However, three intensive CIR events studied by Dwyer et al. (1997) show that the flow anisotropy of the suprathermal particles at 1 AU is significantly inclined with respect to the local average magnetic field, indicating substantial transport of these particles across the magnetic field. Similar to the diffusive shock acceleration, Giacalone et al. (2002) proposed another mechanism, which considers the non-diffusive magnetic mirroring effect in the region between the compression and the Sun, where trapped ions can be effectively accelerated by scattering between converging scattering centres. Another well-known acceleration mechanism is stochastic acceleration, for example, acceleration through the transit-time damping of magnitude variations of the magnetic field in the CIR compression regions (Schwadron et al. 1996) and the Fisk & Gloeckler (2006, 2007, 2008, 2012a,b, 2014) mechanism, which describes that suprathermal particles are accelerated

Table 1. Stream interaction regions at STEREO/A.

| SIR | Year | Start UT doy mm:hh | IF UT doy mm:hh | End UT doy mm:hh |
|-----|------|-----------------------|--------------------|---------------------|
| 1 | 2007 | 192 03:46 | 192 13:12 | 192 20:22 |
| 2 | 2008 | 68 20:48 | 69 13:13 | 69 19:50 |
| 3 | 2010 | 70 20:23 | 71 00:57 | 71 08:11 |
| 4 | 2010 | 94 01:09 | 94 06:00 | 94 13:20 |
| 5 | 2010 | 303 08:16 | 304 02:52 | 304 10:04 |
| 6 | 2011 | 89 06:30 | 89 15:21 | 90 12:37 |
| 7 | 2011 | 126 22:23 | 127 04:19 | 127 11:32 |
| 8 | 2011 | 362 01:27 | 362 09:36 | 362 20:47 |
| 9 | 2012 | 292 21:23 | 293 03:14 | 293 10:39 |
| 10 | 2013 | 97 15:02 | 97 23:09 | 98 08:41 |
| 11 | 2013 | 136 09:41 | 136 13:40 | 137 00:05 |
| 12 | 2013 | 153 13:09 | 154 03:35 | 154 17:12 |

Notes. The universal time (UT) at the starting, stream interface (IF) and ending of twelve SIRs are listed.

in the compressive and thermally isolated turbulence, producing a power law in particle speed with a spectral index of -5 .

In this work, we have investigated the spectral variation and evolution of H^+ during twelve SIRs, all of which show the typical SIR structure and are bounded by a reverse shock. The SIRs were observed by the Solar Terrestrial Relations Observatory Ahead spacecraft (STEREO A). While the term ‘‘suprathermal energy’’ is ill-defined, for this work, we use the term for particles which appreciably exceed the bulk solar wind speed. This is typically around twice the solar wind speed. The phase space density of suprathermal protons during all these events show power-law tails in the downstream regions of the reverse shocks which are the compressed and decelerated fast wind regions (hereafter F’ regions), consistent with previous observations. After the passage of the reverse shocks, spectra of six events evolve to show a clear signature of a turnover at low suprathermal energies in the upstream regions of the reverse shocks which are the undisturbed fast wind regions (hereafter F regions), while the other six events show continuous power-law spectra. Furthermore, we used spectra in the F region normalized by those in the F’ region to study the spectral evolution, assuming power-law spectra at suprathermal velocities in the F’ region. This approach eliminates any effects of the poorly known instrumental efficiency. We found that the above turnover signature is not due to the instrument efficiency. This work therefore verifies that the case study for turnover spectra during CIRs by Yu et al. (2016), Zhao et al. (2016) is not a unique event, but can often be observed.

2. Instrumentation and event selection

Spectral investigations as well as solar wind parameter measurements presented in this paper are based on the Plasma and Suprathermal Ion Composition (PLASTIC) instrument onboard the STEREO A spacecraft. PLASTIC is a time-of-flight mass spectrometer, providing a nominal energy-per-charge coverage from 0.3 to 80 keV e^{-1} (Galvin et al. 2008). Equipped with a stepped E/q electrostatic analyser, a time-of-flight and solid-state detector system, PLASTIC can determine uniquely the mass, charge, and energy of an incident ion (see details in Galvin et al. 2008). The proton data in the following analysis are collected with the solar wind section (SWS) of PLASTIC, which is centred along the line connecting the Sun and the spacecraft, providing a field of view of 45° in the ecliptic and $\pm 20^\circ$

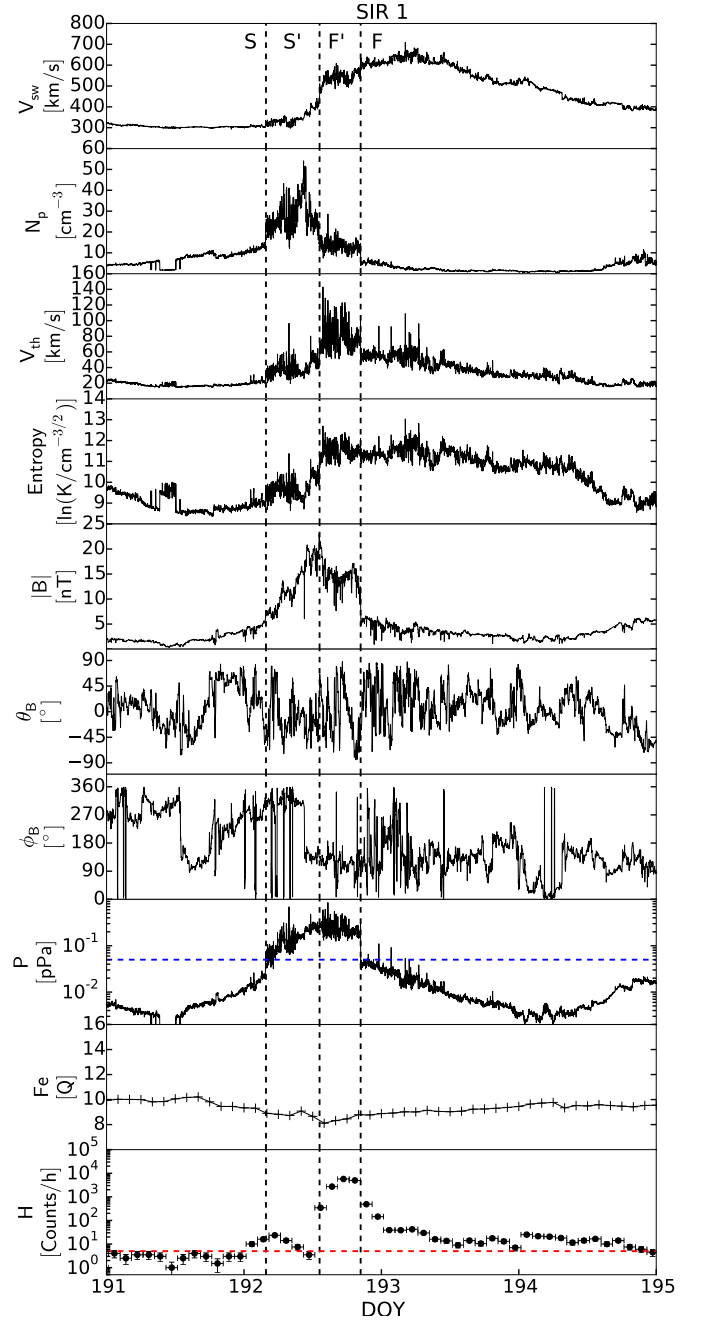


Fig. 1. Time profile of SIR 1 identified by PLASTIC and MAG during the period from DOY 191 to DOY 195, 2007. From top to bottom: 1-min averaged bulk speed of solar wind (V_{sw}), proton density (N_p), thermal speed (V_{th}), specific entropy (derived with N_p and V_{th}), IMF magnitude, IMF polar angle, IMF azimuth angle, total pressure (P derived from $P = n_p v_{th}^2 m + B^2/2\mu_0$), two-hour mean charge state of iron, and count rate of suprathermal protons in the energy range of 10–80 keV. From left to right, we indicate the slow wind, compressed and accelerated slow wind, compressed and decelerated fast wind, and fast wind regions with S, S’, F’, and F respectively, following Richardson et al. (1993), Chotoo et al. (2000). Three vertical black dashed lines indicate the boundaries between these four regions of SIR 1. The horizontal blue and red dashed lines denote 50 pPa and five counts/hour respectively, and are used as thresholds in this work.

in the polar direction towards the Sun. SWS is equipped with two entrance apertures: the main channel and the small channel. During operation, PLASTIC can alternate between these two channels autonomously by monitoring the count rate. This

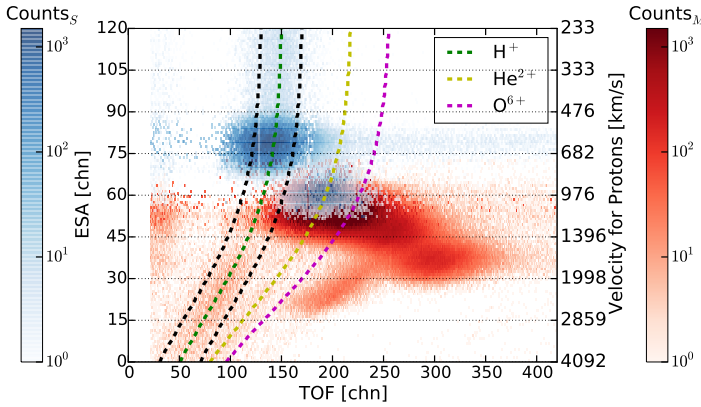


Fig. 2. PLASTIC PHA data measured with the Solar Wind Section accumulated during the three time intervals (the blue, green and cyan coloured regions in Fig. 3) in the F region of SIR 2. All the PHA events are weighted by the base rate (Drews 2013) and shown with blue and red colour for the small (Counts_S) and the main channel (Counts_M) respectively. Measurements of the two channels overlap at around the TOF channels from 150 to 250 and the ESA channels from 52 to 74. The expected positions for H^+ , He^{2+} , and O^{6+} are shown with green, yellow and magenta dashed lines. The proton data extracted for this work is indicated with two black dashed lines while the corresponding proton velocities are given at the right Y axis.

special design allows PLASTIC to measure the bulk solar wind as well as its suprathermal tail with comparable counting statistics, providing us a good opportunity to understand how the source particles inject into the acceleration process and form the suprathermal tail. The measurements of the IMF were performed by the Magnetometer (MAG) of the In-situ Measurements of Particles and CME Transients (IMPACT) suite (Luhmann et al. 2008), which is also onboard the STEREO spacecraft (Kaiser et al. 2008).

All these events in Table 1 are bounded by reverse shocks and exhibit the typical structure of SIRs, as the example shown in Fig. 1. The boundaries between four regions of SIR 1 (S, S', F', and F) are determined with the variations of the specific entropy (Burlaga et al. 1990; Siscoe & Intriligator 1993; Burton et al. 1999; Pagel et al. 2004) and the total pressure (Jian et al. 2006). More specifically, the stream interface is clearly indicated with an abrupt increase in the specific entropy (Burlaga et al. 1990; Siscoe & Intriligator 1993; Burton et al. 1999; Pagel et al. 2004), see the middle vertical dashed line in Fig. 1. We notice that the proton density suddenly decreases as both the bulk and thermal wind speed apparently increase at the interface of SIR 1. These variations of proton density, bulk and thermal velocity also used to be considered as a marker of the stream interface (Burlaga et al. 1990; Siscoe & Intriligator 1993; Burton et al. 1999; Pagel et al. 2004). The boundaries of the SIR compression region, the leading and trailing edges, are determined by the total pressure P (Jian et al. 2006), which is the sum of the plasma and magnetic field pressure. The blue horizontal dashed line in Fig. 1 indicates the 50 pPa threshold suggested by Bućik et al. (2009). Regions above this line can be considered as compressed ones. The mean charge state of iron is used for the event selection to check a possible effect on SIRs from interplanetary coronal mass ejection (ICME) during which the charge state of iron often increases from $\sim 10^+$ to $\sim 15^+$ (Lepri et al. 2001; Lepri & Zurbuchen 2004). The temporal variations of the proton flux in the range of 10–80 keV are shown in the lowest panel of Fig. 1. We clearly see that the count rate of suprathermal protons

peaks inside the F' region, close to the reverse shock, and persists within the leading parts of the fast wind region. This kind of time profile of suprathermal particles was also observed in many other SIR events (Mason et al. 1997; Reames et al. 1997; Chottoo et al. 2000; Bućik et al. 2009; Ebert et al. 2012; Yu et al. 2016, 2017). In this work, we have used pulse height analysis (PHA) data of PLASTIC which provide the most detailed information for each incident ion (Galvin et al. 2008; Drews 2013). The proton data are extracted from a square shape of region on the mass vs. mass-per-charge plot (like Fig. 1 of Yu et al. 2017). The corresponding proton area on the plot of electrostatic analyser channel (ESA) vs. time-of-flight channel (TOF) is indicated with two black dashed lines in Fig. 2. It shows a colour coded intensity map of the number of ions measured at a given ESA step (Y axis) and TOF value (X axis). The blue “counts” are measured by the small channel, the red ones by the main channel. The blue “cloud” around ESA step ~ 75 and $100 < \text{TOF} < 160$ is due to solar wind bulk protons. The blue cloud at ESA channel ~ 60 and $160 < \text{TOF} < 240$ is due to solar wind bulk He^{2+} ions. The red clouds are due to He^{2+} and heavy ions. As shown in this figure, the small channel mainly measure the protons and alpha particles at the solar wind bulk energies while the main channel mostly records heavy ions (bulk as well as suprathermal part) and suprathermal protons. The measurements of the small and the main channel have an overlap at TOF channels between 150 and 250 and ESA channels between 52 and 74, as can be seen by the “blue” He^{2+} . The measurement of the solar wind bulk protons is used as an illustration in this work only. While not all protons fell in this band, we find that we get the best signal to noise with it. The incomplete coverage is compensated by considering it in the instrumental efficiency. For this work, we used mainly the “red” proton counts which correspond to suprathermal protons as can be seen by the Y axis on the right. In addition, we find that the proton data between ~ 45 and ~ 60 ESA channels has a contribution from heavy ions, He^{2+} . However, the contamination of alpha particles does not affect our study of suprathermals at velocities higher than 1400 km s^{-1} . Due to the limited telemetry of PLASTIC, only a sample of PHA events can be transmitted to Earth. Thus, in Fig. 2 we have applied a so-called base rate weighting defined by Drews (2013) to the transmitted PHA data. The proton area defined in this work includes as many suprathermals as possible for good counting statistics, meanwhile, excludes the contamination of alpha particles and instrument background as much as we can.

The criterion of our data selection for this work is: (a) the SIR events exhibit typical structure, for example, well-formed compression regions and clear stream interfaces without ICME influences; (b) the suprathermal proton count rate in the F region exceeds five per hour (the red dashed line in Fig. 1) for at least half a day in order to provide sufficient counting statistics for our spectral analysis; (c) each SIR is bounded by a reverse shock; (d) no contamination of alpha particles at velocities higher than 1400 km s^{-1} . According to the comprehensive statistical survey of SIRs at 1 AU by Jian et al. (2006), the occurrence rate of shocks at SIRs is roughly 24%. Only around 30% of their selected SIRs with shocks have reverse shocks. Our selection criterion is therefore strict, and rejects most SIR events. The reason for that is the instrumental detection efficiency has not been well identified so far. Therefore, we need to choose a reference, power-law spectra in the compression region of SIRs, for our spectral study in the undisturbed fast wind regions associated with SIRs. Given that power-law spectra are often observed in association with interplanetary shocks (McDonald et al. 1976; Van Hollebeke et al. 1978; Reames et al. 1997; Chottoo et al.

2000; Mason et al. 1997; Desai et al. 1999; Mason et al. 2008), we only choose the SIRs bounded with reverse shocks for this work.

3. Observations

Figures 3 and 4 display the SIR events listed in Table 1. Each subfigure contains three panels with the corresponding event number in the upper right corner, showing the measurements of the bulk speed of the solar wind, the specific entropy and four H⁺ spectra. The stream interface is indicated with the black dashed line in each plot. The vertical red region in the upper two panels of each event denotes a two-hour time interval immediately downstream of the reverse shock, that is, two hours before the passage of the shock. The other three coloured regions (blue, green, and cyan) represent three time intervals upstream of the reverse shock. The reverse shock (RS) is right between the red and the blue regions and is indicated by a black triangle. The durations of three time intervals in the F regions are not the same for all SIRs. Because the count rate of suprathermal protons decreases with time after the spacecraft crosses the reverse shock (as Fig. 1 shows), we use larger and larger time intervals in the undisturbed fast wind region, in order to obtain comparable counting statistics. The lowest panel of each subfigure presents the measurements of phase space density for protons, plotted as a function of v_{ion} , where v_{ion} is the ion speed in the spacecraft frame. Four spectra are marked with the colours corresponding to the four coloured time intervals in the upper two panels. We aim to illustrate the spectral variation and evolution from the downstream to upstream of the reverse shock. The phase space density of H⁺ is shown in arbitrary units. We used the same correction to convert from counts to phase space density for all panels in Figs. 2 and 3. We did not correct for instrumental detection efficiency which decreases on time scales of years. This means that the spectra in each panel can be compared with each other. However, the absolute values should not be compared among different SIRs. In addition, at velocities roughly between the solar wind and the suprathermal tail, large variations and deviations can be seen. These are due to the contribution of He²⁺ and the base rate weighting for the measurements obtained around the channel switch between of the two entrance apertures of PLASTIC's SWS, respectively.

Throughout all the SIR events in Figs. 3 and 4, we find some common features. First of all, at the location of the reverse shock a jump of the solar wind velocity is apparent. At the stream interfaces of SIRs, which are marked with black dashed lines, the specific entropy clearly shows an abrupt increase from below 10 to ~ 12 [$\ln(\text{K cm}^{-3/2})$]. The values of the specific entropy remain stable through the F' and the F regions, except for SIRs 5, 7, 9, and 11, in which the entropy exhibits a slight decrease at the shock, but is still higher than that prior to the stream interface. For the spectra downstream of the reverse shocks, we always select data in the two hours just before the shock. Given that all the dashed lines lie to the left of the red bars, we can be assured that all the spectra in the F' regions of this work are purely of fast wind origin. More common characteristics can be found in the spectral measurements. In the solar wind energies, PLASTIC observed a Maxwellian distribution of spectra in all SIR events. At suprathermal energies, we clearly see that all the SIR events exhibit power-law tails in the F' regions, when the ion speed is higher than around 1500 km s⁻¹. Only the spectrum of SIR 8 has a possible rollover at higher velocities (v_{ion}

> 2500 km s⁻¹). The power-law tails presented here are consistent with the classic theoretical models (Fisk & Lee 1980; Jones & Ellison 1991) and previous observations (Mason et al. 1997; Desai et al. 1999; Reames et al. 1997; Chottoo et al. 2000; Mason et al. 2004, 2008).

The focus of this study is to investigate spectral variations of suprathermal tails in the F regions, which differ from SIR to SIR. Spectra of SIRs 1 and 4 show good counting statistics and contain continuous power-law suprathermal tails in the F regions.

In comparison, spectral measurements of SIRs 5, 6, 9, and 10 show large errorbars in some v_{ion} channels (particularly in high v_{ion} channels), which indicates that only few counts were recorded. Although all the spectra of these four SIRs look like power-law shapes at suprathermal velocities, this could be due to statistical effects. Because if all the v_{ion} channels have one count, the index of spectra will be fixed at -4 (Ipavich 1974). Very interesting shapes of suprathermal tails can be seen in SIRs 2, 3, 7, 8, 11, and 12. Three spectra of SIR 2 in the F region exhibit apparent turnovers in the low suprathermal range, around 1500 to 2500 km s⁻¹. The PHA data during these three time intervals in the F region of SIR 2 are also shown in Fig. 2 where we clearly see that the turnovers are neither affected by the channel switch nor the contamination of He²⁺. The same spectral variations are visible in SIRs 7 and 8, although less clearly for the first time period in the F region. SIR 3 shows a power-law tail during the first two hours after passing the reverse shock, however, the turnover shapes at low suprathermal velocities again show up during the two following periods. In SIR 11, two and six hours averaged spectra after the reverse shock show almost the same power law index, while the six-hour averaged spectrum lies slightly lower than the two-hour averaged one. However, in the third stage of the F region, the low suprathermal part of the spectrum eventually evolves into a turnover below roughly 2000 km s⁻¹. In the case of SIR 12, spectra behave very similarly to those of SIR 11.

In summary, in the F' regions of twelve SIRs we have found that power-law shapes of spectra are a common feature. However, the spectra in the F regions do not always have a power-law shape. A spectral turnover in the low suprathermal velocity range (<2500 km s⁻¹) exists in six events.

4. Discussion

Power-law suprathermal tails are often found to be associated with interplanetary shocks, independent of whether the shocks are driven by solar flares (Mazur et al. 1992), coronal mass ejections (CMEs; Mewaldt et al. 2005; Tylka & Lee 2006), or CIRs (Mason et al. 1997; Reames et al. 1997; Desai et al. 1999; Chottoo et al. 2000; Mason et al. 2008; Yu et al. 2016, 2017). These power-law tails are typically believed to be the result of diffusive shock acceleration or first-order Fermi acceleration (Fermi 1949). In addition, a break or rollover of spectra at a few to a few tens of MeV nuc⁻¹ is always observed (Li et al. 2009). Because the energy coverage of PLASTIC is far below the range of the spectral break or rollover, we only measure the power-law part of suprathermal spectra in this work. For the CIR study, Reames et al. (1997) have found that the spectra in the F region of a CIR event in May of 1995 harden with time in the energy range from 40 keV nuc⁻¹ to around 1 MeV nuc⁻¹. The hardening spectra of suprathermal helium with time were also recently observed in the energy range of 0.137–0.193 MeV nuc⁻¹ by Ebert et al. (2012). With the data from the Wind spacecraft at around

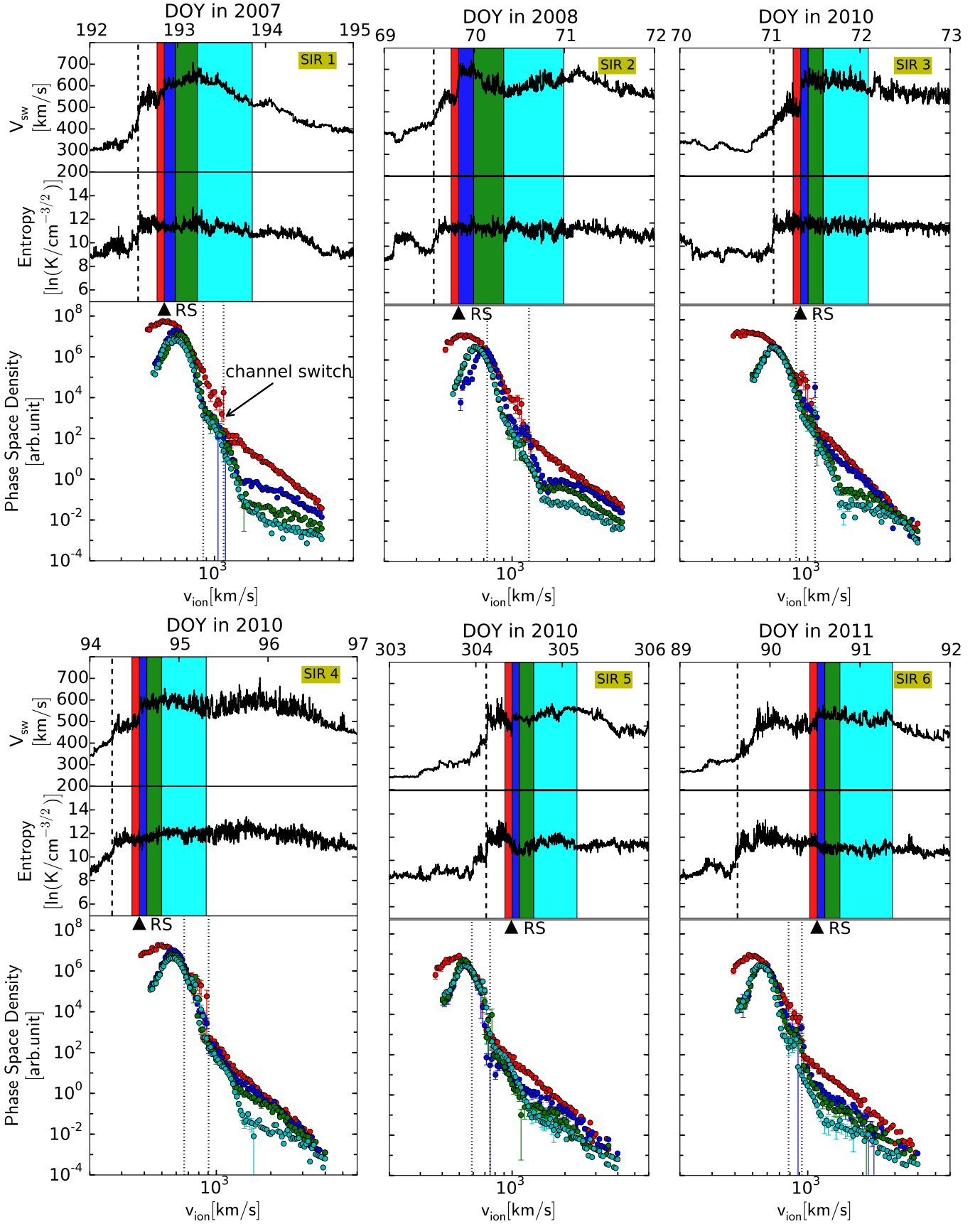


Fig. 3. Spectral evolution of INDIVIDUAL SIR events. Spectral evolution of each SIR event is given from the downstream to upstream of the reverse shock, with the event number in the upper right corner. In each plot, a vertical black dashed line indicates the stream interface while two vertical dotted lines show a range where the channel switch happened during this event. The time interval marked with red colour denotes the downstream, followed by three time intervals with blue, green, and cyan colours inside the upstream region. Four spectra are shown with the same colours as their corresponding time intervals.

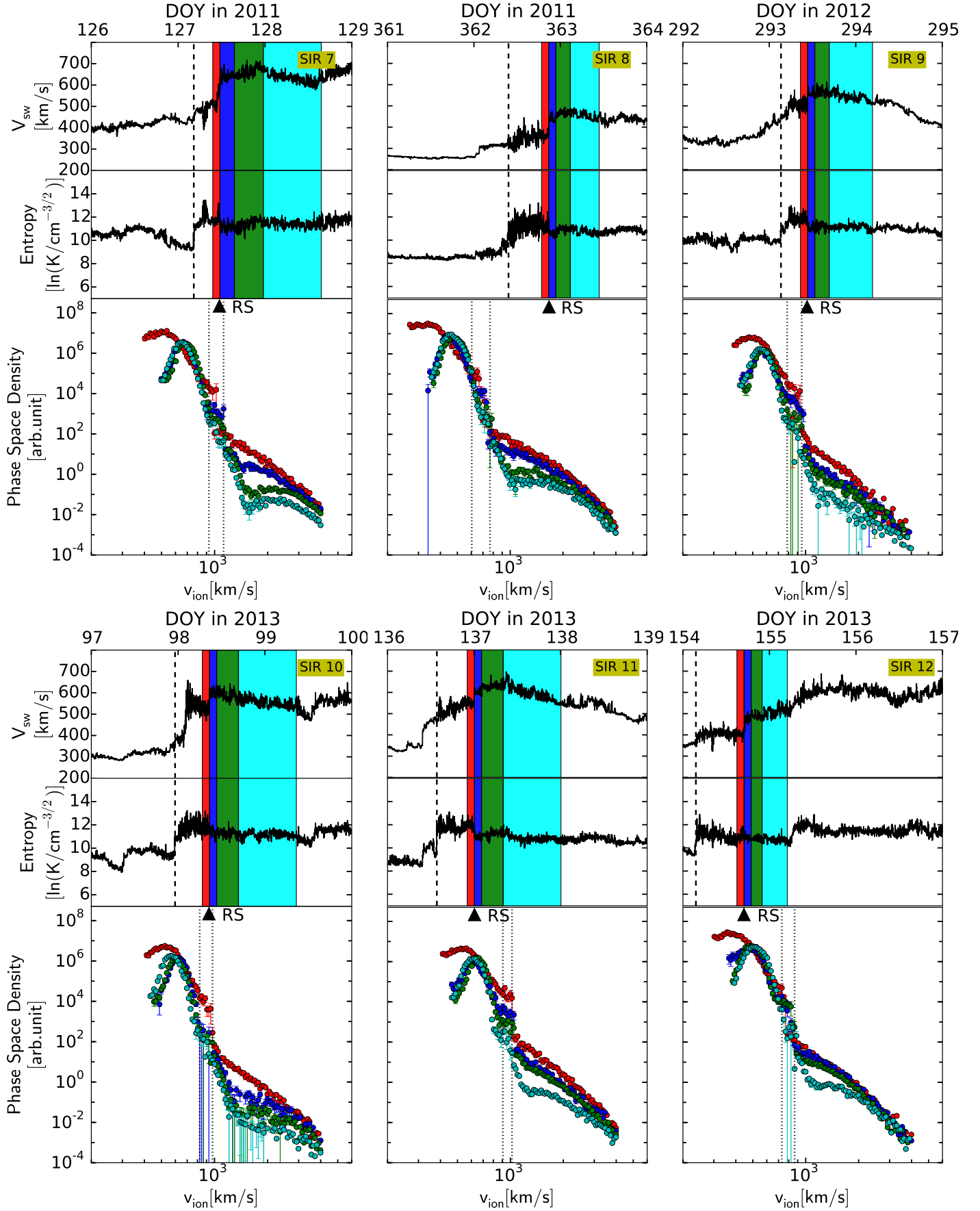


Fig. 4. Spectral evolution of further SIR events. Same format as Fig. 3.

1 1 AU, Ebert et al. (2012) have identified anti-sunwards flows of
 2 suprathermal helium in the compression downstream of a CIR-
 3 driven reverse shock, which transitioned to sunwards flows after
 4 passing the shock. These observations suggest that the shock is a
 5 local source for suprathermal particles in CIR events, which lie
 6 inside 1 AU prior to the shock arrival and beyond 1 AU after its
 7 passage.

8 The phase space density of suprathermal protons $f(v_{\text{ion}})$ in
 9 this work is derived as

$$f(v_{\text{ion}}) = \frac{C(v_{\text{ion}})}{V^P(v_{\text{ion}})V^S(v_{\text{ion}})\eta(v_{\text{ion}})}, \quad (1)$$

10 where $C(v_{\text{ion}})$ is the measured counts, $V^P(v_{\text{ion}})$ is the differential
 11 volume in velocity space, $V^S(v_{\text{ion}})$ is the differential volume in
 12 position space, and $\eta(v_{\text{ion}})$ is the instrument efficiency, referring
 13 to Drews (2013). Except for $\eta(v_{\text{ion}})$, all the other items can be
 14 derived with PLASTIC's measurements. For the power-law tails
 15 at velocities higher than 2500 km s^{-1} shown in Figs. 3 and 4,
 16 it is difficult to determine the absolute values of their spectral
 17 indices due to the poorly known instrument efficiency, $\eta(v_{\text{ion}})$,
 18 which is a function of v_{ion} . In order to eliminate the effect of
 19 instrumental efficiency on the spectral shape, we only focus on
 20 the variations of the relative ratios of the phase space density
 21 from the F region to the F' region, that is, we discuss only the
 22 three normalized spectra in the F region (with the spectrum
 23 measured in the F' region) for each SIR event. Based on the
 24 observations discussed above, we would expect to see a power-
 25 law spectrum in the F' regions with a spectral index γ_{down} . The
 26 phase space density, $f_{\text{down}}(v_{\text{ion}})$, in F' can then be written as

$$f_{\text{down}}(v_{\text{ion}}) = \frac{f'_{\text{down}}(v_{\text{ion}})}{\eta(v_{\text{ion}})} \propto v_{\text{ion}}^{-\gamma_{\text{down}}}, \quad (2)$$

27 where $f'_{\text{down}}(v_{\text{ion}})$ is the uncorrected phase space density in the F'
 28 region as shown in Figs. 3 and 4. Similarly, if the spectra in the
 29 F region upstream of the shock are also power-law shapes,

$$f_{\text{up}}(v_{\text{ion}}) = \frac{f'_{\text{up}}(v_{\text{ion}})}{\eta(v_{\text{ion}})} \propto v_{\text{ion}}^{-\gamma_{\text{up}}}, \quad (3)$$

30 where γ_{up} is the spectral index in the F region and $f'_{\text{up}}(v_{\text{ion}})$ is
 31 uncorrected $f_{\text{up}}(v_{\text{ion}})$. Then the ratio of the phase space densities
 32 in the F to the F' region should also exhibit the power-law
 33 shape with the index $\kappa = \gamma_{\text{up}} - \gamma_{\text{down}}$. The instrumental efficiency
 34 $\eta(v_{\text{ion}})$ cancels out in this normalization process,

$$\frac{f_{\text{up}}(v_{\text{ion}})}{f_{\text{down}}(v_{\text{ion}})} = \frac{f'_{\text{up}}(v_{\text{ion}})}{f'_{\text{down}}(v_{\text{ion}})} \propto v_{\text{ion}}^{-(\gamma_{\text{up}} - \gamma_{\text{down}})} = v_{\text{ion}}^{-\kappa}, \quad (4)$$

35 Figure 5 shows the fitting results of three normalized spectra
 36 of each SIR event in the F regions at $v_{\text{ion}} > 2500 \text{ km s}^{-1}$. The
 37 maximum likelihood estimations (Mattox et al. 1996) of κ are
 38 shown with squares and triangles in the upper and lower panels
 39 respectively. Events in the upper panel are those showing contin-
 40 uous power-law tails in the F regions, while events in the lower
 41 panel evolve into a spectral turnover at $v_{\text{ion}} < 2500 \text{ km s}^{-1}$. The
 42 errorbars are estimated by adding Poisson noise to the measured
 43 data. In the F regions of the upper panel we observed decreas-
 44 ing κ with time in SIRs 1, 4, 6, and 9 except for those of SIRs
 45 5 and 10. With $\kappa = \gamma_{\text{up}} - \gamma_{\text{down}}$ decreasing with time, we see
 46 that γ_{up} must decrease with time or increasing distance from
 47 the reverse shock because γ_{down} is fixed in the F' region. This
 48 indicates a hardening of the spectrum as the observer moves

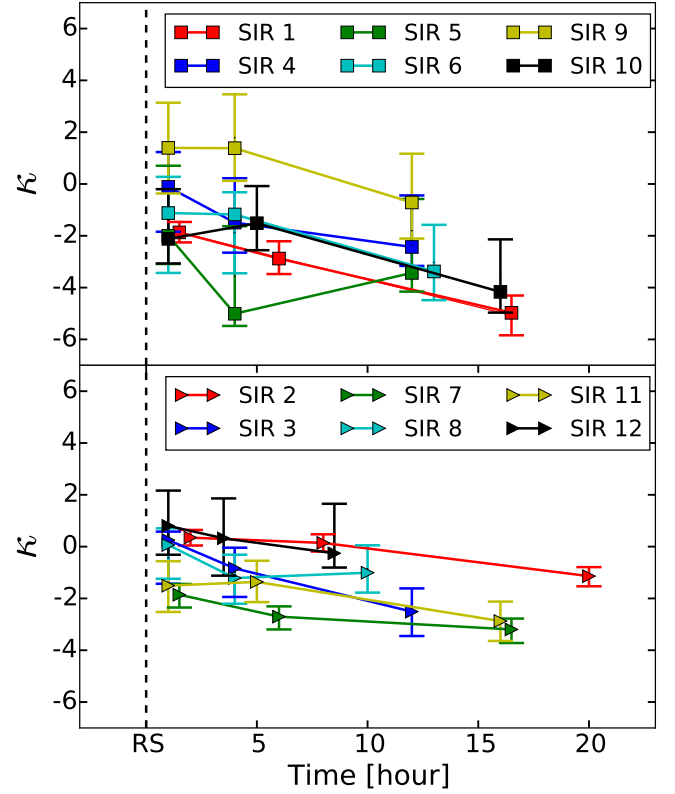


Fig. 5. Temporal variations of κ of normalized spectra in the F regions at velocities higher than 2500 km s^{-1} . The upper panel shows the SIR events that exhibit continuous power laws in both F and F' regions in Figs. 3 and 4, while the other events with turnover spectra at velocities lower than 2500 km s^{-1} are given in the lower panel.

away from the reverse shock, which is consistent with previous
 observations (Reames et al. 1997; Ebert et al. 2012). SIR
 5 exhibits slightly harder suprathermal tail in the second time
 interval than that in the first and third intervals of the F regions.
 SIR 10 has a softer spectrum in the second time interval com-
 pared with that in the other two periods. However, considering
 the error estimation of SIR 10, the spectra might also contin-
 uously harden with time. Similar results can also be seen in the
 lower panel, where SIRs 2, 3, 7, and 12 exhibit hardening spec-
 tra. Especially the counting statistics of SIRs 2 and 7 are good
 enough to show this behaviour. The index variation of SIR 8 is
 similar to that of SIR 5, while the case in SIR 11 is similar to that
 in SIR 10. In short, we observe a overall trend (eight in twelve
 SIRs) of the spectral hardening in the F regions. This trend is
 consistent with previous observations of Reames et al. (1997),
 Ebert et al. (2012) with Wind data and extends their work to a
 lower velocity range down to 2500 km s^{-1} . The hardening spec-
 tra as we move away from the shock is probably indicative of the
 increasing importance of transport effects as the shock is rotated
 further away from the observer. Compared with high-energy
 suprathermal particles, low-energy suprathermal particles suffer
 from more scattering on the sunwards propagating path before
 they reach the observer at 1 AU. In addition, the hardening spec-
 tra in the F regions can be due to the strengthening reverse shock
 with heliocentric distance according to the (Fisk & Lee 1980)
 model.

In Fig. 6, we show two normalized spectra as examples. In
 order to guide the eyes, we extrapolate the power laws down to
 1500 km s^{-1} . We can clearly see that all the normalized spectra

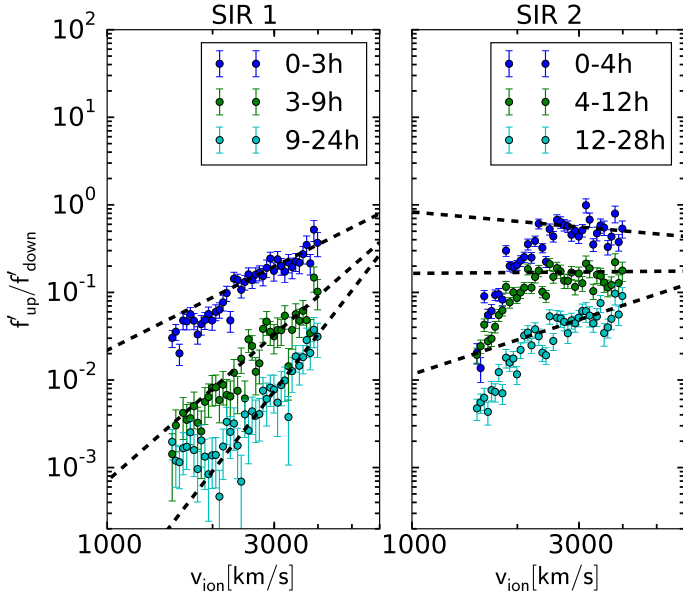


Fig. 6. Ratio of phase space density, $f'_{\text{up}}/f'_{\text{down}}$, during SIRs 1 and 2.

of SIR 1 in Fig. 6 have positive exponents, which means harder spectra in the F regions compared with those in the F' regions. The low-velocity parts ($v_{\text{ion}} < 2500 \text{ km s}^{-1}$) of the spectra during the first and second period of SIR 1 are around or slightly below the extended lines. But the overall shapes are more like power laws. The spectrum in the third time interval of SIR 1 lies around the dashed power-law line at $v_{\text{ion}} > 2000 \text{ km s}^{-1}$. At lower velocities, the relative ratios lie above the expected power-law line, which could be the effect of the solar wind bulk (see Fig. 3). There are more suprathermal particles in the downstream regions, F', than in the upstream regions. Therefore, suprathermals impinge more into the bulk solar wind velocity range in F' than in F. Thus the ratio of the two at low speeds is most affected by the bulk solar wind in those F regions where the flux of suprathermals is lowest. In comparison, the three spectra of SIR 2 have a common characteristic. Below 2500 km s^{-1} , spectra start to turnover towards low velocities, which indicates that the spectra of this event in the F region are not purely of power laws shapes. Similar turnover shapes are also found in SIRs 3, 7, 8, 11, and 12, all of which have already shown the low-velocity turnover in the uncorrected phase space density (see Figs. 3 and 4). Although not all the spectra of SIRs 3, 7, 8, 11, and 12 in the F regions exhibit a turnover like those of SIR 2, they all finally evolve into shapes with turnover. For the other six SIR events, we do not find any hint of turnover spectra. But the turnover feature may be hidden due to the low counting statistics, for example, in SIRs 5, 6, 9, and 10. We note that all the turnover parts of the spectra occur at higher velocities than those affected by the channel switch and He^{2+} . Therefore, we have verified that turnover spectra in the F regions are not an instrumental effect, but due to a real physical process.

5. Conclusions

In this paper, we investigate the spectral variation and evolution at very low energies, just above the solar wind during twelve SIR events, which are all bounded by reverse shocks. Two important spectral characters have been identified. The suprathermal tails have an overall tendency to harden with time in the F

regions, consistent with previous observations. The superior counting rates resulting from PLASTIC's large geometry factor have allowed us to fully cover the solar velocity distribution functions in SIRs from the solar wind bulk all the way up to strongly suprathermal velocities exceeding several multiples of the solar wind speed. This includes the velocity range where the transition from bulk to suprathermal (in the sense of non-thermal) takes place. This observation provides further evidence that protons at 1 AU can be accelerated to suprathermal velocities at the SIR-driven reverse shocks. The hardening spectra can be explained by two processes. On one hand, the reverse shock gets stronger as it moves out into the heliosphere. This should result in harder spectra. On the other hand, the observer is magnetically linked to the shock which is moving further away from him. Therefore transport effects will become increasingly important. One would expect particles with the lowest energy to be most affected. The second observation is that the suprathermal tails are not always power laws in the F regions of SIRs, but half of the events exhibit turnover shapes at low suprathermal velocities. However, in contrast with combined observation from two spacecraft of Yu et al. (2016, 2017), PLASTIC can uniquely provide measurements for the spectral turnover together with much better counting statistics. The origin of the spectral turnover is still unknown. Although the theoretical model by Fisk & Lee (1980) predicts a spectral turnover in the F region, this model is only valid at high energies, where the particle velocity is much higher than the bulk speed of solar wind. Finally, we also point out that the SWS field of view is always towards the Sun, which means it can not directly view the particles scattered back towards the Sun by reverse shocks in the F regions but only those mirrored inside 1 AU to reach it.

Acknowledgements. LB and RFWS acknowledge support by grants 50OC1103 and 50OC1501 from the German Space Agency (DLR). RFWS thanks ISSI for its hospitality and its teams "Exploration of the inner heliosphere" and "Radiation interactions at planetary bodies". JY thanks DAAD for financial support.

References

- Burlaga, L. F., Mish, W. H., & Whang, Y. C. 1990, *J. Geophys. Res.*, **95**, 4247
Burton, M. E., Neugebauer, M., Crooker, N. U., von Steiger, R., & Smith, E. J. 1999, *J. Geophys. Res.*, **104**, 9925
Bučík, R., Mall, U., Korth, A., & Mason, G. M. 2009, *Ann. Geophys.*, **27**, 3677
Chotoo, K., Schwadron, N. A., Mason, G. M., et al. 2000, *J. Geophys. Res.*, **105**, 23107
Desai, M. I., Marsden, R. G., Sanderson, T. R., et al. 1999, *J. Geophys. Res.*, **104**, 6705
Drews, C. 2013, PhD thesis, Christian-Albrechts-Universitaet zu Kiel
Dwyer, J. R., Mason, G. M., Mazur, J. E., et al. 1997, *ApJ*, **490**, L115
Ebert, R. W., Dayeh, M. A., Desai, M. I., & Mason, G. M. 2012, *ApJ*, **749**, 73
Fermi, E. 1949, *Phys. Rev.*, **75**, 1169
Fisk, L. A., & Gloeckler, G. 2006, *ApJ*, **640**, L79
Fisk, L. A., & Gloeckler, G. 2007, *Space Sci. Rev.*, **130**, 153
Fisk, L. A., & Gloeckler, G. 2008, *ApJ*, **686**, 1466
Fisk, L. A., & Gloeckler, G. 2012a, in *American Institute of Physics Conference Series*, eds. J. Heerikhuisen, G. Li, N. Pogorelov, & G. Zank, **1436**, 116
Fisk, L. A., & Gloeckler, G. 2012b, *Space Sci. Rev.*, **173**, 433
Fisk, L. A., & Gloeckler, G. 2014, *J. Geophys. Res. (Space Physics)*, **119**, 8733
Fisk, L. A., & Lee, M. A. 1980, *ApJ*, **237**, 620
Galvin, A. B., Kistler, L. M., Popecki, M. A., et al. 2008, *Space Sci. Rev.*, **136**, 437
Giacalone, J., Jokipii, J. R., & Kóta, J. 2002, *ApJ*, **573**, 845
Gosling, J. T., & Pizzo, V. J. 1999, *Space Sci. Rev.*, **89**, 21
Gosling, J. T., Asbridge, J. R., Bame, S. J., & Feldman, W. C. 1978, *J. Geophys. Res.*, **83**, 1401
Hundhausen, A. J., & Gosling, J. T. 1976, *J. Geophys. Res.*, **81**, 1436
Ipavich, F. M. 1974, *Geophys. Res. Lett.*, **1**, 149
Jian, L., Russell, C. T., Luhmann, J. G., & Skoug, R. M. 2006, *Sol. Phys.*, **239**, 337
Jones, F. C., & Ellison, D. C. 1991, *Space Sci. Rev.*, **58**, 259

- 1 Kaiser, M. L., Kucera, T. A., Davila, J. M., et al. 2008, *Space Sci. Rev.*, **136**, 5
- 2 Lepri, S. T., & Zurbuchen, T. H. 2004, *J. Geophys. Res. (Space Physics)*, **109**,
3 [A01112](#)
- 4 Lepri, S. T., Zurbuchen, T. H., Fisk, L. A., et al. 2001, *J. Geophys. Res.*, **106**,
5 [29231](#)
- 6 Li, G., Zank, G. P., Verkhoglyadova, O., et al. 2009, *ApJ*, **702**, 998
- 7 Luhmann, J. G., Curtis, D. W., Schroeder, P., et al. 2008, *Space Sci. Rev.*, **136**,
8 [117](#)
- 9 Mason, G. M., Mazur, J. E., Dwyer, J. R., Reames, D. V., & von Rosenvinge T. T.
10 1997, *ApJ*, **486**, [L149](#)
- 11 Mason, G. M., Mazur, J. E., Dwyer, J. R., et al. 2004, *ApJ*, **606**, 555
- 12 Mason, G. M., Leske, R. A., Desai, M. I., et al. 2008, *ApJ*, **678**, 1458
- 13 Mattox, J. R., Bertsch, D. L., Chiang, J., et al. 1996, *ApJ*, **461**, 396
- 14 Mazur, J. E., Mason, G. M., Klecker, B., & McGuire, R. E. 1992, *ApJ*, **401**, 398
- 15 McDonald, F. B., Teegarden, B. J., Trainor, J. H., von Rosenvinge, T. T., &
16 Webber, W. R. 1976, *ApJ*, **203**, [L149](#)
- 17 Mewaldt, R. A., Cohen, C. M. S., Labrador, A. W., et al. 2005, *J. Geophys. Res.*
18 *(Space Physics)*, **110**, [A09S18](#)
- 19 Pagel, A. C., Crooker, N. U., Zurbuchen, T. H., & Gosling, J. T. 2004, *J. Geophys.*
20 *Res. (Space Physics)*, **109**, [A01113](#)
- 21 Reames, D. V., Ng, C. K., Mason, G. M., et al. 1997, *Geophys. Res. Lett.*, **24**,
22 [2917](#)
- 23 Richardson, I. G., Barbier, L. M., Reames, D. V., & von Rosenvinge T. T. 1993,
24 *J. Geophys. Res.*, **98**, 13
- 25 Schwadron, N. A., Fisk, L. A., & Gloeckler, G. 1996, *Geophys. Res. Lett.*, **23**,
26 [2871](#)
- 27 Siscoe, G., & Intriligator, D. 1993, *Geophys. Res. Lett.*, **20**, 2267
- 28 Smith, E. J., & Wolfe, J. H. 1976, *Geophys. Res. Lett.*, **3**, 137
- 29 Tylka, A. J., & Lee, M. A. 2006, *ApJ*, **646**, 1319
- 30 Van Hollebeke, M. A. I., McDonald, F. B., Trainor, J. H., & von Rosenvinge T. T.
31 1978, *J. Geophys. Res.*, **83**, 4723
- 32 Yu, J., Berger, L., Wimmer-Schweingruber, R. F., et al. 2016, *AIP Conf. Proc.*,
33 [1720](#)
- 34 Yu, J., Berger, L., Wimmer-Schweingruber, R., et al. 2017, *A&A*, **599**, A13
- 35 Zhao, L., Li, G., Ebert, R. W., et al. 2016, *J. Geophys. Res. (Space Physics)*, **121**,
36 [77](#)

Chapter 7

Conclusions and Outlook

This thesis contains two aspects: instrument and science. The first part is about the background analysis for SOHO/STOF, including how the background is generated and how to estimate the background level of measurements. Using the housekeeping data of STOF, we have found that the UV flux is well related to the count rate of START and STOP triggers of MCPs. We infer that there might be a possible leakage of photons at the entrance, because STOF faces only 7° west of the Sun-SOHO axis. In this case, energetic penetrating particles can be more easily recorded by this instrument than originally expected. In addition, we present an approach to estimate the background of STOF, which is used for the event selection in the science aspect of this thesis. Another benefit of the first part of work is that it can guide us to predict the background of the Suprathermal Electron and Proton (STEP) instrument onboard the Solar Orbiter spacecraft, as both STOF and STEP measure suprathermal particles and suffer from a background created by energetic penetrating particles. More details of the background analysis for STEP is given in the following Appendix A.

The science part of this thesis is described in three publications. In the first one (Yu et al., 2016), we analyze the CIR event which occurred between July 26 and 27 of 2003 and has been widely studied by Jian et al. (2006); Mason et al. (2008); Ebert et al. (2012). Note that these previous observations did not provide charge state information, e.g., He^{++} of solar origin and He^+ of interplanetary origin can both contribute to the measurements of the helium spectra. With data from SOHO/STOF and ACE/SWICS, we have found that suprathermal He^{++} mainly appear inside the compressed fast wind (F') region of this event with the intensity peak close to the trailing edge. The spectrum in the F' region exhibits a power-law suprathermal tail, while three spectra in the fast wind (F) region show power-law tails but with a clear turnover at low suprathermal energies (below ~ 40 keV/nuc). Additionally, we have observed a substantial increase in the $\text{He}^+/\text{He}^{++}$ ratio with time from the F' region to the F region. These observations indicate that the suprathermal alpha particles during this event are mainly locally accelerated in the F' region, while in the F region the observed suprathermal particles are accelerated by the reverse shock beyond 1 AU and travel back to the inner heliosphere along the IMF .

In our second publication (Yu et al., 2017), we performed a statistical study of the spectral evolution from the F' to the F regions of sixteen CIRs. We have identified that six clean CIRs show possible signs of a turnover between ~ 10 -40 keV/nuc in the F regions, while three of them even exhibit this spectral behavior in the F' regions. However, the turnover spectra can not be well fitted with the Fisk and Lee (1980) model. The possible reasons for that have been discussed, e.g., the effect of SEP and

upstream ion events, the cross-field diffusion, and the magnetic mirroring effect between the compression and the Sun. On the other hand, the Fisk and Lee (1980) theory itself assumes that the ion speed is much higher than the bulk speed of solar wind. The suprathermal energies covered by the spectral turnover are too low to satisfy this assumption.

The motivation of our third publication is an independent verification of the former two publications, as both of them report possible turnover spectra associated with CIRs, which have not been observed previously. We need to point out that the turnover spectra are based on combined measurements from two different instrument at two different locations. With data from the SWS of STEREO A/PLASTIC, we clearly observe turnover spectra at low suprathermal energies (below ~ 32 keV/nuc) during six of twelve SIR events. In this work, we exclude the effect of the poorly unknown PLASTIC efficiency on the spectral shapes by using relative ratios of phase space density from the F to the F' regions. We show that the turnover spectra are real and can be often observed. Moreover, the suprathermal tails at high suprathermal energies are found to overall harden from the F' to the F regions, consistent with previous observations (Reames et al., 1997; Ebert et al., 2012) at higher energies.

Although the turnover spectra in the third publication indicate suprathermal particles are not locally accelerated, there is no hint of the source location of these particles. Do they come from cross-field diffusion from the compression regions at around 1 AU according to Dwyer et al. (1997), or from upstream of the SIR-driven reverse shocks beyond 1 AU? Inspired by Ebert et al. (2012), we recently investigated the temporal variations of anisotropy for suprathermal ions measured by STEREO/SEPT (Solar Electron and Proton Telescope) during these 12 events at high suprathermal energies (101-110 keV). The method to calculate anisotropy is based on Dresing et al. (2014) and additionally considers the Compton-Getting effect (Ipavich, 1974; Gieseler, 2008), see results in Figure 7.1. For the most of 12 SIRs (except for SIRs 1, 5, and 10), we identified that the flows of the suprathermal ions transitioned from anti-sunward to sunward within one hour prior to and after the spacecraft crossed the reverse shocks, which is consistent with the result reported by Ebert et al. (2012). These observations provide us with compelling evidence that the spectral turnover observed by STEREO/PLASTIC at suprathermal energies can be the contribution of the shock acceleration beyond 1 AU.

In addition, it should be pointed out that none of above STOF, SWICS, and PLASTIC's SWS directly view the sunward propagating particles, but only those which are again reflected inside 1 AU and return out to the observers, which is not considered in the Fisk and Lee (1980) theory. Then, the reflection at the inner heliosphere will be an attractive topic for the coming future. We plan to use the wide angle partition (WAP in Figure 6.1) of PLASTIC as well as SEPT to learn about the properties of the sunward suprathermal particles during SIRs. We expect that the spectral comparison between sunward and anti-sunward particles will show us some interesting results which may even result in a brand new theory to extend the Fisk and Lee (1980) model.

As discussed in Chapter 2, the turnover spectra cannot be quantitatively explained by the Fisk and Lee (1980) theory because the turnover part was observed at low suprathermal energies at 1 AU but the theory is only valid at higher energies. In addition, turnover spectra observed in this work are for the anti-sunward particles, not for the sunward particles described by the Fisk and Lee (1980) mechanism. Both the problems above can be solved by Solar Orbiter mission: as shown in Figure 2.3, the spectral turnover at low suprathermal energies shifts to high energies with the decreasing ratio of heliocentric radial distance of observer to the CIR-driven shock (r/r_s). We define that the turnover

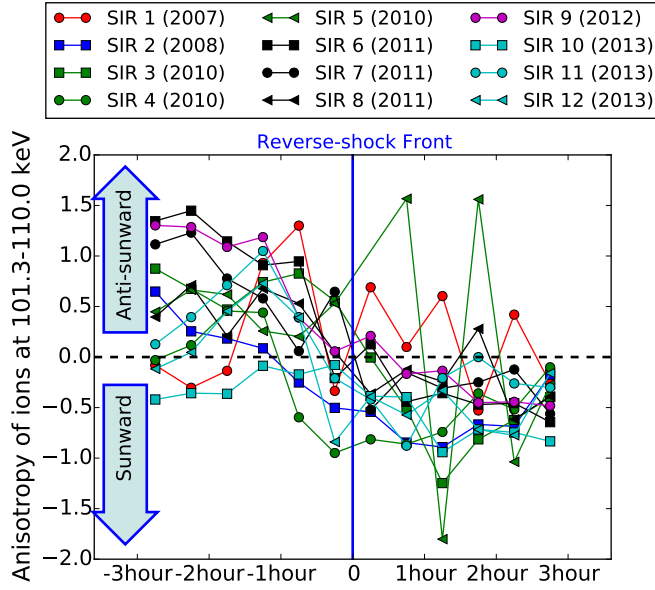


Figure 7.1: Anisotropy measurements for 12 SIR events in the third publication using STEREO/SEPT data.

staying at the velocity where

$$\frac{df}{dv} = 0 \quad (7.1)$$

According to Equation 2.6, the turnover location (v_{to}) can be derived as follows:

$$v_{to} = \frac{-\frac{3}{1-\beta} + \sqrt{\left(\frac{3}{1-\beta}\right)^2 - 4 \cdot \frac{6\kappa_0\beta}{V(1-\beta)^2} \cdot \ln\left(\frac{r}{r_s}\right) \cdot \frac{V}{\kappa_0}}}{2 \cdot \frac{6\kappa_0\beta}{V(1-\beta)^2}} \quad (7.2)$$

If the CIR-driven shocks form at 2-3 AU as introduced in Chapter 2, r/r_s will be 0.93-0.14 at 0.28 AU where Solar Orbiter will reach. Here, we consider $\beta = \frac{1}{3}$ and $\frac{V}{\kappa_0} = 2$ (MeV/nuc) $^{1/2}$, the values used in the Fisk and Lee (1980) paper. Then the corresponding v_{to} will shift to the range of 0.66-0.76 (MeV/nuc) $^{1/2}$. At the same time, the corotating speed $\Omega_{\odot}r$ in the Fisk and Lee (1980) theory is proportional to r , which means the corotating speed at 0.28 AU will be only 28% of that at 1 AU, i.e., around 0.0086 (MeV/nuc) $^{1/2}$. Thus, the assumption $v \gg \Omega_{\odot}r$ of the Fisk and Lee (1980) theory will be easily satisfied at the inner heliosphere. For the measurement of sunward particles, we can use two instruments (Electron and Proton Telescope (EPT) and High-Energy Telescope (HET)) onboard Solar Orbiter which both have a FOV approximately along the Parker spiral magnetic field away from the Sun. The energy coverage of EPT-HET is from 20 keV to hundreds of MeV, see details in Appendix A. Therefore, Solar Orbiter provides an ideal opportunity to quantitatively verify the Fisk and Lee (1980) theory at the inner heliosphere.

We also plan for the future a study of the shock acceleration of pickup ions. Pickup ions were observed to undergo more efficient acceleration in disturbed solar wind, especially during the solar events with shocks (Bamert et al., 2002; Bamert et al., 2004; Kucharek et al., 2003). The enhanced abundance ratios of $\text{He}^+/\text{He}^{++}$ reported in Chapter 4 are consistent with previous observations. To explain the preferential acceleration

of pickup ions, many theories have been proposed such as the shock surfing mechanism (Lee et al., 1996; Zank, 1999; Zank et al., 1996) and multiple reflections at shock front (Scholer and Kucharek, 1999). All these theoretical models commonly assume a shell distribution of pickup in velocity space, which was shown to be unrealistic at 1 AU by Drews (2013). The “ring beam” distribution of pickup ions reported by Drews (2013) opens another door to explain the preferential acceleration of these particles. The angular distribution of suprathermal particles measured by the SWS and WAP sections of PLASTIC may give us information about the injection process of their preferential acceleration.

Appendix A

The Solar Orbiter Mission

Solar Orbiter, an ESA M-class space mission, is planned to launch in 2020 to explore the Sun in unprecedented detail. It aims to make significant breakthroughs in our understanding both of how the inner heliosphere works, and of the effects of solar activity on it. The spacecraft will take a unique instrument combination of both in-situ and remote measurements, approaching the Sun as close as 0.28 AU. Specifically, in-situ measurements will be used alongside remote sensing close to the Sun to relate these measurements back to their source regions and structures on the solar surface. Solar Orbiter will operate both in and out of the ecliptic plane, in order to answer the following interrelated scientific questions:

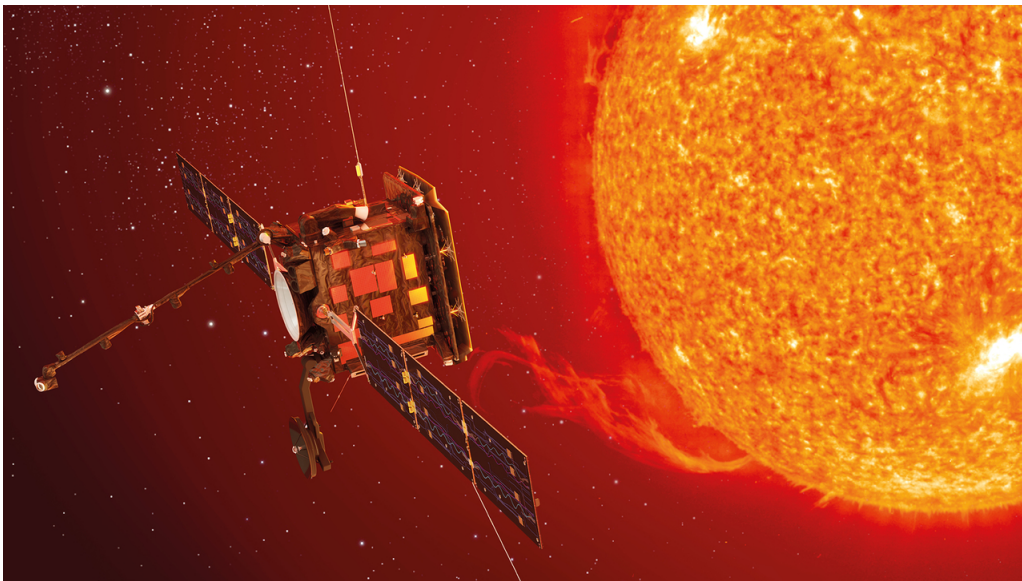


Figure A.1: Artist's illustration of ESA's Solar Orbiter observing the Sun. (Taken from: <http://sci.esa.int/solar-orbiter/>)

- How and where do the solar wind plasma and magnetic field originate in the corona?
- How do solar transients drive heliospheric variability?
- How do solar eruptions produce energetic particle radiation that fills the heliosphere?

- How does the solar dynamo work and drive connections between the Sun and the heliosphere?

To answer these outstanding fundamental questions, in-situ measurements of the solar wind plasma, fields, waves, and energetic particles are essentially made as close as possible to the Sun, so that they are still relatively pristine and their properties have not been modified by subsequent transport and propagation processes. Assisted by simultaneous, high-resolution imaging and spectroscopic observations, these in-situ measurements can be further related back to their source regions and structures on the Sun.

Solar Orbiter is a three-axis stabilized spacecraft, pointing at the Sun. It carries a dedicated heat shield to protect its scientific payload from the high levels of solar flux near the perihelion. Several feed-throughs in the heat shield are available for the remote-sensing instruments to view the Sun. The nominal communication with the ground station is provided by an articulated high-temperature and high-gain antenna, with a medium gain antenna and two low gain antenna as backup. There are in total four in-situ and six remote-sensing instruments onboard Solar Orbiter, and we briefly introduce these instruments below, see Figure A.2.

In-situ Sensing Instruments

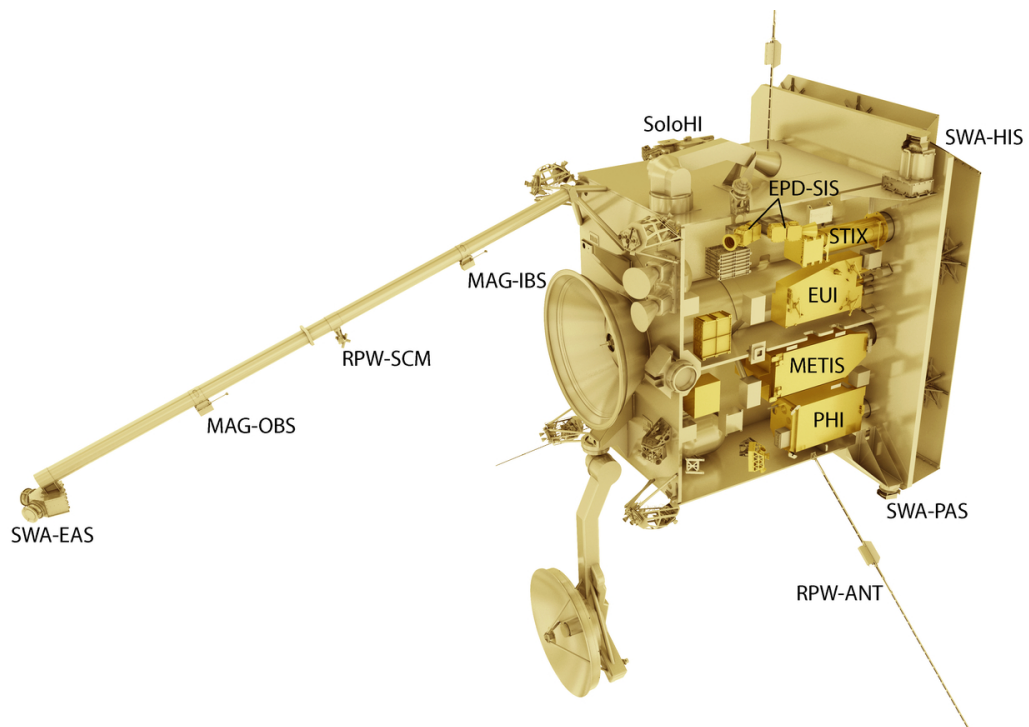


Figure A.2: Payload accommodation onboard the Solar Orbiter spacecraft. The figure is taken from <http://sci.esa.int/solar-orbiter/55772-solar-orbiter-launch-moved-to-2018/>.

- **Energetic Particle Detector (EPD)** consists of four particle detectors which are designed to measure the composition, timing and distribution functions of suprathermal and energetic particles. STEP is one of the four sensors of EPD. More details of EPD are described in the following section.

- **Solar Wind Analyzer (SWA)** contains three sensors and a common data processing unit (DPU). It aims to probe the solar wind between 0.28-1.4 AU in order to establish the fundamental physical links between the solar atmosphere and the solar wind in both quiet and disturbed states. SWA will measure three-dimensional velocity distributions of the major constituents of the solar wind plasma (e.g., protons, alpha particles, electrons and heavy ions).
- **Radio and Plasma Waves (RPW)** comprises three monopole antennas which form a plane perpendicular to the Sun-spacecraft axis. RPW will measure magnetic and electric fields including the concerning waves in the solar wind with a high time resolution from almost DC to 20 MHz, in order to characterize the electromagnetic and electrostatic waves. In addition, this instrument can be remotely controlled to detect solar radio emissions.
- **Magnetometer (MAG)** will utilize two digital fluxgate sensors operated in the dual-magnetometer mode to provide in-situ measurements of the heliospheric magnetic field with high precision. This instrument will help us understand the way the solar magnetic field links into space and evolves over the solar cycle; how heliospheric structures develop in the inner solar system.

Remote Sensing Instruments

- **Extreme Ultraviolet Imager (EUI)** will use two High Resolution Imagers (HRI) working at Lyman- α and 174 Å EUV passbands and one dual band Full Sun Imager (FSI) at 174 and 304 Å. It will take pictures of the solar atmospheric layers above the photosphere in order to study the link between the solar surface and outer corona. Moreover, EUI will also provide the first-ever UV images of the Sun from out of the ecliptic.
- **Multi Element Telescope for Imaging and Spectroscopy (METIS)** will provide images of the solar corona in three different wavelength bands with a single telescope. The visible, ultraviolet and extreme ultraviolet emission of the solar corona will be diagnosed with unprecedented temporal coverage and spatial resolution to study the structure and dynamics of the full corona.
- **Polarimetric and Helioseismic Imager (PHI)** will carry out measurements with a High Resolution Telescope (HRT) imaging a fraction of the solar disk and a Full Disk Telescope (FDT) observing the solar disk. The information of vector magnetic field and the line-of-sight (LOS) velocity of the photosphere will be collected to examine the solar convection zone. At the same time, the continuum intensity in the visible wavelength range will be measured.
- **Solar Orbiter Heliospheric Imager (SoloHI)** will measure the visible sunlight scattered by solar wind electrons and thus images the quasi-steady flow and transient disturbances. With SoloHI's measurements, the SEP acceleration processes, the evolution of solar events (e.g., CMEs and CIRs) in the inner heliosphere and the origin of solar wind will be investigated in detail.
- **Spectral Imaging of the Coronal Environment (SPICE)** will employ a single element off-axis parabolic telescope and a toroidal variable line spaced grating spectrograph, in order to perform extreme ultraviolet imaging spectroscopy to

remotely determine the plasma properties at the Sun and its vicinity. Its main scientific objective is to identify correlations between solar wind streams and their origins on the solar surface.

- **Spectrometer/Telescope for Imaging X-rays (STIX)** will provide imaging spectroscopy of solar thermal and non-thermal X-ray emission in the energy range from 4 to 150 keV. A sequence of quantitative information will be provided by this instrument, for example the timing, location, intensity, spectra of accelerated electrons and the thermal plasma with high temperature.

A.1 EPD/STEP

The Energetic Particle Detector (EPD) suite, shown in Figure A.3, is composed of four particle detectors which can measure electrons, protons, and ions from helium to iron, and operate at partly overlapping energy ranges from 2 keV up to 200 MeV/n. Four EPD sensors share a common unit named Instrument Control Unit (ICU), which is responsible for the data processing and low-voltage power supply, acting as the sole power and data interface of EPD to the Solar Orbiter spacecraft.

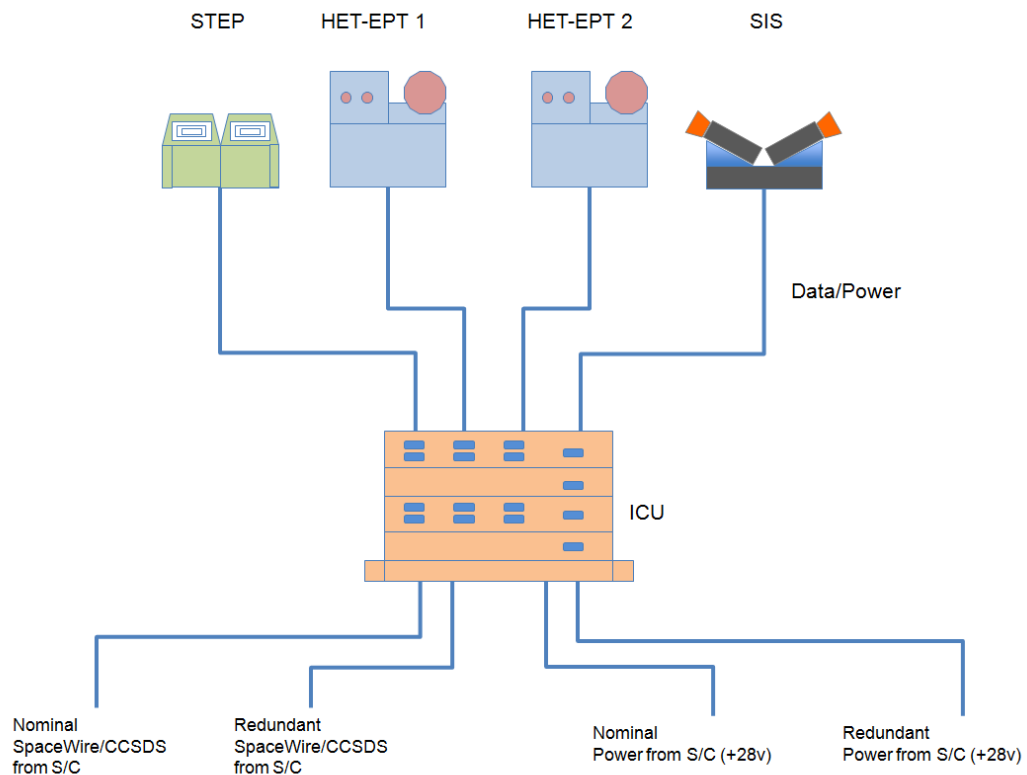


Figure A.3: The functional diagram of EPD's instruments, taken from <http://www.ieap.uni-kiel.de/et/solar-orbiter/>

The EPD sensors

- **Electron and Proton Telescope (EPT)** will take advantage of the magnet/foil-technique, adapted from STEREO/SEPT, to cleanly separate and measure elec-

trons from 20 keV to 400 keV and protons from 20 keV to 7 MeV. It contains two dual double-ended magnet/foil particle telescopes (EPT1 and EPT2) in order to examine the particle anisotropies. For this, EPT1 will point in the orbital plane approximately along the Parker spiral magnetic field towards and away from the Sun. EPT2 will point out of this plane towards North and South.

- **High-Energy Telescope (HET)** will use the dE/dx vs. total E technique for particle identification to measure electrons (300 keV-20 MeV), protons (10 MeV-100 MeV), and heavy ions (20 MeV/nuc-200 MeV/nuc). Similar to EPT, HET is also equipped with two double-ended sensor heads, one pointing along the Parker field towards and away from the Sun, the other out of the ecliptic. EPT and HET share their electronic boxes (E-Boxes). One E-Box hosts the Sun/anti-Sun sensors of EPT and HET, the other E-Box hosts the out-of-ecliptic (or North-South) sensor heads.
- **Suprathermal Ion Spectrograph (SIS)** will identify particles with the TOF technique to provide measurements of helium to iron for an energy range from ~ 100 keV/nuc up to 10 MeV/nuc. It has two particle telescopes pointing along the Parker field towards and away from the Sun, together with a single E-Box. Particles are measured when they traverse the entrance foils and deposit their energy in the SSD at the back of the instrument.
- **Suprathermal Electron and Proton (STEP)** has two telescopes and one E-Box, looking in the same direction and measuring suprathermal electrons (3 keV-65 keV) and protons/ions (3 keV-65 keV), see more details in the following section.

The overall energy coverage achieved by EPD, shown in Figure A.4, is 2 keV to 20 MeV for electrons, 3 keV to 100 MeV for protons, and 8 keV/nuc to 200 MeV/nuc for heavy ions (species-dependent). The design of EPD aims to answer the third Solar Orbiter scientific objective “How do solar eruptions produce energetic particle radiation that fills the heliosphere?”. It requires detailed measurements of SEP sources, acceleration

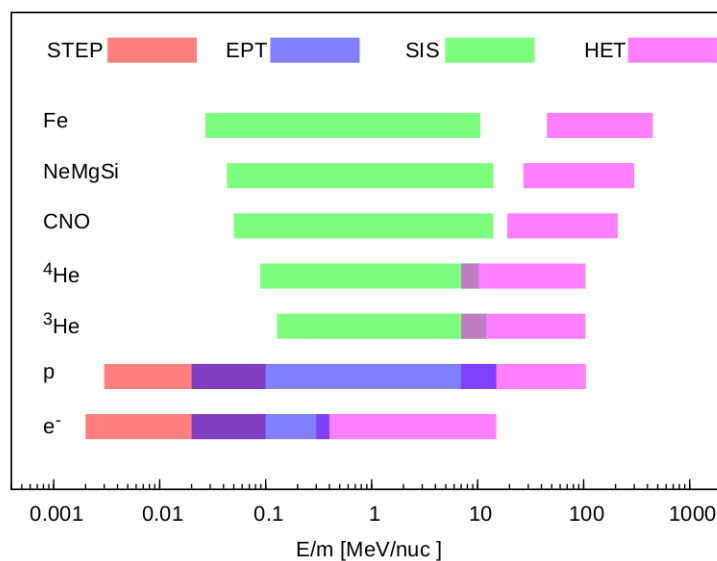


Figure A.4: The energy coverage of EPD sensors, taken from <http://www.ieap.uni-kiel.de/et/solar-orbiter/>

mechanisms, seed populations, and distributions in space and time. Together with in-situ measurements of the magnetic field and plasma environment from other payload of Solar Orbiter, e.g., RPW and MAG, EPD can help us understand what are the sources of energetic particles and how they are accelerated to high energy, released from their sources and distribute in time (Wimmer-Schweingruber et al., 2010).

A.1.1 STEP as a Part of EPD

As shown in the upper panel of Figure A.5, STEP deploys two identical detector units mounted on a common electronics unit on the -Y deck of the spacecraft. Both units point sunward into the direction of the nominal Parker spiral with unobstructed and co-aligned FOVs. When Solar Orbiter goes close to the Sun, the local magnetic field strength will increase significantly, which means charged particles including suprathermal particles will tend to focus along the field lines. On the other hand, these particles will suffer from more scattering due to the wave-particle interactions in the magnetic field of the inner heliosphere (Afanasiev and Vainio, 2013). STEP is designed to study the focusing vs. scattering process of suprathermal particles at the inner heliosphere. From the cutaway drawing of two STEP units in the lower panel of Figure A.5, we can see the internal structure and intuitively understand the working principle of STEP.

The basic principle can be described as follows: one detector unit uses a magnetic deflection system to suppress the incoming electrons at all relevant energies, then yields the proton/ion fluxes only. The other identical detector unit without the magnetic system measures all incident particles in the applicable energy ranges. Due to the same FOV and directing of two detector units, the difference of both measurements is then the electron flux. The magnetic deflection system provides two magnetic fields between the collimator and the detector board. Both magnetic fields do not have an effective influence on the ion trajectories but can effectively deflect away electrons. As shown in Figure A.5, incident electrons are guided to stop in the panel which stands between these two magnetic fields, while the protons/ions pass through the pinhole of the panel. The field between the panel and the SSD board is designed to correct the trajectories of protons/ions, so that protons/ions with identical properties reach the identical pixel of the SSD in both detector units no matter magnetic fields exist or not (see <http://www.physik.uni-kiel.de/de/institute/ieap/ag-wimmer/solo/step>).

A.2 Background Analysis for STEP

STEP uses passively cooled SSDs to detect particles in the suprathermal energy range (3-65 keV). Compared with the traditional electrostatic analyzer used by previous instruments, e.g., STEREO/STE, STEP's SSDs can provide higher sensitivity due to the ultra-thin ohmic contacts. STEP also allows continuous measurements at all applicable energies providing a high duty cycle as no stepped measurements are required to determine the energies (<http://www.ieap.uni-kiel.de/et/solar-orbiter/STEP.php>). The SSD system of STEP consists of 32 detector pixels divided into two groups, 16 big pixels and 16 small pixels, which work in the 'normal' mode and 'burst' mode respectively. All these pixel detectors can be switched on or off through a programmable configuration, which means the active area of the detectors can be changed in flight to adapt the geometry factor to different levels of particle fluxes.

The instrumental noise or background is a very important topic throughout the mission. Variable sources of background, e.g., due to electronic noise and space radiation,

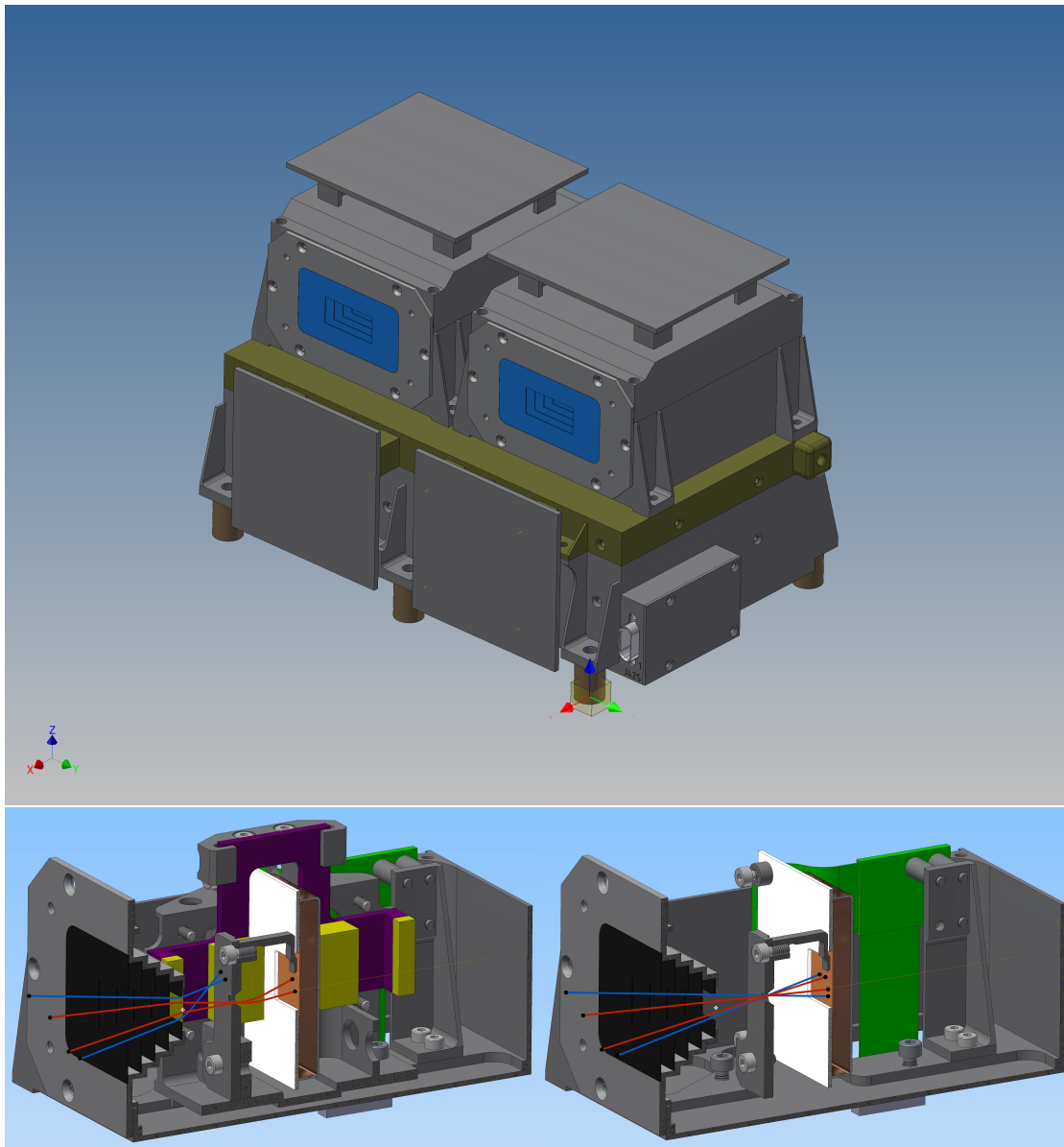


Figure A.5: The profile of STEP's two sensor units and the respective schematic view of the working principle (L. Seimetz, personal communication). Two blue windows in the upper figure are the entrance baffles, behind which are the instrumental collimators (black parts of the lower picture). Inside of the left sensor unit, the instrument deploys a board with a pinhole (the same color as the instrumental housing), a SSD board (the white board), a copper shielding behind the SSD board (the brown component), a magnetic deflection system with permanent magnets (four yellow blocks) and its yoke (the purple element). The only difference between two sensors is the magnetic system assembled in the left sensor, which is used to deflect away the incident electrons (blue trajectories), so that the only remaining ions (red trajectories) are measured.

can affect the output of scientific data. In the following section we will discuss the background caused by the triggers from penetrating particles and their secondaries on SSDs, which is involved by the space radiation.

A.2.1 Flux Spectrum Investigation

When Solar Orbiter is launched, it will encounter a variable radiation environment in the space. For that, STEP has a 'normal' and 'burst' mode to adjust to different radiation levels in the space. During solar quiet times when particle flux is low, STEP works in the 'normal' mode, with 16 big SSD pixels enabled. When intense solar events occur, e.g., CMEs, SEPs, and solar flares, the particle flux can abruptly increase by several orders of magnitude compared to quiet times. During solar events, the small pixels will be activated ('burst mode') in order to avoid saturation of the large pixels. Therefore, it is necessary to at first investigate the particle flux in different interplanetary conditions, and then estimate the corresponding instrumental background.

Solar Quiet Time

In Figure A.6, we use the model spectrum of protons in solar quiet times in the energy range from 1 MeV to 100 GeV given by CREME2009 (<https://creme.isde.vanderbilt.edu/>), which is an on-line tool offering model spectra for various particles over several decades. For electrons, no CREME model is available. So we investigate previous research and finally combine the spectrum in the low energy range (0.3 to 21.5 MeV) reported by Lin et al. (1972) and Simnett and McDonald (1969) respectively, see

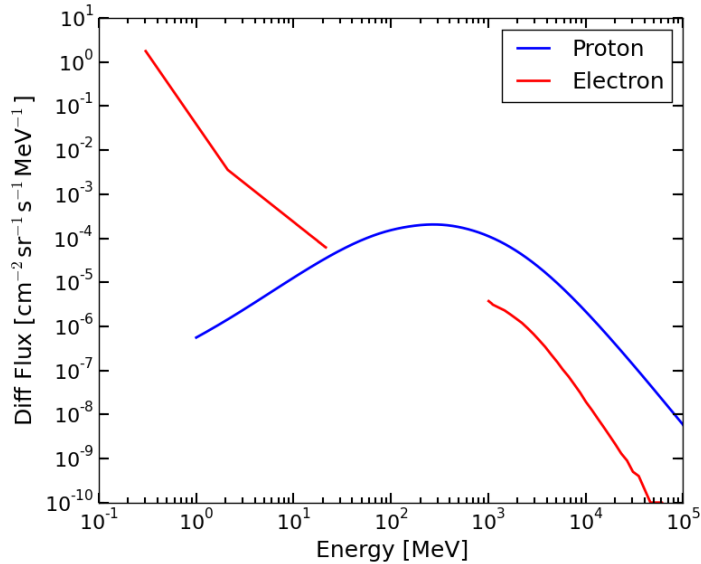


Figure A.6: Energy spectra of proton and electron during solar quiet times. The proton spectrum (blue curve) is obtained from the CREME website. The power law index of the electron spectrum in the energy range from 0.3 to 1.8 MeV is -3.2, as given by Lin et al. (1972), and -1.75 in the energy range (2.7-21.5 MeV) provided by Simnett and McDonald (1969). The electron spectrum in the range of 1-625 GeV is obtained from PAMELA data (Adriani et al., 2011). The spectral gap between 21.5 MeV and 1 GeV is due to no measurements.

below.

$$dJ/dE = 3.89 \times 10^{-2} E^{-3.2} \quad , 0.3 \leq E \leq 1.8 \text{MeV}$$

$$dJ/dE = 1.32 \times 10^{-2} E^{-1.75} \quad , 2.7 \leq E \leq 21.5 \text{MeV}$$

The electron spectrum in the higher energy range from ~ 1 to ~ 625 GeV is given by Adriani et al. (2011). The flux data were obtained from the Payload for Antimatter Matter Exploration and Light-nuclei Astrophysics (PAMELA) mission, which was launched on 15 June 2006 and dedicated to the detection of cosmic rays (see <http://pamela.roma2.infn.it/index.php>).

Solar Event Time

During solar event times, the energy spectra of particles are more variable than quiet times. In order to estimate the worst case that STEP may encounter, we choose the particle spectra of the SEP event on Oct. 28th, 2003. The proton and electron influences during this event are comparable to the largest observed during the previous solar maximum, and within a factor of 2 or 3 of the largest SEP events observed before (Mewaldt et al., 2005). As shown in Figure A.7. The equation to describe the proton spectral shape is a double power-law function:

$$\frac{dJ}{dE} = \begin{cases} 1.14 \times 10^4 E^{-1.04} \cdot \exp(-\frac{E}{27.4}) & , 0.16 \leq E \leq 96.72 \text{MeV} \\ 3.4 \times 10^9 E^{-4.57} & , 96.72 \leq E \leq 400 \text{MeV} \end{cases}$$

and the electron spectrum can be written as:

$$\frac{dJ}{dE} = \begin{cases} 5.68 \times 10^3 E^{-1.9} & , 0.04 \leq E \leq 0.32 \text{MeV} \\ 1.23 \times 10^3 E^{-4.27} & , 1.6 \leq E \leq 8 \text{MeV} \end{cases}$$

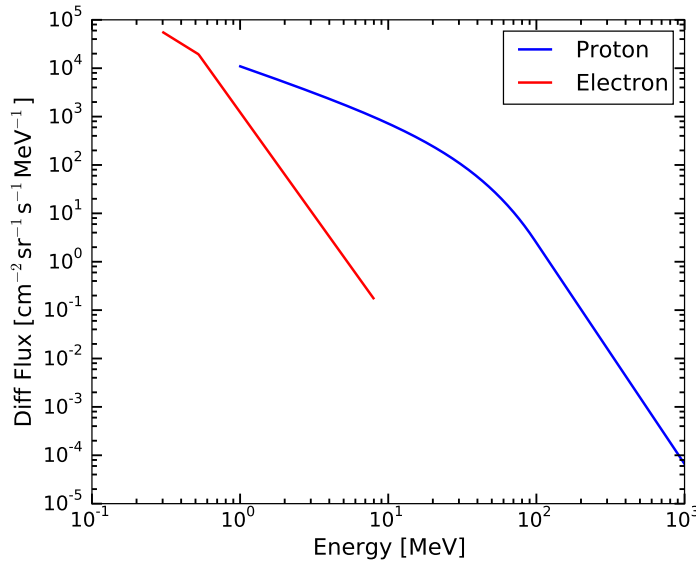


Figure A.7: Energy spectra of proton and electron during the intense SEP event happening on Oct. 28th, 2003 (Mewaldt et al., 2005).

Solar Photon Spectrum

As shown in Figure A.8, the photon spectrum during solar quiet times is given by Hannah et al. (2010) using the data from the Reuven Ramaty High Energy Solar Spectroscopic Imager (RHESSI) mission, which is a NASA solar flare observatory and launched on 5 February, 2002. RHESSI precisely determines the energies of photons in the range from 0.03 to 15 MeV, spanning the hard X-rays and gamma rays. Compared with previous observations (red, blue and green symbols) in Figure A.8, Hannah et al. (2010) provides a wider energy coverage from 3 to 200 keV. The photon flux shows a fast decrease with energy.

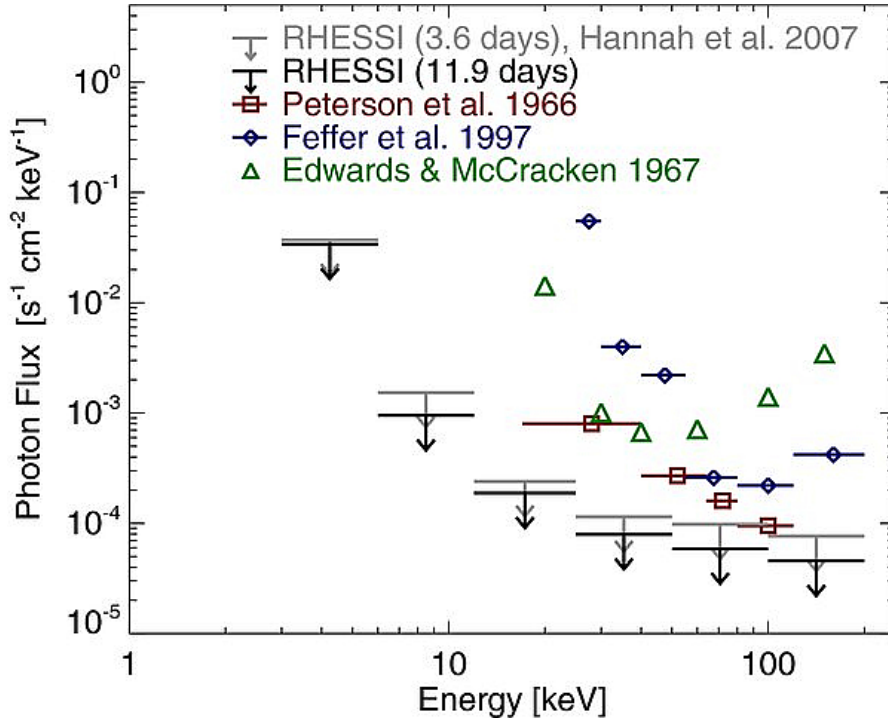


Figure A.8: Photon flux during solar quiet times measured by the RHESSI spacecraft, investigated by Hannah et al. (2010).

For the spectral investigation of photons during solar events, we also use the data of RHESSI. From the website <http://sprg.ssl.berkeley.edu/~tohban/nuggets/articles/article45/gamma.html>, we obtain the photon spectrum during the solar flare happening on December 6, 2006 (shown in Figure A.9). Overall, the photon spectrum exhibits a power-law shape.

A.2.2 Shielding Design

The surface of the SSDs facing the entrance aperture of STEP is covered by a 20 nm thin aluminum dead layer. On the backside of the detector PCB (printed circuit board), we planed to add a thin metal to shield electromagnetic interference (EMI) from other components of STEP. For the material of shielding, we had to decide on aluminum or copper. In order to estimate the performance of these two metal, we built a simulation model for STEP (shown in Figure A.10) using Geant4 (Agostinelli et al., 2003), which is a Monte Carlo toolkit for the simulation of the passage of particles through matter. In this model, we include five components: a SSD and its shielding on the back side, the

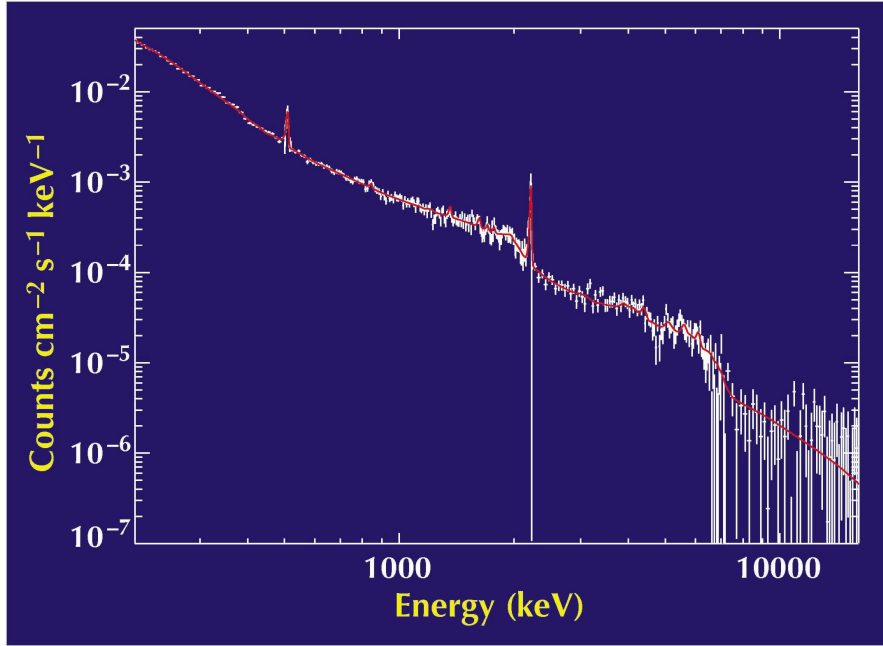


Figure A.9: Energy spectra of gamma-rays during the solar flare event on Dec. 6th, 2006. The plot is taken from <http://sprg.ssl.berkeley.edu/~tohban/nuggets/articles/article45/gamma.html>.

| Parameters | Values |
|------------------------------|--------------------|
| Shielding Material | Al,Cu |
| Shielding Thickness | 0.1 ~ 0.5 mm |
| Input Particles | protons, electrons |
| Housing Material | Al |
| Housing Thickness | 1 mm |
| PCB Material | Polyimide |
| Magnet System Material | Fe |
| Silicon Solid State Detector | 12.8×6.2×0.3 mm |

Table A.1: Simulation parameters for the STEP Geant4 model.

magnet system, PCB and instrument housing. Compared with the three dimensional (3D) drawing of STEP shown in Figure A.5, our Geant4 simulation model is a highly simplified one. Each part of our model is assumed to consist of a certain material, i.e., SSD: silicon; PCB: polyimide; housing: aluminum; magnet system: iron; SSD shielding: aluminum or copper. We use one big SSD to simulate the pixel array, and a box-shape housing instead of the complex one in Figure A.5. The simulation parameters are listed in Table A.1. In total of 20 simulation (2 materials \times 2 particles \times 5 thicknesses) cases were performed. Although the model is simplified, we consider it valid enough to evaluate the performance of the shielding.

For STEP, the main background that we consider in solar quiet times originates from GCRs, which come from outside the solar system and are a slowly varying, highly energetic background source of particles. Specifically, GCRs bombard the Solar Orbiter spacecraft evenly from all directions. Their high energies allow most of them to penetrate

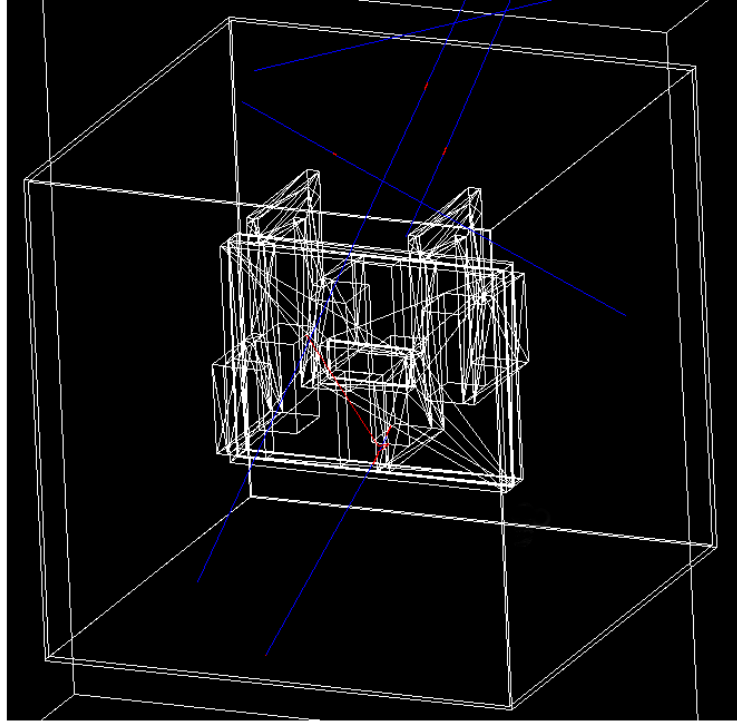


Figure A.10: Geant4 simulation model for STEP. The detector is located in the center, surrounded with PCB, shielding and magnet system. The outer big cube is the simplified instrument housing, protecting all inside parts. Incident particles shoot at STEP from outside the housing, e.g., blue traces indicate penetrating protons while red ones represent secondary electrons generated during the interaction between protons and inside parts of STEP.

the housing of STEP and trigger the SSDs. Therefore, in our Geant4 simulation model, we use an isotropic particle source to shoot at the instrument. Using the simulation results, we can further estimate the response function of STEP. More specifically, we aim to obtain a probability array as shown in Table A.2. The probability is derived from the ratio of counts in a certain deposited-energy bin (DE_Bin) to those in a certain primary energy bin (PE_Bin). The probability can be accurately determined when we simulate with enough number of particles in each PE_Bin. We divide the energy range from 100 keV to 100 GeV into 300 logarithmically spaced bins. For each energy bin, we use a spherical particle source which has a radius $r_{source} = 5$ cm. 200,000 incident particles are shot at the inside STEP model evenly from all directions.

The probability array (see Table A.2) can be used to calculate different background levels based on different input spectra. The count rate of background in one energy-

| | PE_Bin ₁ | PE_Bin ₂ | PE_Bin ₃ | ... | PE_Bin _{i-1} | PE_Bin _i |
|-----------------------|---------------------|---------------------|---------------------|-----|-----------------------|---------------------|
| DE_Bin ₁ | P _{1,1} | P _{1,2} | P _{1,3} | ... | P _{1,i-1} | P _{1,i} |
| DE_Bin ₂ | P _{2,1} | P _{2,2} | P _{2,3} | ... | P _{2,i-1} | P _{2,i} |
| DE_Bin ₃ | P _{3,1} | P _{3,2} | P _{3,3} | ... | P _{3,i-1} | P _{3,i} |
| ⋮ | ⋮ | ⋮ | ⋮ | ⋮ | ⋮ | ⋮ |
| DE_Bin _{j-1} | P _{j-1,1} | P _{j-1,2} | P _{j-1,3} | ... | P _{j-1,i-1} | P _{j-1,i} |
| DE_Bin _j | P _{j,1} | P _{j,2} | P _{j,3} | ... | P _{j,i-1} | P _{j,i} |

Table A.2: The STEP response function can be expressed as a probability array. Each element indicates the probability of particles in a certain primary energy range (PE_Bin) to deposit a certain range of energy (DE_Bin) in STEP's SSD.

deposit bin, e.g., DE_Bin_x, can be computed as follows:

$$\begin{aligned}
 CountRate_x[s^{-1}] &= \sum_{m=1}^i J(E_m) \cdot GF_{source} \cdot \Delta PE_m \cdot p_{x,m} \\
 &= 4\pi^2 r_{source}^2 \sum_{m=1}^i J(E_m) \cdot \Delta PE_m \cdot p_{x,m}
 \end{aligned}$$

where $J(E_x)$ is the spectral function of primary particles which describes the shapes of input spectra. GF_{source} is the geometrical factor of the simulation source. According to Sullivan (1972), the geometrical factor of a detector with area A with particles incident from one side is given by $GF = \pi A$. In the case of our particle source, $A = 4\pi r_{source}^2$. ΔPE_m is the energy range of the PE_Bin_m. The element $p_{x,m}$ of the probability array is the ratio of the count number in DE_Bin_x to the count number that we simulate in PE_Bin_m, i.e., 200,000. The above equation tells us the background count rate in DE_Bin_x has as many as i contributions from primary particles. Here in our case $i = 300$ as given above. $J(E_m) \cdot GF_{source} \cdot \Delta PE_m$ denotes the count rate (unit: sec^{-1}) of primary particles with the differential flux $J(E_m)$ (unit: $\text{cm}^{-2}\text{sr}^{-1}\text{sec}^{-1}\text{keV}^{-1}$) in the energy range ΔPE_m (unit: keV), shooting at the spherical volume with a geometry factor $4\pi^2 r_{source}^2 = 986.96 \text{ cm}^2\text{sr}$. Then we can further derive the count rate on STEP's SSD by multiplying the corresponding probability $p_{x,m}$. The benefit of this method is that GF_{source} , ΔPE_m and $p_{x,m}$ are fixed. The only variable is $J(E_m)$. With different spectra during solar quiet times and solar events given in the former section, we can determine the corresponding instrument background.

Simulation Output

Figures A.11 and A.12 illustrate results from two of 20 simulation cases. The distribution of energy deposit of incident particles vs. their primary energy provides us a intuitive view of the probability array. We find that the distribution pattern relies on the type of incident particles, varying little with the shielding material and thickness. As shown in Figure A.11, no protons can be detected by SSD when their primary energy is lower than ~ 10 MeV, while for electrons this threshold is around 300 keV. This is because the instrument housing rejects low-energy particles entering STEP. In the primary energy range from 10 MeV to 1 GeV, the most probable energy deposit of protons decreases from ~ 2 MeV to ~ 120 keV with increasing primary energy. When the primary energy of protons is higher than 1 GeV, the probability distribution in energy deposit bins becomes

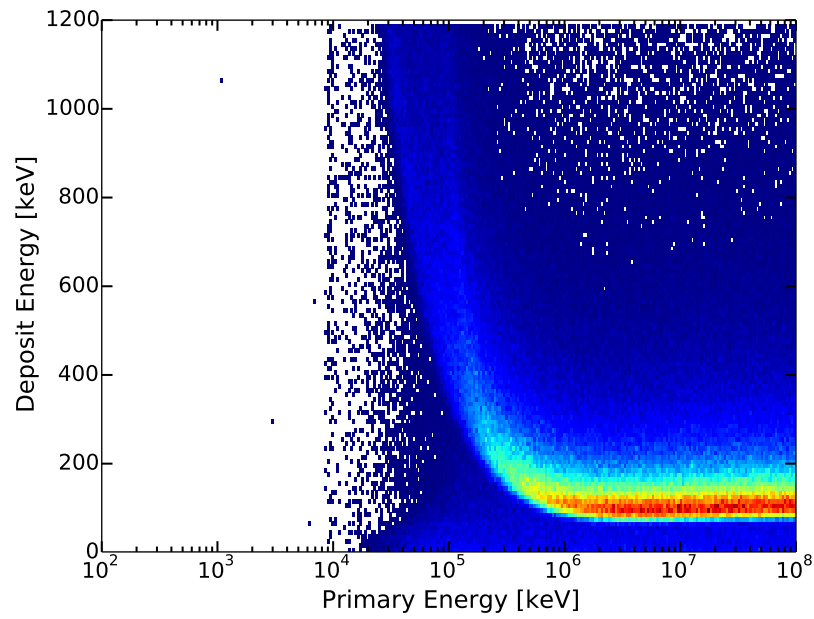


Figure A.11: Distribution of proton deposited energy versus primary energy obtained from the Geant4 simulation for STEP. The SSD is shielded by a 0.2 mm thick copper foil.

essentially stable. In contrast, the primary energy of electrons does not clearly affect the probability distribution as Figure A.12 shows. Penetrating electrons most likely deposit ~ 120 keV in STEP's SSD.

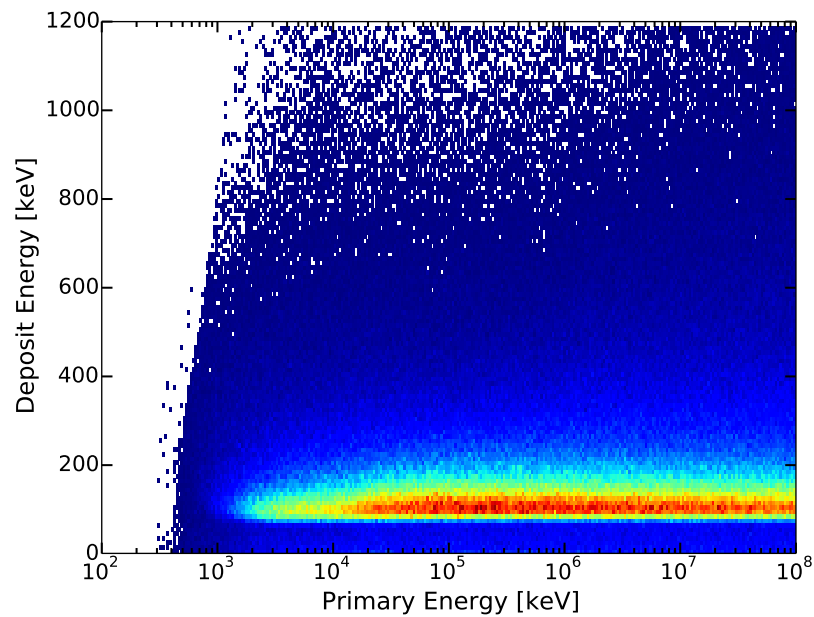


Figure A.12: Same as Figure A.11 but with electrons as incident particles.

Comparison

After obtaining 20 probability arrays from 20 sets of simulations, we evaluate the STEP background count rates caused by both primary and secondary particles during solar quiet times (see Figure A.13). For the background caused by energetic protons shown in the left panel of Figure A.13, ten curves are roughly equivalent, indicating that the STEP background is not sensitive to the shielding material and thickness. On the other hand, these two shielding parameters (material and thickness) can both obviously affect the background level caused by incident energetic electrons. As shown in the right panel of Figure A.13, the copper shielding performs better than the aluminum one and a thick shielding produces slightly less background than a thin one. In addition, we also notice that background count rates caused by penetrating protons and electrons have a similar trend with energy deposit, although the absolute values of proton background are about ten times higher than those of electron background. Differential count rates of background ($CountRate/\Delta DE$, where ΔDE is the energy deposit range) are almost constant with energy deposit in the range of 1-68 keV. Above 68 keV, the background rises up rapidly and peaks at around 120 keV and then evolves into a decreasing phase at higher energies.

Comparing with aluminum shielding, copper shielding produces a background peak at the energy deposit around 8 keV in Figure A.13, i.e., more apparently in the right panel. We found that this peak is caused by secondary photons. The peak can be explained by the characteristic X-rays of copper which are emitted when outer-shell electrons fill a vacancy in the inner shell of a copper atom. This process can happen

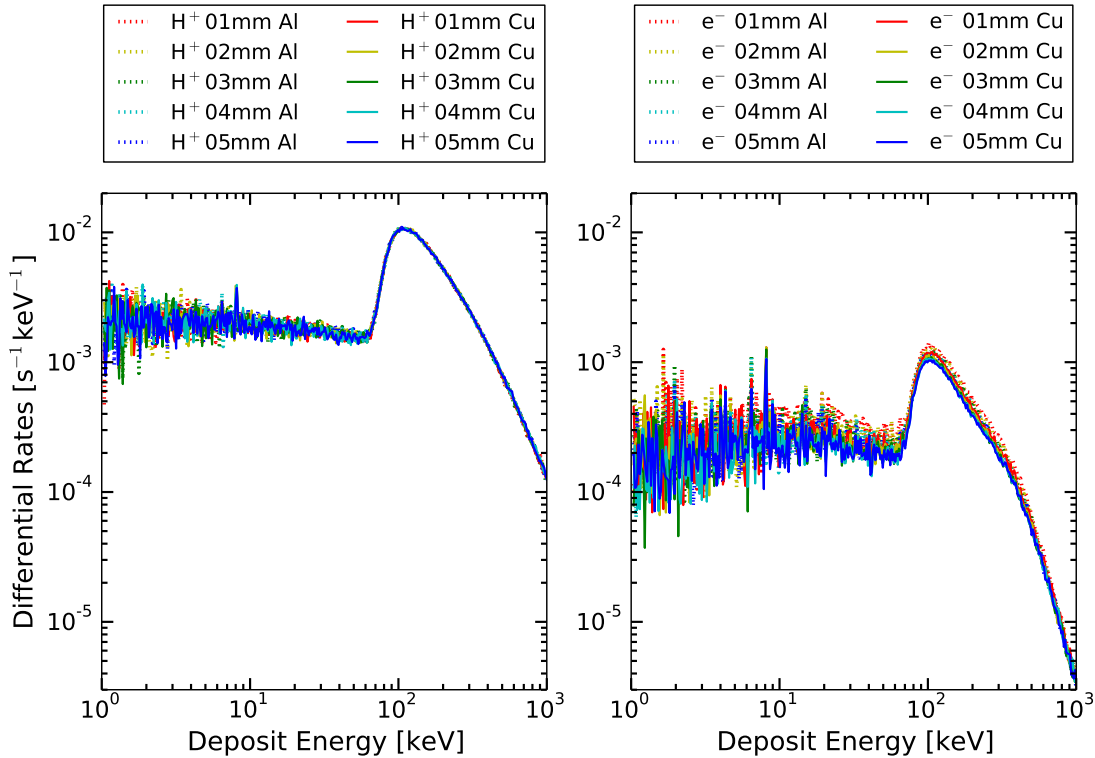


Figure A.13: The differential count rates of the STEP background caused by primary and secondary particles during solar quiet times.

when an element is bombarded with high-energy particles, e.g., electrons and protons. When the incident particle strikes a bound electron (the target electron) in an atom, the target electron is ejected from the inner shell of the atom, leaving with vacant energy level, also known as a core hole. Outer-shell electrons then fall into the inner shell, emitting quantized photons with an energy level equivalent to the energy difference between the higher and lower states. Each element has a unique set of energy levels, and thus the transition from higher to lower energy levels produces X-rays with characteristic frequencies to each element (see <http://en.wikipedia.org/wiki/X-ray>). For copper, there are two characteristic X-ray emission lines at 8.05 and 8.91 keV, which is verified by our simulation in Figure A.19 and provides a good opportunity to calibrate the energy measurement of STEP.

Based on the above comparisons, we decided to choose copper shielding for STEP, as it will generate less background than aluminum one. Additionally, the characteristic X-rays of copper have an advantage for further energy calibration. Regarding the mass limitation of STEP, the shielding thickness is finally set to be 0.2 mm.

A.2.3 Signal to Noise Ratio

We found that the STEP background reaches its maximum at energy deposit around 120 keV. This is close to the observable energy range of this instrument. Therefore, it is important to evaluate the background effect on STEP measurements, i.e., by means of the SNR. We surveyed the spectra during different space conditions in the observable energy range of STEP in order to estimate the 'signal' level of this instrument. The geometrical factor of the big-pixel array is derived to be around 0.008 cm²sr based on the Geant4 simulation.

SNR during Solar Quiet Time

In solar quiet times, the proton spectrum in the energy range of 38-334 keV is given by Lin et al. (1973) in a form of power law with index -1.3:

$$dJ/dE = 5.6E^{-1.3} \text{ cm}^{-2}\text{sr}^{-1}\text{sec}^{-1}\text{keV}^{-1} \quad (38 \leq E \leq 334\text{keV})$$

The 'signal' spectrum of electrons is also a power-law shape with index -2.3, provided by Lin et al. (1972):

$$dJ/dE = 3 \times 10^2 E^{-2.3} \text{ cm}^{-2}\text{sr}^{-1}\text{sec}^{-1}\text{keV}^{-1} \quad (18 \leq E \leq 100\text{keV})$$

Figure A.14 shows that background of STEP is nearly flat in low measurable energy range (up to ~68 keV) with a characteristic X-ray peak at ~8 keV. Due to the small geometry factor of STEP and low flux at 1 AU (compared with that in inner heliosphere.), we cannot see enough signals above 9 keV for proton measurements and 21 keV for electron measurements, where SNR < 1. But we expect that SNR will increase when Solar Orbiter travels close to the Sun. The first reason is that the intensity of solar particles literally drops at a speed of square heliocentric distance associated with the expansion of solar wind. Then at 0.28 AU the intensity shall be 1²/0.28² = 12.76 times of that at 1 AU, see dashed lines in Figure A.14. Secondly, the STEP background during quiet times driven by GCR shall decrease when the spacecraft goes to the Sun as GCR suffers from more reflection of IMF at the inner heliosphere (Wibberenz et al., 2002). So below 68 keV the SNRs for both protons and electrons shall be larger than 1 at 0.28 AU.

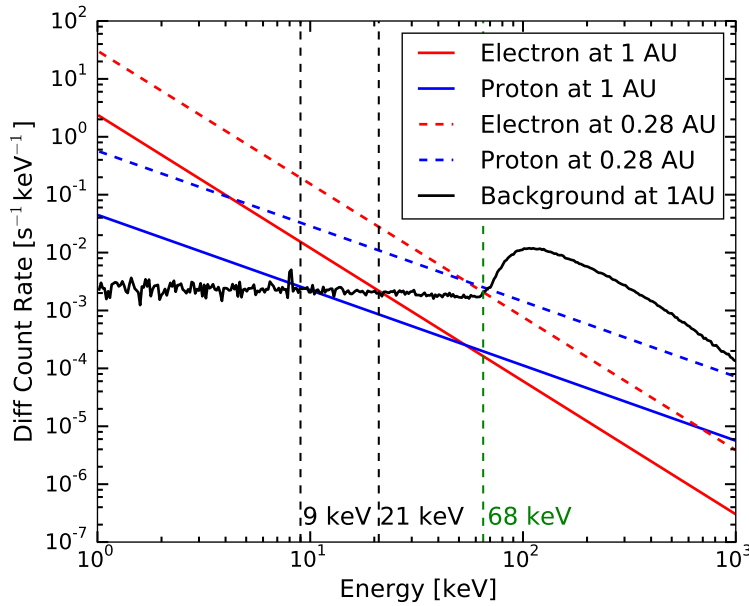


Figure A.14: SNR during solar quiet times at 1 AU for the single SSD which simulates the big-pixel array of STEP. The signal spectra at 1 AU (solid red and blue lines) are referred to Lin et al. (1972, 1973) and extended up to 1 MeV and down to 1 keV. The signal spectra at 0.28 AU (dashed red and blue lines) are interpolated from 1 AU. The instrument background due to energetic penetrating particles is shown with the black line which is calculated with the geometric factor $0.008 \text{ cm}^2\text{sr}$, the spectra given in Figure A.6, and the probability array of Table A.2. Three vertical dashed lines mark the energies where SNR reaches 1.

SNR during Solar Event Time

Other than GCRs, solar energetic particles can also easily penetrate the housing and trigger the detectors as background during solar events. Figure A.15 shows the most intensive event observed by Mewaldt et al. (2005) on Oct. 28th, 2003 (its spectral functions are given in Section A.2.1). The derived differential count rates of background below $\sim 68 \text{ keV}$ are around $10 \text{ keV}^{-1}\text{s}^{-1}$, more than three orders of magnitude higher than those during solar quiet times (see Figure A.14). In other words, solar energetic particles become the dominant source of the STEP background, comparing with GCRs. Unlike the enhanced background level above $\sim 68 \text{ keV}$ in solar quiet times, the background level during this solar event slightly decreases at high observable energies. Thus it will be possible to extract valid data at all observable energies using the background pixels. SNRs during this event are similar to those during solar quiet times, i.e., electrons exhibit better performance of measurement ($\text{SNR} < 1$ above 67.17 keV) than protons ($\text{SNR} < 1$ above 7.78 keV). Compared with solar quiet times, SNRs during solar events should be more variable because the STEP background is mainly contributed by the solar energetic particles whose flux is much higher compared with GCR. In other words, the STEP background greatly relies on the spectral shape of these energetic particles. Therefore, to estimate the STEP background during solar events, it's better to refer to the observations of other energetic particle detectors, e.g., EPT and HET.

Photon Background

Other than energetic protons, electrons and heavy ions, energetic photons can also trigger the STEP. In the inner heliosphere, the Sun is the main source of the photon background. We use a plane photon source in our Geant4 simulation, different from the spherical shape for the proton and electron sources. As shown in Figure A.16, the angle between the FOV direction of STEP and the Sun light is about 37 degrees. We add an aluminum plate in front of STEP with a thickness of 1 cm, perpendicular to the Sun light direction. It represents the shielding of the Solar Orbiter spacecraft and is used to protect scientific instruments behind it. The method to determine the background count rates in one energy deposit bin is given below, slightly different from the equation for protons and electrons:

$$CountRate_x[s^{-1}] = \sum_{m=1}^i J(E_m) \cdot A \cdot \Delta PE_m \cdot p_{x,m}$$

where A is the source area of incident photons. We found that the Solar Orbiter shielding can block photons below around 30keV. Unlike particles such as electrons or protons, photons can penetrate the SSD without energy loss. Figure A.17 shows the differential count rates of STEP background derived with spectrum in Figure A.9. We can find that the background level stays below $10^{-4} \text{ keV}^{-1}\text{s}^{-1}$ for energy deposit lower than 100 keV. Then the background starts to decrease with energy. Even if comparing with the background during solar quiet times, the photon background derived with a solar flare event is more than 1 order lower. We expect that solar photon background in quiet times (Figure A.8) is even less and can be neglected.

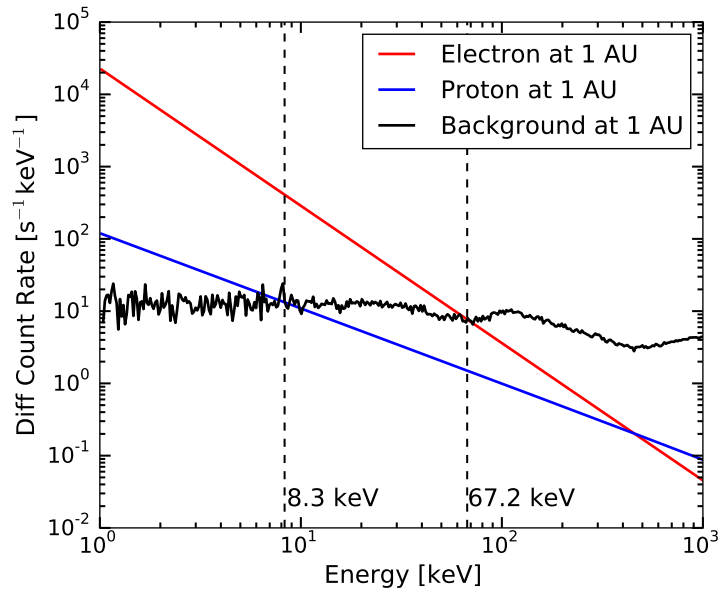


Figure A.15: SNR during the event on 28/10/2013 at 1 AU.

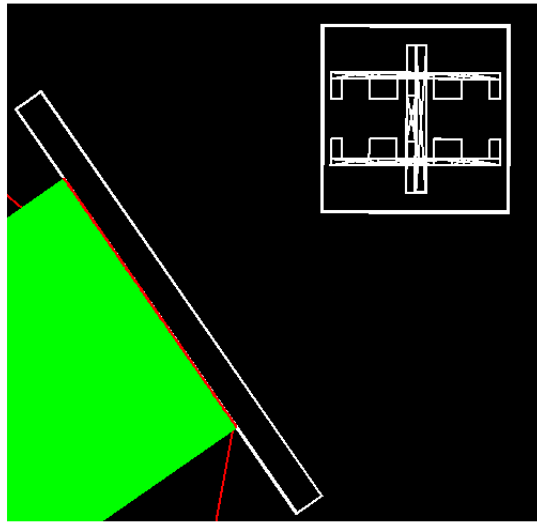


Figure A.16: Geant4 simulation of solar protons at 1 AU. The green area indicates incident photons in the energy range of 1 to 30 keV. Red lines are traces of secondary electrons generated in the interaction process between photons and the spacecraft shielding.

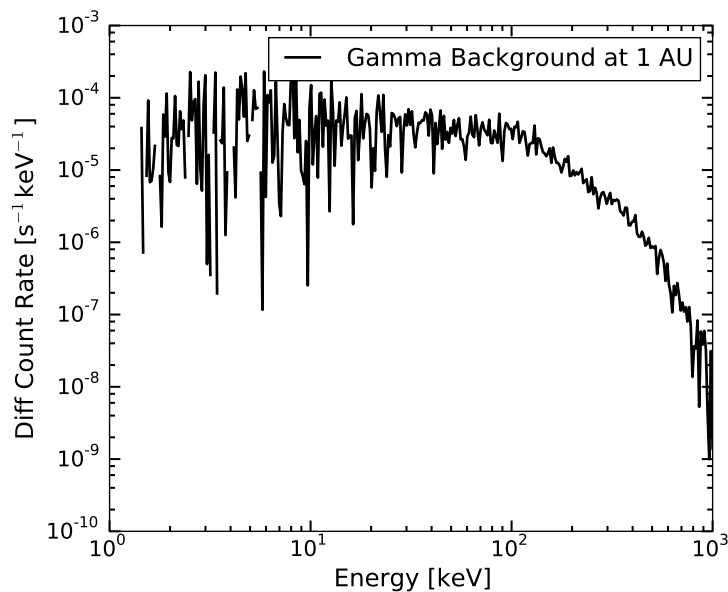


Figure A.17: Photon background derived with the spectrum of gamma-ray illustrated in Figure A.9.

A.2.4 Background Generation Mechanism

Fast charged particles moving through matter can interact with the electrons of the atoms in the material. The interaction excites or ionizes the atoms, leading to an energy loss of the traveling particle. The mean energy deposit per distance travelled is described by the 'Bethe-Bloch' formula (Segrè, 1959). The fluctuations of energy loss by ionization

of a charged particle in a thin layer of matter were theoretically described by Landau (1944). Figure A.18 illustrates the count-rate distribution of energy deposit simulated with protons and electrons. The primary energy range of incident protons and electrons is 10-100 GeV. According to Figure A.11 and A.12, incident particles in this energy range show almost the same distribution of energy deposit. Therefore, we integrate these particles in order to obtain a good counting statistics for our survey. The long tail in high energies (so-called Landau tail) results from the small number of individual collisions, each with a small probability of transferring comparatively large amounts of energy. At low energies, the count rates should decrease to nearly zero around 60 keV, based on the Landau distribution. However, we also find a tail in these energies for both protons and electrons (indicated by cyan shading in Figure A.18), which constitutes the main portion of low-energy background of STEP.

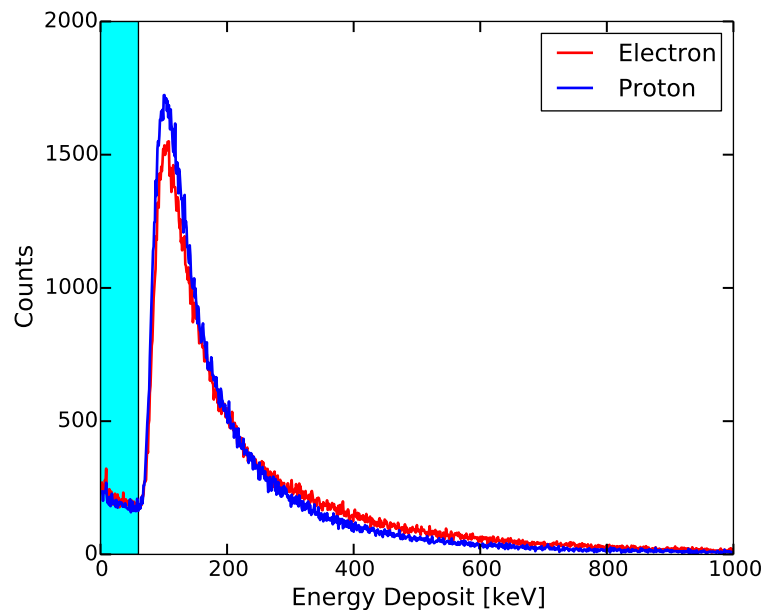


Figure A.18: Distribution among energy deposit (0-1000 keV) of primary and secondary particles. The primary energy range of incident protons and electrons is 10-100 GeV.

The low-energy tail particles illustrated in Figure A.18 have been further studied, i.e., their origin and distribution in the SSD plane, see the results in Figure A.19. As shown in the upper left panel, the low-energy tail particles in Figure A.18 consist of two sources: primary protons (blue curve) and secondaries (green curve) in the similar count-rate level. The peak of secondaries at ~ 8 keV is caused by the characteristic X-rays of copper, which has been discussed before. A very interesting result is the distribution of two origins of tail particles on the SSD plane. Primary low-energy protons only show up at the edges of SSD (see the left middle panel). By contrast, the low-energy secondaries evenly distribute on the SSD plane (see the bottom left panel). For the case of electrons, the results are very similar to protons as shown in three right panels of Figure A.19.

The secondary source of low-energy background is easily understood, as it is well known that these secondaries (e.g., electrons and photons) can be generated in the process of particles traversing matter. But how to explain the background caused by primary particles? We notice that the Landau distribution is used to describe a particle travelling through matter with a fixed thickness. In our simulation, particles are shot at

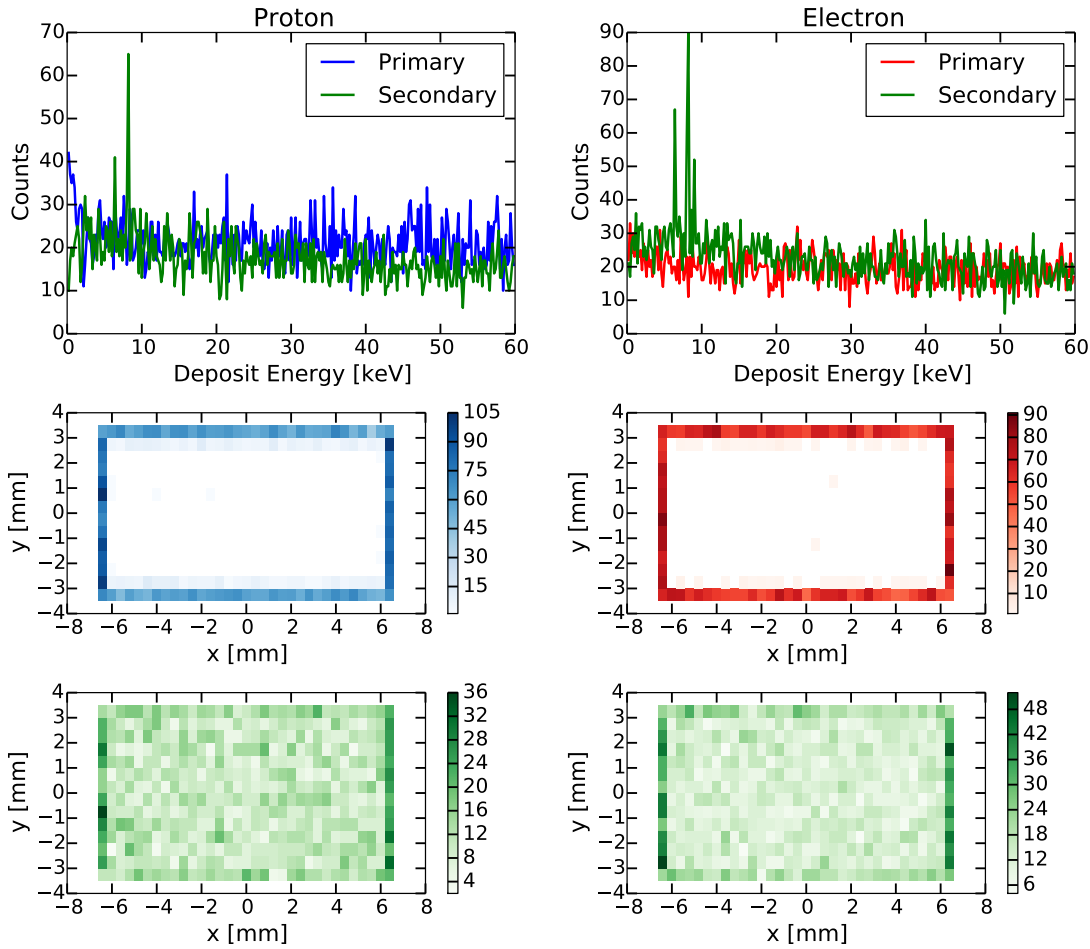


Figure A.19: Primary and secondary origins of low-energy tail particles are in the similar counting level in upper two panels. Primary low-energy particles only show up at the edges of SSD (in the second row of panels), while counts of secondary low-energy particles are evenly distributed on the whole SSD area but increase at SSD edges (in the lower two panels).

STEP isotropically. Their energy loss in one material is related to the length of the path through the material. As Figure A.20 shows, when a primary particle hits the edge of SSD (case 'c'), its energy loss will be smaller than those interacting with SSD in a long path (e.g., case 'a' and 'b'). This can well explain why we always see that the low-energy primary particles appear at the edges of SSD in two middle panels of Figure A.19. Their intrinsic energy is not as high as that of primary penetrating particles, but located in the observable energy range of STEP. Thus, for a secondary photon like 'd' of Figure A.20, its energy deposit may be recorded as a valid particle hit on STEP, although it does not hit the SSD edges. This is the reason why we can see the even distribution of low-energy secondaries on the SSD plane except for the edges (see two lower panels of Figure A.19).

As the energy deposit at SSD edges stays in the observable range of STEP, this kind of particle hit can be measured as background. We name this background generation mechanism as 'Edge Effect'. We can further speculate that this kind of background is proportional to the total length of edges or perimeter of SSD. If we want to suppress

the 'Edge Effect' background, a detector with small ratio of perimeter to active area will be preferable, as active area of a detector dominates the signal level and its edge length determines the low-energy background level.

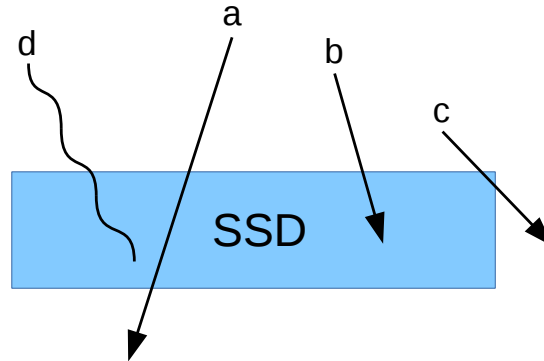


Figure A.20: Four cases of particle hits. 'a': particle penetrates SSD; 'b': particle is absorbed by SSD; 'c': particle hits the edge of SSD; 'd': secondary photon deposits in SSD.

A.2.5 Background Estimation Pixel

All the above analysis of background is based on simulations with the simplified SSD, which has the same thickness and active area as the actual pixel array. We have known that around half background recorded by the simplified SSD is caused by the 'Edge Effect'. But regarding the actual pixel array, we will have more 'edges', so that the background level will increase. By contrast, the signal level will stay at the same level

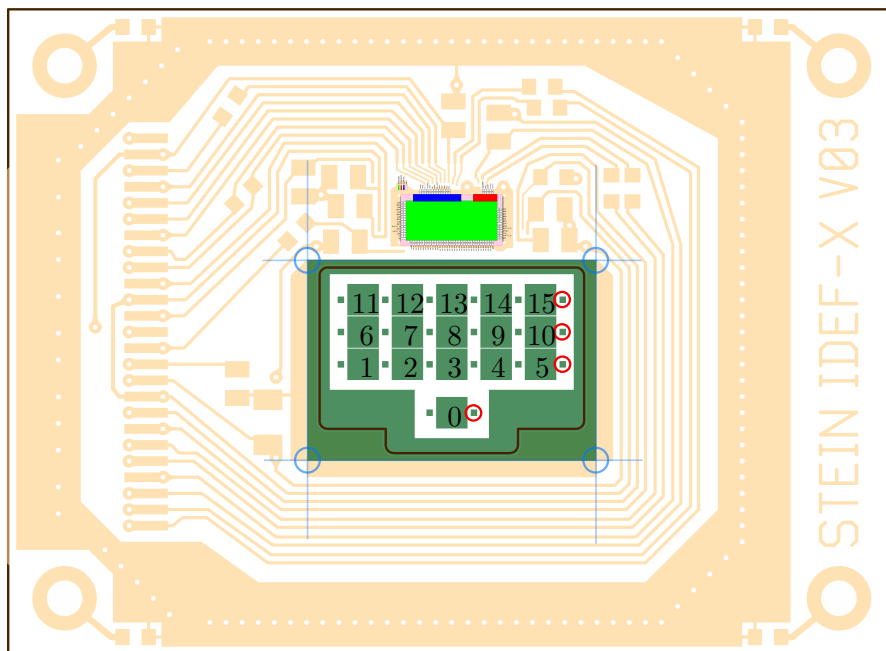


Figure A.21: The SSD board of STEP (S. I. Böttcher, personal communication). Sixteen big pixels are marked with numbers from 0 to 15.

because of unchanged active area of SSD. Therefore, it is very necessary to evaluate the SNR for the case of the pixel array.

Figure A.21 shows the layout of the SSD board of STEP. The pixel array (dark green) is located in the center of board, and consists of 16 big pixels (marked 0-15) and 20 small pixels. Four small pixels (indicated with red circles) are not used. The bottom big and small pixels are used to estimate the background for the upper 3×5 big pixels and 3×5 small pixels respectively. The light green module in Figure A.21 is the readout chip for the pixel array called 'Idef-X-BD', which has 32 input channels. The big-pixel array and small-pixel array will work in the 'normal' and 'burst' mode respectively. During the measuring phase, only one pixel is allowed to be triggered. In other words, STEP will reject an event when more than one pixel is triggered at the same time (more precisely, within the time window of measuring). We call this 'Multiple Hits' in this thesis. This setting can effectively suppress the background caused by energetic particles, energies of which allow them to penetrate the housing and trigger more than one pixel.

Referring to the dimension of the pixel array of the STEP SSD, we built a new SSD module for simulation, including a function of rejecting 'Multiple Hits'. We obtained 15 probability arrays for each 3×5 big pixel, the background of which is summed up to show in Figure A.22, based on the spectra of protons and electrons during solar quiet times. As the new SSD module has the same active area as before, i.e., the same geometric factor, the total count rate of the signal does not change. However, due to the 'Edge Effect' and rejecting 'Multiple Hits', the total background count rate of 15 big pixels has changed slightly. The background level roughly doubles in the low energy deposit from 1 to 68 keV, while in the higher energy range, the background decreases with increasing energy. The increased background in the lower energy range can be well explained by the 'Edge Effect'. The total edge length of the former single SSD is $(12.8+6.8) \cdot 2 = 39.2$ mm. As shown in Figure A.21, the distance of two neighboring big pixels in each column is very small. If a particle hits one of two neighboring edge, e.g., the 'c' case in Figure

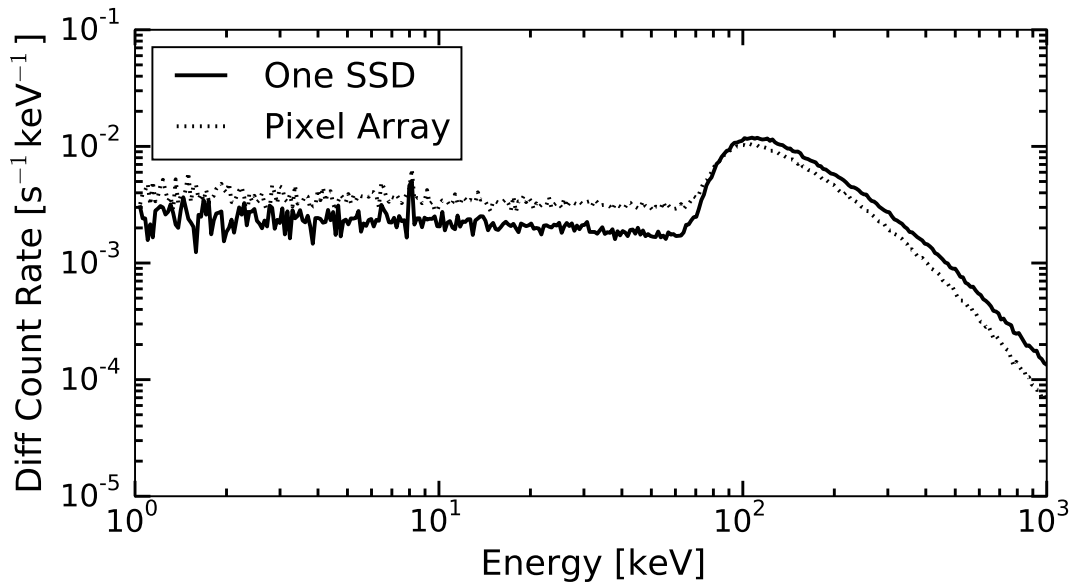


Figure A.22: Comparison of background generated on the single SSD and pixel array based on the spectra of protons and electrons during solar quiet times.

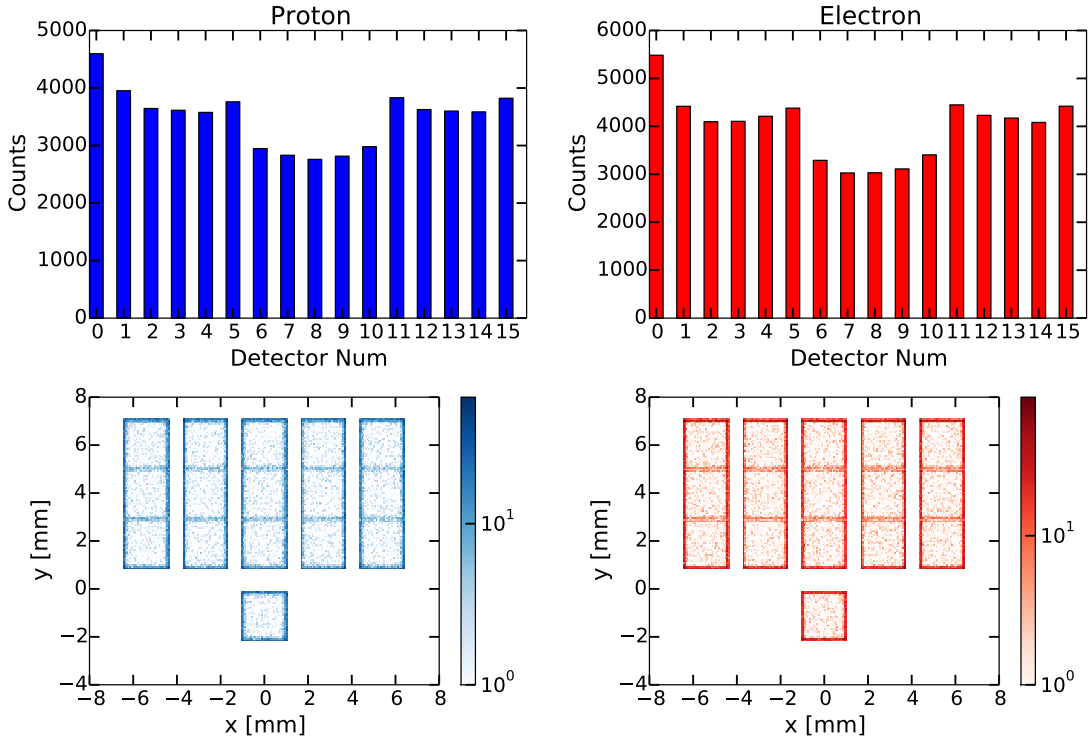


Figure A.23: Upper two panels show the counting of low-energy tail particles (3-65 keV) among 16 big pixels, based on the Geant4 simulation with incident H^+ and e^- . Two lower panels illustrate the position distribution of counting on each big pixels. Energy range of incident primary particles is from 1 to 100 GeV.

A.20, the other pixel will also be probably triggered. Then this particle hit will be rejected by our simulation. So we neglect these close neighboring edges of pixel array, and finally obtain the total length of edges of pixel array which is about 80 mm, roughly twice of former total length (39.2 mm). This is consistent with doubled background in low energies. The decreased background at higher energies is caused by rejecting the 'Multiple Hits'. The energy deposit of a particle is related to the length of the path through the material. High energy deposit indicates particles penetrating at a large incident angle. Then the probability of 'Multiple Hits' will increase. Therefore, the probability of rejecting 'Multiple Hits' should increase with the energy deposit, which is the reason why we see a relatively decreased background with energy deposit in Figure A.22.

Figure A.23 shows the distribution of low-energy tail particles in the energy range of 3-65 keV among 16 big pixels of STEP's SSD. The distributions for incident protons and electrons are very similar. The maximum of count rates both appears in the background pixel '0', while the minimum shows up in pixels '7', '8' and '9'. The reason is that the background pixel is located relatively far away from the 3×5 pixel array. The probability of 'Multiple Hits' is smaller than any other pixel. By contrast, pixels '7', '8' and '9' are all surrounded with other pixels, expecting the high probability of 'Multiple Hits'. In addition, from the lower two panels of Figure A.23, we found the position distribution of counting is a result of the interaction between the 'Edge Effect' and rejecting 'Multiple Hits'. For example, due to the small probability of 'Multiple Hits', the 'Edge Effect' is clearly seen on the background pixel '0' and almost equivalent at four edges. In contrast,

the distance between two neighboring pixels of the pixel array in each column is very small. Then the 'Edge Effect' becomes weaker at these edges, because many of 'Edge Effect' particle hits can be 'Multiple Hits' and are rejected by our simulation. This work tells us that the background in the big pixels will be slightly overestimated if we consider the measurement of the pixel '0' simply as the background. By contrast, the probability of 'Multiple Hits' for the small pixels is much smaller as they are far away from each other compared with their size. So the distribution among 16 small pixels shall be uniform and the measurement on the small background pixel can be considered as the background in any other small pixel.

To more precisely estimate the background in the big pixels, we shall refer to the method introduced in Section A.2.2, i.e., derive the response function for all the pixels. Tables A.3 and A.4 give the product of the probability array and geometrical factor of the simulation source (GF_{source}) for all 16 big pixels of STEP when we simulate with protons and electrons, respectively. To show this product in this thesis, we recombine 300 energy bins of our simulation (see Section A.2.2) into ten energy bins, i.e., 100-398 keV, 398 keV-1.58 MeV, 1.58-6.3 MeV, 6.3-25.1 MeV, 25.1-100 MeV, 100-398 MeV, 398 MeV-1.58 GeV, 1.58-6.3 GeV, 6.3-25.1 GeV, and 25.1-100 GeV. For the range of energy deposit, we define eight bins, i.e., 3-4.4 keV, 4.4-6.47 keV, 6.47-9.5 keV, 9.5-13.96 keV, 13.96-20.5 keV, 20.5-30.13 keV, 30.13-44.25 keV, and 44.25-65 keV. With Tables A.3 and A.4, the background level of all STEP's big pixels can be estimated by applying the spectra of energetic penetrating protons and electrons which we can refer to the measurements of EPT-HET of Solar Orbiter. Then we can compare the estimated background of the background pixel with the real measurements of this pixel. If they are consistent, we can further derive the background level for all the other big pixels in every bin of energy deposit. If not, we need to check the pitch angle distribution of the energetic particles using four-FOV EPT-HET as our current Geant4 simulation assumes an isotropic source of energetic particles. In addition, we need to investigate other sources of background, e.g., photons, using the measurements of STIX onboard Solar Orbiter.

A.3 Conclusions

In this section, we analyze the background for STEP of Solar Orbiter. Similar to SOHO/STOF, the background of STEP is mainly caused by penetrating energetic particles. Based on Geant4 simulations, we find that these penetrating particles are recorded by STEP as a background in two cases. One is when they hit the edges of STEP's SSDs and deposit measurable energy in SSDs. We named it the 'Edge Effect'. The other case is that secondaries created by penetrating particles hit STEP's SSDs. The characteristic X-rays of copper (secondary photons) are clearly visible in the simulation results and can be used for the energy calibration of STEP. Both cases contribute comparable backgrounds. Moreover, we analyze the background distribution in the pixel array. We conclude that the small background pixel can give a good estimate for the other small pixels. However, the big background pixel overestimates the background in the other big pixels. To determine the background for the big pixel array, we present here the response functions for all the big pixels based on the Geant4 simulation. These functions can be used in the future to derive the background for all the big pixels with input spectra measured by other payload of Solar Orbiter.

| Pixel 0 | PE_Bin ₁ | PE_Bin ₁₀ |
|---------------------|---------------------|---------------------|---------------------|---------------------|---------------------|---------------------|---------------------|---------------------|---------------------|----------------------|
| DE_Bin ₁ | 0.00e+00 | 0.00e+00 | 0.00e+00 | 0.00e+00 | 1.48e-03 | 1.81e-03 | 2.80e-03 | 4.44e-03 | 3.95e-03 | 3.95e-03 |
| DE_Bin ₂ | 0.00e+00 | 0.00e+00 | 0.00e+00 | 1.64e-04 | 1.64e-03 | 3.78e-03 | 3.45e-03 | 3.62e-03 | 6.42e-03 | 4.93e-03 |
| DE_Bin ₃ | 0.00e+00 | 0.00e+00 | 0.00e+00 | 0.00e+00 | 2.96e-03 | 6.58e-03 | 7.40e-03 | 9.05e-03 | 7.57e-03 | 8.55e-03 |
| DE_Bin ₄ | 0.00e+00 | 0.00e+00 | 0.00e+00 | 1.64e-04 | 2.96e-03 | 7.40e-03 | 8.39e-03 | 1.43e-02 | 1.22e-02 | 1.15e-02 |
| DE_Bin ₅ | 0.00e+00 | 0.00e+00 | 0.00e+00 | 1.64e-04 | 5.59e-03 | 1.20e-02 | 1.33e-02 | 1.86e-02 | 1.92e-02 | 1.79e-02 |
| DE_Bin ₆ | 0.00e+00 | 0.00e+00 | 0.00e+00 | 1.64e-04 | 7.90e-03 | 1.22e-02 | 2.14e-02 | 2.83e-02 | 3.06e-02 | 2.62e-02 |
| DE_Bin ₇ | 0.00e+00 | 0.00e+00 | 0.00e+00 | 6.58e-04 | 1.09e-02 | 2.43e-02 | 3.29e-02 | 4.38e-02 | 4.41e-02 | 4.15e-02 |
| DE_Bin ₈ | 0.00e+00 | 0.00e+00 | 0.00e+00 | 8.22e-04 | 9.87e-03 | 3.31e-02 | 4.85e-02 | 5.49e-02 | 6.48e-02 | 6.50e-02 |
| Pixel 1 | PE_Bin ₁ | PE_Bin ₁₀ |
| DE_Bin ₁ | 0.00e+00 | 0.00e+00 | 0.00e+00 | 0.00e+00 | 1.48e-03 | 1.15e-03 | 2.47e-03 | 2.80e-03 | 3.95e-03 | 3.13e-03 |
| DE_Bin ₂ | 0.00e+00 | 0.00e+00 | 0.00e+00 | 0.00e+00 | 2.14e-03 | 2.47e-03 | 3.29e-03 | 5.10e-03 | 5.76e-03 | 4.11e-03 |
| DE_Bin ₃ | 0.00e+00 | 0.00e+00 | 0.00e+00 | 0.00e+00 | 3.45e-03 | 3.29e-03 | 4.93e-03 | 7.24e-03 | 5.43e-03 | 7.57e-03 |
| DE_Bin ₄ | 0.00e+00 | 0.00e+00 | 0.00e+00 | 0.00e+00 | 3.45e-03 | 6.42e-03 | 8.06e-03 | 1.18e-02 | 1.45e-02 | 1.09e-02 |
| DE_Bin ₅ | 0.00e+00 | 0.00e+00 | 0.00e+00 | 0.00e+00 | 6.09e-03 | 8.22e-03 | 1.40e-02 | 1.41e-02 | 1.73e-02 | 1.79e-02 |
| DE_Bin ₆ | 0.00e+00 | 0.00e+00 | 0.00e+00 | 1.64e-04 | 6.74e-03 | 1.35e-02 | 1.81e-02 | 2.24e-02 | 2.19e-02 | 2.30e-02 |
| DE_Bin ₇ | 0.00e+00 | 0.00e+00 | 0.00e+00 | 3.29e-04 | 9.54e-03 | 1.88e-02 | 2.85e-02 | 3.62e-02 | 3.47e-02 | 3.03e-02 |
| DE_Bin ₈ | 0.00e+00 | 0.00e+00 | 0.00e+00 | 0.00e+00 | 1.14e-02 | 2.76e-02 | 4.54e-02 | 5.66e-02 | 5.20e-02 | 5.33e-02 |
| Pixel 2 | PE_Bin ₁ | PE_Bin ₁₀ |
| DE_Bin ₁ | 0.00e+00 | 0.00e+00 | 0.00e+00 | 0.00e+00 | 1.64e-03 | 1.81e-03 | 2.14e-03 | 3.45e-03 | 2.96e-03 | 2.80e-03 |
| DE_Bin ₂ | 0.00e+00 | 0.00e+00 | 0.00e+00 | 0.00e+00 | 1.81e-03 | 2.14e-03 | 3.29e-03 | 4.77e-03 | 4.11e-03 | 5.10e-03 |
| DE_Bin ₃ | 0.00e+00 | 0.00e+00 | 0.00e+00 | 0.00e+00 | 4.28e-03 | 3.95e-03 | 4.93e-03 | 6.25e-03 | 6.09e-03 | 6.74e-03 |
| DE_Bin ₄ | 0.00e+00 | 0.00e+00 | 0.00e+00 | 0.00e+00 | 3.78e-03 | 6.25e-03 | 9.05e-03 | 7.90e-03 | 9.38e-03 | 8.22e-03 |
| DE_Bin ₅ | 0.00e+00 | 0.00e+00 | 0.00e+00 | 3.29e-04 | 3.95e-03 | 7.73e-03 | 1.51e-02 | 1.40e-02 | 1.25e-02 | 1.58e-02 |
| DE_Bin ₆ | 0.00e+00 | 0.00e+00 | 0.00e+00 | 1.64e-04 | 5.26e-03 | 1.22e-02 | 1.74e-02 | 2.14e-02 | 2.24e-02 | 2.07e-02 |
| DE_Bin ₇ | 0.00e+00 | 0.00e+00 | 0.00e+00 | 1.64e-04 | 8.39e-03 | 1.99e-02 | 2.63e-02 | 3.36e-02 | 3.29e-02 | 2.88e-02 |
| DE_Bin ₈ | 0.00e+00 | 0.00e+00 | 0.00e+00 | 4.93e-04 | 1.12e-02 | 2.75e-02 | 3.93e-02 | 4.84e-02 | 5.71e-02 | 4.39e-02 |
| Pixel 3 | PE_Bin ₁ | PE_Bin ₁₀ |
| DE_Bin ₁ | 0.00e+00 | 0.00e+00 | 0.00e+00 | 0.00e+00 | 1.15e-03 | 2.63e-03 | 2.63e-03 | 2.80e-03 | 1.97e-03 | 2.14e-03 |
| DE_Bin ₂ | 0.00e+00 | 0.00e+00 | 0.00e+00 | 0.00e+00 | 1.32e-03 | 2.14e-03 | 3.13e-03 | 3.95e-03 | 5.26e-03 | 3.78e-03 |
| DE_Bin ₃ | 0.00e+00 | 0.00e+00 | 0.00e+00 | 1.64e-04 | 1.97e-03 | 3.78e-03 | 7.90e-03 | 6.74e-03 | 5.92e-03 | 7.73e-03 |
| DE_Bin ₄ | 0.00e+00 | 0.00e+00 | 0.00e+00 | 1.64e-04 | 2.14e-03 | 5.76e-03 | 8.22e-03 | 7.90e-03 | 1.10e-02 | 9.38e-03 |
| DE_Bin ₅ | 0.00e+00 | 0.00e+00 | 0.00e+00 | 0.00e+00 | 3.78e-03 | 6.58e-03 | 1.35e-02 | 1.58e-02 | 1.32e-02 | 1.38e-02 |
| DE_Bin ₆ | 0.00e+00 | 0.00e+00 | 0.00e+00 | 1.64e-04 | 5.26e-03 | 1.25e-02 | 1.84e-02 | 1.83e-02 | 1.89e-02 | 2.02e-02 |
| DE_Bin ₇ | 0.00e+00 | 0.00e+00 | 0.00e+00 | 1.64e-04 | 9.38e-03 | 2.07e-02 | 3.09e-02 | 3.08e-02 | 3.57e-02 | 2.71e-02 |
| DE_Bin ₈ | 0.00e+00 | 0.00e+00 | 0.00e+00 | 6.58e-04 | 9.21e-03 | 2.47e-02 | 3.93e-02 | 5.05e-02 | 4.93e-02 | 4.67e-02 |
| Pixel 4 | PE_Bin ₁ | PE_Bin ₁₀ |
| DE_Bin ₁ | 0.00e+00 | 0.00e+00 | 0.00e+00 | 0.00e+00 | 1.15e-03 | 1.97e-03 | 4.28e-03 | 3.13e-03 | 3.62e-03 | 3.13e-03 |
| DE_Bin ₂ | 0.00e+00 | 0.00e+00 | 0.00e+00 | 0.00e+00 | 2.80e-03 | 2.14e-03 | 3.62e-03 | 3.78e-03 | 2.47e-03 | 3.62e-03 |
| DE_Bin ₃ | 0.00e+00 | 0.00e+00 | 0.00e+00 | 0.00e+00 | 1.97e-03 | 4.11e-03 | 5.10e-03 | 6.42e-03 | 7.57e-03 | 7.24e-03 |
| DE_Bin ₄ | 0.00e+00 | 0.00e+00 | 0.00e+00 | 1.64e-04 | 3.62e-03 | 4.61e-03 | 6.74e-03 | 1.14e-02 | 1.09e-02 | 9.05e-03 |
| DE_Bin ₅ | 0.00e+00 | 0.00e+00 | 0.00e+00 | 3.29e-04 | 4.11e-03 | 9.38e-03 | 1.43e-02 | 1.37e-02 | 1.55e-02 | 1.32e-02 |
| DE_Bin ₆ | 0.00e+00 | 0.00e+00 | 0.00e+00 | 1.64e-04 | 6.74e-03 | 1.12e-02 | 1.79e-02 | 1.94e-02 | 2.25e-02 | 1.91e-02 |
| DE_Bin ₇ | 0.00e+00 | 0.00e+00 | 0.00e+00 | 4.93e-04 | 7.57e-03 | 1.89e-02 | 2.45e-02 | 2.98e-02 | 3.21e-02 | 3.03e-02 |
| DE_Bin ₈ | 0.00e+00 | 0.00e+00 | 0.00e+00 | 1.64e-04 | 1.25e-02 | 2.66e-02 | 3.87e-02 | 4.39e-02 | 5.23e-02 | 4.95e-02 |
| Pixel 5 | PE_Bin ₁ | PE_Bin ₁₀ |
| DE_Bin ₁ | 0.00e+00 | 0.00e+00 | 0.00e+00 | 0.00e+00 | 1.48e-03 | 1.15e-03 | 1.48e-03 | 2.14e-03 | 2.96e-03 | 2.47e-03 |
| DE_Bin ₂ | 0.00e+00 | 0.00e+00 | 0.00e+00 | 0.00e+00 | 1.32e-03 | 3.13e-03 | 2.30e-03 | 3.45e-03 | 3.78e-03 | 4.28e-03 |
| DE_Bin ₃ | 0.00e+00 | 0.00e+00 | 0.00e+00 | 0.00e+00 | 1.48e-03 | 3.62e-03 | 5.43e-03 | 6.25e-03 | 7.07e-03 | 7.73e-03 |
| DE_Bin ₄ | 0.00e+00 | 0.00e+00 | 0.00e+00 | 1.64e-04 | 4.44e-03 | 6.58e-03 | 7.73e-03 | 1.15e-02 | 8.22e-03 | 9.38e-03 |
| DE_Bin ₅ | 0.00e+00 | 0.00e+00 | 0.00e+00 | 0.00e+00 | 5.43e-03 | 9.54e-03 | 1.37e-02 | 1.43e-02 | 1.51e-02 | 1.41e-02 |
| DE_Bin ₆ | 0.00e+00 | 0.00e+00 | 0.00e+00 | 1.64e-04 | 7.40e-03 | 1.09e-02 | 2.07e-02 | 2.27e-02 | 2.07e-02 | 2.27e-02 |
| DE_Bin ₇ | 0.00e+00 | 0.00e+00 | 0.00e+00 | 3.29e-04 | 1.02e-02 | 1.84e-02 | 2.60e-02 | 3.21e-02 | 3.59e-02 | 3.75e-02 |
| DE_Bin ₈ | 0.00e+00 | 0.00e+00 | 0.00e+00 | 3.29e-04 | 8.22e-03 | 2.43e-02 | 4.18e-02 | 5.40e-02 | 5.56e-02 | 5.12e-02 |
| Pixel 6 | PE_Bin ₁ | PE_Bin ₁₀ |
| DE_Bin ₁ | 0.00e+00 | 0.00e+00 | 0.00e+00 | 0.00e+00 | 8.22e-04 | 1.15e-03 | 1.64e-03 | 2.47e-03 | 2.14e-03 | 1.48e-03 |
| DE_Bin ₂ | 0.00e+00 | 0.00e+00 | 0.00e+00 | 0.00e+00 | 9.87e-04 | 1.81e-03 | 3.45e-03 | 3.45e-03 | 4.44e-03 | 3.13e-03 |
| DE_Bin ₃ | 0.00e+00 | 0.00e+00 | 0.00e+00 | 0.00e+00 | 3.29e-03 | 3.45e-03 | 3.78e-03 | 4.77e-03 | 2.96e-03 | 4.11e-03 |
| DE_Bin ₄ | 0.00e+00 | 0.00e+00 | 0.00e+00 | 0.00e+00 | 2.96e-03 | 4.28e-03 | 7.73e-03 | 6.91e-03 | 9.38e-03 | 8.72e-03 |
| DE_Bin ₅ | 0.00e+00 | 0.00e+00 | 0.00e+00 | 1.64e-04 | 4.11e-03 | 7.40e-03 | 7.40e-03 | 1.18e-02 | 1.17e-02 | 1.15e-02 |
| DE_Bin ₆ | 0.00e+00 | 0.00e+00 | 0.00e+00 | 3.29e-04 | 6.09e-03 | 9.87e-03 | 1.58e-02 | 1.69e-02 | 1.64e-02 | 1.76e-02 |
| DE_Bin ₇ | 0.00e+00 | 0.00e+00 | 0.00e+00 | 3.29e-04 | 8.22e-03 | 1.32e-02 | 2.39e-02 | 2.43e-02 | 2.99e-02 | 2.55e-02 |
| DE_Bin ₈ | 0.00e+00 | 0.00e+00 | 0.00e+00 | 1.64e-04 | 9.21e-03 | 2.09e-02 | 3.36e-02 | 4.49e-02 | 4.23e-02 | 3.87e-02 |

| Pixel 7 | PE_Bin ₁ | PE_Bin ₁₀ |
|---------------------|---------------------|---------------------|---------------------|---------------------|---------------------|---------------------|---------------------|---------------------|---------------------|----------------------|
| DE_Bin ₁ | 0.00e+00 | 0.00e+00 | 0.00e+00 | 0.00e+00 | 8.22e-04 | 2.47e-03 | 2.14e-03 | 1.81e-03 | 1.64e-03 | 2.96e-03 |
| DE_Bin ₂ | 0.00e+00 | 0.00e+00 | 0.00e+00 | 0.00e+00 | 1.32e-03 | 2.63e-03 | 9.87e-04 | 3.29e-03 | 2.63e-03 | 3.62e-03 |
| DE_Bin ₃ | 0.00e+00 | 0.00e+00 | 0.00e+00 | 0.00e+00 | 2.14e-03 | 3.78e-03 | 3.13e-03 | 4.28e-03 | 4.93e-03 | 6.09e-03 |
| DE_Bin ₄ | 0.00e+00 | 0.00e+00 | 0.00e+00 | 3.29e-04 | 2.63e-03 | 2.96e-03 | 7.07e-03 | 6.25e-03 | 7.40e-03 | 7.40e-03 |
| DE_Bin ₅ | 0.00e+00 | 0.00e+00 | 0.00e+00 | 1.64e-04 | 3.45e-03 | 6.42e-03 | 7.90e-03 | 1.14e-02 | 1.32e-02 | 1.10e-02 |
| DE_Bin ₆ | 0.00e+00 | 0.00e+00 | 0.00e+00 | 1.64e-04 | 4.93e-03 | 9.05e-03 | 1.38e-02 | 1.74e-02 | 1.96e-02 | 1.64e-02 |
| DE_Bin ₇ | 0.00e+00 | 0.00e+00 | 0.00e+00 | 6.58e-04 | 9.54e-03 | 1.53e-02 | 2.19e-02 | 2.12e-02 | 2.75e-02 | 2.65e-02 |
| DE_Bin ₈ | 0.00e+00 | 0.00e+00 | 0.00e+00 | 1.64e-04 | 9.54e-03 | 1.97e-02 | 3.03e-02 | 4.01e-02 | 4.21e-02 | 4.23e-02 |
| Pixel 8 | PE_Bin ₁ | PE_Bin ₁₀ |
| DE_Bin ₁ | 0.00e+00 | 0.00e+00 | 0.00e+00 | 1.64e-04 | 1.15e-03 | 2.14e-03 | 1.15e-03 | 2.80e-03 | 1.97e-03 | 2.30e-03 |
| DE_Bin ₂ | 0.00e+00 | 0.00e+00 | 0.00e+00 | 0.00e+00 | 9.87e-04 | 1.97e-03 | 2.63e-03 | 3.45e-03 | 2.96e-03 | 1.64e-03 |
| DE_Bin ₃ | 0.00e+00 | 0.00e+00 | 0.00e+00 | 1.64e-04 | 1.48e-03 | 2.63e-03 | 4.44e-03 | 4.61e-03 | 5.26e-03 | 5.26e-03 |
| DE_Bin ₄ | 0.00e+00 | 0.00e+00 | 0.00e+00 | 3.29e-04 | 2.96e-03 | 2.80e-03 | 5.76e-03 | 5.43e-03 | 7.57e-03 | 7.24e-03 |
| DE_Bin ₅ | 0.00e+00 | 0.00e+00 | 0.00e+00 | 1.64e-04 | 4.93e-03 | 5.92e-03 | 8.55e-03 | 1.07e-02 | 1.32e-02 | 9.71e-03 |
| DE_Bin ₆ | 0.00e+00 | 0.00e+00 | 0.00e+00 | 1.64e-04 | 7.07e-03 | 1.00e-02 | 1.41e-02 | 1.71e-02 | 1.58e-02 | 1.43e-02 |
| DE_Bin ₇ | 0.00e+00 | 0.00e+00 | 0.00e+00 | 1.64e-04 | 8.55e-03 | 1.69e-02 | 1.86e-02 | 2.55e-02 | 2.43e-02 | 2.68e-02 |
| DE_Bin ₈ | 0.00e+00 | 0.00e+00 | 0.00e+00 | 3.29e-04 | 9.54e-03 | 2.17e-02 | 3.13e-02 | 3.77e-02 | 4.26e-02 | 3.88e-02 |
| Pixel 9 | PE_Bin ₁ | PE_Bin ₁₀ |
| DE_Bin ₁ | 0.00e+00 | 0.00e+00 | 0.00e+00 | 0.00e+00 | 1.15e-03 | 1.64e-03 | 1.81e-03 | 2.14e-03 | 2.14e-03 | 2.63e-03 |
| DE_Bin ₂ | 0.00e+00 | 0.00e+00 | 0.00e+00 | 0.00e+00 | 1.97e-03 | 2.14e-03 | 2.47e-03 | 4.44e-03 | 3.78e-03 | 3.95e-03 |
| DE_Bin ₃ | 0.00e+00 | 0.00e+00 | 0.00e+00 | 0.00e+00 | 1.64e-03 | 3.45e-03 | 3.45e-03 | 4.93e-03 | 5.10e-03 | 3.95e-03 |
| DE_Bin ₄ | 0.00e+00 | 0.00e+00 | 0.00e+00 | 3.29e-04 | 2.47e-03 | 5.59e-03 | 5.43e-03 | 8.55e-03 | 6.25e-03 | 6.91e-03 |
| DE_Bin ₅ | 0.00e+00 | 0.00e+00 | 0.00e+00 | 1.64e-04 | 3.29e-03 | 7.90e-03 | 9.54e-03 | 1.12e-02 | 1.00e-02 | 1.05e-02 |
| DE_Bin ₆ | 0.00e+00 | 0.00e+00 | 0.00e+00 | 0.00e+00 | 4.28e-03 | 9.71e-03 | 1.50e-02 | 1.61e-02 | 1.68e-02 | 1.38e-02 |
| DE_Bin ₇ | 0.00e+00 | 0.00e+00 | 0.00e+00 | 8.22e-04 | 8.55e-03 | 1.66e-02 | 1.99e-02 | 2.45e-02 | 2.45e-02 | 2.30e-02 |
| DE_Bin ₈ | 0.00e+00 | 0.00e+00 | 0.00e+00 | 1.64e-04 | 8.39e-03 | 2.35e-02 | 2.96e-02 | 3.95e-02 | 3.88e-02 | 3.88e-02 |
| Pixel 10 | PE_Bin ₁ | PE_Bin ₁₀ |
| DE_Bin ₁ | 0.00e+00 | 0.00e+00 | 0.00e+00 | 1.64e-04 | 4.93e-04 | 2.14e-03 | 2.80e-03 | 3.29e-03 | 1.64e-03 | 2.80e-03 |
| DE_Bin ₂ | 0.00e+00 | 0.00e+00 | 0.00e+00 | 0.00e+00 | 1.32e-03 | 1.64e-03 | 3.13e-03 | 3.45e-03 | 4.61e-03 | 3.13e-03 |
| DE_Bin ₃ | 0.00e+00 | 0.00e+00 | 0.00e+00 | 0.00e+00 | 2.14e-03 | 2.96e-03 | 4.28e-03 | 5.43e-03 | 6.58e-03 | 6.74e-03 |
| DE_Bin ₄ | 0.00e+00 | 0.00e+00 | 0.00e+00 | 1.64e-04 | 3.45e-03 | 5.59e-03 | 6.91e-03 | 7.57e-03 | 7.90e-03 | 7.57e-03 |
| DE_Bin ₅ | 0.00e+00 | 0.00e+00 | 0.00e+00 | 3.29e-04 | 5.10e-03 | 7.73e-03 | 1.00e-02 | 1.22e-02 | 1.20e-02 | 1.04e-02 |
| DE_Bin ₆ | 0.00e+00 | 0.00e+00 | 0.00e+00 | 3.29e-04 | 5.43e-03 | 1.05e-02 | 1.74e-02 | 1.56e-02 | 1.32e-02 | 1.81e-02 |
| DE_Bin ₇ | 0.00e+00 | 0.00e+00 | 0.00e+00 | 0.00e+00 | 1.04e-02 | 1.43e-02 | 2.43e-02 | 2.53e-02 | 2.80e-02 | 2.99e-02 |
| DE_Bin ₈ | 0.00e+00 | 0.00e+00 | 0.00e+00 | 3.29e-04 | 9.71e-03 | 2.17e-02 | 3.22e-02 | 3.68e-02 | 4.16e-02 | 3.85e-02 |
| Pixel 11 | PE_Bin ₁ | PE_Bin ₁₀ |
| DE_Bin ₁ | 0.00e+00 | 0.00e+00 | 0.00e+00 | 0.00e+00 | 1.48e-03 | 8.22e-04 | 1.81e-03 | 2.96e-03 | 3.13e-03 | 2.63e-03 |
| DE_Bin ₂ | 0.00e+00 | 0.00e+00 | 0.00e+00 | 1.64e-04 | 1.32e-03 | 2.30e-03 | 4.11e-03 | 5.59e-03 | 5.59e-03 | 3.78e-03 |
| DE_Bin ₃ | 0.00e+00 | 0.00e+00 | 0.00e+00 | 0.00e+00 | 1.97e-03 | 4.61e-03 | 6.42e-03 | 6.74e-03 | 5.76e-03 | 4.44e-03 |
| DE_Bin ₄ | 0.00e+00 | 0.00e+00 | 0.00e+00 | 0.00e+00 | 3.29e-03 | 6.42e-03 | 7.57e-03 | 1.22e-02 | 9.71e-03 | 1.14e-02 |
| DE_Bin ₅ | 0.00e+00 | 0.00e+00 | 0.00e+00 | 0.00e+00 | 5.10e-03 | 9.05e-03 | 1.28e-02 | 1.56e-02 | 1.64e-02 | 1.46e-02 |
| DE_Bin ₆ | 0.00e+00 | 0.00e+00 | 0.00e+00 | 1.64e-04 | 6.42e-03 | 1.12e-02 | 1.73e-02 | 2.40e-02 | 2.22e-02 | 2.12e-02 |
| DE_Bin ₇ | 0.00e+00 | 0.00e+00 | 0.00e+00 | 0.00e+00 | 1.00e-02 | 1.89e-02 | 2.76e-02 | 4.01e-02 | 3.60e-02 | 3.14e-02 |
| DE_Bin ₈ | 0.00e+00 | 0.00e+00 | 0.00e+00 | 1.64e-04 | 1.14e-02 | 2.75e-02 | 3.68e-02 | 5.31e-02 | 5.15e-02 | 5.53e-02 |
| Pixel 12 | PE_Bin ₁ | PE_Bin ₁₀ |
| DE_Bin ₁ | 0.00e+00 | 0.00e+00 | 0.00e+00 | 0.00e+00 | 1.48e-03 | 1.64e-03 | 3.29e-03 | 2.30e-03 | 2.14e-03 | 1.15e-03 |
| DE_Bin ₂ | 0.00e+00 | 0.00e+00 | 0.00e+00 | 0.00e+00 | 1.97e-03 | 2.30e-03 | 4.77e-03 | 4.61e-03 | 4.44e-03 | 5.10e-03 |
| DE_Bin ₃ | 0.00e+00 | 0.00e+00 | 0.00e+00 | 0.00e+00 | 1.97e-03 | 4.11e-03 | 6.74e-03 | 7.07e-03 | 6.58e-03 | 5.10e-03 |
| DE_Bin ₄ | 0.00e+00 | 0.00e+00 | 0.00e+00 | 0.00e+00 | 2.80e-03 | 5.76e-03 | 8.39e-03 | 8.39e-03 | 1.04e-02 | 1.00e-02 |
| DE_Bin ₅ | 0.00e+00 | 0.00e+00 | 0.00e+00 | 3.29e-04 | 3.62e-03 | 7.40e-03 | 1.00e-02 | 1.27e-02 | 1.28e-02 | 1.51e-02 |
| DE_Bin ₆ | 0.00e+00 | 0.00e+00 | 0.00e+00 | 1.64e-04 | 6.25e-03 | 1.32e-02 | 1.78e-02 | 2.01e-02 | 2.12e-02 | 1.84e-02 |
| DE_Bin ₇ | 0.00e+00 | 0.00e+00 | 0.00e+00 | 1.64e-04 | 9.38e-03 | 1.97e-02 | 2.85e-02 | 3.47e-02 | 3.60e-02 | 3.27e-02 |
| DE_Bin ₈ | 0.00e+00 | 0.00e+00 | 0.00e+00 | 4.93e-04 | 1.02e-02 | 2.73e-02 | 3.24e-02 | 5.21e-02 | 4.77e-02 | 4.82e-02 |
| Pixel 13 | PE_Bin ₁ | PE_Bin ₁₀ |
| DE_Bin ₁ | 0.00e+00 | 0.00e+00 | 0.00e+00 | 0.00e+00 | 1.15e-03 | 1.64e-03 | 1.81e-03 | 2.96e-03 | 2.96e-03 | 2.80e-03 |
| DE_Bin ₂ | 0.00e+00 | 0.00e+00 | 0.00e+00 | 0.00e+00 | 1.97e-03 | 2.47e-03 | 2.63e-03 | 4.28e-03 | 3.45e-03 | 4.61e-03 |
| DE_Bin ₃ | 0.00e+00 | 0.00e+00 | 0.00e+00 | 0.00e+00 | 2.30e-03 | 3.13e-03 | 5.76e-03 | 7.07e-03 | 6.25e-03 | 5.10e-03 |
| DE_Bin ₄ | 0.00e+00 | 0.00e+00 | 0.00e+00 | 1.64e-04 | 1.97e-03 | 5.76e-03 | 5.76e-03 | 1.00e-02 | 1.02e-02 | 9.54e-03 |
| DE_Bin ₅ | 0.00e+00 | 0.00e+00 | 0.00e+00 | 0.00e+00 | 3.95e-03 | 6.58e-03 | 1.14e-02 | 1.50e-02 | 1.20e-02 | 1.63e-02 |
| DE_Bin ₆ | 0.00e+00 | 0.00e+00 | 0.00e+00 | 3.29e-04 | 5.76e-03 | 1.20e-02 | 1.92e-02 | 2.09e-02 | 2.34e-02 | 2.17e-02 |
| DE_Bin ₇ | 0.00e+00 | 0.00e+00 | 0.00e+00 | 0.00e+00 | 8.88e-03 | 1.58e-02 | 2.48e-02 | 3.24e-02 | 3.47e-02 | 3.44e-02 |
| DE_Bin ₈ | 0.00e+00 | 0.00e+00 | 0.00e+00 | 3.29e-04 | 1.15e-02 | 2.62e-02 | 3.65e-02 | 4.57e-02 | 5.15e-02 | 5.49e-02 |

| Pixel 14 | PE_Bin ₁ | PE_Bin ₁₀ |
|---------------------|---------------------|---------------------|---------------------|---------------------|---------------------|---------------------|---------------------|---------------------|---------------------|----------------------|
| DE_Bin ₁ | 0.00e+00 | 0.00e+00 | 0.00e+00 | 0.00e+00 | 1.32e-03 | 1.48e-03 | 1.81e-03 | 1.97e-03 | 4.28e-03 | 2.14e-03 |
| DE_Bin ₂ | 0.00e+00 | 0.00e+00 | 0.00e+00 | 1.64e-04 | 1.97e-03 | 2.96e-03 | 4.11e-03 | 4.61e-03 | 5.76e-03 | 3.62e-03 |
| DE_Bin ₃ | 0.00e+00 | 0.00e+00 | 0.00e+00 | 1.64e-04 | 1.64e-03 | 4.44e-03 | 5.76e-03 | 5.43e-03 | 6.74e-03 | 6.91e-03 |
| DE_Bin ₄ | 0.00e+00 | 0.00e+00 | 0.00e+00 | 0.00e+00 | 2.63e-03 | 8.88e-03 | 7.40e-03 | 9.38e-03 | 8.55e-03 | 1.02e-02 |
| DE_Bin ₅ | 0.00e+00 | 0.00e+00 | 0.00e+00 | 1.64e-04 | 5.43e-03 | 1.04e-02 | 1.12e-02 | 1.12e-02 | 1.27e-02 | 1.27e-02 |
| DE_Bin ₆ | 0.00e+00 | 0.00e+00 | 0.00e+00 | 4.93e-04 | 6.74e-03 | 1.32e-02 | 1.55e-02 | 2.09e-02 | 2.27e-02 | 2.32e-02 |
| DE_Bin ₇ | 0.00e+00 | 0.00e+00 | 0.00e+00 | 1.64e-04 | 1.14e-02 | 1.73e-02 | 2.30e-02 | 3.21e-02 | 3.11e-02 | 3.36e-02 |
| DE_Bin ₈ | 0.00e+00 | 0.00e+00 | 0.00e+00 | 3.29e-04 | 1.18e-02 | 2.42e-02 | 3.90e-02 | 4.84e-02 | 4.95e-02 | 4.85e-02 |
| Pixel 15 | PE_Bin ₁ | PE_Bin ₁₀ |
| DE_Bin ₁ | 0.00e+00 | 0.00e+00 | 0.00e+00 | 0.00e+00 | 4.93e-04 | 1.15e-03 | 1.15e-03 | 2.96e-03 | 2.96e-03 | 3.29e-03 |
| DE_Bin ₂ | 0.00e+00 | 0.00e+00 | 0.00e+00 | 0.00e+00 | 9.87e-04 | 2.96e-03 | 3.45e-03 | 4.11e-03 | 4.44e-03 | 4.93e-03 |
| DE_Bin ₃ | 0.00e+00 | 0.00e+00 | 0.00e+00 | 1.64e-04 | 2.63e-03 | 5.10e-03 | 5.92e-03 | 8.55e-03 | 7.07e-03 | 6.42e-03 |
| DE_Bin ₄ | 0.00e+00 | 0.00e+00 | 0.00e+00 | 1.64e-04 | 3.45e-03 | 4.93e-03 | 8.39e-03 | 8.88e-03 | 9.38e-03 | 1.18e-02 |
| DE_Bin ₅ | 0.00e+00 | 0.00e+00 | 0.00e+00 | 1.64e-04 | 4.28e-03 | 9.54e-03 | 1.20e-02 | 1.50e-02 | 1.15e-02 | 1.45e-02 |
| DE_Bin ₆ | 0.00e+00 | 0.00e+00 | 0.00e+00 | 3.29e-04 | 6.42e-03 | 1.40e-02 | 1.66e-02 | 1.88e-02 | 2.34e-02 | 2.42e-02 |
| DE_Bin ₇ | 0.00e+00 | 0.00e+00 | 0.00e+00 | 4.93e-04 | 9.21e-03 | 1.94e-02 | 2.57e-02 | 3.13e-02 | 3.59e-02 | 3.36e-02 |
| DE_Bin ₈ | 0.00e+00 | 0.00e+00 | 0.00e+00 | 0.00e+00 | 1.25e-02 | 2.48e-02 | 4.34e-02 | 5.28e-02 | 5.84e-02 | 5.12e-02 |

Table A.3: This table gives the product of the probability array and the geometrical factor of the simulation source (GF_{source}) for all 16 big pixels of STEP when we simulated with protons. Eight energy deposit ranges are 3-4.4 keV, 4.4-6.47 keV, 6.47-9.5 keV, 9.5-13.96 keV, 13.96-20.5 keV, 20.5-30.13 keV, 30.13-44.25 keV, and 44.25-65 keV. Ten primary energy ranges are 100-398 keV, 398 keV-1.58 MeV, 1.58-6.3 MeV, 6.3-25.1 MeV, 25.1-100 MeV, 100-398 MeV, 398 MeV-1.58 GeV, 1.58-6.3 GeV, 6.3-25.1 GeV, and 25.1-100 GeV.

| Pixel 0 | PE_Bin ₁ | PE_Bin ₂ | PE_Bin ₃ | PE_Bin ₄ | PE_Bin ₅ | PE_Bin ₆ | PE_Bin ₇ | PE_Bin ₈ | PE_Bin ₉ | PE_Bin ₁₀ |
|---------------------|---------------------|---------------------|---------------------|---------------------|---------------------|---------------------|---------------------|---------------------|---------------------|----------------------|
| DE_Bin ₁ | 0.00e+00 | 4.93e-04 | 2.30e-03 | 3.29e-03 | 3.78e-03 | 4.61e-03 | 6.25e-03 | 3.95e-03 | 5.10e-03 | 3.78e-03 |
| DE_Bin ₂ | 0.00e+00 | 4.93e-04 | 3.13e-03 | 4.61e-03 | 6.25e-03 | 5.43e-03 | 6.74e-03 | 5.76e-03 | 4.77e-03 | 7.90e-03 |
| DE_Bin ₃ | 0.00e+00 | 9.87e-04 | 4.61e-03 | 8.39e-03 | 9.54e-03 | 7.40e-03 | 6.74e-03 | 1.07e-02 | 6.25e-03 | 8.88e-03 |
| DE_Bin ₄ | 0.00e+00 | 2.47e-03 | 8.39e-03 | 1.51e-02 | 1.38e-02 | 1.43e-02 | 1.38e-02 | 1.55e-02 | 1.45e-02 | 1.37e-02 |
| DE_Bin ₅ | 0.00e+00 | 2.63e-03 | 1.18e-02 | 1.76e-02 | 1.84e-02 | 2.07e-02 | 1.91e-02 | 1.97e-02 | 1.97e-02 | 1.89e-02 |
| DE_Bin ₆ | 0.00e+00 | 4.11e-03 | 1.66e-02 | 2.34e-02 | 2.57e-02 | 2.60e-02 | 3.26e-02 | 2.88e-02 | 2.75e-02 | 2.96e-02 |
| DE_Bin ₇ | 1.64e-04 | 5.43e-03 | 2.47e-02 | 3.73e-02 | 3.91e-02 | 3.85e-02 | 4.28e-02 | 4.28e-02 | 4.01e-02 | 3.88e-02 |
| DE_Bin ₈ | 0.00e+00 | 1.17e-02 | 3.70e-02 | 5.05e-02 | 6.15e-02 | 5.82e-02 | 6.73e-02 | 6.60e-02 | 7.11e-02 | 6.27e-02 |
| Pixel 1 | PE_Bin ₁ | PE_Bin ₂ | PE_Bin ₃ | PE_Bin ₄ | PE_Bin ₅ | PE_Bin ₆ | PE_Bin ₇ | PE_Bin ₈ | PE_Bin ₉ | PE_Bin ₁₀ |
| DE_Bin ₁ | 0.00e+00 | 3.29e-04 | 1.48e-03 | 2.63e-03 | 1.97e-03 | 3.29e-03 | 4.44e-03 | 4.11e-03 | 2.96e-03 | 2.96e-03 |
| DE_Bin ₂ | 0.00e+00 | 4.93e-04 | 3.29e-03 | 3.62e-03 | 3.62e-03 | 4.11e-03 | 4.28e-03 | 4.61e-03 | 2.47e-03 | 4.77e-03 |
| DE_Bin ₃ | 0.00e+00 | 1.64e-04 | 2.96e-03 | 7.57e-03 | 6.09e-03 | 1.02e-02 | 5.92e-03 | 6.91e-03 | 7.07e-03 | 9.05e-03 |
| DE_Bin ₄ | 0.00e+00 | 1.48e-03 | 6.09e-03 | 9.71e-03 | 1.37e-02 | 1.10e-02 | 1.02e-02 | 1.25e-02 | 1.14e-02 | 1.20e-02 |
| DE_Bin ₅ | 0.00e+00 | 2.63e-03 | 5.76e-03 | 1.23e-02 | 1.48e-02 | 1.66e-02 | 1.35e-02 | 1.76e-02 | 1.30e-02 | 1.64e-02 |
| DE_Bin ₆ | 0.00e+00 | 4.44e-03 | 1.02e-02 | 1.81e-02 | 2.17e-02 | 2.11e-02 | 2.02e-02 | 2.37e-02 | 2.43e-02 | 2.11e-02 |
| DE_Bin ₇ | 0.00e+00 | 5.76e-03 | 1.78e-02 | 2.68e-02 | 3.67e-02 | 3.50e-02 | 3.44e-02 | 3.41e-02 | 3.44e-02 | 3.36e-02 |
| DE_Bin ₈ | 0.00e+00 | 5.43e-03 | 2.65e-02 | 4.82e-02 | 5.07e-02 | 5.05e-02 | 5.02e-02 | 5.26e-02 | 5.18e-02 | 5.13e-02 |
| Pixel 2 | PE_Bin ₁ | PE_Bin ₂ | PE_Bin ₃ | PE_Bin ₄ | PE_Bin ₅ | PE_Bin ₆ | PE_Bin ₇ | PE_Bin ₈ | PE_Bin ₉ | PE_Bin ₁₀ |
| DE_Bin ₁ | 0.00e+00 | 0.00e+00 | 1.48e-03 | 2.63e-03 | 4.44e-03 | 2.14e-03 | 2.80e-03 | 2.96e-03 | 3.13e-03 | 1.97e-03 |
| DE_Bin ₂ | 0.00e+00 | 8.22e-04 | 2.47e-03 | 3.45e-03 | 2.63e-03 | 3.78e-03 | 5.43e-03 | 3.95e-03 | 2.30e-03 | 3.95e-03 |
| DE_Bin ₃ | 0.00e+00 | 1.97e-03 | 3.78e-03 | 4.77e-03 | 6.58e-03 | 6.25e-03 | 7.24e-03 | 5.76e-03 | 3.95e-03 | 6.91e-03 |
| DE_Bin ₄ | 0.00e+00 | 1.48e-03 | 8.22e-03 | 9.05e-03 | 1.10e-02 | 1.05e-02 | 9.54e-03 | 9.71e-03 | 1.12e-02 | 1.14e-02 |
| DE_Bin ₅ | 0.00e+00 | 2.63e-03 | 8.72e-03 | 1.09e-02 | 1.32e-02 | 1.37e-02 | 1.32e-02 | 1.35e-02 | 1.32e-02 | 1.43e-02 |
| DE_Bin ₆ | 1.64e-04 | 3.45e-03 | 1.07e-02 | 1.83e-02 | 2.43e-02 | 2.32e-02 | 2.17e-02 | 2.25e-02 | 1.84e-02 | 2.02e-02 |
| DE_Bin ₇ | 0.00e+00 | 5.92e-03 | 2.06e-02 | 2.62e-02 | 3.52e-02 | 3.32e-02 | 3.31e-02 | 3.42e-02 | 3.37e-02 | 3.49e-02 |
| DE_Bin ₈ | 0.00e+00 | 6.74e-03 | 2.98e-02 | 3.95e-02 | 4.57e-02 | 5.48e-02 | 4.67e-02 | 5.02e-02 | 4.79e-02 | 4.19e-02 |

| Pixel 3 | PE_Bin ₁ | PE_Bin ₂ | PE_Bin ₃ | PE_Bin ₄ | PE_Bin ₅ | PE_Bin ₆ | PE_Bin ₇ | PE_Bin ₈ | PE_Bin ₉ | PE_Bin ₁₀ |
|---------------------|---------------------|---------------------|---------------------|---------------------|---------------------|---------------------|---------------------|---------------------|---------------------|----------------------|
| DE_Bin ₁ | 0.00e+00 | 1.64e-04 | 2.14e-03 | 2.47e-03 | 2.30e-03 | 2.30e-03 | 3.29e-03 | 2.96e-03 | 2.96e-03 | 2.30e-03 |
| DE_Bin ₂ | 0.00e+00 | 8.22e-04 | 2.96e-03 | 3.78e-03 | 4.28e-03 | 3.45e-03 | 3.95e-03 | 3.29e-03 | 4.11e-03 | 3.29e-03 |
| DE_Bin ₃ | 0.00e+00 | 1.97e-03 | 3.45e-03 | 5.26e-03 | 7.07e-03 | 6.58e-03 | 7.73e-03 | 7.57e-03 | 6.09e-03 | 6.91e-03 |
| DE_Bin ₄ | 0.00e+00 | 2.80e-03 | 7.40e-03 | 8.88e-03 | 1.28e-02 | 1.09e-02 | 1.07e-02 | 1.09e-02 | 8.72e-03 | 9.21e-03 |
| DE_Bin ₅ | 0.00e+00 | 2.63e-03 | 8.06e-03 | 1.12e-02 | 1.20e-02 | 1.48e-02 | 1.35e-02 | 1.27e-02 | 1.63e-02 | 1.25e-02 |
| DE_Bin ₆ | 0.00e+00 | 3.78e-03 | 1.18e-02 | 1.69e-02 | 1.84e-02 | 2.02e-02 | 2.22e-02 | 2.42e-02 | 2.20e-02 | 2.19e-02 |
| DE_Bin ₇ | 0.00e+00 | 5.26e-03 | 2.02e-02 | 2.52e-02 | 2.83e-02 | 3.36e-02 | 3.31e-02 | 3.29e-02 | 3.06e-02 | 2.52e-02 |
| DE_Bin ₈ | 0.00e+00 | 1.09e-02 | 3.17e-02 | 4.11e-02 | 4.69e-02 | 5.07e-02 | 4.72e-02 | 5.49e-02 | 4.77e-02 | 4.64e-02 |
| Pixel 4 | PE_Bin ₁ | PE_Bin ₂ | PE_Bin ₃ | PE_Bin ₄ | PE_Bin ₅ | PE_Bin ₆ | PE_Bin ₇ | PE_Bin ₈ | PE_Bin ₉ | PE_Bin ₁₀ |
| DE_Bin ₁ | 0.00e+00 | 3.29e-04 | 3.29e-04 | 1.81e-03 | 2.14e-03 | 3.29e-03 | 2.96e-03 | 2.80e-03 | 1.32e-03 | 2.80e-03 |
| DE_Bin ₂ | 0.00e+00 | 6.58e-04 | 2.30e-03 | 4.77e-03 | 4.28e-03 | 3.29e-03 | 6.09e-03 | 5.10e-03 | 3.78e-03 | 6.09e-03 |
| DE_Bin ₃ | 1.64e-04 | 8.22e-04 | 3.95e-03 | 8.22e-03 | 7.73e-03 | 6.25e-03 | 7.24e-03 | 7.24e-03 | 7.24e-03 | 5.92e-03 |
| DE_Bin ₄ | 0.00e+00 | 2.47e-03 | 8.06e-03 | 7.73e-03 | 1.28e-02 | 1.09e-02 | 1.37e-02 | 1.04e-02 | 7.57e-03 | 9.05e-03 |
| DE_Bin ₅ | 0.00e+00 | 2.96e-03 | 9.54e-03 | 1.17e-02 | 1.60e-02 | 1.63e-02 | 1.64e-02 | 1.46e-02 | 1.38e-02 | 1.45e-02 |
| DE_Bin ₆ | 0.00e+00 | 4.11e-03 | 1.35e-02 | 1.56e-02 | 1.86e-02 | 1.76e-02 | 2.55e-02 | 2.40e-02 | 1.96e-02 | 2.11e-02 |
| DE_Bin ₇ | 0.00e+00 | 5.59e-03 | 1.88e-02 | 2.48e-02 | 3.39e-02 | 2.94e-02 | 3.41e-02 | 3.37e-02 | 3.27e-02 | 3.17e-02 |
| DE_Bin ₈ | 0.00e+00 | 9.21e-03 | 3.01e-02 | 4.00e-02 | 5.31e-02 | 4.82e-02 | 4.72e-02 | 5.15e-02 | 4.95e-02 | 5.15e-02 |
| Pixel 5 | PE_Bin ₁ | PE_Bin ₂ | PE_Bin ₃ | PE_Bin ₄ | PE_Bin ₅ | PE_Bin ₆ | PE_Bin ₇ | PE_Bin ₈ | PE_Bin ₉ | PE_Bin ₁₀ |
| DE_Bin ₁ | 0.00e+00 | 1.64e-04 | 9.87e-04 | 2.80e-03 | 3.62e-03 | 2.47e-03 | 2.63e-03 | 4.61e-03 | 3.29e-03 | 2.47e-03 |
| DE_Bin ₂ | 0.00e+00 | 6.58e-04 | 2.47e-03 | 4.11e-03 | 3.62e-03 | 4.28e-03 | 4.11e-03 | 4.61e-03 | 3.45e-03 | 4.61e-03 |
| DE_Bin ₃ | 0.00e+00 | 6.58e-04 | 2.96e-03 | 4.93e-03 | 6.58e-03 | 7.73e-03 | 8.22e-03 | 6.25e-03 | 8.55e-03 | 8.22e-03 |
| DE_Bin ₄ | 0.00e+00 | 2.30e-03 | 6.91e-03 | 1.04e-02 | 1.28e-02 | 1.20e-02 | 1.17e-02 | 1.07e-02 | 1.10e-02 | 1.33e-02 |
| DE_Bin ₅ | 0.00e+00 | 1.97e-03 | 1.02e-02 | 1.35e-02 | 1.74e-02 | 1.58e-02 | 1.64e-02 | 1.38e-02 | 1.35e-02 | 1.86e-02 |
| DE_Bin ₆ | 0.00e+00 | 4.77e-03 | 1.32e-02 | 1.97e-02 | 2.39e-02 | 2.39e-02 | 2.30e-02 | 2.32e-02 | 2.53e-02 | 2.43e-02 |
| DE_Bin ₇ | 0.00e+00 | 3.95e-03 | 1.97e-02 | 2.62e-02 | 3.52e-02 | 3.27e-02 | 3.45e-02 | 3.37e-02 | 3.26e-02 | 3.44e-02 |
| DE_Bin ₈ | 0.00e+00 | 7.24e-03 | 2.55e-02 | 3.87e-02 | 4.62e-02 | 4.70e-02 | 4.74e-02 | 5.43e-02 | 5.07e-02 | 4.82e-02 |
| Pixel 6 | PE_Bin ₁ | PE_Bin ₂ | PE_Bin ₃ | PE_Bin ₄ | PE_Bin ₅ | PE_Bin ₆ | PE_Bin ₇ | PE_Bin ₈ | PE_Bin ₉ | PE_Bin ₁₀ |
| DE_Bin ₁ | 0.00e+00 | 3.29e-04 | 1.15e-03 | 1.64e-03 | 2.80e-03 | 1.64e-03 | 1.97e-03 | 1.97e-03 | 3.29e-03 | 1.81e-03 |
| DE_Bin ₂ | 0.00e+00 | 6.58e-04 | 2.30e-03 | 2.96e-03 | 3.13e-03 | 3.95e-03 | 4.44e-03 | 3.13e-03 | 2.30e-03 | 4.11e-03 |
| DE_Bin ₃ | 0.00e+00 | 1.32e-03 | 2.96e-03 | 4.61e-03 | 5.26e-03 | 6.25e-03 | 4.93e-03 | 5.43e-03 | 4.28e-03 | 5.10e-03 |
| DE_Bin ₄ | 0.00e+00 | 6.58e-04 | 6.09e-03 | 7.57e-03 | 1.05e-02 | 9.54e-03 | 8.39e-03 | 7.24e-03 | 9.87e-03 | 8.06e-03 |
| DE_Bin ₅ | 0.00e+00 | 1.48e-03 | 7.57e-03 | 1.10e-02 | 1.05e-02 | 1.30e-02 | 1.10e-02 | 1.30e-02 | 1.10e-02 | 1.10e-02 |
| DE_Bin ₆ | 0.00e+00 | 2.30e-03 | 1.18e-02 | 1.64e-02 | 1.56e-02 | 1.45e-02 | 1.79e-02 | 1.48e-02 | 1.84e-02 | 1.48e-02 |
| DE_Bin ₇ | 0.00e+00 | 4.77e-03 | 1.53e-02 | 2.24e-02 | 2.73e-02 | 2.39e-02 | 2.52e-02 | 2.66e-02 | 2.62e-02 | 2.68e-02 |
| DE_Bin ₈ | 0.00e+00 | 5.76e-03 | 2.22e-02 | 2.90e-02 | 3.91e-02 | 3.88e-02 | 4.41e-02 | 4.15e-02 | 3.96e-02 | 3.70e-02 |
| Pixel 7 | PE_Bin ₁ | PE_Bin ₂ | PE_Bin ₃ | PE_Bin ₄ | PE_Bin ₅ | PE_Bin ₆ | PE_Bin ₇ | PE_Bin ₈ | PE_Bin ₉ | PE_Bin ₁₀ |
| DE_Bin ₁ | 0.00e+00 | 3.29e-04 | 9.87e-04 | 1.97e-03 | 2.30e-03 | 1.97e-03 | 2.14e-03 | 1.81e-03 | 2.63e-03 | 1.48e-03 |
| DE_Bin ₂ | 0.00e+00 | 0.00e+00 | 1.32e-03 | 2.30e-03 | 3.29e-03 | 3.62e-03 | 2.80e-03 | 3.29e-03 | 3.45e-03 | 3.95e-03 |
| DE_Bin ₃ | 0.00e+00 | 6.58e-04 | 2.80e-03 | 3.45e-03 | 6.09e-03 | 4.44e-03 | 4.61e-03 | 4.93e-03 | 4.93e-03 | 3.95e-03 |
| DE_Bin ₄ | 0.00e+00 | 1.81e-03 | 5.43e-03 | 5.92e-03 | 9.38e-03 | 7.90e-03 | 1.05e-02 | 7.07e-03 | 7.07e-03 | 6.74e-03 |
| DE_Bin ₅ | 1.64e-04 | 2.63e-03 | 6.91e-03 | 1.07e-02 | 9.71e-03 | 9.05e-03 | 1.15e-02 | 9.05e-03 | 1.22e-02 | 9.21e-03 |
| DE_Bin ₆ | 0.00e+00 | 4.11e-03 | 9.71e-03 | 1.27e-02 | 1.79e-02 | 1.18e-02 | 1.41e-02 | 1.33e-02 | 1.56e-02 | 1.50e-02 |
| DE_Bin ₇ | 0.00e+00 | 5.10e-03 | 1.51e-02 | 1.83e-02 | 2.73e-02 | 2.55e-02 | 2.32e-02 | 2.25e-02 | 2.32e-02 | 2.55e-02 |
| DE_Bin ₈ | 0.00e+00 | 8.72e-03 | 2.30e-02 | 3.13e-02 | 3.77e-02 | 4.24e-02 | 3.87e-02 | 3.77e-02 | 3.98e-02 | 3.39e-02 |
| Pixel 8 | PE_Bin ₁ | PE_Bin ₂ | PE_Bin ₃ | PE_Bin ₄ | PE_Bin ₅ | PE_Bin ₆ | PE_Bin ₇ | PE_Bin ₈ | PE_Bin ₉ | PE_Bin ₁₀ |
| DE_Bin ₁ | 0.00e+00 | 0.00e+00 | 4.93e-04 | 9.87e-04 | 9.87e-04 | 2.47e-03 | 1.81e-03 | 1.64e-03 | 2.30e-03 | 1.97e-03 |
| DE_Bin ₂ | 0.00e+00 | 6.58e-04 | 2.47e-03 | 2.30e-03 | 2.47e-03 | 2.63e-03 | 2.80e-03 | 3.95e-03 | 2.63e-03 | 3.29e-03 |
| DE_Bin ₃ | 0.00e+00 | 1.48e-03 | 2.63e-03 | 3.45e-03 | 4.93e-03 | 6.09e-03 | 4.77e-03 | 5.10e-03 | 5.92e-03 | 5.26e-03 |
| DE_Bin ₄ | 0.00e+00 | 2.80e-03 | 4.11e-03 | 7.40e-03 | 7.57e-03 | 1.05e-02 | 7.90e-03 | 6.09e-03 | 7.07e-03 | 6.25e-03 |
| DE_Bin ₅ | 0.00e+00 | 2.63e-03 | 6.42e-03 | 9.54e-03 | 1.14e-02 | 1.14e-02 | 9.71e-03 | 1.10e-02 | 1.22e-02 | 1.00e-02 |
| DE_Bin ₆ | 0.00e+00 | 4.61e-03 | 6.91e-03 | 1.35e-02 | 1.84e-02 | 1.61e-02 | 1.43e-02 | 1.69e-02 | 1.27e-02 | 1.73e-02 |
| DE_Bin ₇ | 0.00e+00 | 4.44e-03 | 1.68e-02 | 1.96e-02 | 2.22e-02 | 2.29e-02 | 2.19e-02 | 2.14e-02 | 2.70e-02 | 2.63e-02 |
| DE_Bin ₈ | 0.00e+00 | 5.92e-03 | 2.32e-02 | 2.93e-02 | 3.78e-02 | 3.62e-02 | 3.52e-02 | 3.60e-02 | 3.34e-02 | 3.82e-02 |
| Pixel 9 | PE_Bin ₁ | PE_Bin ₂ | PE_Bin ₃ | PE_Bin ₄ | PE_Bin ₅ | PE_Bin ₆ | PE_Bin ₇ | PE_Bin ₈ | PE_Bin ₉ | PE_Bin ₁₀ |
| DE_Bin ₁ | 0.00e+00 | 4.93e-04 | 1.48e-03 | 1.64e-03 | 1.97e-03 | 1.81e-03 | 1.15e-03 | 2.14e-03 | 2.47e-03 | 2.14e-03 |
| DE_Bin ₂ | 0.00e+00 | 3.29e-04 | 2.96e-03 | 2.96e-03 | 3.13e-03 | 3.29e-03 | 2.96e-03 | 2.63e-03 | 3.13e-03 | 4.11e-03 |
| DE_Bin ₃ | 0.00e+00 | 1.32e-03 | 3.13e-03 | 4.44e-03 | 5.59e-03 | 5.59e-03 | 3.95e-03 | 6.25e-03 | 4.44e-03 | 4.28e-03 |
| DE_Bin ₄ | 0.00e+00 | 1.48e-03 | 5.10e-03 | 4.61e-03 | 7.40e-03 | 8.72e-03 | 9.05e-03 | 7.57e-03 | 7.07e-03 | 7.07e-03 |
| DE_Bin ₅ | 0.00e+00 | 2.96e-03 | 4.11e-03 | 1.02e-02 | 1.23e-02 | 1.17e-02 | 1.25e-02 | 1.02e-02 | 1.07e-02 | 8.39e-03 |
| DE_Bin ₆ | 1.64e-04 | 3.29e-03 | 1.18e-02 | 1.28e-02 | 1.66e-02 | 1.79e-02 | 1.64e-02 | 1.63e-02 | 1.58e-02 | 1.38e-02 |
| DE_Bin ₇ | 0.00e+00 | 5.26e-03 | 1.74e-02 | 2.06e-02 | 2.40e-02 | 2.35e-02 | 2.14e-02 | 2.45e-02 | 2.55e-02 | 2.34e-02 |
| DE_Bin ₈ | 0.00e+00 | 5.26e-03 | 2.86e-02 | 2.96e-02 | 3.96e-02 | 3.70e-02 | 4.11e-02 | 4.03e-02 | 4.00e-02 | 3.45e-02 |

| Pixel 10 | PE_Bin ₁ | PE_Bin ₂ | PE_Bin ₃ | PE_Bin ₄ | PE_Bin ₅ | PE_Bin ₆ | PE_Bin ₇ | PE_Bin ₈ | PE_Bin ₉ | PE_Bin ₁₀ |
|---------------------|---------------------|---------------------|---------------------|---------------------|---------------------|---------------------|---------------------|---------------------|---------------------|----------------------|
| DE_Bin ₁ | 0.00e+00 | 3.29e-04 | 6.58e-04 | 1.97e-03 | 2.14e-03 | 1.48e-03 | 2.63e-03 | 3.45e-03 | 2.30e-03 | 1.97e-03 |
| DE_Bin ₂ | 0.00e+00 | 3.29e-04 | 2.96e-03 | 1.97e-03 | 3.78e-03 | 4.28e-03 | 3.62e-03 | 2.80e-03 | 3.45e-03 | 4.44e-03 |
| DE_Bin ₃ | 0.00e+00 | 4.93e-04 | 3.78e-03 | 5.59e-03 | 4.77e-03 | 5.10e-03 | 6.25e-03 | 6.58e-03 | 5.76e-03 | 5.76e-03 |
| DE_Bin ₄ | 0.00e+00 | 1.81e-03 | 5.43e-03 | 7.24e-03 | 1.05e-02 | 1.00e-02 | 1.04e-02 | 6.91e-03 | 9.54e-03 | 1.02e-02 |
| DE_Bin ₅ | 0.00e+00 | 2.14e-03 | 6.25e-03 | 9.05e-03 | 1.22e-02 | 1.20e-02 | 9.71e-03 | 1.09e-02 | 1.20e-02 | 1.10e-02 |
| DE_Bin ₆ | 0.00e+00 | 2.80e-03 | 8.39e-03 | 1.51e-02 | 1.81e-02 | 1.78e-02 | 1.74e-02 | 1.96e-02 | 1.38e-02 | 1.76e-02 |
| DE_Bin ₇ | 0.00e+00 | 4.11e-03 | 1.56e-02 | 1.83e-02 | 2.24e-02 | 2.45e-02 | 2.93e-02 | 2.76e-02 | 2.65e-02 | 2.50e-02 |
| DE_Bin ₈ | 0.00e+00 | 5.92e-03 | 2.32e-02 | 3.01e-02 | 3.90e-02 | 4.41e-02 | 3.85e-02 | 4.44e-02 | 4.18e-02 | 3.41e-02 |
| Pixel 11 | PE_Bin ₁ | PE_Bin ₂ | PE_Bin ₃ | PE_Bin ₄ | PE_Bin ₅ | PE_Bin ₆ | PE_Bin ₇ | PE_Bin ₈ | PE_Bin ₉ | PE_Bin ₁₀ |
| DE_Bin ₁ | 0.00e+00 | 4.93e-04 | 9.87e-04 | 2.47e-03 | 2.47e-03 | 4.61e-03 | 4.11e-03 | 3.62e-03 | 2.30e-03 | 3.45e-03 |
| DE_Bin ₂ | 0.00e+00 | 6.58e-04 | 2.14e-03 | 2.30e-03 | 3.78e-03 | 4.44e-03 | 4.11e-03 | 3.78e-03 | 3.62e-03 | 5.43e-03 |
| DE_Bin ₃ | 0.00e+00 | 6.58e-04 | 4.44e-03 | 6.91e-03 | 5.43e-03 | 6.74e-03 | 6.25e-03 | 6.42e-03 | 8.39e-03 | 7.57e-03 |
| DE_Bin ₄ | 0.00e+00 | 1.48e-03 | 5.76e-03 | 8.06e-03 | 1.14e-02 | 1.17e-02 | 1.27e-02 | 1.25e-02 | 1.09e-02 | 9.87e-03 |
| DE_Bin ₅ | 0.00e+00 | 2.30e-03 | 1.05e-02 | 1.38e-02 | 1.32e-02 | 1.66e-02 | 1.89e-02 | 1.61e-02 | 1.41e-02 | 1.45e-02 |
| DE_Bin ₆ | 0.00e+00 | 4.11e-03 | 1.25e-02 | 1.66e-02 | 1.92e-02 | 2.48e-02 | 2.11e-02 | 2.37e-02 | 2.15e-02 | 2.42e-02 |
| DE_Bin ₇ | 0.00e+00 | 5.76e-03 | 1.84e-02 | 2.68e-02 | 3.32e-02 | 3.32e-02 | 3.54e-02 | 3.08e-02 | 3.55e-02 | 3.59e-02 |
| DE_Bin ₈ | 0.00e+00 | 4.44e-03 | 2.99e-02 | 4.26e-02 | 5.25e-02 | 4.69e-02 | 5.59e-02 | 4.98e-02 | 5.51e-02 | 5.13e-02 |
| Pixel 12 | PE_Bin ₁ | PE_Bin ₂ | PE_Bin ₃ | PE_Bin ₄ | PE_Bin ₅ | PE_Bin ₆ | PE_Bin ₇ | PE_Bin ₈ | PE_Bin ₉ | PE_Bin ₁₀ |
| DE_Bin ₁ | 0.00e+00 | 0.00e+00 | 1.81e-03 | 1.97e-03 | 2.80e-03 | 2.47e-03 | 2.47e-03 | 1.64e-03 | 2.47e-03 | 2.47e-03 |
| DE_Bin ₂ | 0.00e+00 | 0.00e+00 | 2.80e-03 | 3.62e-03 | 3.29e-03 | 5.59e-03 | 4.61e-03 | 5.92e-03 | 6.09e-03 | 4.28e-03 |
| DE_Bin ₃ | 0.00e+00 | 1.48e-03 | 4.28e-03 | 6.25e-03 | 6.42e-03 | 6.58e-03 | 5.76e-03 | 7.57e-03 | 6.25e-03 | 7.40e-03 |
| DE_Bin ₄ | 0.00e+00 | 1.97e-03 | 5.92e-03 | 1.02e-02 | 1.18e-02 | 1.07e-02 | 1.09e-02 | 9.38e-03 | 1.05e-02 | 9.38e-03 |
| DE_Bin ₅ | 1.64e-04 | 1.81e-03 | 8.55e-03 | 1.30e-02 | 1.43e-02 | 1.28e-02 | 1.25e-02 | 1.22e-02 | 1.53e-02 | 1.45e-02 |
| DE_Bin ₆ | 0.00e+00 | 3.29e-03 | 1.25e-02 | 1.84e-02 | 1.88e-02 | 2.50e-02 | 2.27e-02 | 2.11e-02 | 2.39e-02 | 2.25e-02 |
| DE_Bin ₇ | 0.00e+00 | 6.25e-03 | 1.78e-02 | 2.37e-02 | 3.11e-02 | 3.21e-02 | 3.16e-02 | 3.49e-02 | 3.39e-02 | 3.31e-02 |
| DE_Bin ₈ | 0.00e+00 | 8.22e-03 | 2.57e-02 | 3.91e-02 | 4.47e-02 | 4.97e-02 | 4.82e-02 | 5.38e-02 | 4.49e-02 | 5.21e-02 |
| Pixel 13 | PE_Bin ₁ | PE_Bin ₂ | PE_Bin ₃ | PE_Bin ₄ | PE_Bin ₅ | PE_Bin ₆ | PE_Bin ₇ | PE_Bin ₈ | PE_Bin ₉ | PE_Bin ₁₀ |
| DE_Bin ₁ | 0.00e+00 | 4.93e-04 | 4.93e-04 | 1.32e-03 | 2.63e-03 | 3.29e-03 | 2.63e-03 | 2.47e-03 | 2.14e-03 | 2.30e-03 |
| DE_Bin ₂ | 0.00e+00 | 4.93e-04 | 3.78e-03 | 2.80e-03 | 3.62e-03 | 4.61e-03 | 5.10e-03 | 3.62e-03 | 4.61e-03 | 4.11e-03 |
| DE_Bin ₃ | 0.00e+00 | 1.48e-03 | 4.11e-03 | 5.76e-03 | 5.76e-03 | 7.07e-03 | 7.24e-03 | 5.92e-03 | 8.88e-03 | 6.58e-03 |
| DE_Bin ₄ | 0.00e+00 | 2.47e-03 | 5.76e-03 | 1.05e-02 | 1.02e-02 | 1.05e-02 | 1.05e-02 | 1.17e-02 | 1.32e-02 | 1.07e-02 |
| DE_Bin ₅ | 0.00e+00 | 1.48e-03 | 9.05e-03 | 1.28e-02 | 1.43e-02 | 1.81e-02 | 1.17e-02 | 1.68e-02 | 1.38e-02 | 1.37e-02 |
| DE_Bin ₆ | 1.64e-04 | 5.10e-03 | 1.17e-02 | 1.84e-02 | 2.15e-02 | 1.92e-02 | 2.22e-02 | 2.15e-02 | 2.24e-02 | 2.09e-02 |
| DE_Bin ₇ | 0.00e+00 | 5.10e-03 | 1.79e-02 | 2.58e-02 | 3.14e-02 | 2.68e-02 | 3.47e-02 | 3.29e-02 | 3.14e-02 | 3.04e-02 |
| DE_Bin ₈ | 0.00e+00 | 9.21e-03 | 2.78e-02 | 3.85e-02 | 4.97e-02 | 4.92e-02 | 5.08e-02 | 5.21e-02 | 4.97e-02 | 4.69e-02 |
| Pixel 14 | PE_Bin ₁ | PE_Bin ₂ | PE_Bin ₃ | PE_Bin ₄ | PE_Bin ₅ | PE_Bin ₆ | PE_Bin ₇ | PE_Bin ₈ | PE_Bin ₉ | PE_Bin ₁₀ |
| DE_Bin ₁ | 0.00e+00 | 3.29e-04 | 1.97e-03 | 1.48e-03 | 2.96e-03 | 1.97e-03 | 2.47e-03 | 3.13e-03 | 1.97e-03 | 2.80e-03 |
| DE_Bin ₂ | 0.00e+00 | 9.87e-04 | 2.14e-03 | 3.62e-03 | 4.93e-03 | 3.62e-03 | 3.95e-03 | 3.62e-03 | 3.62e-03 | 3.78e-03 |
| DE_Bin ₃ | 0.00e+00 | 6.58e-04 | 4.61e-03 | 5.43e-03 | 7.40e-03 | 5.26e-03 | 7.24e-03 | 6.58e-03 | 8.72e-03 | 6.25e-03 |
| DE_Bin ₄ | 0.00e+00 | 2.96e-03 | 7.24e-03 | 1.07e-02 | 1.14e-02 | 1.07e-02 | 9.54e-03 | 1.17e-02 | 1.10e-02 | 8.39e-03 |
| DE_Bin ₅ | 0.00e+00 | 2.47e-03 | 8.72e-03 | 1.40e-02 | 1.41e-02 | 1.25e-02 | 1.30e-02 | 1.27e-02 | 1.56e-02 | 1.60e-02 |
| DE_Bin ₆ | 1.64e-04 | 3.62e-03 | 1.35e-02 | 1.55e-02 | 2.20e-02 | 1.89e-02 | 2.04e-02 | 2.32e-02 | 2.25e-02 | 2.07e-02 |
| DE_Bin ₇ | 0.00e+00 | 2.96e-03 | 1.99e-02 | 2.71e-02 | 2.91e-02 | 3.01e-02 | 3.08e-02 | 3.36e-02 | 3.59e-02 | 3.32e-02 |
| DE_Bin ₈ | 0.00e+00 | 6.58e-03 | 3.55e-02 | 3.93e-02 | 5.05e-02 | 4.92e-02 | 4.54e-02 | 4.75e-02 | 4.75e-02 | 4.62e-02 |
| Pixel 15 | PE_Bin ₁ | PE_Bin ₂ | PE_Bin ₃ | PE_Bin ₄ | PE_Bin ₅ | PE_Bin ₆ | PE_Bin ₇ | PE_Bin ₈ | PE_Bin ₉ | PE_Bin ₁₀ |
| DE_Bin ₁ | 0.00e+00 | 1.64e-04 | 1.48e-03 | 3.45e-03 | 3.13e-03 | 2.96e-03 | 2.47e-03 | 5.10e-03 | 2.30e-03 | 2.96e-03 |
| DE_Bin ₂ | 0.00e+00 | 3.29e-04 | 2.47e-03 | 4.11e-03 | 2.63e-03 | 3.95e-03 | 4.93e-03 | 4.61e-03 | 5.59e-03 | 3.78e-03 |
| DE_Bin ₃ | 0.00e+00 | 6.58e-04 | 4.77e-03 | 6.09e-03 | 6.25e-03 | 8.55e-03 | 8.88e-03 | 7.40e-03 | 8.22e-03 | 6.91e-03 |
| DE_Bin ₄ | 0.00e+00 | 1.64e-03 | 7.57e-03 | 8.06e-03 | 9.71e-03 | 1.18e-02 | 1.07e-02 | 1.20e-02 | 1.30e-02 | 1.12e-02 |
| DE_Bin ₅ | 0.00e+00 | 1.81e-03 | 1.10e-02 | 1.04e-02 | 1.53e-02 | 1.38e-02 | 1.66e-02 | 1.76e-02 | 1.69e-02 | 1.68e-02 |
| DE_Bin ₆ | 0.00e+00 | 5.10e-03 | 1.61e-02 | 1.94e-02 | 2.22e-02 | 2.42e-02 | 2.09e-02 | 2.19e-02 | 2.19e-02 | 2.43e-02 |
| DE_Bin ₇ | 0.00e+00 | 4.28e-03 | 1.94e-02 | 2.53e-02 | 3.32e-02 | 3.19e-02 | 3.27e-02 | 3.82e-02 | 3.41e-02 | 3.60e-02 |
| DE_Bin ₈ | 0.00e+00 | 6.42e-03 | 3.45e-02 | 3.82e-02 | 4.28e-02 | 4.84e-02 | 4.82e-02 | 4.95e-02 | 5.18e-02 | 4.98e-02 |

Table A.4: Same as Table A.3, but shoot STEP with electrons.

Appendix B

STOF Sweep Voltage Description

This technical document was provided by Dr. Berndt Klecker, the former principal investigator of SOHO/CELIAS. Because there is no online source for this document for us to cite, we decided to attach it here.

o851 **STOF Stepping Sequence.**

In the nominal operation mode the STOF electrostatic analyzer voltage (Sweep-HV) is periodically shifted in discrete steps between the minimum and the maximum value to scan a defined range of incident particle energy. Rise and fall between the minimum and the maximum voltage are divided into 120 steps each, so that a full sweep cycle consists of a total of 240 voltage steps. The duration of each step is 1.25 seconds, this adds up to 300 seconds for one cycle. The voltage steps are sized according to a logarithmic scale, each step produces an increase or decrease of approximately 3 percent referenced to the previous step. The initial value, offset and exponent of the sweep voltage cycle may be adjusted by the parameters of the FBSTRPAR command.

The pulse height analyzer (PHA) electronics uses offset-, gain- and threshold parameters that depend on the sweep voltage setting. These PHA-parameters are switched every 3 steps of the sweep voltage, so these triplets of voltage steps are called PHA-steps. According to the 120 voltage steps between the minimum and the maximum value there are 40 PHA-steps (= different parameter settings), this makes 80 PHA-steps for one sweep cycle. At the beginning of each PHA-step the control parameters are loaded before the analysis is started and at the end of PHA-steps analysis is disabled.

The setting of the sweep voltage and all other control is handled by the Data Processing Unit (DPU) via the command interface. As a protective measure the maximum stepsize is limited by the commandable delta-limit, which is imposed by the DPU. There are also commandable limits for the minimum and the maximum sweep voltage: maximum voltage limit, minimum sweep step limit and maximum sweep step limit. The stepping scheme of 240 voltage steps for one sweep cycle cannot be modified, therefore nominal voltage values less than the minimum limit are substituted by the minimum limit value, and nominal voltage values greater than the maximum limit are substituted by the maximum limit value.

The required commands are listed in the control command section.

16STOF Sweep Voltage Setting

The STOF stepping cycle consists of 2 phases:

- 1) logarithmic rise of the high voltage from the minimum to the maximum value
- 2) logarithmic decay of the high voltage to the minimum value.

The rise and decay is controlled by a DAC in 120 steps each, a total of 240 steps for a full cycle. The time interval between steps is 1.25 seconds.

Definitions:

| | | |
|----------------------------|-----------------------------------------------------------------------------------------------------------------------------------------------------------------------------|-------------------------------------------|
| brdrs _n [0:239] | | Sweep-cycle step number |
| sc[0:237, mod 3] | $c = 3 \times \text{INT}(n/3)$ | Step number for new PHA parameter setting |
| sv[0:119] | $sv = n$ for $n < 120$ (rise) $sv = 239 - n$ for $n \geq 120$ (fall) Limits: for $sv \leq sp_{\min}$: $sv = sp_{\min}$ for $sv \geq sp_{\max}$: $sv = sp_{\max}$ | Voltage Step number (set-value #) |
| brdrw15sp[0:117, mod 3] | $sp = c$ for $n < 120$ (rise) $sp = 237 - c$ for $n \geq 120$ (fall) Limits: for $sp \leq sp_{\min}$: $sp = sp_{\min}$ for $sp \geq sp_{\max}$: $sp = sp_{\max}$ | PHA Parameter-Set number |

STOF HV-Sweep DAC Setting:

$$\text{DAC_SWEEP_S} = \text{INT} (U_0 * \text{ALS3}^{\text{SV}} + U_{\text{OFFSET}})$$

Default Parameters (stored in EPROM):

$$\underline{\text{ne_ALS3}} = (\text{Usweep}_{\max} / \text{Usweep}_{\min})^{1/119} = (5000 / 100)^{1/119} = 50^{1/119} = 1.033420468$$

$$U_0 = \text{Chnl}(5000 \text{ V}) / 50 = 3800 / 50 = 76.055$$

$$U_{\text{OFFSET}} = -2.4$$

Last parameter change 24.07.96:

$$\text{ALS3} = (\text{Usweep}_{\max} / \text{Usweep}_{\min})^{1/119} = (2650,6 / 141)^{1/119} = 1.024960$$

$$U_0 = 141.00$$

$$U_{\text{OFFSET}} = -2.398440$$

DAC to Usweep conversion:

$$\text{Usweep} = 5000/3800 * \text{DAC} = 1,315789473684 * \text{DAC}$$

$$\text{Voltage step 0: Usweep} = 182.37 \text{ Volt}$$

$$\text{Voltage step 119: Usweep} = 3484.47 \text{ Volt}$$

Control Commands

| | | |
|----------|------------------------|--------------------------------------------------------------|
| FBSLIMSW | STOF Sweep Limit: | upper voltage limit + delta limit |
| FBSLIMST | STOF Stepping Range: | last step + first step |
| FBSSWV | STOF Sweep Voltage: | static set value (Manual Mode) DAC = 1023 -> 11,130 Volts |
| FBSENASS | STOF Sweep-HV Enable | |
| FBSDISSS | STOF Sweep-HV Disable | |
| FBSS1ON | STOF Sweep_1 ON | |
| FBSS1OF | STOF Sweep_1 OFF | |
| FBSS2ON | STOF Sweep_2 ON | |
| FBSS2OF | STOF Sweep_2 OFF | |
| FBSTRPAR | STOF Parameter Loading | see definition next page |

rd

Command FBSTRPAR

(Last Change 24.07.96)

| | Byte Nr. | Old Value | New Value | Word Nr. | Word |
|---------------|-------------|------------|------------|----------|--------|
| SwGainS | 54 | 84 | 84 | 27 | 0x5454 |
| l360SwGainH | 55 | 84 | 84 | | |
| TS1 | 53/52 | 146 | 146 | 26 | 0x0092 |
| TS2 | 51/50/49/48 | 0.987750 | 0.987750 | 24 | 0x3F7C |
| | | | | 25 | 0xDD2F |
| TS3 | 47/46 | 21 | 21 | 23 | 0x0015 |
| AS1 | 45/44 | 4 | 4 | 22 | 0x0004 |
| AS2 | 43/42 | 807 | 807 | 21 | 0x0327 |
| AS4 | 41/40 | 180 | 180 | 20 | 0x00B4 |
| LS1_0 | 39/38 | 36 | 36 | 19 | 0x0024 |
| LS1_1 | 37/36 | 30 | 30 | 18 | 0x001E |
| ALS3 | 35/34/33/32 | 1.024960 | 1.024960 | 16 | 0x3F83 |
| par | | | | 17 | 0x31E4 |
| LS4 | 31/30 | 6 | 6 | 15 | 0x0006 |
| LS5 | 29/28 | 84 | 84 | 14 | 0x0054 |
| LS6 | 27/26 | 2.097660 | 2.099766 | 13 | 0x0219 |
| GAmpS_0 | 25/24 | 1.000 | 1.000 | 12 | 0x0100 |
| GAmpS_1 | 23/22 | 5.597660 | 5.597660 | 11 | 0x0599 |
| U0 | 21/20/19/18 | 141.000000 | 141.000000 | 9 | 0x430D |
| | | | | 11 | 10 |
| | | | | | 0x0000 |
| UOffset | 17/16 | -2.398440 | -2.398440 | 8 | 0xFD9A |
| TH1 | 15/14 | 21 | 21 | 7 | 0x0015 |
| TH2 | 13/12 | 25 | 25 | 6 | 0x0019 |
| tlparAH_0 | 11/10 | 150 | 150 | 5 | 0x0096 |
| AH_1 | 9/8 | 60 | 60 | 4 | 0x003C |
| LH_0 | 7/6 | 41 | 41 | 3 | 0x0029 |
| LH_1 | 5/4 | 33 | 33 | 2 | 0x0021 |
| STOFLoGain | 2 | 115 | 115 | 1 | 0x1C73 |
| STOFHiGain | 3 | 28 | 28 | | |
| HSTOFLoGain | 0 | 40 | 40 | 0 | 0x0428 |
| rsHSTOFHiGain | 1 | 4 | 4 | | |

see next page for the control algorithm of these parameters

Bibliography

Adriani, O., Barbarino, G., Bazilevskaia, G., Bellotti, R., Boezio, M., Bogomolov, E., Bongi, M., Bonvicini, V., Borisov, S., Bottai, S., et al. Cosmic-ray electron flux measured by the PAMELA experiment between 1 and 625 GeV. *Physical Review Letters*, 106(20):201101, 2011.

Afanasiev, A. and Vainio, R. Monte Carlo Simulation Model of Energetic Proton Transport through Self-generated Alfvén Waves. *The Astrophysical Journal Supplement*, 207:29, August 2013. doi: 10.1088/0067-0049/207/2/29.

Agostinelli, S., Allison, J., Amako, K., Apostolakis, J., Araujo, H., Arce, P., Asai, M., Axen, D., Banerjee, S., Barrand, G., Behner, F., Bellagamba, L., Boudreau, J., Broglia, L., Brunengo, A., Burkhardt, H., Chauvie, S., Chuma, J., Chytráček, R., Cooperman, G., Cosmo, G., Degtyarenko, P., Dell'Acqua, A., Depaola, G., Dietrich, D., Enami, R., Feliciello, A., Ferguson, C., Fesefeldt, H., Folger, G., Foppiano, F., Forti, A., Garelli, S., Giani, S., Giannitrapani, R., Gibin, D., Cadenas, J. G., González, I., Abril, G. G., Greeniaus, G., Greiner, W., Grichine, V., Grossheim, A., Guatelli, S., Gumplinger, P., Hamatsu, R., Hashimoto, K., Hasui, H., Heikkinen, A., Howard, A., Ivanchenko, V., Johnson, A., Jones, F., Kallenbach, J., Kanaya, N., Kawabata, M., Kawabata, Y., Kawaguti, M., Kelner, S., Kent, P., Kimura, A., Kodama, T., Kokoulin, R., Kossov, M., Kurashige, H., Lamanna, E., Lampén, T., Lara, V., Lefebvre, V., Lei, F., Liendl, M., Lockman, W., Longo, F., Magni, S., Maire, M., Medernach, E., Minamimoto, K., de Freitas, P. M., Morita, Y., Murakami, K., Nagamatsu, M., Nartallo, R., Nieminen, P., Nishimura, T., Ohtsubo, K., Okamura, M., O'Neale, S., Oohata, Y., Paech, K., Perl, J., Pfeiffer, A., Pia, M., Ranjard, F., Rybin, A., Sadilov, S., Salvo, E. D., Santin, G., Sasaki, T., Savvas, N., Sawada, Y., Scherer, S., Sei, S., Sirotenko, V., Smith, D., Starkov, N., Stoecker, H., Sulkimo, J., Takahata, M., Tanaka, S., Tcherniaev, E., Tehrani, E. S., Tropeano, M., Truscott, P., Uno, H., Urban, L., Urban, P., Verderi, M., Walkden, A., Wander, W., Weber, H., Wellisch, J., Wenaus, T., Williams, D., Wright, D., Yamada, T., Yoshida, H., and Zschesche, D. Geant4—a simulation toolkit. *Nuclear Instruments and Methods in Physics Research Section A: Accelerators, Spectrometers, Detectors and Associated Equipment*, 506(3):250 – 303, 2003. ISSN 0168-9002. doi: [http://dx.doi.org/10.1016/S0168-9002\(03\)01368-8](http://dx.doi.org/10.1016/S0168-9002(03)01368-8). URL <http://www.sciencedirect.com/science/article/pii/S0168900203013688>.

Alfvén, H. On the theory of comet tails. *Tellus*, 9, 1957.

Balogh, A., Bothmer, V., Crooker, N. U., Forsyth, R. J., Gloeckler, G., Hewish, A., Hilchenbach, M., Kallenbach, R., Klecker, B., Linker, J. A., Lucek, E., Mann, G., Marsch, E., Posner, A., Richardson, I. G., Schmidt, J. M., Scholer, M., Wang, Y.-M., Wimmer-Schweingruber, R. F., Aellig, M. R., Bochsler, P., Hefti, S., and Mikić, Z. The Solar Origin of Corotating Interaction Regions and Their Formation in the

- Inner Heliosphere. *Space Science Reviews*, 89:141–178, July 1999. doi: 10.1023/A:1005245306874.
- Bame, S. J., Hundhausen, A. J., Asbridge, J. R., and Strong, I. B. Solar Wind Ion Composition. *Physical Review Letters*, 20:393–395, February 1968. doi: 10.1103/PhysRevLett.20.393.
- Bame, S. J., Asbridge, J. R., Hundhausen, A. J., and Montgomery, M. D. Solar wind ions: $^{56}\text{Fe}^{+8}$ to $^{56}\text{Fe}^{+12}$, $^{28}\text{Si}^{+7}$, $^{28}\text{Si}^{+8}$, $^{28}\text{Si}^{+9}$, and $^{16}\text{O}^{+6}$. *Journal of Geophysical Research*, 75:6360, 1970. doi: 10.1029/JA075i031p06360.
- Bame, S. J., Asbridge, J. R., Feldman, W. C., Montgomery, M. D., and Kearney, P. D. Solar wind heavy ion abundances. *Solar Physics*, 43:463–473, August 1975. doi: 10.1007/BF00152368.
- Bamert, K., Wimmer-Schweingruber, R., Kallenbach, R., Hilchenbach, M., Klecker, B., Bogdanov, A., and Wurz, P. Origin of the may 1998 suprathermal particles: solar and heliospheric observatory/charge, element, and isotope analysis system/(highly) suprathermal time of flight results. *Journal of Geophysical Research: Space Physics (1978–2012)*, 107(A7):SSH–6, 2002.
- Bamert, K., Kallenbach, R., Wimmer-Schweingruber, R. F., Hilchenbach, M., and Klecker, B. Suprathermal ions of solar and interstellar origin associated with the April 9–12, 2001, CMEs. *Advances in Space Research*, 34:161–165, January 2004. doi: 10.1016/j.asr.2003.01.036.
- Barnes, C. W. and Simpson, J. A. Evidence for interplanetary acceleration of nucleons in corotating interaction regions. *Astrophysical Journal*, 210:L91–L96, December 1976. doi: 10.1086/182311.
- Barouch, E. and Burlaga, L. F. Causes of Forbush decreases and other cosmic ray variations. *Journal of Geophysical Research*, 80:449–456, February 1975. doi: 10.1029/JA080i004p00449.
- Beck, J. G. A comparison of differential rotation measurements – (invited review). *Solar Physics*, 191(1):47–70, Jan 2000. ISSN 1573-093X. doi: 10.1023/A:1005226402796. URL <https://doi.org/10.1023/A:1005226402796>.
- Berger, L. *Velocity distribution functions of heavy ions in the solar wind at 1 AU*. PhD thesis, Kiel, Christian-Albrechts-Universität, Diss., 2008, 2008.
- Bertaux, J., Kyrölä, E., Quémerais, E., Pellinen, R., Lallement, R., Schmidt, W., Berthé, M., Dimarellis, E., Goutail, J., Taulemesse, C., et al. Swan: A study of solar wind anisotropies on soho with lyman alpha sky mapping. *Solar physics*, 162(1-2):403–439, 1995.
- Biermann, L. Kometenschweife und solare Korpuskularstrahlung. *Zeitschrift für Astrophysik*, 29:274, 1951.
- Biermann, L. Physical Processes in Comet Tails and their Relation to Solar Activity. In Swings, P., editor, *Liege International Astrophysical Colloquia*, volume 4 of *Liege International Astrophysical Colloquia*, pages 251–262, 1952.
- Biermann, L. Solar corpuscular radiation and the interplanetary gas. *The Observatory*, 77:109–110, June 1957.

- Bonetti, A., Bridge, H. S., Lazarus, A. J., Rossi, B., and Scherb, F. Explorer 10 Plasma Measurements. *Journal of Geophysical Research*, 68:4017, July 1963.
- Broggini, C. Nuclear Processes at Solar Energy. In Riemann, S. and Lohmann, W., editors, *Physics in Collision*, page 21, August 2003.
- Brueckner, G., Howard, R., Koomen, M., Korendyke, C., Michels, D., Moses, J., Socker, D., Dere, K., Lamy, P., Llebaria, A., et al. The large angle spectroscopic coronagraph (lasco). In *The SOHO Mission*, pages 357–402. Springer, 1995.
- Bryant, D. A., Cline, T. L., Desai, U. D., and McDonald, F. B. Continual Acceleration of Solar Protons in the MeV Range. *Physical Review Letters*, 14:481–484, March 1965. doi: 10.1103/PhysRevLett.14.481.
- Burlaga, L. F. Interplanetary stream interfaces. *J. Geophys. Res.*, 79:3717, 1974. doi: 10.1029/JA079i025p03717.
- Burton, M. E., Smith, E. J., Balogh, A., Forsyth, R. J., Bame, S. J., Phillips, J. L., and Goldstein, B. E. ULYSSES out-of-ecliptic observations of interplanetary shocks. *Astronomy and Astrophysics*, 316:313–322, December 1996.
- Burton, M. E., Neugebauer, M., Crooker, N. U., von Steiger, R., and Smith, E. J. Identification of trailing edge solar wind stream interfaces: A comparison of Ulysses plasma and composition measurements. *Journal of Geophysical Research*, 104:9925–9932, May 1999. doi: 10.1029/JA104iA05p09925.
- Bučík, R., Mall, U., Korth, A., and Mason, G. M. On acceleration of 1 MeV/n He ions in the corotating compression regions near 1 AU: STEREO observations. *Annales Geophysicae*, 27:3677–3690, September 2009. doi: 10.5194/angeo-27-3677-2009.
- Chotoo, K., Schwadron, N. A., Mason, G. M., Zurbuchen, T. H., Gloeckler, G., Posner, A., Fisk, L. A., Galvin, A. B., Hamilton, D. C., and Collier, M. R. The suprathermal seed population for corotating interaction region ions at 1 AU deduced from composition and spectra of H⁺, He⁺⁺, and He⁺ observed on Wind. *Journal of Geophysical Research*, 105:23107–23122, October 2000. doi: 10.1029/1998JA000015.
- Decker, R. B., Krimigis, S. M., Roelof, E. C., Hill, M. E., Armstrong, T. P., Gloeckler, G., Hamilton, D. C., and Lanzerotti, L. J. Voyager 1 in the Foreshock, Termination Shock, and Heliosheath. *Science*, 309:2020–2024, September 2005. doi: 10.1126/science.1117569.
- Delaboudiniere, J.-P., Artzner, G., Brunaud, J., Gabriel, A. H., Hochedez, J., Millier, F., Song, X., Au, B., Dere, K., Howard, R., et al. *EIT: extreme-ultraviolet imaging telescope for the SOHO mission*. Springer, 1995.
- Desai, M. I., Marsden, R. G., Sanderson, T. R., Lario, D., Roelof, E. C., Simnett, G. M., Gosling, J. T., Balogh, A., and Forsyth, R. J. Energy spectra of 50-keV to 20-MeV protons accelerated at corotating interaction regions at Ulysses. *Journal of Geophysical Research*, 104:6705–6720, April 1999. doi: 10.1029/1998JA900176.
- Desai, M. I., Mason, G. M., Müller-Mellin, R., Korth, A., Mall, U., Dwyer, J. R., and von Rosenvinge, T. T. The spatial distribution of upstream ion events from the Earth’s bow shock measured by ACE, Wind, and STEREO. *Journal of Geophysical Research (Space Physics)*, 113:A08103, August 2008. doi: 10.1029/2007JA012909.

- Dessler, A. J. Solar wind and interplanetary magnetic field. *Reviews of Geophysics*, 5 (1):1–41, 1967.
- Dresing, N., Gómez-Herrero, R., Heber, B., Klassen, A., Malandraki, O., Dröge, W., and Kartavykh, Y. Statistical survey of widely spread out solar electron events observed with STEREO and ACE with special attention to anisotropies. *Astronomy and Astrophysics*, 567:A27, July 2014. doi: 10.1051/0004-6361/201423789.
- Drews, C. *Interstellar Pickup Ions at 1 AU with STEREO/PLASTIC*. PhD thesis, Kiel, Christian-Albrechts-Universität, Diss., 2013, 2013.
- Drury, L. O. An introduction to the theory of diffusive shock acceleration of energetic particles in tenuous plasmas. *Reports on Progress in Physics*, 46:973–1027, August 1983. doi: 10.1088/0034-4885/46/8/002.
- Dwyer, J. R., Mason, G. M., Mazur, J. E., Jokipii, J. R., von Rosenvinge, T. T., and Lepping, R. P. Perpendicular Transport of Low-Energy Corotating Interaction Region-associated Nuclei. *The Astrophysical Journal*, 490:L115–L118, November 1997. doi: 10.1086/311003.
- Ebert, R. W., Dayeh, M. A., Desai, M. I., and Mason, G. M. Corotating Interaction Region Associated Suprathermal Helium Ion Enhancements at 1 AU: Evidence for Local Acceleration at the Compression Region Trailing Edge. *Astrophysical Journal*, 749:73, April 2012. doi: 10.1088/0004-637X/749/1/73.
- Fan, C. Y., Pick, M., Pyle, R., Simpson, J. A., and Smith, D. R. Protons associated with centers of solar activity and their propagation in interplanetary magnetic field regions corotating with the Sun. *Journal of Geophysical Research*, 73:1555, March 1968. doi: 10.1029/JA073i005p01555.
- Fermi, E. On the origin of the cosmic radiation. *Physical Review*, 75(8):1169, 1949.
- Fisk, L. A. and Gloeckler, G. The Common Spectrum for Accelerated Ions in the Quiet-Time Solar Wind. *Astrophysical Journal Letter*, 640:L79–L82, March 2006. doi: 10.1086/503293.
- Fisk, L. A. and Gloeckler, G. Acceleration and Composition of Solar Wind Suprathermal Tails. *Space Science Reviews*, 130:153–160, June 2007. doi: 10.1007/s11214-007-9180-8.
- Fisk, L. A. and Gloeckler, G. Acceleration of Suprathermal Tails in the Solar Wind. *Astrophysical Journal*, 686:1466–1473, October 2008. doi: 10.1086/591543.
- Fisk, L. A. and Lee, M. A. Shock acceleration of energetic particles in corotating interaction regions in the solar wind. *Astrophysical Journal*, 237:620–626, April 1980. doi: 10.1086/157907.
- Fisk, L. A., Gloeckler, G., and Schwadron, N. A. On Theories for Stochastic Acceleration in the Solar Wind. *Astrophysical Journal*, 720:533–540, September 2010. doi: 10.1088/0004-637X/720/1/533.
- Fleck, B. *The SOHO mission*. Springer, 1995.

- Fröhlich, C., Romero, J., Roth, H., Wehrli, C., Andersen, B. N., Appourchaux, T., Domingo, V., Telljohann, U., Berthomieu, G., Delache, P., et al. Virgo: Experiment for helioseismology and solar irradiance monitoring. In *The SOHO Mission*, pages 101–128. Springer, 1995.
- Gabriel, A., Grec, G., Charra, J., Robillot, J.-M., Cortés, T. R., Turck-Chièze, S., Bocchia, R., Boumier, P., Cantin, M., Cespédes, E., et al. Global oscillations at low frequency from the soho mission (golf). In *The SOHO Mission*, pages 61–99. Springer, 1995.
- Gieseler, J. *Ionen in der inneren Heliosphäre: STEREO-SEPT-Ergebnisse unter Berücksichtigung des Compton-Getting-Effekts*. PhD thesis, Inst. für Experimentelle und Angewandte Physik der Christian-Albrechts-Univ., 2008.
- Gloeckler, G. Ubiquitous Suprathermal Tails on the Solar Wind and Pickup Ion Distributions. In Velli, M., Bruno, R., Malara, F., and Bucci, B., editors, *Solar Wind Ten*, volume 679 of *American Institute of Physics Conference Series*, pages 583–588, September 2003. doi: 10.1063/1.1618663.
- Gloeckler, G., Cain, J., Ipavich, F. M., Tums, E. O., Bedini, P., Fisk, L. A., Zurbuchen, T. H., Bochsler, P., Fischer, J., Wimmer-Schweingruber, R. F., Geiss, J., and Kallenbach, R. Investigation of the composition of solar and interstellar matter using solar wind and pickup ion measurements with SWICS and SWIMS on the ACE spacecraft. *Space Science Reviews*, 86:497–539, July 1998. doi: 10.1023/A:1005036131689.
- Gosling, J. T. and Pizzo, V. J. Formation and Evolution of Corotating Interaction Regions and their Three Dimensional Structure. *Space Science Reviews*, 89:21–52, July 1999. doi: 10.1023/A:1005291711900.
- Gringauz, K. I., Bezrukikh, V. V., Ozerov, V. D., and Rybchinskii, R. E. A Study of the Interplanetary Ionized Gas, High-Energy Electrons and Corpuscular Radiation from the Sun by Means of the Three-Electrode Trap for Charged Particles on the Second Soviet Cosmic Rocket. *Soviet Physics Doklady*, 5:361, September 1960.
- Gringauz, K. I., Bezrukikh, V. V., and Musatov, L. S. Solar-Wind Observations with the Venus 3 Probe. *Cosmic Research*, 5:216, March 1967.
- Gringauz, K., Bezrukikh, V., Ozerov, V., and Ribchinsky, R. Some results of experiments in interplanetary space by means of charged particle traps on soviet space probes. *Space Res*, 2:539–553, 1961.
- Hannah, I., Hudson, H., Hurford, G., and Lin, R. Constraining the hard x-ray properties of the quiet sun with new rhesi observations. *Astrophysical Journal*, 724(1):487, 2010.
- Harrison, R., Sawyer, E., Carter, M., Cruise, A., Cutler, R., Fludra, A., Hayes, R., Kent, B., Lang, J., Parker, D., et al. The coronal diagnostic spectrometer for the solar and heliospheric observatory. In *The SOHO Mission*, pages 233–290. Springer, 1995.
- Hilchenbach, M., Hsieh, K. C., Hovestadt, D., Klecker, B., Grünwaldt, H., Bochsler, P., Ipavich, F. M., Bürgi, A., Möbius, E., Gliem, F., Axford, W. I., Balsiger, H., Bornemann, W., Coplan, M. A., Galvin, A. B., Geiss, J., Gloeckler, G., Hefti, S., Judge, D. L., Kallenbach, R., Laeverenz, P., Lee, M. A., Livi, S., Managadze, G. G., Marsch, E., Neugebauer, M., Ogawa, H. S., Reiche, K.-U., Scholer, M., Verigin, M. I.,

- Wilken, B., and Wurz, P. Detection of 55-80 keV Hydrogen Atoms of Heliospheric Origin by CELIAS/HSTOF on SOHO. *Astrophysical Journal*, 503:916–922, August 1998. doi: 10.1086/306022.
- Hill, M. E., Schwadron, N. A., Hamilton, D. C., Di Fabio, R. D., and Squier, R. K. Interplanetary Suprathermal He⁺ and He⁺⁺ Observations During Quiet Periods from 1 to 9 AU and Implications for Particle Acceleration. *The Astrophysical Journal Letters*, 699:L26–L30, July 2009. doi: 10.1088/0004-637X/699/1/L26.
- Hovestadt, D., Hilchenbach, M., Bürgi, A., Klecker, B., Laeverenz, P., Scholer, M., Grünwaldt, H., Axford, W. I., Livi, S., Marsch, E., Wilken, B., Winterhoff, H. P., Ipavich, F. M., Bedini, P., Coplan, M. A., Galvin, A. B., Gloeckler, G., Bochsler, P., Balsiger, H., Fischer, J., Geiss, J., Kallenbach, R., Wurz, P., Reiche, K.-U., Gliem, F., Judge, D. L., Ogawa, H. S., Hsieh, K. C., Möbius, E., Lee, M. A., Managadze, G. G., Verigin, M. I., and Neugebauer, M. CELIAS - Charge, Element and Isotope Analysis System for SOHO. *Solar Physics*, 162:441–481, December 1995. doi: 10.1007/BF00733436.
- Hovestadt, D., Hilchenbach, M., Bürgi, A., Klecker, B., Laeverenz, P., Scholer, M., Grünwaldt, H., Axford, W., Livi, S., Marsch, E., et al. Cielias—charge, element and isotope analysis system for soho. In *The SOHO Mission*, pages 441–481. Springer, 1995.
- Ipavich, F. M. The Compton-Getting Effect for low energy particles. *Geophysical Research Letters*, 1:149–152, 1974. doi: 10.1029/GL001i004p00149.
- Jian, L., Russell, C. T., Luhmann, J. G., and Skoug, R. M. Properties of Stream Interactions at One AU During 1995–2004. *Solar Physics*, 239:337–392, December 2006. doi: 10.1007/s11207-006-0132-3.
- Jian, L., Russell, C. T., Luhmann, J. G., and Skoug, R. M. Evolution of solar wind structures from 0.72 to 1 AU. *Advances in Space Research*, 41:259–266, 2008. doi: 10.1016/j.asr.2007.03.023.
- Jokipii, J. R. Cosmic-Ray Propagation. I. Charged Particles in a Random Magnetic Field. *Astrophysical Journal*, 146:480, November 1966. doi: 10.1086/148912.
- Jokipii, J. R. and Lee, M. A. Compression Acceleration in Astrophysical Plasmas and the Production of $f(v) v^{\text{prop}} v^{-5}$ Spectra in the Heliosphere. *Astrophysical Journal*, 713:475–483, April 2010. doi: 10.1088/0004-637X/713/1/475.
- Klassen, A., Gómez-Herrero, R., Böhm, E., Müller-Mellin, R., Heber, B., and Wimmer-Schweingruber, R. COSTEP/SOHO observations of energetic electrons far upstream of the Earth’s bow-shock. *Annales Geophysicae*, 26:905–912, May 2008. doi: 10.5194/angeo-26-905-2008.
- Kohl, J. á., Esser, R., Gardner, L., Habbal, S., Daigneau, P., Dennis, E., Nystrom, G., Panasyuk, A., Raymond, J., Smith, P., et al. The ultraviolet coronagraph spectrometer for the solar and heliospheric observatory. *Solar Physics*, 162(1-2):313–356, 1995.
- Krieger, A. S., Timothy, A. F., and Roelof, E. C. A Coronal Hole and Its Identification as the Source of a High Velocity Solar Wind Stream. *Solar Physics*, 29:505–525, April 1973. doi: 10.1007/BF00150828.

BIBLIOGRAPHY

- Kucharek, H., Möbius, E., Li, W., Farrugia, C. J., Popecki, M. A., Galvin, A. B., Klecker, B., Hilchenbach, M., and Bochsler, P. A. On the source and acceleration of energetic He⁺: A long-term observation with ACE/SEPICA. *Journal of Geophysical Research (Space Physics)*, 108:8040, October 2003. doi: 10.1029/2003JA009938.
- Landau, L. On the energy loss of fast particles by ionization. *J. Phys.(USSR)*, 8:201–205, 1944.
- Lazarus, A. J., Richardson, J. D., Decker, R. B., and McDonald, F. B. Voyager 2 Observations of Corotating Interaction Regions (CIRs) in the Outer Heliosphere. *Space Science Reviews*, 89:53–59, July 1999. doi: 10.1023/A:1005252113717.
- Lee, M. A., Shapiro, V. D., and Sagdeev, R. Z. Pickup ion energization by shock surfing. *Journal of Geophysical Research*, 101:4777–4790, March 1996. doi: 10.1029/95JA03570.
- Lin, R., Anderson, K., and Cline, T. Detection of interplanetary electrons from 18 keV to 1.8 MeV during solar quiet times. *Physical Review Letters*, 29(15):1035, 1972.
- Lin, R., McGuire, R., and Anderson, K. Observation of 38-334-keV interplanetary protons during solar quiet times. *Physical Review Letters*, 31:1268–1271, 1973.
- Marshall, F. E. and Stone, E. C. Characteristics of sunward flowing proton and alpha particle fluxes of moderate intensity. *Journal of Geophysical Research*, 83:3289–3298, July 1978. doi: 10.1029/JA083iA07p03289.
- Mason, G. M., Mazur, J. E., Dwyer, J. R., Reames, D. V., and von Rosenvinge, T. T. New Spectral and Abundance Features of Interplanetary Heavy Ions in Corotating Interaction Regions. *Astrophysical Journal Letters*, 486:L149–L152, September 1997. doi: 10.1086/310845.
- Mason, G. M., Leske, R. A., Desai, M. I., Cohen, C. M. S., Dwyer, J. R., Mazur, J. E., Mewaldt, R. A., Gold, R. E., and Krimigis, S. M. Abundances and Energy Spectra of Corotating Interaction Region Heavy Ions Observed during Solar Cycle 23. *Astrophysical Journal*, 678:1458–1470, May 2008. doi: 10.1086/533524.
- McComas, D. J., Bame, S. J., Barker, P., Feldman, W. C., Phillips, J. L., Riley, P., and Griffiee, J. W. Solar Wind Electron Proton Alpha Monitor (SWEPAM) for the Advanced Composition Explorer. *Space Science Reviews*, 86:563–612, July 1998. doi: 10.1023/A:1005040232597.
- McDonald, F. B., Teegarden, B. J., Trainor, J. H., von Rosenvinge, T. T., and Webber, W. R. The interplanetary acceleration of energetic nucleons. *Astrophysical Journal*, 203:L149–L154, February 1976. doi: 10.1086/182040.
- Mewaldt, R. A., Jokipii, J. R., Lee, M. A., Möbius, E., and Zurbuchen, T. H., editors. *Acceleration and Transport of Energetic Particles Observed in the Heliosphere.*, volume 528 of *American Institute of Physics Conference Series*, September 2000.
- Mewaldt, R., Cohen, C., Labrador, A., Leske, R., Mason, G., Desai, M., Lopper, M., Mazur, J., Selesnick, R., and Haggerty, D. Proton, helium, and electron spectra during the large solar particle events of October–November 2003. *Journal of Geophysical Research: Space Physics (1978–2012)*, 110(A9), 2005.

- Müller, D., Marsden, R. G., Cyr, O. S., Gilbert, H. R., et al. Solar orbiter. *Solar Physics*, 285(1-2):25–70, 2013.
- Müller-Mellin, R., Kunow, H., Fleissner, V., Pehlke, E., Rode, E., Röschmann, N., Scharmberg, C., Sierks, H., Ruzsnyak, P., McKenna-Lawlor, S., et al. Costep—comprehensive suprathermal and energetic particle analyser. In *The SOHO Mission*, pages 483–504. Springer, 1995.
- Ness, N. F., Scarce, C. S., and Seek, J. B. Initial Results of the Imp 1 Magnetic Field Experiment. *Journal of Geophysical Research*, 69:3531–3569, September 1964. doi: 10.1029/JZ069i017p03531.
- Neugebauer, M. and Snyder, C. W. Mariner 2 Observations of the Solar Wind, 1, Average Properties. *Journal of Geophysical Research*, 71:4469, October 1966.
- Neugebauer, M. and Snyder, C. W. Mariner 2 Observations of the Solar Wind, 2, Relation of Plasma Properties to the Magnetic Field. *Journal of Geophysical Research*, 72:1823, April 1967. doi: 10.1029/JZ072i007p01823.
- Neugebauer, M., Forsyth, R. J., Galvin, A. B., Harvey, K. L., Hoeksema, J. T., Lazarus, A. J., Lepping, R. P., Linker, J. A., Mikic, Z., Steinberg, J. T., von Steiger, R., Wang, Y.-M., and Wimmer-Schweingruber, R. F. Spatial structure of the solar wind and comparisons with solar data and models. *Journal of Geophysical Research*, 103: 14587–14600, July 1998. doi: 10.1029/98JA00798.
- Nolte, J. T., Krieger, A. S., Timothy, A. F., Gold, R. E., Roelof, E. C., Vaiana, G., Lazarus, A. J., Sullivan, J. D., and McIntosh, P. S. Coronal holes as sources of solar wind. *Solar Physics*, 46:303–322, February 1976. doi: 10.1007/BF00149859.
- Odenwald, S. F. and Green, J. L. Bracing for a solar superstorm. *Scientific american*, 299(2):80–87, 2008.
- Parker, E. N. Dynamics of the Interplanetary Gas and Magnetic Fields. *Astrophysical Journal*, 128:664, November 1958. doi: 10.1086/146579.
- Parker, E. N. *Interplanetary dynamical processes*. 1963.
- Reames, D. V., Ng, C. K., Mason, G. M., Dwyer, J. R., Mazur, J. E., and von Rosenvinge, T. T. Late-phase acceleration of energetic ions in corotating interaction regions. *Geophysical Research Letters*, 24:2917–2920, 1997. doi: 10.1029/97GL02841.
- Richardson, I. G., Barbier, L. M., Reames, D. V., and von Rosenvinge, T. T. Corotating MeV/amu ion enhancements at 1 AU or less from 1978 to 1986. *Journal of Geophysical Research*, 98:13–32, January 1993. doi: 10.1029/92JA01837.
- Roberts, P. H. Kinematic Dynamo Models. *Philosophical Transactions of the Royal Society of London Series A*, 272:663–698, August 1972. doi: 10.1098/rsta.1972.0074.
- Roelof, E. C. Propagation of Solar Cosmic Rays in the Interplanetary Magnetic Field. In Ögelman, H. and Wayland, J. R., editors, *Lectures in High-Energy Astrophysics*, page 111, 1969.
- Schatten, K. H. Current sheet magnetic model for the solar corona. *NASA Special Publication*, 308:44, 1972.

- Scherrer, P., Bogart, R., Bush, R., Hoeksema, J., Kosovichev, A., Schou, J., Rosenberg, W., Springer, L., Tarbell, T., Wolfson, C., et al. The solar oscillations investigation-michelson doppler imager. *Solar Physics*, 162(1-2):129–188, 1995.
- Scholer, M. Injection and Acceleration Processes in Corotating Interaction Regions: Theoretical Concepts. *Space Science Reviews*, 89:105–114, July 1999. doi: 10.1023/A:1005228819169.
- Scholer, M. and Kucharek, H. Interaction of pickup ions with quasi-parallel shocks. *Geophysical Research Letters*, 26:29–32, 1999. doi: 10.1029/1998GL900239.
- Schwadron, N. A., Fisk, L. A., and Gloeckler, G. Statistical acceleration of interstellar pick-up ions in co-rotating interaction regions. *Geophysical Research Letters*, 23:2871–2874, 1996. doi: 10.1029/96GL02833.
- Segrè, E. *Experimental nuclear physics*, volume 3. Wiley, 1959.
- Simnett, G. and McDonald, F. Observations of Cosmic-Ray electrons between 2.7 and 21.5 MeV. *Astrophysical Journal*, 157:1435, 1969.
- Smith, C. W., L’Heureux, J., Ness, N. F., Acuña, M. H., Burlaga, L. F., and Scheifele, J. The ACE Magnetic Fields Experiment. *Space Science Reviews*, 86:613–632, July 1998. doi: 10.1023/A:1005092216668.
- Snyder, C. W. and Neugebauer, M. Interplanetary solar-wind measurements by Mariner II. In Muller, P., editor, *Space Research Conference*, page 89, 1964.
- Snyder, C. W. and Neugebauer, M. Interplanetary Solar-Wind Measurements by Mariner II. In Chang, C. C. and Huang, S. S., editors, *Plasma Space Science*, volume 3 of *Astrophysics and Space Science Library*, page 67, January 1965. doi: 10.1007/978-94-011-7542-5.8.
- Sullivan, J. D. Erratum: Geometrical factor and directional response of single and multi-element particle telescopes, Nucl. Instr. and Meth. 95 (1971) 5-11. *Nuclear Instruments and Methods*, 98:187, 1972.
- Tian, H., DeLuca, E., Cranmer, S., De Pontieu, B., Peter, H., Martínez-Sykora, J., Golub, L., McKillop, S., Reeves, K., Miralles, M., et al. Prevalence of small-scale jets from the networks of the solar transition region and chromosphere. *Science*, 346(6207):1255711, 2014.
- Valtonen, E., Peltonen, J., Peltonen, P., Eronen, T., Hoisko, E., Louhola, M., Lumme, M., Nieminen, A., Riihonen, E., Teittinen, M., et al. Energetic and relativistic nuclei and electron experiment of the soho mission. *Nuclear Instruments and Methods in Physics Research Section A: Accelerators, Spectrometers, Detectors and Associated Equipment*, 391(2):249–268, 1997.
- Van Hollebeke, M. A. I., McDonald, F. B., Trainor, J. H., and von Rosenvinge, T. T. The radial variation of corotating energetic particle streams in the inner and outer solar system. *Journal of Geophysical Research*, 83:4723–4731, October 1978. doi: 10.1029/JA083iA10p04723.
- Wang, Y.-M. and Sheeley, N. R., Jr. Sources of the Solar Wind at Ulysses during 1990-2006. *Astrophysical Journal*, 653:708–718, December 2006. doi: 10.1086/508929.

- Wang, Y.-M., Sheeley, N. R., Jr., Walters, J. H., Brueckner, G. E., Howard, R. A., Michels, D. J., Lamy, P. L., Schwenn, R., and Simnett, G. M. Origin of Streamer Material in the Outer Corona. *Astrophysical Journal Letter*, 498:L165–L168, May 1998. doi: 10.1086/311321.
- Wibberenz, G., Richardson, I. G., and Cane, H. V. A simple concept for modeling cosmic ray modulation in the inner heliosphere during solar cycles 20-23. *Journal of Geophysical Research (Space Physics)*, 107:1353, November 2002. doi: 10.1029/2002JA009461.
- Wilhelm, K., Curdt, W., Marsch, E., Schühle, U., Lemaire, P., Gabriel, A., Vial, J.-C., Grewing, M., Huber, M., Jordan, S., et al. Sumer-solar ultraviolet measurements of emitted radiation. *Solar Physics*, 162(1-2):189–231, 1995.
- Wimmer-Schweingruber, R. F., von Steiger, R., and Paerli, R. Solar wind stream interfaces in corotating interaction regions: SWICS/Ulysses results. *J. Geophys. Res.*, 102:17407 – 17417, 1997.
- Wimmer-Schweingruber, R. F., v. Steiger, R., and Paerli, R. Solar wind stream interfaces in corotating interaction regions: New SWICS/Ulysses results. *J. Geophys. Res.*, 104: 9933 – 9945, 1999.
- Wimmer-Schweingruber, R. F., Rodriguez-Pacheco, J., Lin, R. P., Mason, G. M., Heber, B., Valtonen, E., Sanchez, S., Blanco, J., Prieto, M., Martin, C., Ho, G., Andrews, B., Burmeister, S., Boettcher, S., Kulkarni, S. R., Seimetz, L., and Schuster, B. The Energetic Particle Detector Suite for Solar Orbiter. In *38th COSPAR Scientific Assembly*, volume 38 of *COSPAR Meeting*, page 2, 2010.
- Yu, J., Berger, L., Wimmer-Schweingruber, R. F., Hilchenbach, M., Kallenbach, R., Klecker, B., and Guo, J. Suprathermal helium associated with corotating interaction regions: A case study. *AIP Conference Proceedings*, 1720:070010, 2016. doi: <http://dx.doi.org/10.1063/1.494384>. URL <http://scitation.aip.org/content/aip/proceeding/aipcp/10.1063/1.4943847>.
- Yu, J., Berger, L., Wimmer-Schweingruber, R., Bochsler, P., Klecker, B., Hilchenbach, M., and Kallenbach, R. Suprathermal helium in corotating interaction regions: combined observations from SOHO/CELIAS/STOF and ACE/SWICS. *Astronomy and Astrophysics*, 599:A13, March 2017. doi: 10.1051/0004-6361/201628641.
- Zank, G. Pickup Ion Injection and Acceleration at Perpendicular Shocks. *International Cosmic Ray Conference*, 7:468, 1999.
- Zank, G. P., Pauls, H. L., Cairns, I. H., and Webb, G. M. Interstellar pickup ions and quasi-perpendicular shocks: Implications for the termination shock and interplanetary shocks. *Journal of Geophysical Research*, 101:457–478, January 1996. doi: 10.1029/95JA02860.
- Zhao, X.-P. and Hundhausen, A. J. Organization of solar wind plasma properties in a tilted, heliomagnetic coordinate system. *Journal of Geophysical Research*, 86:5423–5430, July 1981. doi: 10.1029/JA086iA07p05423.
- Ziegler, J. F. and Chu, W. K. Stopping Cross Sections and Backscattering Factors for ^4He Ions in Matter, $Z = 1-92$, $E(^4\text{He}) = 400-4000$ keV. *Atomic Data and Nuclear Data Tables*, 13:463, 1974. doi: 10.1016/0092-640X(74)90009-6.

BIBLIOGRAPHY

Ziegler, J. F. *The Stopping and Ranges of Ions in Matter: Handbook of Stopping Cross-Sections for Energetic Ions in All Elements*, volume 5. Elsevier, 2013.

Acknowledgments

Firstly, I would like to express my sincere gratitude to my supervisors Prof. Wimmer-Schweingruber and Dr. Berger for their continuous support of my Ph.D studies and related research. I benefited a lot from the frequent discussion with them about the progress of my research. I thank Dr. Heidrich-Meisner for her review of this thesis.

My sincere thanks also goes to the members of the solar-wind group lead by Prof. Wimmer-Schweingruber. The regular meeting greatly widened my research giving it new perspectives.

I thank the DAAD for the financial support of my full scholarship for my Ph.D research as well as the funding from DLR. I thank our secretary Ms. Nebendahl for all the paperwork related to me.

Last but not the least, I would like to thank my family: my wife (Dr. Cheng) who gave up her job, accompanied me to Kiel and gave birth to our daughter and son, and my parents and sister for supporting me spiritually.

Eidesstattliche Erklärung

Ich versichere an Eides Statt durch meine eigenhändige Unterschrift, dass ich die vorliegende Arbeit selbstständig und ohne fremde Hilfe angefertigt habe. Stellen, die wörtlich oder dem Sinn nach auf Publikationen anderer Autoren beruhen, sind als solche kenntlich gemacht. Ich versichere außerdem, dass ich keine andere als die angegebene Literatur verwendet habe. Diese Versicherung bezieht sich auch auf alle in dieser Arbeit enthaltenen Grafiken, Skizzen, bildlichen Darstellungen und dergleichen.

Die Arbeit als Ganzes wurde bisher keiner anderen Prüfungsbehörde vorgelegt. Teile der Arbeit wurden bereits in begutachteten Fachzeitschriften veröffentlicht und sind als solche erkennbar. Die Quellennachweise der in den einzelnen Veröffentlichungen referenzierten Inhalte finden sich in der jeweiligen Veröffentlichung selbst und werden nicht zusätzlich im Quellennachweis dieser Arbeit aufgeführt. Für das Einbinden der Veröffentlichungen in diese Arbeit wurde die ausdrückliche Genehmigung der publizierenden Fachzeitschrift eingeholt.

Außerdem erkläre ich, dass die Arbeit unter Einhaltung der Regeln guter wissenschaftlicher Praxis der Deutschen Forschungsgemeinschaft entstanden ist.
